STRUCTURE AND PROPERTIES OF NANOPARTICULATE MICA – THERMOPLASTIC COMPOSITES

A THESIS

SUBMITTED TO THE

UNIVERSITY OF PUNE

FOR THE DEGREE OF

DOCTOR OF PHILOSOPHY

IN

CHEMISTRY

BY

S. SUBRAMANIYAM

POLYMER SCIENCE AND ENGINEERING DIVISION

NATIONAL CHEMICAL LABORATORY

PUNE - 411 008

AUGUST 2005

CERTIFICATE

This is to certify that the work incorporated in the thesis entitled "**Structure and Properties of Nanoparticulate Mica–Thermoplastic Composites "** submitted by Mr. S. Subramaniyam was carried out by him under my supervision at the National Chemical Laboratory, Pune. Such material as has been obtained from other sources has been duly acknowledged in the thesis.

Date: .08.2005

National Chemical Laboratory — Dr. S. Radhakrishnan

Pune 411 008 — Research Guide

DECLARATION

I hereby declare that the work incorporated in the thesis entitled "**Structure and Properties of Nanoparticulate Mica–Thermoplastic Composites**" submitted for the degree of Doctor of Philosophy to the University of Pune, has been carried out by me at the National Chemical Laboratory, Pune under the supervision of Dr. S. Radhakrishnan. The work is original and has not been submitted in part or full by me for any other degree or diploma to this or any other university.

Date: .08.2005

National Chemical Laboratory
Pune 411 008

S. Subramaniyam
Research Student

Acknowledgements

I take this opportunity with a deep sense of gratitude to pen down my sincere thanks to my research advisor Dr. S. Radhakrishnan, for his keen interest, thought provoking discussions, benign countenance, cheerful disposition and constructive criticism throughout the course of this doctoral study.

I would like to thank Ms. Pawaskar, Mr. Gaikwad and Mr. Godbole for the instrumental analysis of various samples.

The selfless help offered by Easwar, Jayanthi, Mallikarjuna, Devraj and Selvakannan at various points of time is gratefully acknowledged.

I would like to acknowledge my colleagues in Lab No: 948 – Dr. Deshpande, Dr. Rahul, Dr. Shivkalyan, Dr. Arindam, Dr. Sreejith, Francis, Swarnendu, Pradip, Santosh, Narendra, V. V. Radhakrishnan, Shalaka, Ramanujam, Jaykarna and Raut for keeping my spirits up during my tenure here.

I would like to thank my seniors Dr. Ramesh, Dr. Murugan, Dr. Amar Gopal, Dr. Thiagarajan, Dr. Krishnaswamy, Dr. Pasupathy, Dr. Mangaleswaran, Sankar, Pai, Nirmalya and Suresh Kumar for their guidance at various junctures.

I would also like to thank my dear friends Girish, Nagendra, Anirban, Ramakrishna, Vijayraj, Shankar, Suresh Kumar, Thirunavukkarasu, Murugan, Kishore, Ilango, Ramesh Kumar, Victor, Shivakumar, Srinivasa Rao, Abhishek, Sonu, Pratap, Harish and many others whose good wishes have fuelled me along to this stage.

I wish to thank the Director, National Chemical Laboratory, Pune for the infrastructure and UGC for the financial assistance.

Finally, I would like to thank my parents, sisters and relatives for their love, warmth, understanding and ethics.

National Chemical Laboratory *(S. Subramaniyam)*

Pune 411008

CONTENTS

1.1 Introduction

Mankind has progressed from the Stone Age, through the Bronze, Iron, and Steel Ages into its current age, the Age of Polymers. An age in which synthetic polymers are and will be the material of choice. Though mankind had been using naturally occurring polymers such as cotton, wool, rubber, gums and leather since times immemorial, it was the rapid development and huge expansion of the petrochemicals industry giving synthetic polymeric materials which are used by the modern society. The two important reasons behind the phenomenal commercial success of plastics has been its relatively high resistance to chemical, atmospheric and biological attack and the comparative ease with which the physical properties of the materials could be varied by either modifying the chemical structure or by incorporating various additives in these plastics. This versatility is a direct consequence of the large size and the associated geometric possibilities latent in the macromolecules. Expanding industrial activities and ever-rising living standards create a continuous demand for improved materials that satisfy increasingly stringent requirements such as higher strength, modulus, thermal and electrical conductivity, HDT, lower thermal expansion coefficient and reduced cost. It was this constant search that led to the development of composites technology.

1.2 Composites

By definition, a composite is a material that is made up of two or more distinct phases with a recognizable interface or boundary. There can be a variety of materials which could be used for the formation of composites such as ceramics, metals, plastics, carbon fibres, glass, etc.

Polymer composites are plastics within which there are embedded particles or fibres with the major component being the polymer (matrix) and the particles being additives (dispersed phase). Such composites exhibit quite different properties than the original materials individually. This arises due to various effects:

1) polymer molecules wrapping around the stiff additive particles/ fibres
2) interfacial forces between the two phases
3) distribution of stress/ applied load
4) reinforcing effect, etc.

A major driving force behind the development of composites has been to produce materials with improved specific mechanical properties over existing materials. In addition, polymer composites are useful in applications where the environment would be detrimental to other materials. Cost is ever present in the engineering equation and it is the balance of cost and performance that determine whether or not a polymer composite will be preferred over an alternative structural material option.

1.3 Classification of Composites

Composites, in general are classified either based on the structural components or the matrix.

1.3.1 Structural Components based Composites

1. Fibre Reinforced Composites- these contain reinforcements having much greater length than their cross-sectional dimensions. They may be continuous (with lengths running the full length of the composite) or discontinuous (of short lengths). These fibres may be unidirectional, cross woven or random. Typical examples are glass fibre reinforced

plastics, carbon fibres in epoxy resins, wood (a composite of cellulose in a matrix of lignin), vehicle tyres in which rubber is reinforced with nylon cords.

2. Particulate Filled Composites- these include materials reinforced by spheres, rods, beads, flakes, and many other shapes of roughly equal axes. The example of these are polymeric materials incorporated with different fillers such as glass spheres or finely divided powders, polymers with fine rubber particles, etc.
3. Laminar Composites- these are composed of two or more layers held together by the matrix binder. These have two of their dimensions much larger than the third. Wooden laminates, plywood and some combinations of metal foils, glasses, plastics, film and papers are laminar composites. Some ceramic and metallic composites also fall in this category.
4. Skeletal Composites – These are composed of continuous skeletal matrix filled by a second matrix. For example, honeycomb structure of the polymer filled with additives.

1.3.2 Matrix based Composites

1. Ceramic Matrix Composites (CMC)- Ceramic matrices are often used with carbon, ceramic, metal and glass fibres. These are used in rocket engine parts and protective shields. Glass matrices are mostly reinforced with carbon and metal oxide fibres. Heat resistant parts for engine, exhausts and electrical components are their primary applications. Carbon matrices with carbon whiskers or carbon fibres as reinforcement are used for desired properties. Carbon in the form of diamond and graphite has high heat capacity per unit weight and therefore selected as ablative materials.

2. Metal Matrix Composites (MMC)- Metal matrices of iron, nickel, tungsten, titanium, aluminium, and magnesium are generally used for high temperature usage in oxidizing environment.
3. Polymer Matrix Composites (PMC)- The reinforcing filler particles are dispersed in a thermoset or a thermoplastic resin in these composites. Henceforth, the focus in this thesis would be restricted to polymeric composites, which provides the framework for further discussions.

1.4 Advantages of Composites

The chief among the many advantages that composites offer over traditional materials are

- ✓ High strength
- ✓ Lower weight
- ✓ Great freedom of shape or flexibility in design
- ✓ High dielectric strength
- ✓ Dimensional stability and fatigue endurance
- ✓ Corrosion and environmental resistance
- ✓ Low tooling costs

Composites, literally have a endless number of applications. Due to their high strength to weight ratio, they have applications ranging from aerospace to sports goods. Because of their electrical insulating properties, composites are used widely in appliances, tools and other machinery. Additionally, corrosion-resistant composite tanks and pipes offer

extended service life over metals. Strong and stiff glass fibers carry loads imposed on the composite while the resin matrix spreads the load across the fibers.

1.5 Fillers for Polymer Composites

Historically, fillers have been used in polymers, paints, thickening agents, extenders or composites as cost effective materials. Actually, they play a more important role than being a mere inert additive.[1-5] More appropriately, they are christened functional fillers, mineral additives or reinforcing agents. For decades, mineral fillers have been added to thermoplastics and thermosets to form composites. Compared to neat resins, these composites have a number of improved properties including tensile strength, heat distortion temperature and modulus. Thus for structural applications, composites have become very popular and are sold in billion-pound quantities. Clearly, the idea of adding fillers to thermoplastics and thermosets to improve properties, and in some cases decrease the cost, has been very successful for many years. However, as one desirable property is changed, nearly all of the other physical and mechanical properties are affected. Hence, it is essential to optimize the filler type, composition and the processing parameters to obtain the best performance from these materials.

1.5.1 Characteristics of Fillers

Some of the important characteristics of fillers that have a considerable influence on its properties in consonance with a polymer matrix are the average particle size, particle size distribution, particle shape, particle integrity, surface properties and abrasion. Fine particles increase the mechanical properties but are difficult to disperse thereby increasing the viscosity. The shape of the filler particle is found to have a

tremendous effect on flexural modulus. Aspect ratio, defined as the ratio of the longest length of a particle to its thickness thereby becomes extremely significant. As a mineral's shape progresses from a cube to a block to a plate to a flake to a fibre, the aspect ratio increases as shown in the figure 1.1. The melt viscosity of the composite is found to be a

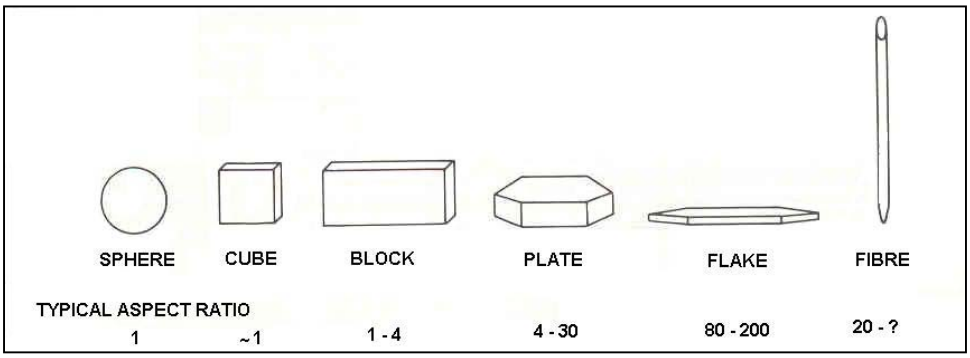

Figure 1.1 Aspect ratios of various fillers

function of the filler loading level, surface area and aspect ratio. Narrower distribution of similarly shaped particles results in a higher melt viscosity. A critical aspect ratio is necessary in a composite to allow a functional filler to receive an applied stress. A primary particle is the smallest unit that has a coherent shape. Aggregates are defined as primary particles that have been fused together. Agglomerates represent an additional degree of structuring, where primary particles or aggregates are bonded together in nonintergrown unions such that the total surface area does not differ significantly from the sum of individual areas. Some minerals like talc and mica are easily delaminated along the crystallographic planes. Although friability of minerals is a factor, their structural strength can be so tough that abrasivity becomes an issue. Abrasion properties

are quantified by the moh's hardness scale. Sharp edges and rod shaped particles have greater abrasive effects than smooth or rounded particles.

1.5.2 Types of Fillers

There is a plethora of fillers to choose from these days and the selection is mostly done based on the end application.[6,7] Both natural and synthetic compounds are used as fillers. Most of the fillers like calcium carbonate, clays, talc, mica, wollastonite, glass fibre, silica, aluminium hydroxide, magnesium hydroxide and magnesium carbonate are used extensively in thermoplastics. Relative abundance and high purity of calcium carbonate, lamellar structure and softness of mica and talc, high aspect ratio of wollastonite, special reinforcing capabilities of glass fibre, antiblocking nature of silica, flame retardance of aluminium hydroxide, coating applications of magnesium hydroxide and smoke suppressant characteristics of magnesium carbonate vouch for their functional uses.

1.6 From Composites to Nanocomposites

Polymer nanocomposites combine the concept of composites and nanometer size materials. In the conventional composites (thermoplastic or thermoset), the filler may enhance one property while compromising on others. In contrast to the conventional systems where the reinforcement is on the order of microns, discrete constituents of the order of a few nanometers exemplify polymer nanocomposites.[8-11] This empowers us to tailor revolutionary material combinations. These new materials circumvent classic material performance trade-offs by accessing new properties and exploiting unique

synergism between materials.[12-14] This only occurs when the length-scale of morphology and the fundamental physics associated with a property coincide on the nanoscale. Size does matter and the physics, which dominates the processes at the nanometer length scale, has qualitative differences from the physics that dominates our macroscopic world. Uniform dispersion of these nanoscopically sized filler particles produces ultra-large interfacial area per unit volume between the nanofiller and host polymer. This immense internal interfacial area and the nanoscopic dimensions fundamentally differentiate polymer nanocomposites from traditional composites and filled thermoplastics.

Considering the number of potential nano-sized materials, polymeric resins, and applications, the field of polymer nanocomposites is immense. Development of multicomponent materials, whether microscale or nanoscale, must simultaneously balance four interdependent areas: constituent-selection, fabrication, processing, and performance. This is still in its infancy for polymer nanocomposites. Developing an understanding of the characteristics of this interphase region, its dependence on nanoelement surface chemistry, the relative arrangement of constituents and, ultimately, its relationship to the properties, is a current research frontier in nanocomposites. Equally important is the development of a general understanding of the morphology-property relationships for mechanical, barrier, and thermal response of these systems.

1.6.1 Advantages of Nanocomposites over Conventional Composites

Some of the major advantages that nanocomposites offer over traditional polymeric composites are

- ✓ Dramatic improvements in mechanical properties like tensile and flexural modulus, strength, elongation and toughness at much lower concentrations of the additive.
- ✓ Greater thermal stability and higher HDT.
- ✓ Excellent fire retardant characteristics.
- ✓ Considerable improvement in barrier properties due to the tortuous path created by the flaky fillers when dispersed in the polymer matrix.
- ✓ Very good transparency because of the length scale involved that decreases scattering.
- ✓ Relatively better biodegradation.
- ✓ Good scratch resistance.
- ✓ Easier processing due to avoidance of cumbersome fabrication techniques and lower filler loading levels.

1.7 Preparative Strategies for Nanocomposites

There are a lot of methods to synthesize nanoparticles in general, but the discussion here would be restricted to preparation of nanoparticles using polymer matrices,[15,16] which would eventually result in nanocomposites. These strategies could be classified in to five major categories. They are

1) Sol-gel processing

2) Incorporation of metals and metal complexes in polymers by coordination interactions

3) Intercalation in 2D layered structures

4) Intercalation in 3D frameworks

5) Incorporation of inorganic particles and clusters

1.7.1 Sol-gel Processing

The formation of a nanocomposite or an organic/ inorganic hybrid material is carried out either by a sequential two-step process, wherein a secondary network is formed in a primary one, or by the simultaneous formation of the two networks. The resulting materials are microscopically phase separated, but macroscopically uniform. A major drawback in this approach is the difference in the relative thermal stabilities of the two components placing a severe restriction on the preparative conditions due to the lower thermal stability of the organic polymer. This problem could be easily circumvented by the sol-gel process in which complex metal oxide frameworks are accessed by simple hydrolysis and condensation reactions at ambient temperatures starting with the respective molecular precursors. The morphologies and properties of the resulting materials can be controlled by the reaction conditions and the precursors used, e.g. type of solvent/ catalyst used, catalyst to alkoxy ratios, etc.

Organic polymers with functional groups that have specific interactions with compounds created in the sol–gel process, e.g. hydrogen bonding to residual silanol groups on the formed silica can be chosen to have a high degree of homogeneity and optical transparency to avoid macrophase separation in the nanocomposites. Towards this end, organic polymers with hydrogen bonding ability such as poly(2MOx), PVP, poly(DMAA), PVA, PMMA, PVAc, polyamides, polyethersulfones[17], polymeric perfluoroalkylsulfonates (Nafion)[18-21], and hydroxy end-capped polysiloxanes were incorporated into sol–gel reaction mixtures[22-27]. The sol–gel process can be employed

using a variety of different inorganic precursors and is not limited to SiO_2 alone. Examples are composites of poly(BA), PDMS or poly(PTA) with titania/ silica or pure titania species[28-32]. Composite materials with inorganic species such as zirconia or mixed silica–titania or silica–alumina have been produced using Nafion as the polymer component[33,34].

The high porosity of a silica network formed by the sol–gel process can be used for an impregnation of the material with polymers as well as with monomers, which can be polymerized in situ. Thus, PMMA/ silica hybrids were prepared, and it was found that the mechanical properties of the pure silica species could be improved significantly depending on the amount of PMMA included and by the addition of a coupling agent such as methacryloxytrimethoxysilane[35].

Polyimide–silica gel hybrids have been prepared by the simultaneous formation of polyimides and a silica network formed in a sol–gel process. The hydrolysis and condensation of TMOS was carried out in a solution of *N,N*-dimethylacetamide (DMAc) containing 5% LiCl, $CaCl_2$ or $ZnCl_2$, and a polyimide intermediate. Films were cast from the resulting mixtures and the solvent was gradually evaporated. The results of this procedure were clear, transparent, pale yellow or amber-colored hybrid films in which the salts were dispersed at the molecular level. Pyrolysis of the composites at 600 ºC gave mesoporous silica[36].

Silicon alkoxides possessing polymerizable alkoxy groups have been synthesized to obtain non-shrinking nanocomposites. The alkoxy groups were liberated during the sol-gel processing as the corresponding alcohols[37,38].

The sol–gel process of transition metals such as titanium, zirconium, or vanadium is very fast compared to that of silicon, and therefore a better control over the polycondensation is required to obtain homogeneous composite materials in a simultaneous inorganic and organic polymerization reaction. This can be achieved via a partial substitution of alkoxides groups in the precursors by stronger complexing ligands such as bidentate systems.[39-41]

A slight variant of this process is the polymer mediated growth (PMG) or matrix mediated growth technique. Radhakrishnan et al. have utilized this technique to synthesize a number of compounds like $CaCO_3$, $CuCl_2$, CdS, $CaSO_4$, etc. wherein the morphology, crystalline phase, orientation and growth habit of these compounds could be easily tailored.[42-45]

1.7.2 Incorporation of Metals and Metal Complexes in Polymers by Coordination Interactions

Polymerization and copolymerization of metal coordinating monomers, coordination of metals to preformed polymers and direct incorporation of the metal into the polymer chain are some of the methods for inclusion of metals in organic polymers. Metal ions such as Zn[46], Ni[47], Ru[48], Pd[49], and lanthanides[50] were incorporated as salts in to matrices of poly(vinyl pyridines)[46], poly(vinyl amines)[51] or poly(L-histidine)[52], as homo or copolymers exploiting the lewis basicity of the respective matrices. Palladium salts incorporated into a polyolefin containing unsaturated side groups such as polybutadiene or polyisoprene can cause crosslinking between the polymer chains by

palladium catalyzed Heck-type reactions. This methodology used to obtain crosslinked polymeric systems is called "reactive blending"[49,53,54].

Metals could also be incorporated in to the polymers by the use of metal co-ordinating monomers and subsequent polymerization or copolymerization.[55-58]. Metals coordinated with ligands that include functional groups that are able to initiate a polymerization reaction, or that can be transformed to have such a functionality[59-62] are used to form metal core macromolecules. Fe(II) and Ru(II) complexes, with one to three (4,4'-halomethyl)-2,2'-bipyridine (bpy) ligands, have been used to initiate living cationic oxazoline polymerizations[59,61,62] to obtain polymers with very low polydispersities.

1.7.3 Intercalation in 2D layered materials

The 2D materials, which are of interest in these type of nanocomposites, are the layered silicates. The layered silicates belong to the family of 2:1 layered silicates popularly known as Phyllosilicates. Their crystal structure consists of layers made up of two tetrahedrally coordinated silicon atoms fused to an edge-shared octahedral sheet of either aluminum or magnesium hydroxide as shown in the figure 1.2. Sheets of atoms, of the general composition $(Si,Al)_4O_{10}(OH)_2$, are stacked one above another in various ways and with different kinds of atoms lying between the layers and holding them together. The layer thickness is around 1 nm, and the lateral dimensions of these layers may vary from 30 nm to several microns or larger, depending on the particular layered silicate.[63,64] Stacking of the layers leads to a regular van der Waals gap known as the inter layer gallery. Isomorphic substitution of the Al and Mg ions creates negative charges that are counter balanced by the alkali or alkaline metal cations residing in the gallery.

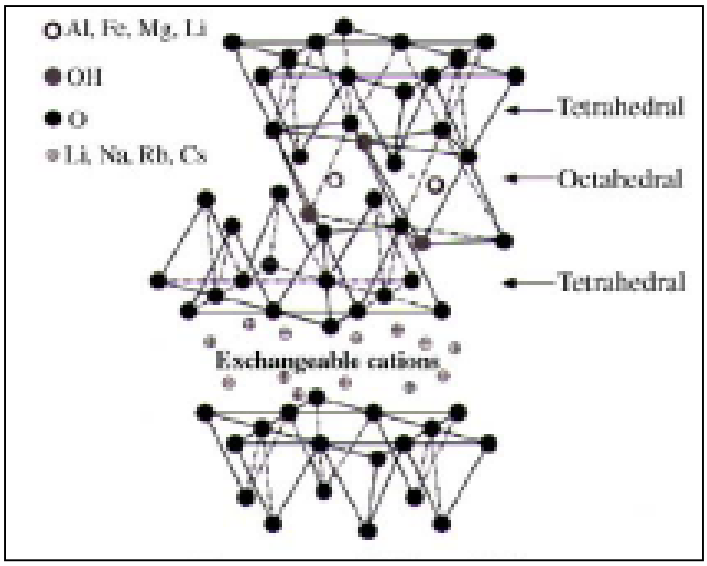

Figure 1.2 The structure of a 2:1 layered silicate

The silicates are generally hydrophobized by ion exchange reactions to improve the wettability of the silicate by the polymer.

2D materials intercalated in a polymeric matrix, in principle fall in to three major categories based on the level and type of dispersion in the polymeric matrix as shown in the figure 1.3. They are

(a) **Intercalated nanocomposites** in which the layered silicate is dispersed in the polymeric matrix in a crystallographically regular fashion with an interlayer spacing of a few nanometers (< 6 nm) irrespective of the polymer to silicate ratio. The polymer chain is intercalated between the silicate layers resulting in a well ordered multilayer morphology consisting of alternate silicate and polymer layers.

(b) **Delaminated/ Exfoliated nanocomposites** in which the individual silicate layers are separated in the polymer matrix by average distances greater than 8 nm.[65] The silicate

platelets are uniformly dispersed in the polymeric matrix and no peaks are seen in the XRD scans of these materials indicating the collapse of an ordered structure.

(c) **Flocculated nanocomposites** in which the intercalated and stacked silicate layers are flocculated to some extent due to the hydroxylated edge–edge interactions of the silicate layers.

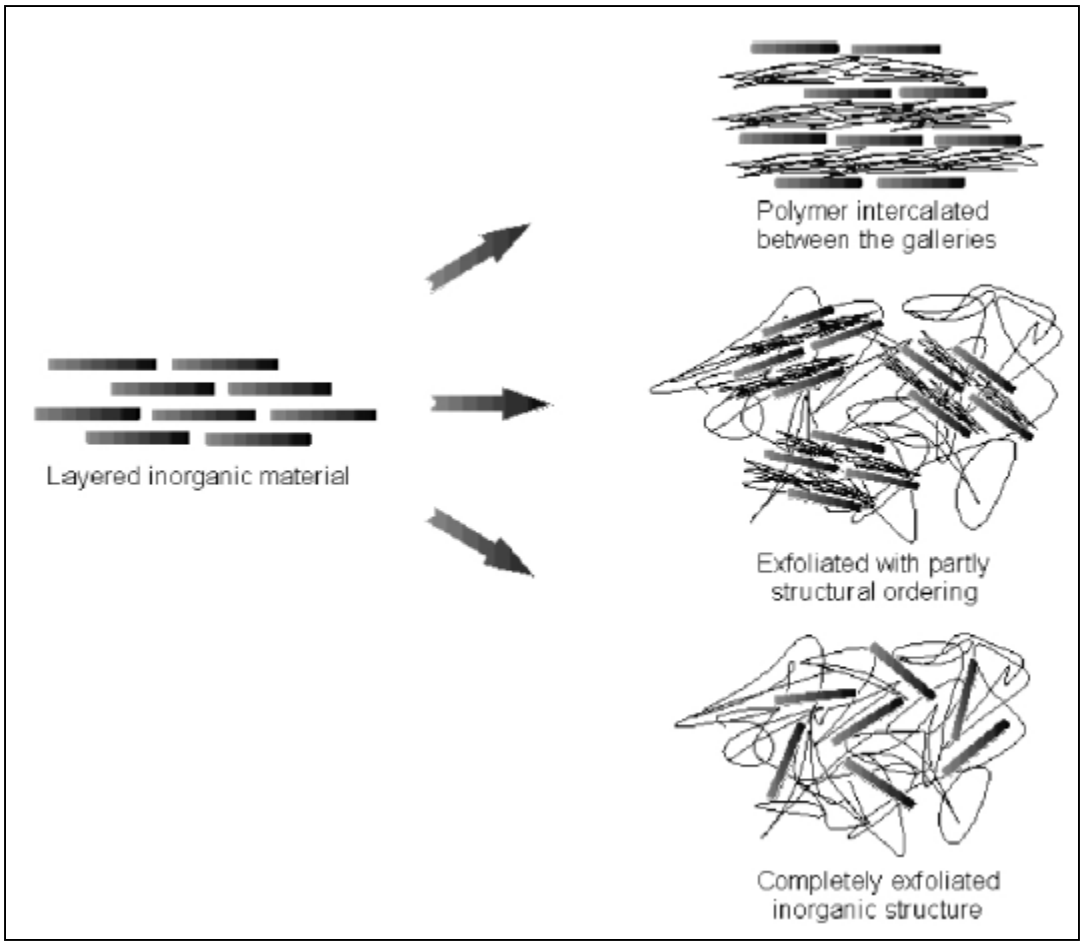

Figure 1.3 Schematic showing different types of nanocomposites

Exfoliated systems display greater property enhancements as compared to intercalated structures due to their superior dispersion but are more difficult to achieve. These nanocomposites can be prepared by three main strategies. They are as follows

1.7.3a Intercalation of Polymer / Prepolymer from Solution

A negative variation in the Gibb's free energy is expected to be the prerequisite for the exchange of the polymer with the previously intercalated solvent in the interlayer gallery. The driving force for the polymer intercalation in to the layered silicate is the entropy gained by desorption of solvent molecules, which makes up for the loss in entropy of the confined intercalated chains. Intercalation from solution has been reported from both aqueous and non-aqueous media. PEO,[66] PVP,[67] PVA[68] and PEVA[69] have been intercalated from aqueous solutions whereas PCL,[70] PLA,[71] HDPE[72] and some liquid crystalline polymers[73] have been intercalated in organic solvents.

1.7.3b In situ Intercalative Polymerization

This is a method in which the monomer is first intercalated in to the layered silicate and subsequently polymerized there itself resulting in an increase in the basal spacing. Polymerization can be initiated either by heat, radiation, by the diffusion of a suitable initiator or a catalyst. This was the actual method adopted by the Toyota researchers, which heralded a new dawn in the field of polymer nanocomposites.[74] Nylon-6,[75] PCL,[76-78] PU,[79-81] PMMA,[82,83] PS,[84-87] PBO,[88] PE,[89-91] PP,[92,93] PET,[94-96] and epoxy[97-101] based MMT nanocomposites have been synthesized by this method.

1.7.3c Melt Intercalation

In this method, the polymer and the silicate is annealed statically/ under shear by heat or radiation above the polymer's melting point. The method is environmentally benign due to the absence of solvents and is compatible with the current industrial processing techniques like extrusion and injection molding making it economically viable. A range of structures from intercalated to exfoliated can be obtained by this method depending on the degree of penetration of the polymer chains in to the silicate layer. PS,[102,103] PS/ PE,[104] PEO,[105] N6,[106-109] PP,[110-114] PE,[115] PET,[116] PBT,[117] SAN,[118] PC,[119] PLA[120,121] and PBS[122,123] based layered silicate nanocomposites have been realized by this method.

1.7.4 Intercalation in 3D Frameworks

Zeolites are crystalline aluminosilicates with well defined pores smaller than 2 nm. There are a variety of naturally occurring as well as synthetic zeolites. Zeolites have attracted much interest as catalysts and adsorbents due to their thermal stability and intraporous acidity. Molecular sieves are also crystalline framework materials, but of a non-aluminosilicate nature. M41S-materials belong to the class of mesoporous three-dimensional (3D) solids with ordered porosity in the pore size range 2–10 nm. Due to their special properties, such as the controllable pore size, there is a plethora of possible applications of these materials[124,125]. All these porous inorganic solids are excellent hosts for intercalation reactions because they contain well defined empty pores and channels. A unique feature of these materials is their ability to discriminate between shapes and sizes of molecules. Therefore, the design of new materials requires a match of the features of

the guest with those of the host. Contrary to the layered materials, which are able to delaminate completely if the forces produced by the intercalated polymers overcome the attracting energy of the single layers, this is not possible in the case of the stable 3D framework structures. The obtained composites can be viewed as host–guest hybrid materials. There are two possible routes towards this kind of hybrid material: (i) direct threading of preformed polymer through the host channels (soluble and melting polymers) which is usually limited by the size, conformation, and diffusion behavior of the polymers, and (ii) the in situ polymerization in the pores and channels of the hosts as shown in the figure 1.4.

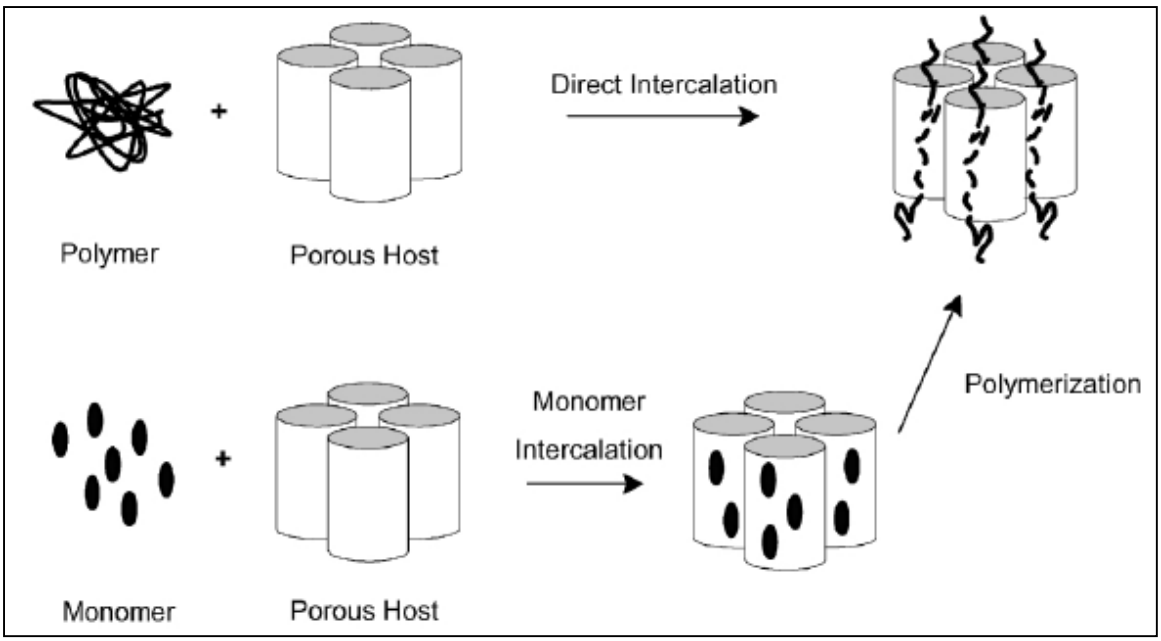

Figure 1.4 Intercalation in 3D frameworks

Nanocomposites of zeolite 13X, and crosslinked or linear PS and poly(EA) were prepared to form either a pseudo-interpenetrating polymer network (PIPN) or a full

interpenetrating polymer network (IPN). A surface-mediated cationic polymerization technique was applied for the formation of poly(PVE)–HY–zeolite hybrid materials containing polyenylium sequences[126].

The active protons of HY zeolites were used for cationic polymerizations of several vinyl monomers inside the pores. In porous materials where no such protons are present, such as MCM-41, arylmethylium was incorporated. Utilizing this method, the synthesis of well-defined poly(vinyl ethers) or poly(vinylcarbazole) under conditions of constricted geometry can be achieved[127].

1.7.5 Incorporation of Inorganic Particles and Clusters

Nanocomposites based on nanosized inorganic particles and clusters are an emerging field of research activity due to the interesting properties of the particles, such as their behavior as quantum dots or their possible super-para and super-ferromagnetism, in combination with the other properties of the materials including, for example, their optical transparency. Another advantage of such hybrid composites/ particles in an organic polymer matrix is the possible protection of systems that are sensitive towards environmental conditions (oxygen, humidity, etc.) by coverage with a protecting polymeric skin or inclusion in a polymeric matrix[128].

Encapsulation of small inorganic particles by a polymer layer, the so-called core–shell particles, can be carried out by an emulsion polymerization process. Polymerization occurs primarily at the surface of unmodified particles due to the adsorption of the monomer on the surface, followed by polymerization in the adsorbed layer[129-131]. 3-(trimethoxysilyl)propyl coated silica particles were prepared by the Stober method[132,133] followed by a surface-modification[134]. These particles were self assembled in a film and

UV copolymerized with different monomers such as MA, MMA, HEMA, and TFEA. The systems were able to selectively filter light with a bandwidth less than 20 nm[135].

The thermal decomposition of volatile metal compounds in a polymer matrix leads to the formation of zero valent metal particles, or particles of their oxides dispersed in the polymer matrix. Cobalt and iron carbonyls in the presence of polymers such as polybutadiene, polystyrene, polypropylene, different block copolymers, etc. were accessed by this method.[136-138]

In recent years, POSS inorganic – organic hybrid polymers have been developed up to a commercial scale. The chemistry of these systems is based on the design of well-defined inorganic oligomers with only a single polymerization or initiation site per cluster. Each of these clusters has an inorganic silica-like core and is surrounded by eight organic groups, seven of which are inert towards polymerization and only one is active. Polymerization at this single site results in a linear polymer with pendent inorganic clusters of approximately 1.5 nm diameter. The unique property of such materials is that there is no crosslinking and the linear polymeric structure allows for an easier processing and characterization of these systems by conventional analytical methods[139]. Different polymer backbones have been synthesized using a variety of different substitution patterns at the silica cage.

1.8 Mica as a Layered Silicate Reinforcement

Mica is the generic name given to a family of hydrous potassium aluminium silicates having similar properties.[63,64,140] The main commercial source of mica is pegmatite rock, where large books of mica can be separated from feldspar and quartz.

Mica deposits occur in pockets all over the world with a good number of reserves in India as indicated in the figures 1.5a and 1.5b respectively.

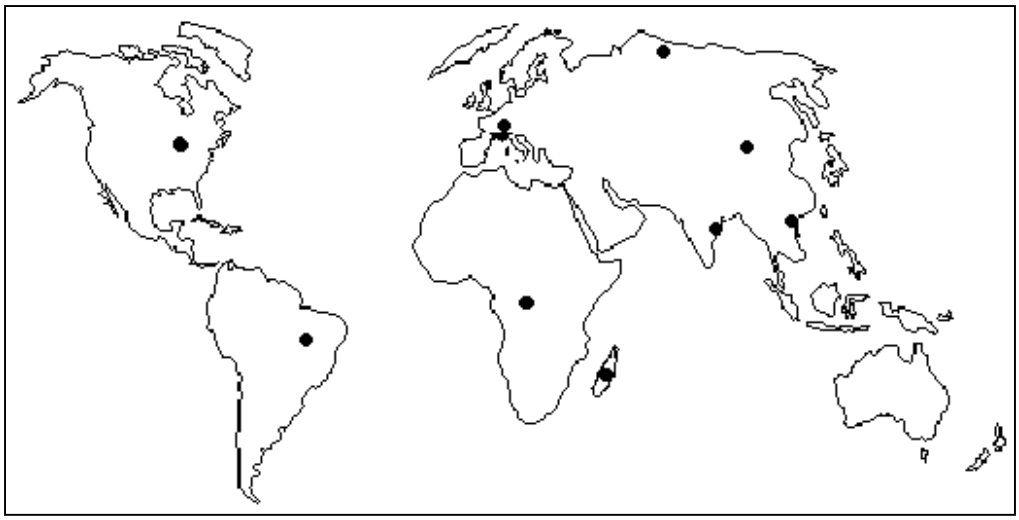

Figure 1.5a Global availability of mica

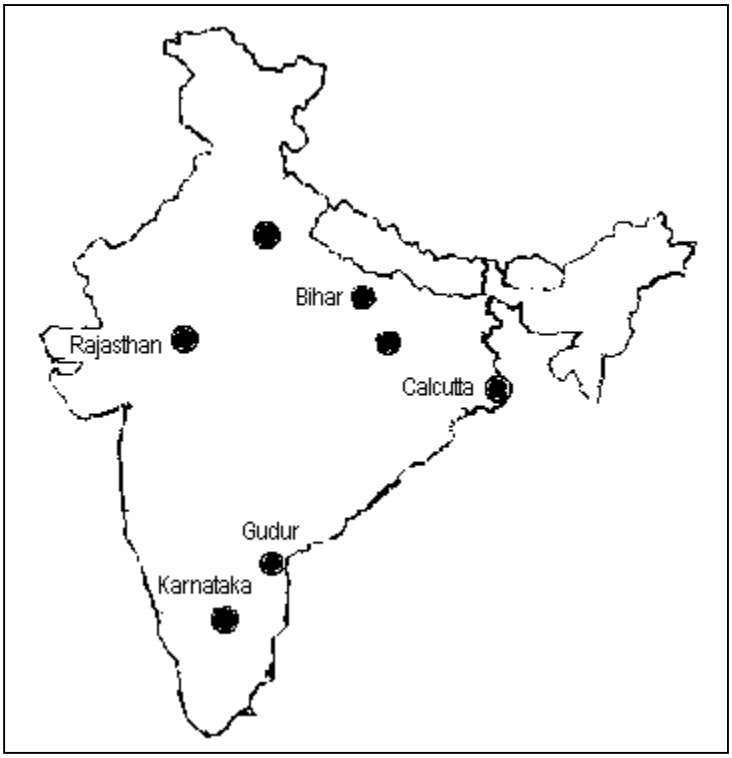

Figure 1.5b Mica availability in India

Condensation in a 1:1 ratio of a silica sheet with an alumina sheet gives rise to a 1:1, dimorphic or two-sheet mineral such as koalinite as shown in the figure 1.6a. Here, the tips of the silica tetrahedral project in to a hydroxyl plane of the octahedral sheet, replacing two-thirds of the hydroxyl ions. In a 2:1, trimorphic or three-sheet mineral, two silica sheets condense with an alumina sheet. The resultant layered structure is such that the alumina sheet is sandwiched between two sheets of inward-pointing, linked silica tetrahedra which is exemplified by the micas as shown in the figure 1.6b. The mica layers are not electrically balanced and require the presence of extra cations in interlamellar positions. However, there is one major difference between the micas and the conventional clay minerals like MMT. The layers in mica have a greater deficiency of charge and the balancing cations are held more strongly. There is evidence of ionic bonding, linking successive sheets through these additional cations. Unlike MMT-type minerals, the layers of mica cannot be expanded by water, nor can the cations between them be removed or exchanged.

The two principal types of mica commercially used are muscovite mica and phlogopite mica. The structure of an ideal muscovite may be written as $KAl_2(Si_3Al)O_{10}(OH)_2$, the positive charge deficiency due to substitution of Al^{3+} for Si^{4+} being balanced by the interlayer K^+ ions, giving a layer thickness or basal spacing of 1nm. The K^+ ions are in twelve-fold coordination, situated centrally on the lines joining the centers of the ditrigonal network of oxygen ions of opposing silicate layers. Muscovite is dioctahedral whereas phlogopite is trioctahedral [$KMg_3(Si_3Al)O_{10}(OH)_2$]. In a relatively less common variety of mica named chlorite, the trioctahedral mica-like layers alternate regularly with a hydroxide layer, having the general composition of

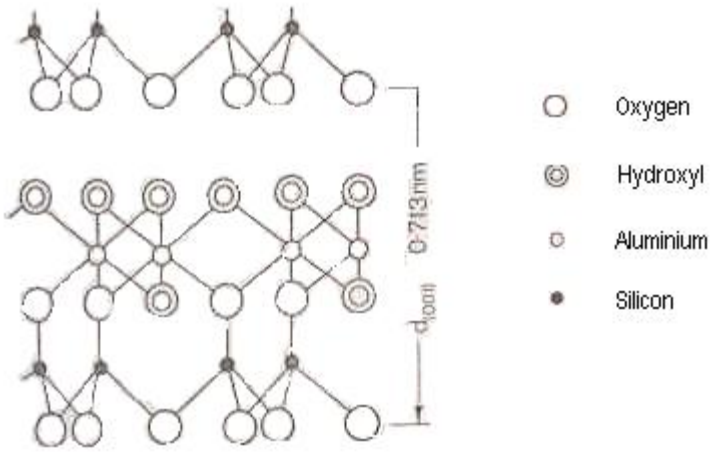

Figure 1.6a The layer structure of koalinite viewed along the *a*-axis

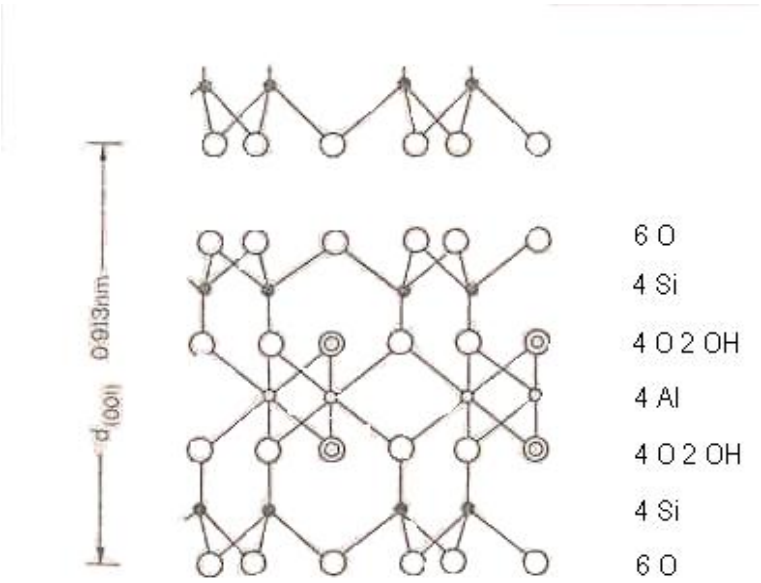

Figure 1.6b The layer structure of a 2: 1 silicate viewed along the *a*-axis

$(MgFe)_3(Si_3Al)_4O_{10}(OH)_2$ and $(MgAl)_3(OH)_6$ showing a repeat distance of about 1.42 nm. These occur in sedimentary deposits and are much softer. They are essentially hydrated silicates of magnesium and aluminium with a proportion of iron either in ferrous or ferric form. The charge deficiency in the mica-like layer is partly balanced by the positively charged hydroxide layer.

Some of the aspects that make mica a reinforcement par excellence for plastics are

- ✓ It has a remarkable mix of chemical, electrical, mechanical and thermal properties rarely found in any other product.
- ✓ It is transparent, flexible, and elastic and can be ground to very fine particles with a high-aspect ratio.
- ✓ It is chemically inert and can easily resist the action of heat, light, water, oil, solvents, alkalis and various chemicals.
- ✓ It is moisture proof, infusible, non-combustible having high tensile and flexural strengths and modulus of elasticity.
- ✓ It has excellent anti-sticking and anti-friction properties.
- ✓ It is relatively soft, with moh's hardness between 2.5 to 3.0 which helps to minimize equipment wear and abrasion during processing. It also eliminates abrasive effects on steel plates.
- ✓ It has a high degree of whiteness (81-85%).
- ✓ It has a high surface area and high-aspect-ratio.
- ✓ It acts as a noise control and vibration-damping agent.

- ✓ It is strongly absorbent to UV radiations and prevents penetration of destructive sun-rays, moisture, heat and atmospheric gases, etc. thereby helping to increase the service life and decorative value of the end products.
- ✓ It serves to reinforce the product, prevents microscopic ruptures, reduces warping, increases service temperature and lowers thermal expansion and conductivity. It does not change color at elevated temperatures or in the presence of resins and other mineral additives.
- ✓ Mica particle both transmits and reflects light producing decorative effects and designs. Since mica platelets tend to orient parallel to the mould surface, it imparts a better surface appearance than those attributed by glass fiber reinforcements and are superior to those obtained with fillers such as calcium carbonate, talc, etc.
- ✓ In thermoplastics, mica promotes uniform cell structure acting as a nucleating agent, lowers its density, reduces the cost, adds low temperature impact resistance and reduces flammability.

The largest thermoplastic application of mica is in polyolefins. These reinforced compounds are now replacing engineering plastics like ABS and nylon and steel in many applications. Most mica-polyolefin resins are used in automotive applications. Some typical commercial products are air conditioner/ heater housings, instrument panels, crash pad retainers, fender lines, battery trays and fan shrouds. The under the hood applications usually take advantage of the higher HDT of mica. HDPE/ mica composites are also used for some interior parts, such as blow molded seat backs. Weight savings by replacement of metals is a driving force for many of these applications. PP/ mica composites can be as

stiff as steel, but weigh only 45 % as much.[141] Another interesting use of mica is in PP-PE copolymer foam for loudspeakers and musical instruments. Uniform and improved vibrational properties are found with mica, due to the high velocity of the sound in the mineral. The higher speed allows for a more compact speaker cone. A large market for mica-polyolefin composites is in appliances and hand tools. Thus mica qualifies as an exceptional filler, more so in case of thermoplastics.

1.9 Polymer Crystallization

It is a well known fact that polymers with some level of order in them tend to crystallize. The crystallization of polymers influences its morphology, structure and properties to a great extent. Recent studies have suggested that the polymer micro crystal is formed by folding of a single polymer molecule back and forth upon itself in a folded lamella type of structure as shown in figure 1.7 (Folded Lamellae theory).[142-145] This theory explains the formation of spherulites. The development of a crystalline polymer takes place in two stages, viz.1) Nucleation and 2) Growth. Crystallization starts with the

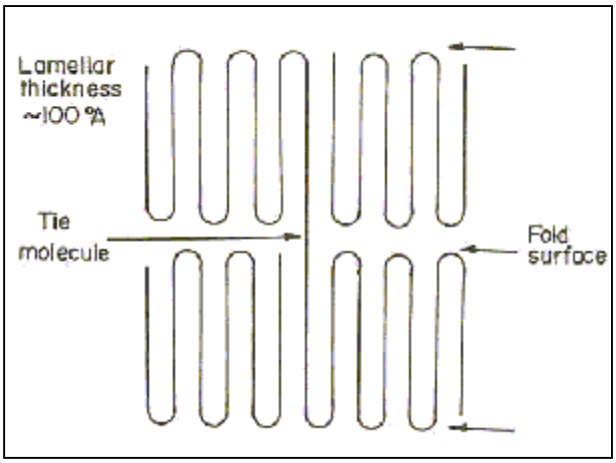

Figure 1.7 A schematic chainfold conformation

formation of an embryo. An embryo consists of a parallel array of chain strands. It grows or shrinks by acceptance or rejection of strands of the same length. If the size of the embryo is greater than the critical size (called the critical size nucleus), it grows spontaneously because this growth is associated with a decrease in the free energy. The polymer molecules are driven to uncoil high entropy conformations. The driving force for this is the lowering of enthalpy as the molecular strands are bound together in a crystalline array.

As shown in the figure 1.8, the chain is added on by folding along an edge. When the molecule ends, the step that results is the preferred place for another molecule to start crystallizing. The regular folding of the chains causes the crystal to split up into sectors. This feature is unique to polymers. The lamellae provide sources of nucleation for other

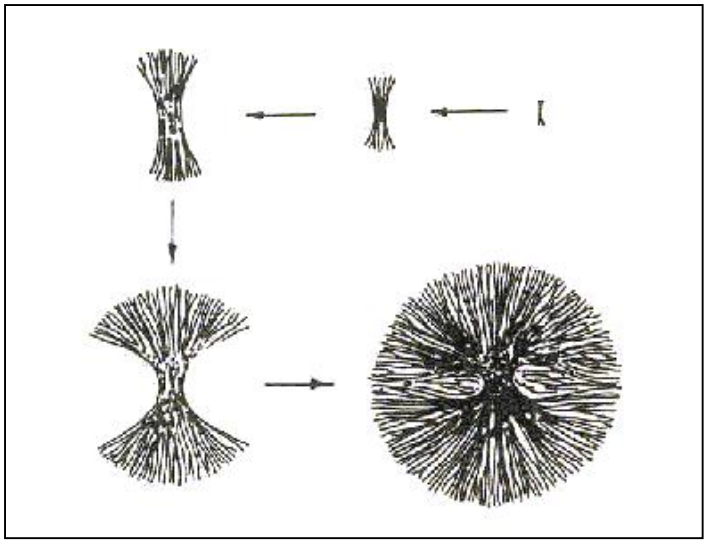

Figure 1.8 Stages in the formation of a spherulite

lamellae by taking in pure polymer from the surrounding amorphous matrix and achieve a paraboidal shape called dendrites. Growing lamellae get twisted and the shape of the growing bundle of lamellae becomes spherical. This is the spherulite. The time required

for the randomly coiled molecule in the melt to change its shape into a regularly folded form so that it can join a single lamella, is much longer than the crystal growth rate. Hence sections of the molecules are incorporated into neighboring lamellae crystals, the intervening lengths forming a part of the amorphous interlayer. The spherulites grow in size until they impinge at the boundaries so that their boundaries are polyhedral. The spherulites may be from sub micron to few microns in diameter.

1.9.1 Mechanism of Polymer Crystallization

Crystallization is a first order thermodynamic phase transition. Two basic processes in crystallization are initiation or nucleation, by which a new phase is initiated within a parent phase, and subsequent growth of the new phase at the expense of the parent. Two main theories describing crystallization of polymers have been developed. One uses a thermodynamic approach and provides a description of crystallization and morphology, and the other offers a kinetic description of the formation and growth of the nucleus.

Nuclei can be formed either homogeneously by means of static fluctuations in the parent phase or heterogeneously catalyzed by the presence of heterogeneities. In the latter process, nucleation starts on or in surfaces, cavities, and cracks of insoluble impurities. An example of heterogeneous nucleation is self-nucleation, caused by crystals chemically identical with the polymer. When impurities or residual crystals are present, the nucleation rate depends on the thermal history of the polymer and, more specifically, on the previous melting temperature; eventually, a temperature is reached at which all the possible seeds are destroyed. After the nucleus has formed, a new layer grows after

secondary nucleation, a process similar to primary nucleation. Therefore, polymer crystallization, whether manifested by observation of the growth rate, or the overall crystallization rate, is a result of the rate of formation and growth of stable nuclei as well as the rate at which untransformed chain units are brought to the growing faces.

The steady state nucleation rate per unit volume and time can be expressed by

$$N = N_O \exp\left(-\frac{E_D}{RT} - \frac{\Delta G^*}{RT} \right) \tag{1.1}$$

where N_o is a constant, E_D is the energy of transport in the solid-liquid interface, and ΔG^* is the free energy of formation of a stable nucleus. Because ΔG^* is a function of temperature, the nucleation rate is also function of temperature in accordance with equation 1.1. The nucleation rate is zero at the melting temperature and at absolute zero, reaching a maximum value at an intermediate temperature. The steady state nucleation rate given by the above equation can be incorporated into the expression for the overall crystallization rate or the spherulitic growth rate.

1.9.2 Kinetics of Crystallization

The theory which attempts to explain the kinetics of crystallization has been expounded by Von Galore, Johnson Mehl and Avrami. It is based on the analysis of growth from centers, nucleated either homogeneously or heterogeneously, and then proceeding in a given number of directions until impingement occurs, which is considered to stop development. The corresponding expression is

$$\ln(1 - X_t) = -Kt^n \tag{1.2}$$

where X = crystallinity

t = time

K = constant

n = Avrami exponent

Avrami's equation[142-144] is valid only for the initial part of the process and gives errors at later stages. This equation takes in to account, the different nucleation mechanisms and the impingement of crystals during the later stages of crystallization. As molecular weight increases, the deviation from Avrami equation occurs at a lower degree of crystallinity.

The Avarami exponent 'n' is very sensitive to the type of crystallization, presence of impurities, etc. As seen from its exponential relation with crystallinity, even a small change in 'n' brings about a tremendous change in the rate of crystallization.

$$G = G_O \exp\left(-\frac{E}{RT} - \frac{dF}{RT}\right) \tag{1.3}$$

where G_o = constant

G = growth rate at temperature T

E = activation energy for transport across liquid solid interface and

dF = free energy of formation of nuclei of critical size.

For crystallization to occur, considerable molecular mobility is necessary. Thus the temperature range for crystallization is between the glass transition temperature T_g and the crystalline melting point T_m. The overall rate of crystal formation is equal to the

product of the nucleation rate N and the growth rate G. The growth rate is diffusion controlled and is maximum just below T_m. The nucleation rate is maximum just above T_g. Therefore, the overall crystallite formation rate is maximum at a temperature about half way between T_g and T_m as indicated in the figure 1.9. Increasing the molecular weight of a polymer decreases its rate of crystallization because the diffusion rates in the melt/ solution are reduced. The progress of crystallization from the melt is generally described by the Avrami equation.

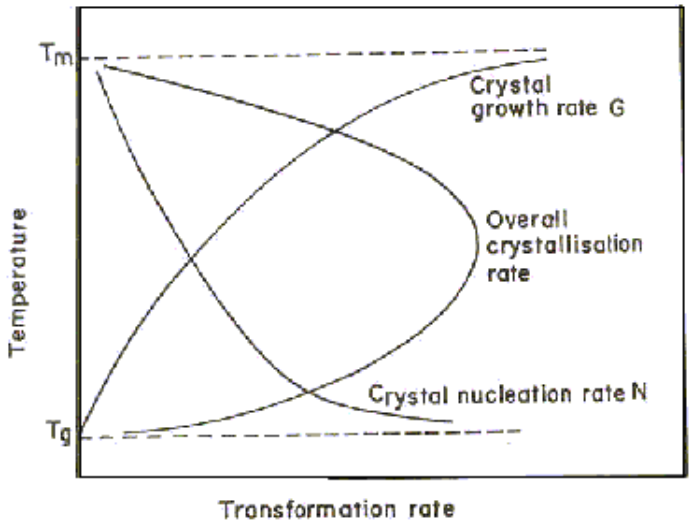

Figure 1.9 Crystallization profile as a function of temperature for a polymer

1.9.3 Importance of Nucleation in Polymer Crystallization

The morphology of semicrystalline polymers is crucial to their applications. Homogeneous nucleation generally does not provide consistent properties, as nuclei appear throughout the crystallization, giving a broad distribution of sizes, and hence crystallization is controlled too much by processing conditions. Heterogeneous nucleation gives crystals of consistent size, as all nuclei are present at the start of crystallization and

the nucleant controls crystallization. Heterogeneous nucleation may be caused by initiator residues, impurities, etc. or by addition of a specialized nucleating agent. Nucleation can occur on the surface of filler/ reinforcement where the action of fillers is due to the surface wetting and matched crystal structure around the environment of the filler. Nucleating agents tend to have rigid planar structures which are expected to provide the site for the first few polymer segments to adsorb and provide stable embryo nuclei.

Particulate and fibrous fillers can provide oriented growth from their surfaces. Transcrystalline structures are formed because of row nucleation leading to closely packed surface nuclei that inhibit lateral growth, leaving perpendicular growth to predominate near surfaces. Nucleation activity may be because of specific sites on the filler or polymer adsorption giving greater melt density near the surface than in the bulk. From a commercial viewpoint, nucleated PP molding compositions are frequently used for the manufacture of thin-walled (<0.4 mm) injection molded articles, which in case of a high MFI PP grade means a 30 % reduction of the cycle time. The nucleation of PP is also important for improving the optical properties of films; nucleated films having lower haze, higher gloss and improved clarity. Tendency towards delamination, excessive flash formation, sinking and voiding are found to decrease in parts molded from nucleated PP.

1.10 Dielectric Relaxations

1.10.1 Basic Principles of Dielectric Relaxations

A material is classified as “dielectric” if it has the ability to store energy when an external electric field is applied. If a DC voltage source is placed across a parallel plate capacitor, more charge is stored when a dielectric material is between the plates than if no

material (a vacuum) is between the plates. The dielectric material increases the storage capacity of the capacitor by neutralizing charges at the electrodes, which ordinarily would contribute to the external field. Thus, the ratio of the capacitance with the dielectric material to that without the material (vacuum) is known as the dielectric constant. The mode of charge storage in a dielectric material is depicted in the figure 1.10.

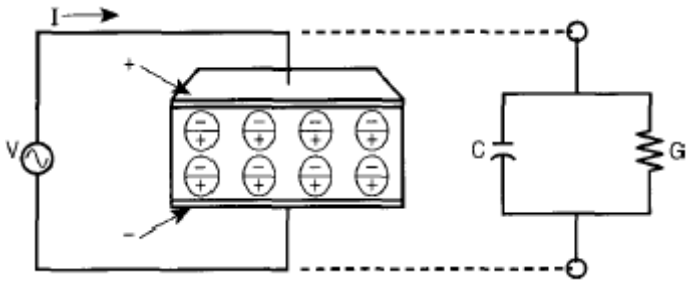

Figure 1.10 Charge storage in a dielectric in parallel plate configuration

If an AC sinusoidal voltage source is placed across the same capacitor, the resulting current will be made up of a charging current and a loss current that is related to the dielectric constant. This gives rise to a complex dielectric constant (ε), that consists of a real part (ε^{1}) which represents the storage and an imaginary part (ε^{11}) that represents loss. The real and the imaginary components are 90˚ out of phase with each other. Some amount of the energy stored in a dielectric gets dissipated which is quantified by the dissipation factor or loss factor/ tangent. Loss tangent is defined as the energy lost to the energy stored.

1.10.2 Permittivity in an Alternating Field

When a voltage is applied across the dielectric, energy is stored by one of the following mechanisms. They are

1) Electronic polarization
2) Atomic polarization
3) Orientation polarization
4) Interfacial or Space Charge polarization

Each dielectric mechanism has a characteristic relaxation frequency. As the frequency becomes larger, the slower mechanisms drop off. Electronic polarization occurs in neutral atoms when an electric field displaces the nucleus with respect to the electrons that surround it. Atomic polarization occurs when neighboring positive and negative ions "stretch" under an applied electric field. Both electronic and atomic polarizations create induced moments depending on the polarizability of the atoms or molecules. Unequal sharing of electrons between the atoms of a molecule causes a permanent dipole moment. In the absence of an external electric field, these moments are oriented in a random order such that no net polarization is present. Under an external electric field, the dipoles rotate to align with the electric field causing orientation polarization to occur. It is this orientation polarization, which is of fundamental importance in dielectric spectroscopy. Interfacial or space charge polarization occurs when the motion of migrating charges is impeded. The accumulated charges distort the field resulting in a net polarization. At high frequencies, electronic and atomic polarizations contribute to energy storage, which involves a resonance phenomenon. At low frequencies, orientation polarization contributes to energy storage and this involves a relaxation phenomenon.

In an alternating field of frequency f, the dipolar part of the polarization is a complex quantity. The orientation polarization may be out of phase with the applied field (i.e. the dipolar motion can no longer follow the applied field). When the polarization

becomes complex the permittivity becomes complex and, for a single relaxation mechanism called a Debye relaxation[149]

$$\varepsilon^* = \varepsilon_\infty + \frac{(\varepsilon_0 - \varepsilon_\infty)}{(1 + i\omega\tau)} \tag{1.4}$$

Where ε* - complex permittivity

ε_0 – permittivity at ω=0 or static permittivity

ε_α – permittivity in a field of infinitely high frequency

ω – frequency of the field

τ – relaxation time

Seperating the real and imaginary components of the complex permittivity, we have

$$\varepsilon^* = \varepsilon^1 - j\varepsilon^{11} \tag{1.5}$$

where $j^2 = -1$, ε^1 is the real and ε^{11} the imaginary component given by

$$\varepsilon^1 = \varepsilon_\infty + \frac{(\varepsilon_0 - \varepsilon_\infty)}{(1 + \omega^2\tau^2)} \tag{1.6}$$

$$\varepsilon^{11} = \frac{(\varepsilon_0 - \varepsilon_\infty)}{1 + \omega^2\tau^2} \tag{1.7}$$

τ, the relaxation time, has the dimension of time and, since the dielectric process is a rate process, is equal to the reciprocal of the mean rate coefficient, k. Such molecular rate processes usually follow an Arrhenius temperature law, written as (1.8) or (1.9)

$$k = \frac{1}{\tau} = A^1 \exp\frac{(-\Delta H^*)}{(RT)} \tag{1.8}$$

$$\tau = A \exp\frac{(\Delta H^*)}{(RT)} \tag{1.9}$$

where A(=1/ A^1) is a numerical constant

ΔH* is the Arrhenius activation enthalpy per mole

From equation (1.9)

$$\frac{d(\ln \tau)}{d(1/T)} = \frac{\Delta H^*}{R} \tag{1.10}$$

Thus a plot of ln τ against (1/ T) yields a slope of (ΔH*/ R). The relationship between the relaxation time τ and the frequency of maximum loss is found by differentiating equation (1.7) with respect to the angular frequency and equating to zero.

$$\frac{d\varepsilon^{11}}{d\omega} = 0 \tag{1.11}$$

at $1/\tau = \omega_{max.} = 2\pi f_{max.}$

Combining equations (1.9) and (1.10), a plot of $\ln(f_{max.})$ against (1/ T) gives a slope of (ΔH*/ R). Polymers generally don't show a single sharp dispersion as in the Debye case. There is a spread of relaxation times due to molecular weight distribution. In these cases, the complex permittivity is given by Cole-Cole equation.

$$\varepsilon^* = \varepsilon_\infty + \frac{(\varepsilon_0 - \varepsilon_\infty)}{1 + (i\omega\tau)^\beta} \tag{1.12}$$

where $0 \leq \beta \leq 1$.

1.10.3 Dielectric Relaxations in a Semicrystalline Polymer

Three distinct dielectric relaxation processes are observed in the case of semicrystalline polymers. They are the α, β and γ processes with the high temperature process being the α process. The α process is commonly considered to be connected with

the crystal fraction in the semicrystalline material. The β process in such polymers has been connected with the amorphous fraction and has been associated with the glass-rubber transition. The low temperature γ process is believed to have an amorphous phase origin but many have considered it to have an important component from the crystal phase too. In some cases, there might also be a δ relaxation.

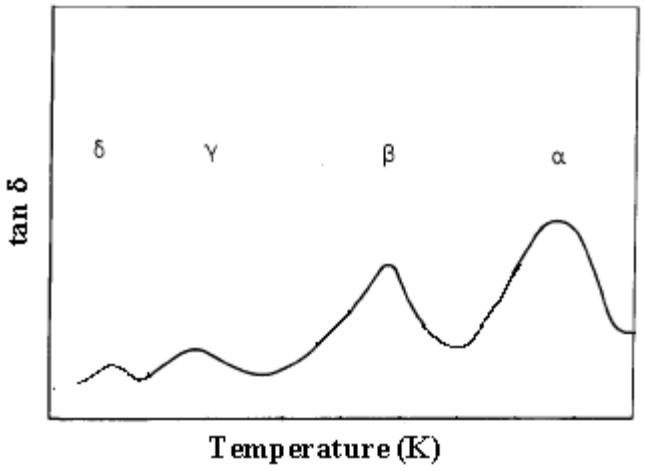

Figure 1.11 Relaxation processes in a semicrystalline polymer

Due to the fact that the dielectric constants in the dispersion region depend markedly on the frequency and temperature of measurements, the study of dielectric properties could be performed either by measuring dielectric constants isothermally over an available frequency and temperature range or by measuring dielectric constants isochronally over the possible temperature range at a fixed frequency. The latter technique is employed frequently owing to its simplicity, efficiency and economy in the instrumentation. Dielectric data can be represented as plots of ε^{1}, ε^{11} or tan δ as a function of frequency. When the data are plotted in this manner in the dispersion region, ε^{1} shows a gradient, while ε^{11} and tan δ show a maximum. Plots of ε^{1} and ε^{11} versus frequency are

combined with the time-temperature superposition method of analysis to interpret the dielectric data also known as the William-Landel-Ferry (WLF) method.[150] In the dielectric dispersion data, one finds that the available frequency range (up to three and a half decades) is not enough to obtain the dielectric data covering the good portion of the dispersion. In order to obtain isothermal data covering the entire frequency range of the dispersion from data obtained from equipment capable of measuring dielectric properties of only a few decades, Ferry et al. have devised an empirical transformation procedure between the time scale and temperature. The transformation is done so that the data obtained at temperatures above and below the temperature of interest can be transferred to data at the reference temperature, while expanding the frequency range at the reference temperature beyond the frequency range of the actual experiment.

The time-temperature characteristics of the relaxation processes can also be plotted in an Arrhenius manner as shown in the figure 1.12. The slopes of the various

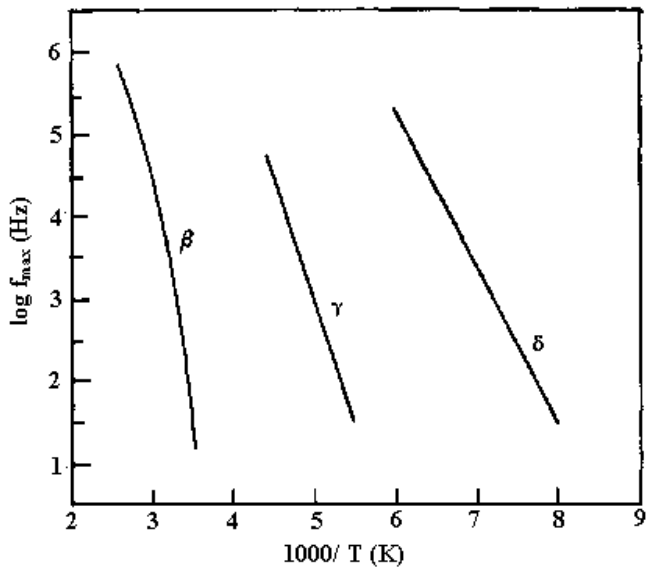

Figure 1.12 Schematic dielectric loss map for a semicrystalline polymer

processes give the activation energies for those processes, respectively. This plot allows the mapping of the position of the loss peaks. It is to be noted that for all dispersions, $f_{max.}$ moves to higher frequencies as the temperature increases. The β process is characterized by a non-linear curve and has a much higher activation energy than the γ process. The glass transition is the narrow region on the temperature scale where the thermal expansion coefficient undergoes a discontinuity and below which configurational rearrangements of polymer chain backbones are extremely slow due to which the non linearity is observed.[151]

1.11 Aim and Scope

The above review of the historical developments in the field of composites and nanocomposites indicates that there is a good scope for improvement in the properties of commodity polymers, in particular PP by incorporating them with functional fillers. Naturally occurring minerals, clays and zeolites can be incorporated in plastics to improve their performance. Naturally occurring mica has excellent potential for such applications in PP. Earlier studies on PP nanocomposites are mainly centered around intercalated clays (MMT) and there is exhaustive literature available for the same. However, the naturally occurring mica cannot be intercalated/ delaminated by these procedures. Mica type silicates, when fully delaminated, possess aspect ratios in the same range as fibres, a feature that makes them attractive as molecular reinforcements. Above all, there is a wealth of mica reserves in India, which are waiting to be exploited.

The main aim of the present investigations is to explore various possibilities of delaminating the naturally occurring mica. Amongst the various possibilities, in site

polymerization appears to be the most attractive for this since it does not require prior hydrophobic treatment. It is hence proposed to incorporate/ diffuse an appropriate monomer in the interlaminar spaces of the mica crystal lattice and polymerize the same so as to cause large scale delamination. The nanosize particles obtained from such synthesis will be incorporated in a polymer matrix, which can be subsequently mixed with a suitable thermoplastic to form nanoparticulate mica filled composites.

These studies were carried out successfully and this thesis describes the interesting results obtained. The effect of the synthesized nanoparticulate mica on the structure and properties of popular thermoplastic matrices like PP and PPS were also studied. Crystallization behavior and morphology were studied with respect to structure whereas the properties studied included thermal, mechanical and electrical properties. PP is a high volume, commercially important commodity plastic whereas PPS is a technologically relevant engineering thermoplastic. Thus the impact of these nanocomposites on both the commercial and the technological fronts have been addressed in this thesis.

1.12 References

1) Mascia, L. *Thermoplastics: Materials Engineering*; Applied Science Publishers Ltd.: Essex, 1982.

2) Gachter, R. In *Plastics Additives Handbook*; Gachter, R., Muller, H., Eds.; Hanser Publishers Ltd.: Munich, 1987.

3) Lutz, J. T. In *Thermoplastic Polymer Additives-Theory and Practice*; Marcel Dekker, Inc.: New York, 1989.

4) Murphy, J. *The Additives for Plastics Handbook*; Elsevier Advanced Technology: Oxford, 1996.

5) Pritchard, G. *Plastic Additives – An A-Z Reference*; Chapman and Hall: London, 1998.

6) Sekutowski, D. In *Plastics Additives and Modifiers Handbook*; Edenbaum, J., Ed.; Chapman & Hall: London, 1996.

7) Rothon, R. N. *Adv. Polym. Sci*. **1999**, *139*, 67.

8) Gianellis, E. P. *Adv. Mater*. **1996**, *8*, 29.

9) Gianellis, E. P. *In Materials Chemistry: An Emerging Discipline*; ACS: New York, 1995.

10) Dagani, R. *C. & EN*. **1999**, *77*, 25.

11) Calvert, P. *Nature* **1999**, *399*, 210.

12) LeBaron, P. C.; Wang, Z.; Pinnavaia, T. *J. Appl. Clay Sci*. **1999**, *15*, 11.

13) Thayer, A. M. *C. & EN*. **2003**, *81*, 15.

14) Krishnamoorthi, R.; Vaia, R. A.; Gianellis, E. P. *Chem. Mater*. **1996**, *8*, 1728.

15) Kickelbick, G. *Prog. Polym. Sci*. **2003**, *28*, 83.

16) Liu, T.; Burger, C.; Chu, B. *Prog. Polym. Sci*. **2003**, *28*, 5.

17) Juangvanich, N.; Mauritz, K. A. *J. Appl. Polym. Sci*. **1998**, *67*, 1799.

18) Deng, Q.; Moore, R. B.; Mauritz, K. A. *Chem. Mater.* **1995**, *7*, 2261.

19) Deng, Q.; Jarrett, W.; Moore R. B.; Mauritz, K. A. *J. Sol–Gel Sci. Technol.* **1996**, *7*, 177.

20) Shao, P.L.; Mauritz, K. A.; Moore, R. B. *J. Polym. Sci., Part B: Polym. Phys.* **1996**, *34*, 873.

21) Mauritz, K. A. *Mater. Sci. Eng.* **1998**, *C6*, 121.

22) Chujo, Y.; Saegusa, T. *Adv. Polym. Sci*. **1992**, *100*, 11.

23) Saegusa, T.; Chujo, Y. *Makromol. Chem. Macromol. Symp.* **1991**, *51*, 1.

24) Saegusa, T.; Chujo, Y. *Makromol. Chem. Macromol. Symp.* **1992**, *64*, 1.

25) Tamaki, R.; Chujo, Y. *Appl. Organomet. Chem*. **1998**, *12*, 755.

26) Landry, C. J. T.; Coltrain, B. K.; Wesson, J. A.; Zumbulyadis, N.; Lippert, J. L. *Polymer* **1992**, *33*, 1496.

27) Wang, S.; Ahmad, Z.; Mark, J. E. *Polym. Bull.* **1993**, *31*, 323.

28) Mauritz, K. A.; Jones, C. K. *J. Appl. Polym. Sci*. **1990**, *40*, 1401.

29) Wen, J.; Mark, J. E. *Polymer* **1995**, *27*, 492.

30) Ahmad, Z.; Sarwar, M. I.; Wang, S.; Mark, J. E. *Polymer* **1997**, *38*, 4523.

31) Ahmad, Z.; Sarwar, M. I.; Mark, J. E. *J. Appl. Polym. Sci*. **1998**, *70*, 297.

32) Breiner, J. M.; Mark J. E. *Polymer* **1998**, *39*, 5483.

33) Shao, P. L.; Mauritz, K. A.; Moore, R. B. *Chem. Mater.* **1995**, *7*, 192.

34) Apicatachutapan, W.; Moore, R. B.; Mauritz, K. A. *J. Appl. Polym. Sci*. **1996**, *62*, 417.

35) Pope, E. J. A.; Asami, M.; Mackenzie, J. D. *J. Mater. Res.* **1989**, *4*, 1018.

36) Avadhani, C. V.; Chujo, Y. *Appl. Organomet. Chem*. **1997**, *11*, 153.

37) Ellsworth, M. W.; Novak, B. M. *J. Am. Chem. Soc.* **1991**, *113*, 2756.

38) Novak, B. M.; Davies, C. *Macromolecules* **1991**, *24*, 5481.

39) Sanchez, C.; In, M.; Toledano, P.; Griesmar, P. *Mater. Res. Soc. Symp. Proc.* **1992**, *271*, 669.

40) In, M.; Gerardin, C.; Lambard, J.; Sanchez, C. *J. Sol–Gel Sci. Technol.* **1995**, *5*, 101.

41) Campero, A.; Soto, A. M.; Maquet, J.; Sanchez, C. *Mater. Res. Soc. Symp. Proc.* **1996**, *435*, 527.

42) Radhakrishnan, S.; Schultz, J. M. *J. Cryst. Growth* **1992**, *116*, 378.

43) Radhakrishnan, S. *J. Cryst. Growth* **1993**, *129*, 191.

44) Radhakrishnan, S. *J. Cryst. Growth* **1994**, *141*, 437.

45) Saujanya, C.; Radhakrishnan, S. *J. Mater. Sci.* **1998**, *33*, 1063.

46) Belfiore, L. A.; Pires, A. T. N.; Wang, Y.; Graham, H.; Ueda, E. *Macromolecules* **1992**, *25*, 1411.

47) Belfiore, L. A.; Graham, H.; Ueda, E. *Macromolecules* **1992**, *25*, 2935.

48) Belfiore, L. A.; McCurdie, M. P.; Ueda, E. *Macromolecules* **1993**, *26*, 6908.

49) Bosse, F.; Das, P.; Belfiore, L. A. *Macromolecules* **1995**, *28*, 6993.

50) Das, P. K.; Ruzmaikina, I.; Belfiore, L. A. *J. Polym. Sci., Part B: Polym. Phys.* **2000**, *38*, 1931.

51) Belfiore, L. A.; Indra, E.; Das, P. *Macromol. Symp.* **1997**, *114*, 35.

52) McCurdie, M. P.; Belfiore, L. A. *J. Polym. Sci., Part B: Polym. Phys.* **1999**, *37*, 301.

53) Belfiore, L. A.; Bosse, F.; Das, P. *Polymer Int.* **1995**, *36*, 165.

54) Belfiore, L. A.; McCurdie, M. P. *J. Polym. Sci., Part B: Polym. Phys.* **1995**, *33*, 105.

55) Biswas, M.; Mukherjee, A. *Adv. Polym. Sci*. **1994**, *115*, 89.

56) Hagihara, N.; Sonogashira, K.; Takahashi, S. *Adv. Polym. Sci*. **1981**, *41*, 141.

57) Archer, R. D. *Coord. Chem. Rev.* **1993**, *128*, 49.

58) Nguyen, P.; Gomez-Elipe, P.; Manners, I. *Chem. Rev.* **1999**, *99*, 1515.

59) Lamba, J. J. S.; Fraser, C. L. *J. Am. Chem. Soc.* **1997**, *119*, 1801.

60) Collins, J. E.; Fraser, C. L. *Macromolecules* **1998**, *31*, 6715.

61) McAlvin, J. E.; Fraser, C. L. *Macromolecules* **1999**, *32*, 1341.

62) McAlvin, J. E.; Fraser, C. L. *Macromolecules* **1999**, *32*, 6925.

63) Theng, B. K. G. *The Chemistry of Clay-Organic Reactions*; Wiley: New York, 1974.

64) Brindley, G. W. *Crystal Structures of Clay Minerals and their X-Ray Identification*; Mineralogical Society: London, 1980.

65) Alexandre, M.; Dubois, P. *Mater. Sci. Eng*. **2000**, *28*, 1.

66) Aranda, P.; Ruiz-Hitzky, E. *Chem. Mater.* **1992**, *4*, 1395.

67) Francis, C. W. *Soil Sci*. **1973**, *115*, 40.

68) Greenland, D. J. *J. Colloid Sci*. **1963**, *18*, 647.

69) Zhao, X.; Urano, K.; Ogasawara, S. *Colloid Polym. Sci.* **1989**, *267*, 899.

70) Jimenez, G.; Ogata, N.; Kawai, H.; Ogihara, T. *J. Appl. Polym. Sci.* **1997**, *64*, 2211.

71) Ogata, N.; Jimenez, G.; Kawai, H.; Ogihara, T. *J. Polym. Sci., Part B: Polym. Phys*. **1997**, *35*, 389.

72) Jeon, H. G.; Jung, H. T.; Lee, S. W.; Hudson, S. D. *Polym. Bull.* **1998**, *41*, 107.

73) Kawasumi, M.; Hasegawa, N.; Usuki, A.; Okada, A. *Mater. Sci. Eng*. **1998**, *6*, 135.

74) Okada, A.; Kawasumi, M.; Usuki, A.; Kojima, Y.; Kurauchi, T.; Kamigaito, O. In *Polymer based Molecular Composites*; Schaefer, D. W., Mark, J. E., Eds.; MRS Symposium Proceedings: Pittsburgh, 1990; Vol. 171, p 45.

75) Usuki, A.; Kawasumi, M.; Kojima, Y.; Okada, A.; Kurauchi, T.; Kamigaito, O. *J. Mater. Res*. **1993**, *8*, 1174.

76) Messersmith, P. B.; Giannelis, E. P. *Chem. Mater*. **1993**, *5*, 1064.

77) Pantoustier, N.; Alexandre, M.; Degee, P.; Calberg, C.; Jerome, R.; Henrist, C.; Cloots, R.; Rulmont, A.; Dubois, P. *e-Polymer* **2001**, *9*, 1.

78) Pantoustier, N.; Lepoittevin, B.; Alexandre, M.; Kubies, D.; Calberg, C.; Jerome, R.; Dubois, P. *Polym. Eng. Sci.* **2002**, *42*, 1928.

79) Chen, T. K.; Tien, Y. I.; Wei, K. H. *J. Polym. Sci., Part A: Polym. Chem*. **1999**, *37*, 2225.

80) Wang, Z.; Pinnavaia, T. J. *Chem. Mater*. **1998**, *10*, 3769.

81) Yao, K. J.; Song, M.; Hourston, D. J.; Luo, D. Z. *Polymer* **2002**, *43*, 1017.

82) Okamoto, M.; Morita, S.; Taguchi, H.; Kim, Y. H.; Kotaka, T.; Tateyama, H. *Polymer* **2000**, *41*, 3887.

83) Okamoto, M.; Morita, S.; Kotaka, T. *Polymer* **2001**, *42*, 2685.

84) Akelah, A.; Moet, M. *J. Mater. Sci*. **1996**, *31*, 3589.

85) Doh, J. G.; Cho, I. *Polym. Bull.* **1998**, *41*, 511.

86) Weimer, M. W.; Chen, H.; Giannelis, E. P.; Sogah, D. Y. *J. Am. Chem. Soc*. **1999**, *121*, 1615.

87) Zhu, J.; Morgan, A. B.; Lamelas, F. J.; Wilkie, C. A. *Chem. Mater.* **2001**, *13*, 3774.

88) Hsu, S. L. C.; Chang, K. C. *Polymer* **2002**, *43*, 4097.

89) Bergman, J. S.; Chen, H.; Giannelis, E. P.; Thomas, M. G.; Coates, G. W. *Chem. Commun.* **1999**, *21*, 2179.

90) Jin, Y-H.; Park, H-J.; Im, S-S.; Kwak, S-Y.; Kwak, S. *Macromol. Rapid Commun.* **2002**, *23*, 135.

91) Heinemann, J.; Reichert, P.; Thomson, R.; Mulhaupt, R. *Macromol. Rapid Commun*. **1999**, *20*, 423.

92) Tudor, J.; Willington, L.; O'Hare, D.; Royan, B. *Chem. Commun*. **1996**, *17*, 2031.

93) Sun, T.; Garces, J. M. *Adv. Mater*. **2002**, *14*, 128.

94) Ke, Y. C.; Long, C.; Qi, Z. *J. Appl. Polym. Sci*. **1999**, *71*, 1139.

95) Tsai, T. Y. In *Polymer–Clay Nanocomposites*; Pinnavaia, T. J., Beall, G. W. Eds.; Wiley: London, 2000.

96) Imai, Y.; Nishimura, S.; Abe, E.; Tateyama, H.; Abiko, A.; Yamaguchi, A.; Aoyama, T.; Taguchi, H. *Chem. Mater*. **2002**, *14*, 477.

97) Messersmith, P. B.; Giannelis, E. P. *Chem. Mater*. **1994**, *6*, 1719.

98) Wang, Z.; Pinnavaia, T. J. *Chem. Mater*. **1994**, *6*, 468.

99) Lan, T.; Pinnavaia, T. J. *Chem. Mater*. **1994**, *6*, 2216.

100) Wang, Z.; Lan, T.; Pinnavaia, T. J. *Chem. Mater*. **1996**, *8*, 2200.

101) Kornmann, X.; Thomann, R.; Mulhaupt, R.; Finter, J.; Berglund, L. A. *Polym. Eng. Sci*. **2002**, *42*, 1815.

102) Vaia, R. A.; Gianellis, E. P. *Macromolecules* **1997**, *30*, 8000.

103) Vaia, R. A.; Ishii, H.; Giannelis, E. P. *Chem. Mater*. **1993**, *5*, 1694.

104) Ryu, J. G.; Kim, H.; Lee, J. W. *Polym. Eng. Sci.* **2004**, *44*, 1198.

105) Vaia, R. A.; Vasudevan, S.; Krawiec, W.; Scanlon, L. G.; Giannelis, E. P. *Adv. Mater*. **1995**, *7*, 154.

106) Liu, L. M.; Qi, Z. N.; Zhu, X. G. *J. Appl. Polym. Sci*. **1999**, *71*, 1133.

107) Fornes, T. D.; Yoon, P. J.; Keskkula, H.; Paul, D. R. *Polymer* **2001**, *42*, 9929.

108) Fornes, T. D.; Yoon, P. J.; Hunter, D. L.; Keskkula, H.; Paul, D. R. *Polymer* **2002**, *43*, 5915.

109) Hasegawa, N.; Okamoto, H.; Kato, M.; Usuki, A.; Sato, N. *Polymer* **2003**, *44*, 2933.

110) Usuki, A.; Kato, M.; Okada, A.; Kurauchi, T. *J. Appl. Polym. Sci.* **1997**, *63*, 137.

111) Hasegawa, N.; Kawasumi, M.; Kato, M.; Usuki, A.; Okada, A. *J. Appl. Polym. Sci.* **1998**, *67*, 87.

112) Nam, P. H.; Maiti, P.; Okamoto, M.; Kotaka, T.; Hasegawa, N.; Usuki, A. *Polymer* **2001**, *42*, 9633.

113) Liu, X.; Wu, Q. *Polymer* **2001**, *42*, 10013.

114) Manias, E.; Touny, A.; Wu, L.; Lu, B.; Strawhecker, K.; Gilman, J. W.; Chung, T. C. *Polym. Mater. Sci. Eng*. **2000**, *82*, 282.

115) Wang, K. H.; Choi, M. H.; Koo, C. M.; Choi, Y. S.; Chung, I. J. *Polymer* **2001**, *42*, 9819.

116) Davis, C. H.; Mathias, L. J.; Gilman, J. W.; Schiraldi, D. A.; Shields, J. R.; Trulove, P.; Sutto, T. E.; Delong, H. C. *J. Polym. Sci., Part B: Polym. Phys.* **2002**, *40*, 2661.

117) Chisholm, B. J.; Moore, R. B.; Barber, G.; Khouri, F.; Hempstead, A.; Larsen, M.; Olson, E.; Kelley, J.; Balch, G.; Caraher, J. *Macromolecules* **2002**, *35*, 5508.

118) Kim, S. W.; Jo, W. H.; Lee, M. S.; Ko, M. B.; Jho, J. Y. *Polymer* **2001**, *42*, 9837.

119) Huang, X.; Lewis, S.; Brittain, W. J.; Vaia, R. A. Macromolecules **2000**, *33*, 2000.

120) Maiti, P.; Yamada, K.; Okamoto, M.; Ueda, K.; Okamoto, K. *Chem. Mater*. **2002**, *14*, 4654.

121) Paul, M-A.; Alexandre, M.; Degee, P.; Henrist, C.; Rulmont, A.; Dubois, P. *Polymer* **2003**, *44*, 443.

122) Sinha Ray, S.; Okamoto, K.; Maiti, P.; Okamoto, M. *J. Nanosci. Nanotechnol*. **2002**, *2*, 171.

123) Sinha Ray, S.; Okamoto, K.; Okamoto, M. *Macromolecules* **2003**, *36*, 2355.

124) Stein, A.; Melde, B. J. *Adv. Mater*. **2000**, *12*, 1403.

125) Schollhorn, R. *Chem. Mater*. **1996**, *8*, 1735.

126) Graeser, A.; Spange, S. *Chem. Mater*. **1998**, *10*, 1814.

127) Spange, S.; Graeser, A.; Muller, H.; Zimmermann, Y.; Rehak, P.; Jaeger, C.; Fuess, H.; Baehtz, C. *Chem. Mater*. **2001**, *13*, 3698.

128) Godovski, D. Y. *Adv. Polym. Sci*. **1995**, *119*, 79.

129) Hergeth, W. D.; Peller, M.; Hauptmann, P. *Acta. Polym.***1986**, *37*, 468.

130) Hergeth, W. D.; Starre, P.; Schmutzler, K. *Polymer* **1988**, *29*, 1323.

131) Hergeth, W. D.; Steinau, U. J.; Bittrich, H. J.; Simon, G. *Polymer* **1989**, *30*, 254.

132) Stober, W.; Fink, A.; Bohn, E. *J. Colloid Inter. Sci.* **1968**, *26*, 62.

133) Badley, R. D.; Ford, W. T.; McEnroe, F. J.; Assink, R. A. *Langmuir* **1990**, *6*, 792.

134) Philipse, A. P.; Vrij, A. *J. Colloid Inter. Sci.* **1989**, *128*, 121.

135) Sunkara, H. B.; Jethmalani, J. M.; Ford, W. T. *ACS Symp. Ser.* **1995**, *585*, 181.

136) Smith, T. W.; Wychick, D. *J. Phys. Chem.* **1980**, *84*, 1621.

137) Hess, P. H.; Parker, Jr. P. H. *J. Appl. Polym. Sci*. **1966**, *10*, 1915.

138) Berger, M.; Manuel, T. A. *J. Polym. Sci. Polym. Chem. Ed.* **1966**, *4*, 1509.

139) Lee, A.; Lichtenhan, J. D. *Macromolecules* **1998**, *39*, 4970.

140) Wyckoff, R. W. G. *Crystal Structures*; Interscience: New York, 1968; Vol. 4.

141) Canova, L. A. In *Handbook of Polypropylene and Polypropylene Composites*; Karian, H. G., Ed.; Marcel Dekker: New York, 1999.

142) Karger-Kocsis, J. In *Polypropylene-Structure, Blends and Composites*; Chapman & Hall: London, 1995.

143) Wunderlich, W. B. *Macromolecular Physics*; Academic: New York, 1975; Vol. 1.

144) Mandelkern, L. *Crystallization of Polymers*; McGraw Hill: New York, 1964.

145) Wunderlich, W. B. *Macromolecular Physics*; Academic: New York, 1975; Vol. 2.

146) Avrami, M. J. *J. Chem. Phys.* **1939**, *7*, 1103.

147) Avrami, M. J. *J. Chem. Phys.* **1940**, *8*, 212.

148) Avrami, M. J. *J. Chem. Phys.* **1941**, *9*, 177.

149) Parker, T. G. In *Polymer Science – A Material Science Handbook*; Jenkins, A. D., Ed.; North Holland: Amsterdam, 1972.

150) Ferry, J. D. *Viscoelastic Properties of Polymers*, 3rd ed.; John Wiley: New York, 1980.

151) Tager, A. *Physical Chemistry of Polymers*, 2nd ed.; Mir Publishers: Moscow, 1978.

2.1 Introduction

The detailed experimental procedures and various characterization techniques employed in these studies are documented in this chapter. Three different types of naturally occurring mica were used viz. phlogopite, muscovite (both commercially available) and chlorite (relatively rare). PP and PPS were the polymer matrices used for making the composites. Two different types of PP were used in this study, both of which were injection molding grades (Indothane SM85N and AM120N). PP was chosen because it is a readily available polymer in a variety of grades and exhibits a range of polymorphic structures which can easily be controlled by crystallization conditions. PPS is a high performance thermoplastic that has potential applications in wear resistant parts, coatings, etc. The structure development, morphology and properties of these PP/ mica, PPS/ mica composites and nanocomposites were investigated by various physico-chemical characterization techniques as described in this chapter.

2.2 Materials

The various chemicals used in the present study along with their grades and make are given in the following table 2.1

Table 2.1 Materials used

Chemical	Grade	Make
Phlogopite mica	Pract grade	S.D.Fine Chemicals, India
Muscovite mica	Wet ground, 325 mesh	Premier Mica Company, India
Chlorite mica	-	Nichika Corporation, Japan
Sodium sulfide	LR grade	Loba Chemie, India

1,4-Dibromobenzene	LR grade	Merck
NMP	LR grade	Merck
Methanol	LR grade	Merck
Acetone	LR grade	Merck
PP	SM85N	IPCL, India
PP	AM120N	SJS Plastiblends, India
PPS	Ryton P-4 powder	Chevron Phillips, Singapore
Crystal violet	LR grade	Loba Chemie, India

2.3 Synthesis of Nanoparticulate Mica

Scheme-1

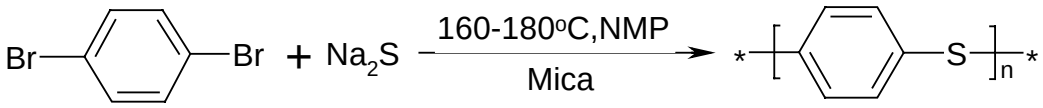

1, 4-dibromobenzene was first intercalated with mica by heating a mixture of both in NMP at 80 ºC – 100 ºC for 6-8 hours. This solution was then treated with a stoichiometric equivalent of powdered sodium sulfide dissolved in methanol. The excess methanol was distilled out, the reaction flask fitted with a condenser and the dispersion heated at 160-180 ºC for 12 hours. After cooling the reaction flask to room temperature, the PPS formed was precipitated by adding excess methanol to the dispersion. The solution was centrifuged and filtered to obtain nanoparticulate mica embedded in PPS

matrix. This was washed repeatedly with methanol to remove any unreacted portions if present and then dried *in vacuo* overnight at 60 ºC. The formation of nanoparticulate mica as well as the PPS yield was monitored as a function of the initial mica loading levels and the average particle size of the initial mica, the details of which are furnished in the next chapter.

2.4 Preparation of PP Powder from Pellets

It was necessary to obtain PP in a powdered form to aid the study of crystallization behavior of PP/ mica composites and nanocomposites. The SM85N grade of PP was chosen because of its moderate MFI of 8-12 and amenability to crystallization behavior studies. PP pellets were dissolved in xylene (5-6% of solution) at 120 ºC and the resulting gel like mass was precipitated in acetone with vigorous stirring. The solution was filtered, washed thoroughly with acetone and dried at 60 ºC *in vacuo* for 12 hours to obtain PP in the form of a fine powder.

2.5 Preparation of PP/ Mica Composites and Nanocomposites by Powder Blending

The PP with commercial mica composites and PP/ nanoparticulate mica composites were prepared by taking the desired quantity of mica/ nanomica and dry-mixing it with PP powder in an agate mortar. A range of compositions of mica/ nanomica with respect to PP were made and these samples were utilized for studies on crystallization behavior.

2.6 Melt Compounding of PPS/ Mica Composites/ Nanocomposites

The desired quantity of nanomica/ commercial mica was first mixed with Ryton PPS and ground to a fine powder in an agate mortar. This powder was fed into the barrel of a MFI unit (International Engineering Industries, Mumbai) maintained at 285 ºC. The melt compounded PPS/ mica composites and nanocomposites were extruded from the MFI unit with a 5 kg load.

2.7 Micro Compounding/ Micro Injection Molding of PP/ Mica Composites and Nanocomposites

The tensile and flexural test specimens were prepared by micro compounding/ micro injection molding using a DSM MICRO 5 unit, which are shown in the figures 2.1 and 2.2, respectively. The temperature of the barrel was set at 210 ºC and the speed of the co-rotating screws was set at 80 rpm. After compounding for about 2-4 minutes, the extrudate was fed into the cylinder of the micro injection molding unit whose temperature was preset at 220 ºC. The melt was injected into the mold at room temperature to get the standard test specimen for tensile and flexural tests in the form of a dumbbell and rectangular strip, respectively.

The specifications of the micro scale compounding and molding units are given in tables 2.2 and 2.3, respectively.

Figure 2.1 DSM microcompounding unit

Figure 2.2 DSM microinjection molding unit

Table 2.2 Micro compounder Specifications

Sr. No	Specifications	Microcompounder	Unit
1	Total Capacity	+/- 6	cm^3
2	Net Capacity	5	cm^3
3	Screw Speed	5 – 400	rpm
4	Screw Length	107.5	mm
5	Controlled Heating Zones	4	No.
6	Maximum Operating temperature	350	°C
7	Heating Time (from 20 to 240°C)	< 15	mins.
8	Cooling Time (from 240 to 80°C)	14	mins.
9	Cooling Time Using Extra Cooling Element (Water)	8	mins.
10	Cooling Water Flow	3	min^{-1}
11	Weight	95	kg
12	Dimension	W70 D40 H80	cm
13	Main Voltage	208 / 240	Volt
14	Power	1.75	K Watt
15	Drive Motor(DC)	0.35	K Watt

Table 2.3 Micro injection Molding Unit Specifications

Sr. No	Specifications	Micro Injection Moulding Machine	Unit
1	Dimension	650 x 300 x 250	mm
2	Barrel Capacity	+ / - 3.5	cm^3
3	Duration of the injection cycle	5	mins.
4	Heating Zone	2	No.
5	Max. Service Temperature	350	°C
6	Heating Time (from 20 to 240°C)	2	mins.
7	Compressed-air pressure	3 – 16	Bar
8	Compresses-air consumption for 0.5s stroke	9.5	sec^{-1}
9	Total Heating Power	0.7	KW
10	Weight	20	Kg
11	Main Voltage	208 – 240	Volt

2.8 Melt Crystallization of PP/ Mica Composites and Nanocomposites for Crystallization Behavior Studies

A small amount of the powder blended PP with mica was first melted on a microscopic slide for 1-2 minutes and covered with a cover slip. The slide was then quickly transferred to the hot stage of an optical polarizing microscope (Leitz, Germany) preset at the crystallization temperature of 125 ºC. The crystallization behavior was investigated by continuously mapping the growth of spherulites and intensity of transmitted light (grey scale) under crossed polars coupled with an image analyzer system. The exact and detailed procedure adopted for studying the crystallization behavior has been given in section 2.11.3.

2.9 Melt Crystallized samples for Structure Development Studies

2.9.1 PP/ Mica Composites and Nanocomposites

Powder blended PP/ mica sample (0.3 g) was pelletized using a single end compaction die at a pressure of 3 tonnes for 2 minutes to obtain thin discs (12 mm diameter, 2mm thickness). The pellet was placed in between two glass slides and kept on a hot plate preset at 200 ºC for 10 minutes. The slide was then transferred to another hot plate maintained at 125 ºC and the sample allowed to crystallize isothermally at that temperature for 20 minutes. The sample was then quenched in cold water, dried and analyzed for structure development by WAXD.

2.9.2 PPS/ Mica Composites and Nanocomposites

Powder blended PPS/ mica pellets were made in the same manner as mentioned above. The pellet was subsequently placed in between two teflon sheets, heated on a hot plate set at 300 ºC for 5 minutes after which it was transferred on to another hot stage maintained at 250 ºC and crystallized isothermally for 90 minutes. Later, the sample was quenched in cold water, dried and analyzed by WAXD for structure development.

2.10 Preparation of PP/ Mica and PPS/ Mica samples for Dielectric Studies

2.10.1a Compression Molding of PP/ Mica samples

The discs required for dielectric measurements were made by compression molding using a polymer press (Technosearch, India). Melt compounded PP/ mica sample (2 g) was introduced in between the platens and molded at 170 ºC for 4 minutes at a pressure of 0.5 tonnes after which it was quenched in cold water. This sample was dried and used for gold coating.

2.10.1b Compression Molding of PPS/ Mica samples

The melt compounded PPS/ mica samples were compression molded at 270 ºC for 3-4 minutes at a pressure of 0.5 tonnes in between two teflon sheets. It was then quenched in cold water and dried.

2.10.2 Gold Electrode Coating of the samples

The PP/ mica and PPS/ mica samples were coated with gold on either side in order to provide proper contact and eliminate space charges during dielectric measurements. The electrode area was restricted to 25 mm x 25 mm using a mask centrally placed on the samples and leaving the edges uncoated to prevent shorting of electrodes. The gold coating was done with a HINDHIVAC vacuum coating unit (Model – 12A4D) at 10^{-6} torr by thermal evaporation of high purity (>99%) gold wire.

2.11 Characterization Techniques

2.11.1 UV – Vis Spectroscopy for Dye Adsorption Technique

UV-Vis spectroscopy was used to qualitatively evaluate the surface areas of the three different micas used (phlogopite, muscovite and chlorite). A known amount of each mica (0.20 g) was added to a dilute solution (25 x 10^{-6} M) of crystal violet in NMP in three different beakers and the dispersion, allowed to stand for 48 hours. Then, the mica was filtered and the UV spectra of the respective filtrates were recorded in the range of 200-600 nm (Ocean Optics UV Spectrophotometer). The spectrophotometer utilizes a DH-2000 deuterium light source and a HR 2000 CG-UV-NIR detector.

2.11.2 Infrared Spectroscopy

IR spectrum was recorded to confirm the formation of PPS during nanoparticulate mica synthesis upon in situ intercalative polymerization. The powdered specimens were sampled as KBr pellets in a Shimadzu FT-IR 8300 spectrometer in the range of 400-4000 cm^{-1}.

2.11.3 Optical Polarizing Microscopy

The study of crystallization behavior and morphology was enabled by a polarizing microscope[4,5] (Leitz Laborlux 12 Pol, Germany) coupled to an image analyzer system (VIDPRO 32, Leading Edge, Australia). Most of the analyses were performed under crossed polars i.e. polarizer and analyzer axes kept at 90 º with respect to each other.

Figure 2.3 shows the essential parts of the optical polarizing microscope. It consists of a light source (Tungsten lamp 25 W), a condensor, a polarizer, a sample stage with controlled heating arrangement, objective assembly, an analyzer and eyepiece/ microphotography arrangement. In another arrangement, the video camera interfaced with a computer was connected in place of the microphotography unit. The image analysis system contained a video camera connected to a computer via the software which provided image grabbing, image storage and analysis facilities. The images were continuously recorded during the isothermal crystallization process for every 10 or 30 seconds interval and then analyzed by recording the spot intensity (grey scale) at any given location of the screen. It was possible to direct small changes (up to 1 pixel) occurring at any chosen point, during the crystallization of the matrix. The graphics provided in the software was used to plot the intensity of transmitted light under the cross-polar condition with respect to real time. This gives essentially the crystal growth rate at the T_c and the instrument was calibrated for a known sample like PP.[6-8] The induction period, half time and growth rate of the polymer were evaluated from the intensity Vs time plots. Figure 2.4 shows a typical crystallization curve of pure PP and that of the nanocomposite. It can be seen that the fast crystallization process can be accurately monitored. The variation in background intensity for different samples is due

to variation in thickness and transparency.

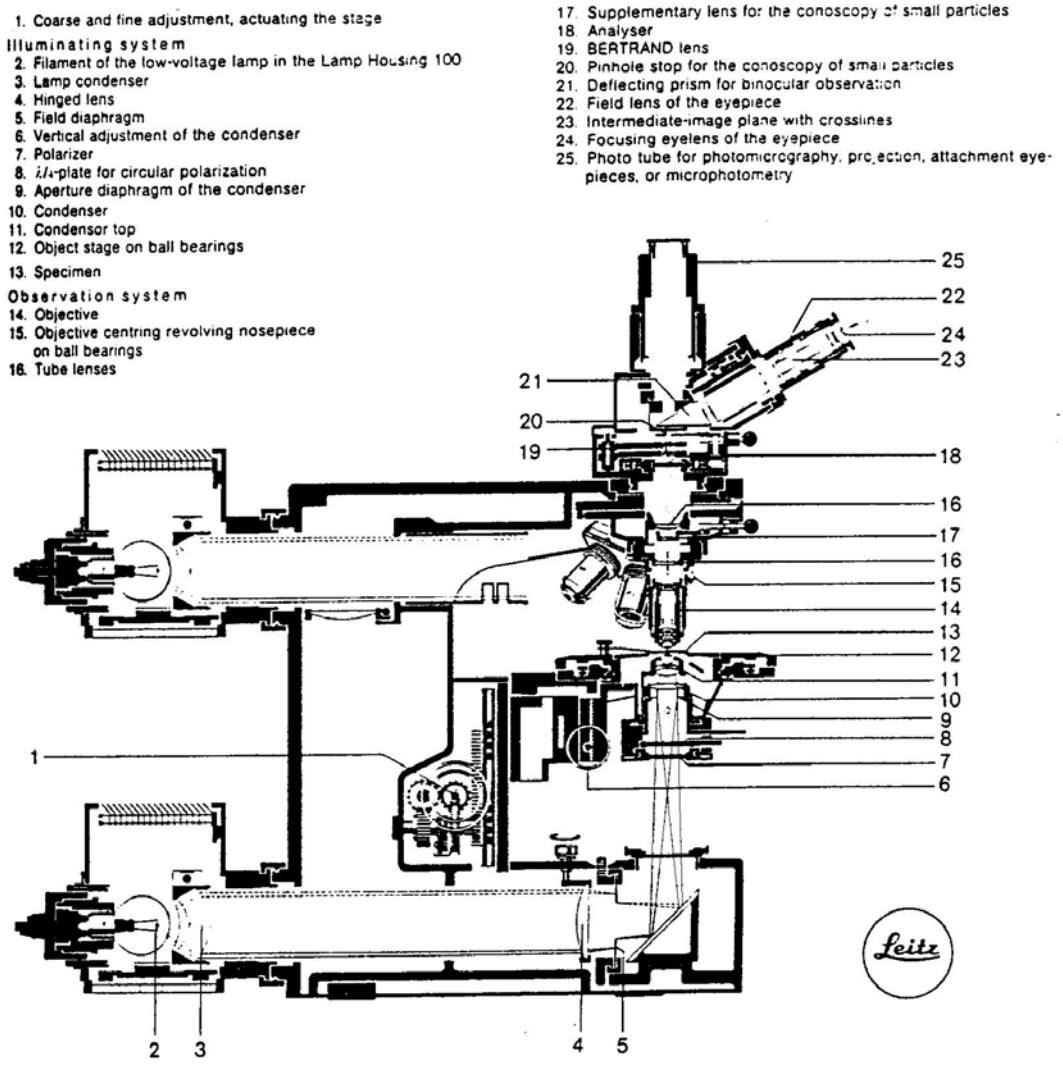

Figure 2.3 A Leitz optical polarizing microscope showing its essential parts

.

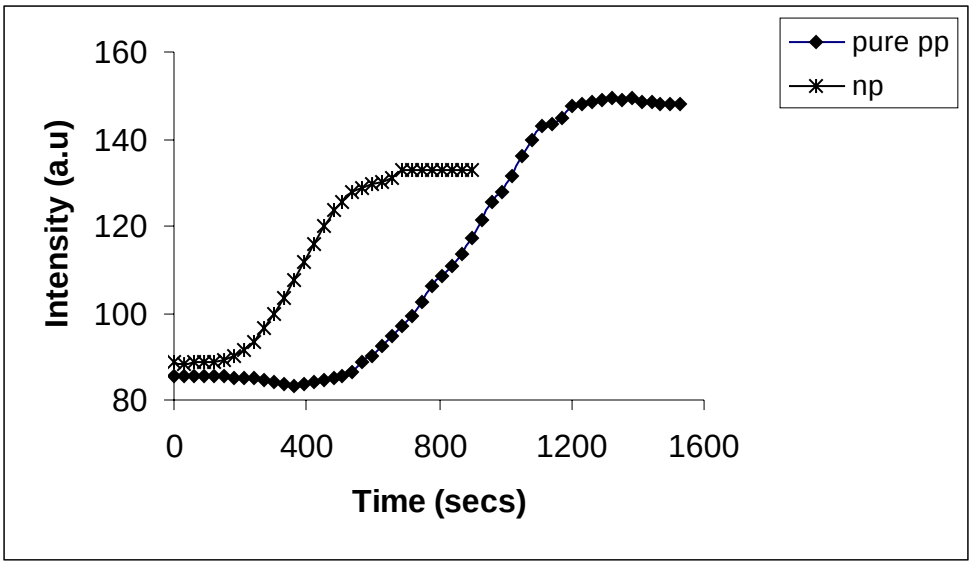

Figure 2.4 Crystallization profiles of PP and PP/ nanophlogopite samples

2.11.4 Differential Scanning Calorimetry

The melting temperature, crystallization temperature and the respective enthalpies of all the composite samples were determined by a DSC 7 (Perkin-Elmer).[9] The sample masses were between 0.008-0.012 g and the heating/ cooling runs were carried out under a nitrogen atmosphere. PP/ mica samples were recorded in the range of 50 ºC-200 ºC whereas PPS/ mica samples were scanned from 50 ºC-300 ºC. The scans were recorded under a constant heating rate of 10 ºC/ min, held at that temperature for a minute and then cooled at the same rate. The calculations are based on the 1st heating and cooling runs for molded and precrystallized samples so as to monitor the structure development.

2.11.5 Thermo Gravimetric Analysis

The degradation pattern and thermal stability of the various composites and nanocomposites were followed by TGA[10] wherein the % weight loss of the sample was analyzed as a function of temperature. The sample masses were between 0.005-0.010 g and they were heated from 50 ºC to 700 ºC at the rate of 10 ºC/ min under nitrogen atmosphere. Onset of degradation, maximum degradation temperature and the weight loss at the maximum degradation temperature were the parameters determined from the TGA curves.

2.11.6 Scanning Electron Microscopy

SEM[11] studies were performed to investigate the surface morphology/ microstructure of the injection molded samples as well as the mode of fracture in tensile specimens of PP/ mica composites/ nanocomposites. The flexural testing bars were sectioned vertically to look at the microstructure whereas the samples fractured after tensile testing were taken as such. The samples were mounted vertically on the standard specimen holder by using silver paste. The cross-section of the compression molded PPS/ mica composites and nanocomposites were examined to establish the homogeneous microstructure of PPS/ nano-mica system as opposed to the heterogeneous microstructure of PPS/ mica samples. The PPS samples were stuck vertically on to the conductive tape already pasted on the mounting stub. All the samples were coated with a thin layer of gold in plasma coating unit ES000 to prevent charging of the specimen. The micrographs of the samples with 10 KV EHT and 25 PA beam current were recorded by a CCD camera attached on to the high resolution recording unit.

2.11.7 Transmission Electron Microscopy

The nano-mica/ PPS samples were dispersed in 2-chloronapthalene at 200 ºC so as to dissolve the PPS surrounding the mica particles and a drop was cast on to the carbon coated TEM grid. The TEM[12] measurements of the mica samples cast on the carbon coated grids were carried out on a JEOL model 1200 ES instrument at an accelerating voltage of 120 KV.

2.11.8 X-Ray Diffraction

The samples were characterized extensively by wide angle X-ray diffraction (WAXD). The samples were run using a Philips X-Ray Diffractometer (PW 1730, Cu Kα radiation (wavelength, $\lambda = 0.154054$ nm) operated at 40 KV/ 30 mA). The samples were scanned in fixed time (FT) mode with a scan rate of 5°/min in the 2θ range of 10°-60° for powdered mica samples obtained after in situ polymerization whereas the melt crystallized PP and PPS samples were scanned from 10°- 45°.

WAXD patterns were indexed for known crystal structures by comparing the obtained d-spacing with expected d-spacing. The crystal structure of unknown specimen was determined by iterative techniques correcting the lattice parameters so as to obtain the d-values closest to the observed ones. Crystallinity (C_i) was determined from WAXD as follows: the amorphous scattering curve was first determined graphically by deconvolution of the experimental curve. The area under the main crystalline peaks (ψ_c) and the area of the amorphous halo (ψ_a) were measured after due correction for the background scattering. C_i was calculated from the equation

$$C_i = \left(\frac{\psi_c}{\psi_a + \psi_c} \right) \tag{2.1}$$

The crystallite size was measured using Scherrer's formula[13] by considering the full width at half the maximum intensity of the diffraction peak as

$$L = \left(\frac{B\lambda}{\Delta\theta \cos\theta} \right) \tag{2.2}$$

where B = constant equal to 1

λ = wavelength of CuKα radiation equal to 1.54054 Aº

$\Delta\theta$ = breadth of the peak in radians

θ = diffraction angle

L = crystallite size

2.11.9 Impedance Analyzer

All the dielectric relaxation studies[14] were carried out with a Solartron SI 1255 impedance analyzer with a dielectric interface 1296 in a parallel plate configuration. The gold coated samples were placed in an evacuated chamber with a heating arrangement and connected to the frequency generator. The impedance analyzer software was used to obtain ε', ε'' and tan δ for each run. The dielectric relaxations of PP/ mica samples were recorded over a temperature range of –70 ºC to +70 ºC whereas PPS/ mica samples were scanned from +30 ºC to +170 ºC.

2.11.10 Tensile Testing

The tensile properties of the dumbbell shaped specimens were evaluated with a Instron Series IX Automated Materials Testing System 1.04. The test conditions and the sample specifications used were as follows

Temperature	25 ºC
Humidity	< 30%
Sample rate	10 pts/ sec
Crosshead speed	50 mm/ min
Specimen type	ASTM D-638
Extensometer gauge length	35 mm
Grip distance	55 mm
Thickness	1.3 mm
Width	4.66 mm

2.11.11 Flexural Testing

The flexural testing was done by the 3 point bending method utilizing a Instron Series IX Automated Materials Testing System 1.04. The test conditions and the sample specifications used were as follows

Temperature	25 ºC
Humidity	< 30%
Sample rate	10 pts/ sec
Crosshead speed	1.3 mm/ min
Specimen type	ASTM D-690

Width	12 mm
Depth	3.18 mm
Span	50 mm

2.12 References

1) Shah, V. *Handbook of Plastics Testing Technology*, 2nd ed.; John Wiley: New York, 1998.
2) *Handbook of Plastics Test Methods*; Brown, R. P., Ed.; Longman: Harlow, 1981.
3) Ward, I. M. *Mechanical Properties of Solid Polymers*, 2nd ed.; John Wiley: Chichester, 1983.
4) Sawyer, L. C.; Grubb, D. T. *Polymer Microscopy*; Chapman and Hall: London, 1987.
5) Meeten, G. H. *Optical Properties of Polymers*; Elsevier Applied Science Publishers: London, 1986.
6) Khare, A.; Mitra, A.; Radhakrishnan, S. *J. Mater. Sci.* **1996**, *31*, 5691.
7) Radhakrishnan, S.; Saujanya, C. *J. Mater. Sci.* **1998**, *33*, 1069.
8) Saujanya, C.; Radhakrishnan, S. *Polymer* **2001**, *42*, 6723.
9) *Thermal Characterization of Polymeric Materials*, 2nd ed.; Turi, E. A., Ed.; Academic Press: San Diego, 1997; Vol. 1.
10) Turi, E. A. *Thermal Characterization of Polymeric Materials*; Academic Press: London, 1981.
11) Goldstein, J. I., Lyman, C. E., Newbury, D. E., Lifshin, E., Echlin, P., Sawyer, L., Joy, D. C., Michael, J. R. *Scanning Electron Microscopy and X-Ray Microanalysis*, 3rd ed.; Kluwer Academic: New York, 2003.
12) Williams, D. B., Carter, C. B. *Transmission Electron Microscopy: A Textbook for Materials Science*; Plenum Press: New York, 1996; Vol. 1.

13) Alexander, L. E. *X-Ray Diffraction Methods in Polymer Science*; John Wiley: New York, 1969.

14) *Dielectric Properties of Polymers*; Karasz, F. E. Ed.; Plenum: New York, 1972.

3.1 Introduction

In particle filled polymer composites, with mica fast gaining prominence as a replacement for glass fibres in various engineering plastics and general thermoplastics, value addition in terms of its properties deserves some special attention. Automotives, electronics and structural applications have emerged to be the drivers for the thrust in this area. The nanoparticulate form of mica is expected to offer much better property enhancements as compared to its micron-sized equivalent. Towards this end, we have devised a new synthetic strategy to obtain nanoparticulate form of naturally occurring mica by in situ intercalative polymerization.

Micas are complex hydrous aluminosilicates that belong to a class of layered silicates called phyllosilicates.[1,2] As discussed in chapter-1 of this thesis, the naturally occurring micas have different types of layered structures in which there appears to be sufficient spacing for a monomer such as 1,4-dibromobenzene to diffuse/ ionically interact.[3-6] This, when subsequently polymerized, can lead to the downsizing of the mica particles. Such a technique is expected to lead to mica particles embedded in a polymer matrix and provide in situ nanocomposite. This chapter describes the synthesis of nanoparticulate mica using three types of naturally occurring micas.

3.2 Experimental

In a typical reaction, 1,4-dibromobenzene (*p*-DBB) was first intercalated with natural mica particles (sieved) by heating a mixture (in a desired proportion) of both in NMP (100 ml) at 80-100 °C for 8-10 hours. This was treated with a stoichiometric equivalent of sodium sulfide dissolved in a small quantity of methanol (20 ml). After

distilling off the methanol, the dispersion was heated at 160-180 °C for 12 hours. After cooling the reaction flask to room temperature, the PPS formed as per the reaction

Scheme-1

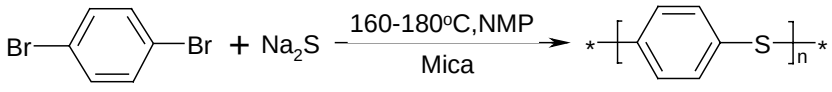

was precipitated by adding excess methanol to the dispersion. The solution was filtered and the PPS with nanoparticulate mica was repeatedly washed with methanol and then dried in vacuum for 24 hours. This powdered sample was used for all the characterizations.

The nanoparticle formation was studied as a function of the initial mica loading and the average particle size of the initial mica taken to understand the various parameters that affect its formation. An alternative route in which a solution of sodium sulfide in methanol was first intercalated with mica and subsequently polymerized was also explored.

3.2.1 Particle Size Variation

The micas were sieved through various mesh sizes to obtain different average particle sizes of 41, 48, 72 and 120 microns. All these experiments were carried out at a mica loading of 17-wt % with respect to the monomer (i.e.) 1,4-dibromobenzene. The complete details of the experiment in case of phlogopite, muscovite and chlorite are depicted in tables 3.1, 3.2 and 3.3 respectively. The yield of PPS for the blank reaction (without mica) between 1,4-dibromobenzene and sodium sulfide was 45 %.

Table 3.1 Particle size variation data in phlogopite

Mica particle size (μ)	1,4-dibromobenzene (g)	Sodium sulfide (g)	Reaction time (hrs)	PPS yield (Wt.%)	Mica/PPS ratio
41	3.54	3.6	12	49	1: 2
48	3.54	3.6	12	49	1: 2
72	3.54	3.6	12	45	1: 2
120	3.54	3.6	12	45	1: 2

Table 3.2 Particle size variation data in muscovite

Mica particle size (μ)	1,4-dibromobenzene (g)	Sodium sulfide (g)	Reaction time (hrs)	PPS yield (Wt.%)	Mica/PPS ratio
41	7.08	7.2	12	58	1: 3
48	7.08	7.2	12	57	1: 3
72	7.08	7.2	12	49	1: 2
120	7.08	7.2	12	49	1: 2

Table 3.3 Particle size variation data in chlorite

Mica particle size (μ)	1,4-dibromobenzene (g)	Sodium sulfide (g)	Reaction time (hrs)	PPS yield (Wt.%)	Mica/PPS ratio
41	7.08	7.2	12	60	1: 5
48	7.08	7.2	12	58	1: 3
72	7.08	7.2	12	55	1: 3
120	7.08	7.2	12	54	1: 3

3.2.2 Mica Loading Level Variation

The effect of varied mica loading levels (with respect to the monomer) on the PPS yield was ascertained by varying the loading by 4, 8, 11, 17, 30 and 46-wt % of mica. All the experiments were carried out with mica having an average particle size of 41 μ. The details of the experiments with phlogopite, muscovite and chlorite are shown in the tables 3.4, 3.5 and 3.6, respectively.

Table 3.4 Mica loading level variation in phlogopite

Mica loading (Wt.%)	1,4-dibromobenzene (g)	Sodium sulfide (g)	Reaction time (hrs)	PPS yield (Wt.%)	Mica/PPS ratio
0	3.54	3.6	9	45	_
4	3.54	3.6	12	51	1: 12
8	3.54	3.6	12	65	1: 6
11	3.54	3.6	12	56	1: 4
17	3.54	3.6	12	49	1: 2
30	3.54	3.6	12	49	1: 1
46	3.54	3.6	12	45	2: 1

Table 3.5 Mica loading level variation in muscovite

Mica loading (Wt.%)	1,4-dibromobenzene (g)	Sodium sulfide (g)	Reaction time (hrs)	PPS yield (Wt.%)	Mica/PPS ratio
0	3.54	3.6	9	45	_
4	7.08	7.2	12	48	1: 12

8	7.08	7.2	12	55	1: 6
11	7.08	7.2	12	58	1: 4
17	7.08	7.2	12	54	1: 2
30	7.08	7.2	12	46	1: 1
46	3.54	3.6	12	48	2: 1

Table 3.6 Mica loading level variation in chlorite

Mica loading (Wt.%)	**1,4-dibromobenzene (g)**	**Sodium sulfide (g)**	**Reaction time (hrs)**	**PPS yield (Wt.%)**	**Mica/PPS ratio**
0	3.54	3.6	9	45	_
4	7.08	7.2	12	45	1: 9
8	7.08	7.2	12	46	1: 5
11	7.08	7.2	12	54	1: 4
17	7.08	7.2	12	60	1: 4
30	7.08	7.2	12	69	1: 2

3.2.3 Reversed Intercalation

In this experiment, 3.60 g of sodium sulfide was first powdered and dissolved in 50-60 ml of methanol. This was added to a suspension of 0.75 g of mica in 100 ml of NMP and allowed to stand for 8-10 hours. Later, 3.54 g of 1,4-dibromobenzene was added to the dispersion, the excess methanol distilled and the reaction mixture heated at 160-180 °C for 12 hours. The PPS formed was precipitated and processed as mentioned above. This experiment was carried out only with phlogopite mica having an average particle size of 41μ. The yield of the PPS formed was around 49 % and has a mica/ PPS

ratio of 1: 2. This experiment clearly suggests that either of these monomers could be intercalated and subsequently polymerized to obtain nanoparticulate mica.

3.3 Results and Discussion

3.3.1 Effect of Mica Particle Size and Loading Levels on PPS Yield

The formation of nanoparticulate mica as well as the PPS yield was studied as a function of the initial concentration and the average particle size of the initial mica taken in the reaction mixture. Figure 3.1 and 3.2 indicates the variation of the PPS yield obtained with the concentration as well as the initial particle size of the mica added in the reaction mixture, respectively.

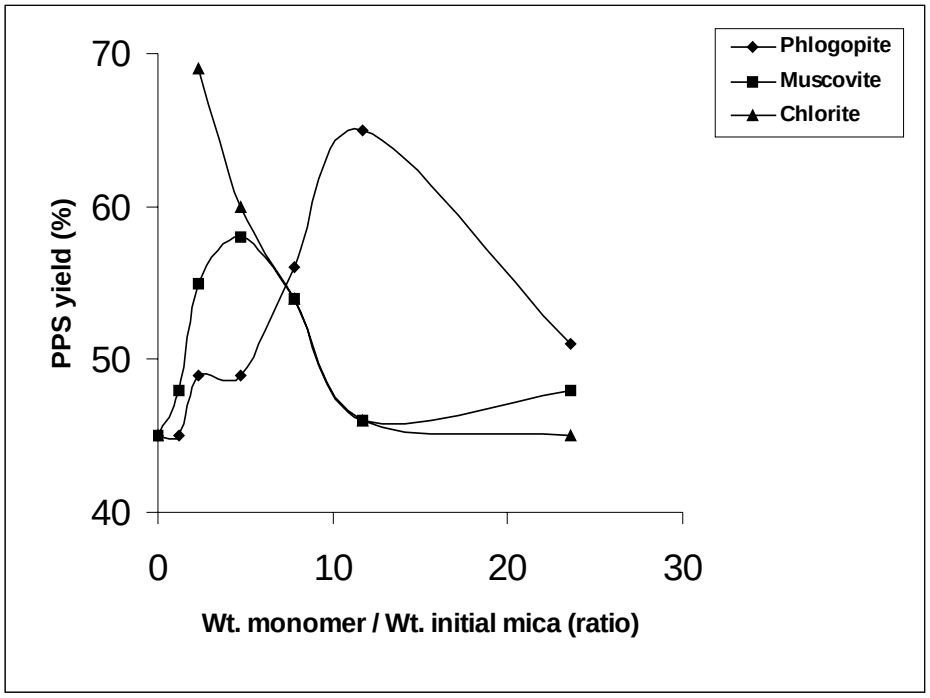

Figure 3.1 Effect of mica on the PPS yield as a function of monomer / mica ratio

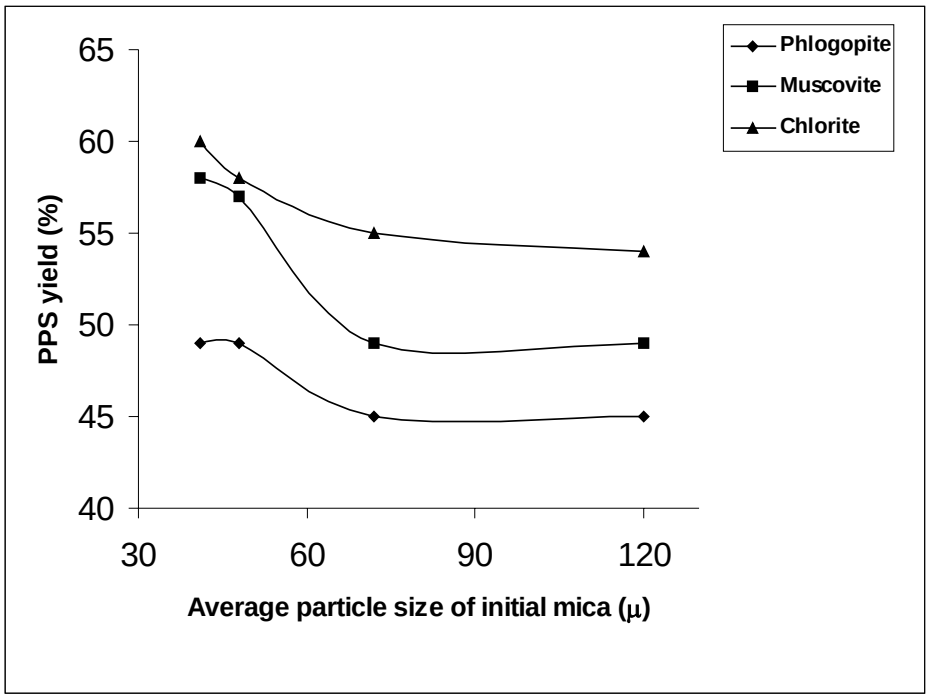

Figure 3.2 PPS yield as a function of particle size of mica taken initially

It is evident that the polymer (PPS) yield depends very much on the presence of mica as well as the type of mica used which suggests that the polymerization takes place preferably on the mica particle surface. Further, it's observed that the particle size of the mica used also plays a decisive role in controlling the polymerization / yield as shown in figure 3.2. Many reasons could be speculated for these observations. Firstly, the monomer was allowed to penetrate the mica interlayer sites and then the polymerization reaction with sodium sulfide was carried out. Thus, the extent of reactant available was controlled by the mica particles. Secondly, the surface area of the particles increases with the decrease in the particle size and hence the interfacial effects at the solid /liquid boundary become prominent. This clearly brings out the diffusion of the 1,4-

dibromobenzene and its intercalation in the mica interlayer gallery. It may be pointed out here that mica particles have been reported to adsorb / absorb organic molecules such as dyes, surface modifiers etc.[7,8] Increasing mica loading levels results in increased PPS yield up to a threshold after which there is little change in the polymer yield. The yield increase could be explained in terms of additional reactive sites being available on the mica where the monomer gets intercalated. A slight decrease in the yield at much higher loading levels might be the result of agglomeration / binding of the particles by the polymer. It is interesting to note that chlorite mica has a threshold concentration greater than that of muscovite and phlogopite which may be due to its more open structure as seen in the figures 3.3-3.5. The intercalation of 1,4-dibromobenzene on the mica particles and its subsequent polymerization thus leads to a significant delamination of mica. These observations were confirmed by WAXD studies which are presented later in this chapter.

3.3.2 Theoretical Estimation of the Extent of Intercalation

The amount of 1,4-dibromobenzene intercalation in to phlogopite, muscovite and chlorite was theoretically estimated from the respective unit cell formulae and the number of molecules present in each unit cell. Phlogopite and chlorite are monoclinic whereas muscovite is hexagonal. The unit cell parameters of each mica type along with the crystal system and the number of molecules per unit cell are given in table 3.7

The precise structural formulae for phlogopite, muscovite and chlorite needed to calculate the extent of monomer intercalation were taken from literature.[6] The formulas mentioned in the earlier chapter-1 are quite general in nature and so were not used.

Table 3.7 Crystal structure data of different micas

Mica type	Crystal System	Unit Cell Parameters	No: of molecules / unit cell
Phlogopite	Monoclinic	a = 5.31 Å b = 9.21 Å c = 10.13 Å β = 100º1′	2
Muscovite	Hexagonal	a = 5.3 Å c = 30.1 Å	3
Chlorite	Monoclinic	a = 5.314-5.362 Å b = 9.205-9.289 Å c = 28.363-28.64 Å β = 97º10′	4

Phlogopite $K_{0.95}(Mg_{2.8}Li_{0.2})(Si_{3.25}Al_{0.75})O_{10}F_2$

Muscovite $KR_3(Al,Si)_4O_{10}(OH,F)_2$

Chlorite $(Mg,Al)_5(Si,Al)_4O_{10}(OH)_8$

The molecular weight of each of these micas was calculated and multiplied by the number of molecules per unit cell of the respective micas to obtain the molecular weight of the unit cell. This was used to ascertain the number of 1,4-dibromobenzene (mol.wt. – 236) moieties that could be adsorbed on to each mica surface.

Molecular weight of phlogopite unit cell - 832 g.

Molecular weight of muscovite unit cell - 1474 g.

Molecular weight of chlorite unit cell - 3090 g.

If one assumes that the 1,4-dibromobenzene penetrates the crystal lattice at the inter-layer sites and interacts with the potassium atoms, each unit cell of chlorite could be expected to intercalate 10-13 monomer molecules whereas muscovite and phlogopite can intercalate only 4-6 and 2-3 monomer units respectively. Figures 3.3, 3.4 and 3.5 show the space filling models of phlogopite, muscovite and chlorite respectively depicting the possible modes of 1,4-dibromobenzene intercalation in them. Since the extent of intercalation calculated theoretically shows the order chlorite > muscovite > phlogopite, we surmised that the extent of polymerization would be greater in chlorite as compared to that of muscovite and phlogopite. This should result in a better delamination of chlorite with respect to muscovite and phlogopite, which was actually found to be the case as would be seen later in this chapter.

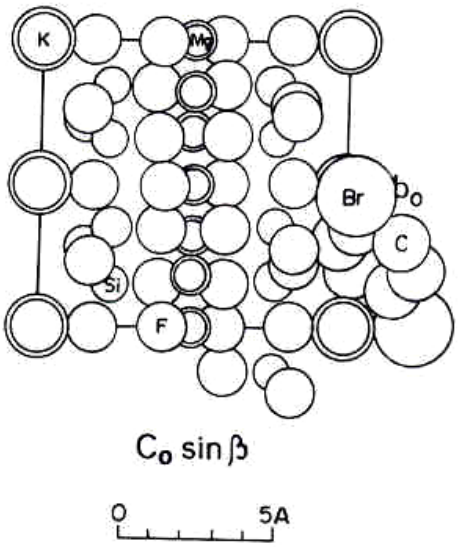

Figure 3.3 Space filling model of phlogopite projected along the a_0 axis depicting the probable sites for 1,4-dibromobenzene interaction

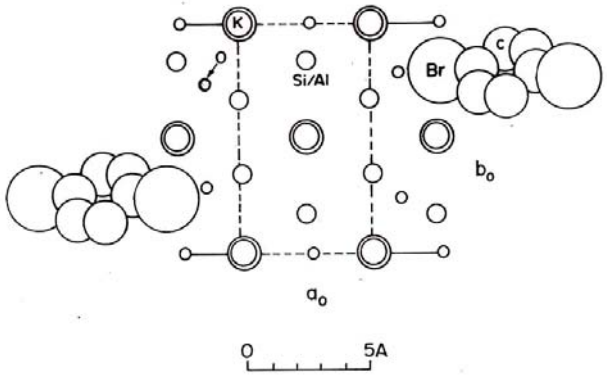

Figure 3.4 Space filling model of muscovite projected along the c_0 axis and the probable sites for interaction of 1,4-dibromobenzene

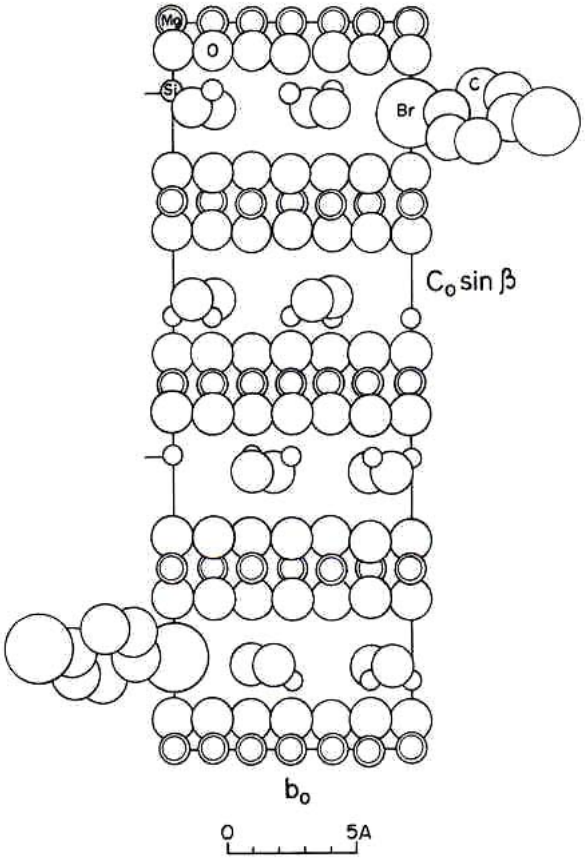

Figure 3.5 Space filling model of chlorite projected along the a_0 axis and the probable sites for interaction of 1,4-dibromobenzene

3.3.3 Qualitative Analysis of Mica Surface Area by UV-Vis Spectroscopy

Adsorption and interaction at the alkali metal ions of mica have been reported in the past for ionic dyes like crystal violet, methylene blue etc.[9-11] Changes in the spectral characteristics of such dyes have also been studied in great detail.[12] The change in the UV spectrum in those cases was speculated to be due to the formation of aggregates which result due to the interaction between the π electrons of the neighboring dye molecules.[13,14]

When cationic dyes were adsorbed to clays, the corresponding UV spectra of the dyes were found to undergo a shift towards higher or lower wavelengths.[15,16] The absorption of cationic dyes in synthetic saponite occurs by a cation exchange reaction. Exchangeable metal ions (Na^+) are simultaneously released in to the aqueous solution when dyes are intercalated in to the clays. It was thought that this particular interaction of the mica with ionic dyes could help in qualitatively evaluating the intercalation efficiency of the various micas. Accordingly the dye, crystal violet was chosen for this purpose whose structure is shown in the figure 3.6. A known quantity of all the three micas was soaked in a solution of crystal violet in NMP for a fixed amount of time. The different dispersions were subsequently filtered and the UV spectra of the filtrates were recorded. The overlay of the spectra obtained in case of the three different micas is shown in the figure 3.7.

The concentration of the dye solution in all the cases was maintained the same and the level of dilution was quite high (25×10^{-6} M). Since the UV results depict the absorbance of the filtrates, the actual amount of the dye absorbed is (1 – optical absorbance). In fact, our hypothesis was proved true by the results obtained as seen in the figure 3.7. The intercalating efficacy of chlorite was found to be greater than that of muscovite, which in turn was found to be better than phlogopite.

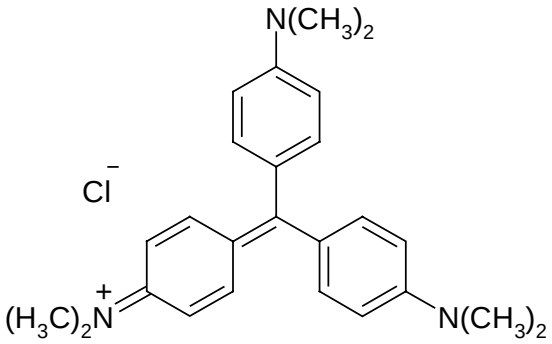

Figure 3.6 Structure of Crystal Violet

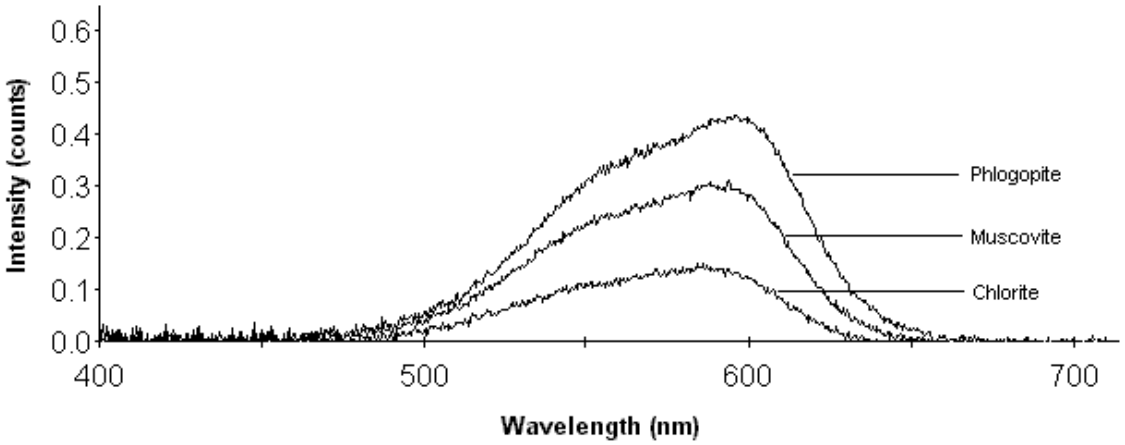

Figure 3.7 UV spectra of the filtrates from dye after soaking mica particles. Extent of dye absorbed by mica is (1 - optical absorbance)

3.3.4 FT-IR Studies

The nanoparticulate mica synthesized by in situ intercalative polymerization is embedded in a PPS matrix. To confirm the presence of PPS, IR spectra of the mica samples and the PPS obtained from the blank reaction between 1,4-dibromobenzene and sodium sulfide (without mica) were recorded and compared with the standard commercial Ryton PPS (P4 powder grade). The IR spectra of the commercial PPS, lab synthesized PPS and phlogopite mica/ PPS are shown in the figures 3.8-3.10.

It is seen that the spectrum of lab synthesized PPS clearly resembles that of the commercial Ryton PPS. It exhibits all the major peaks characteristic of PPS. The peak intensities reflect the different levels of crystallinity and amorphous nature. The absorbance ratio between the bands at 1072 cm^{-1} and 1092 cm^{-1} is a relative measure of the relative crystallinity of the polymer.[17-19] The assignments for the various peaks after Zimmerman et al.[20] are given in table 3.8.

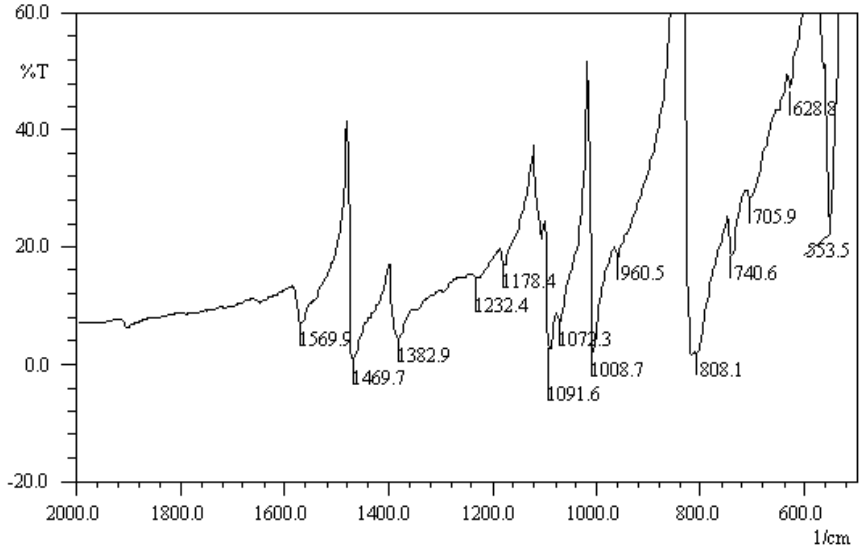

Figure 3.8 IR spectrum of commercial Ryton PPS

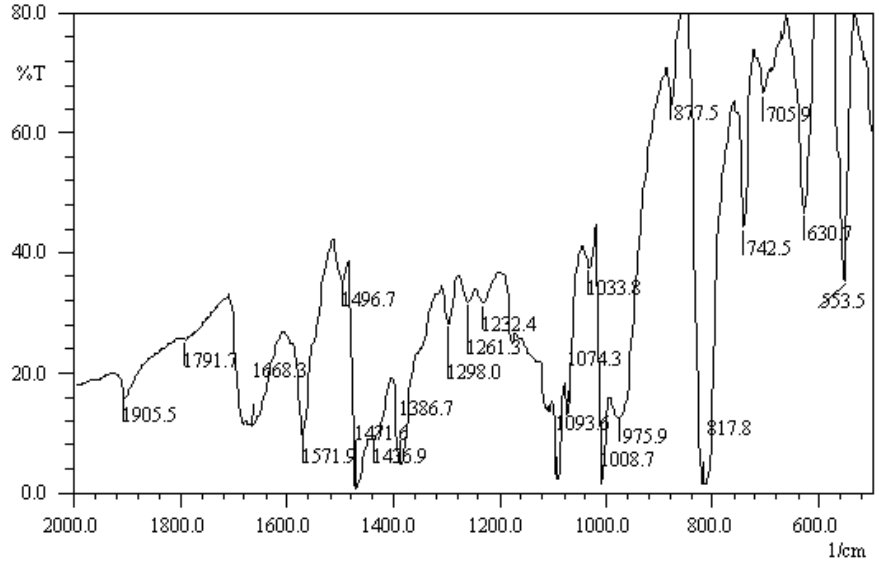

Figure 3.9 IR spectrum of lab synthesized PPS (without mica)

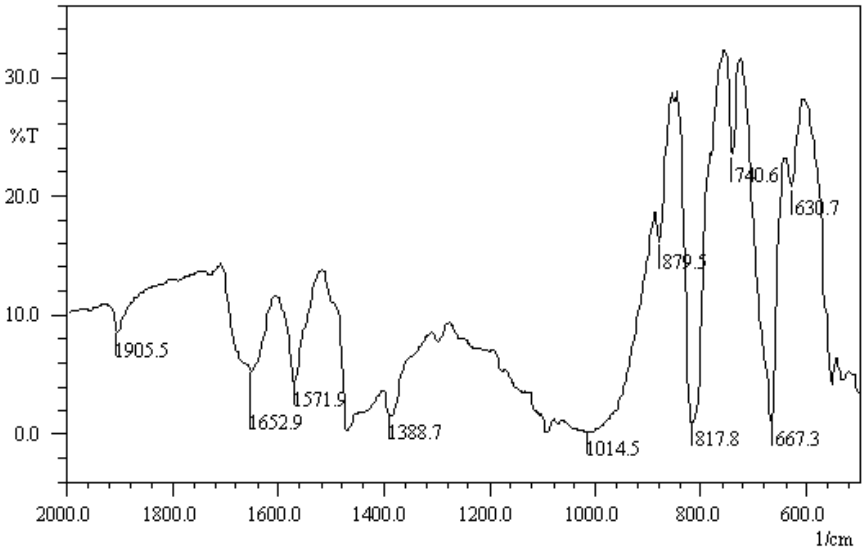

Figure 3.10 IR spectrum of phlogopite mica/ PPS

Table 3.8 IR band assignment for PPS

Peak position (cm^{-1})	IR band assignment
1570	-
1470	Ring stretching
1380	-
1091	Anti-symmetric ring S stretching
1072	Symmetric ring S stretching
1009	C-H in plane deformation
809	C-H in out of plane deformation
740	Out of plane skeletal deformation

3.3.5 Thermal Studies

The nanoparticulate mica obtained by in situ polymerization was to be compounded with PP and PPS for investigating the crystallization behavior and structure development in the corresponding nanocomposites. So, it was essential to characterize the melting temperature, the crystallization temperature and the degradation pattern of the PPS in which the nanoparticulate mica is embedded. The DSC profiles of commercial Ryton PPS and lab synthesized PPS (without mica) are shown in the figures 3.11 and 3.12, respectively. It is easily seen that the lab synthesized PPS is fast crystallizing with a higher melting temperature because of its lower molecular weight and higher crystallinity.

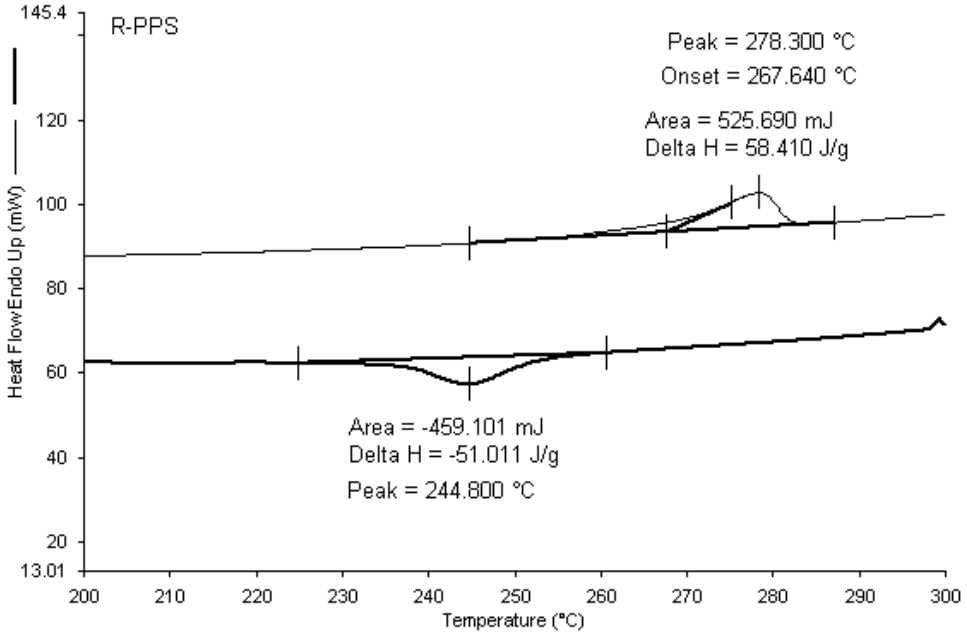

Figure 3.11 DSC thermogram of commercial Ryton PPS

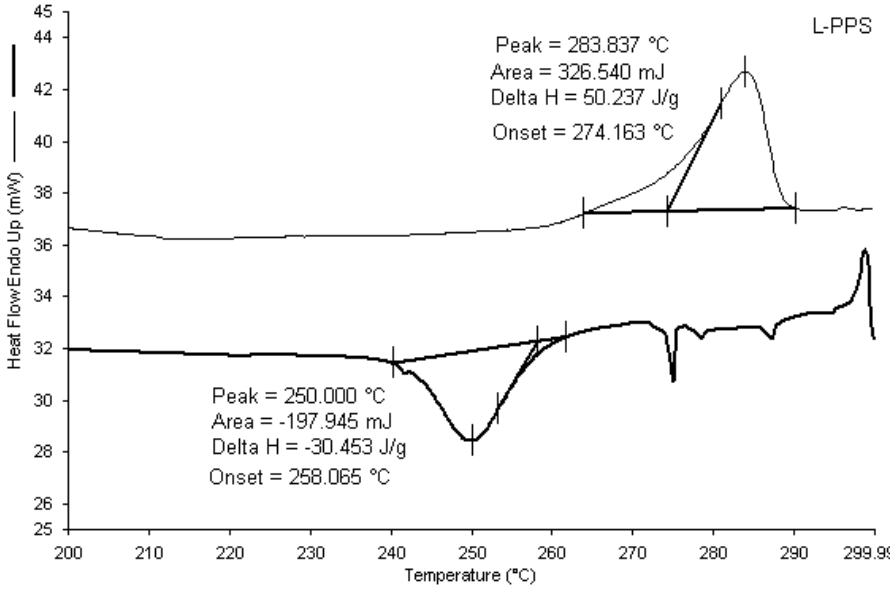

Figure 3.12 DSC thermogram of lab synthesized PPS

The thermograms of commercial Ryton PPS, lab synthesized PPS and PPS with phlogopite mica are shown in the figures 3.13 to 3.15.

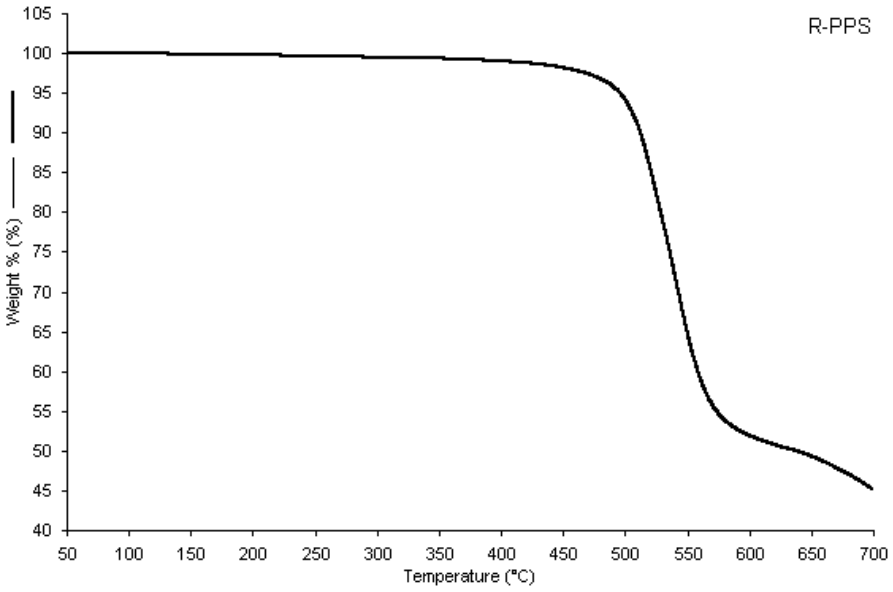

Figure 3.13 TGA of commercial Ryton PPS

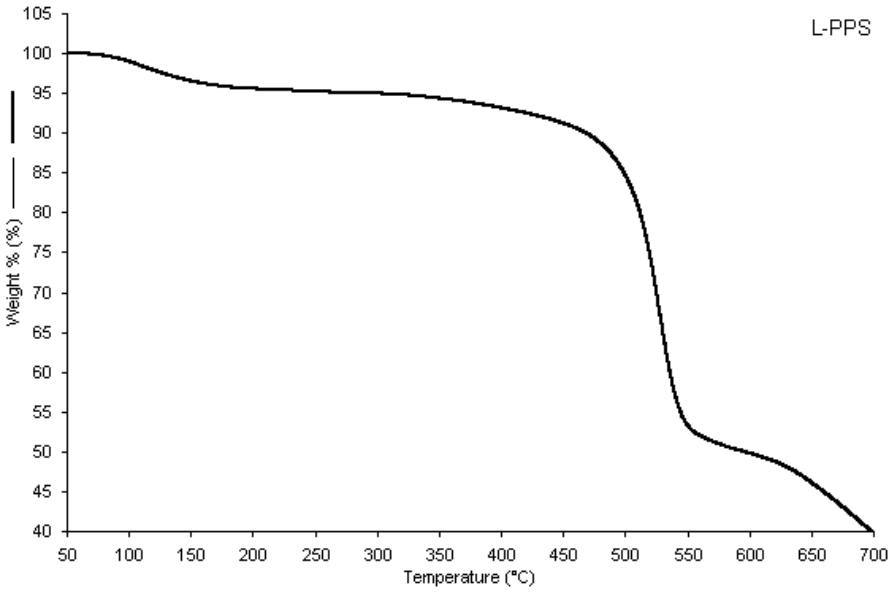

Figure 3.14 TGA of lab synthesized PPS (without mica)

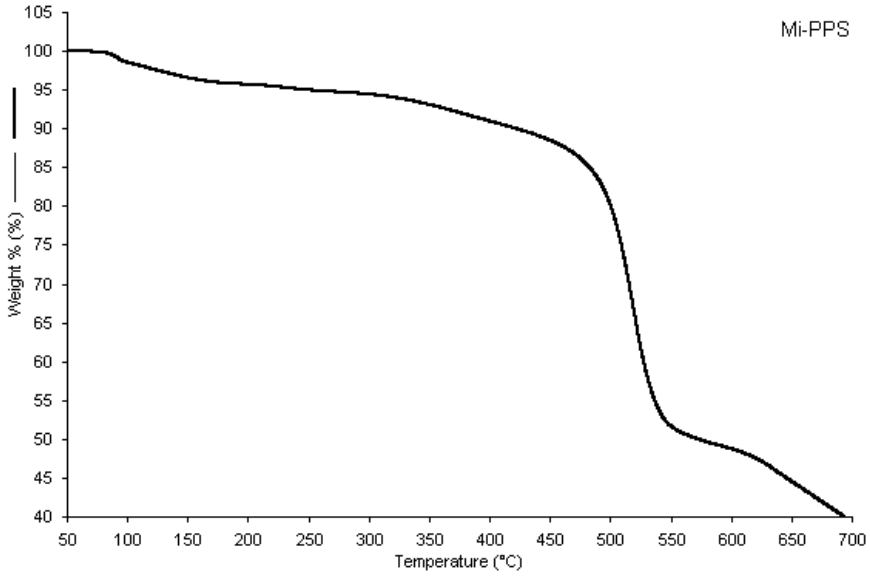

Figure 3.15 TGA of phlogopite mica/ PPS

It is seen that the lab synthesized PPS has two degradation steps as against the single step for the commercial Ryton PPS, which might be attributed to its lower molecular weight.

3.3.6 WAXD Analysis

The synthesized nano-mica was characterized extensively by WAXD. The WAXD overlays for various loading levels of phlogopite, muscovite and chlorite are shown in the figures 3.16 to 3.18 respectively. In all cases, it is seen that the original mica particles exhibit a very sharp XRD pattern while those after in situ intercalative polymerization reaction become increasingly broader and in some cases, certain diffraction peaks totally disappear. In case of phlogopite, three prominent peaks (020, 003 and 004) are observed in the diffraction profile. The 020 peak almost disappears at 4 wt.% loading whereas the intensities of the 003 and the 004 peaks diminish considerably.

The peak positions are retained but a substantial peak broadening is observed indicating the breakdown of the layered structure of mica. The same trend can be observed both in the case of muscovite as well as chlorite. In muscovite, we find that the 006 peak vanishes at a considerably low monomer loading (i.e.) higher mica loading whereas the intensity of the 009, 00 $\bar{1}$2 and 00 $\bar{1}$5 peaks diminish significantly as the mica loading level approaches 4 wt.%. In chlorite too, all the peak intensities are reduced quite a bit but a considerable broadening of the peaks is also observed which suggests that the delamination in case of chlorite is even better than in the case of phlogopite and muscovite.

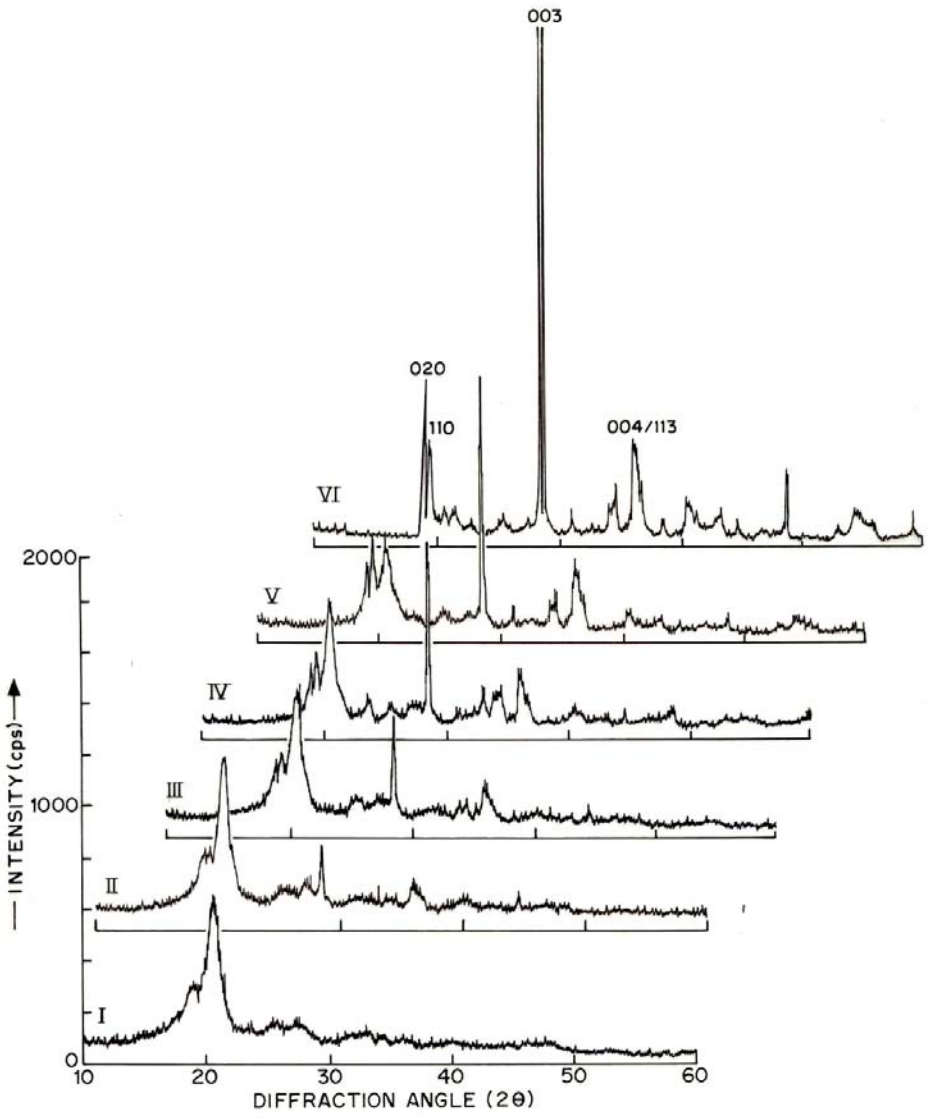

Figure 3.16 WAXD scans for phlogopite mica after in situ polymerization. Curves II to V correspond to 4, 11, 17 and 30 wt.% of phlogopite mica. Curves I and VI represent pure PPS and commercial phlogopite respectively.

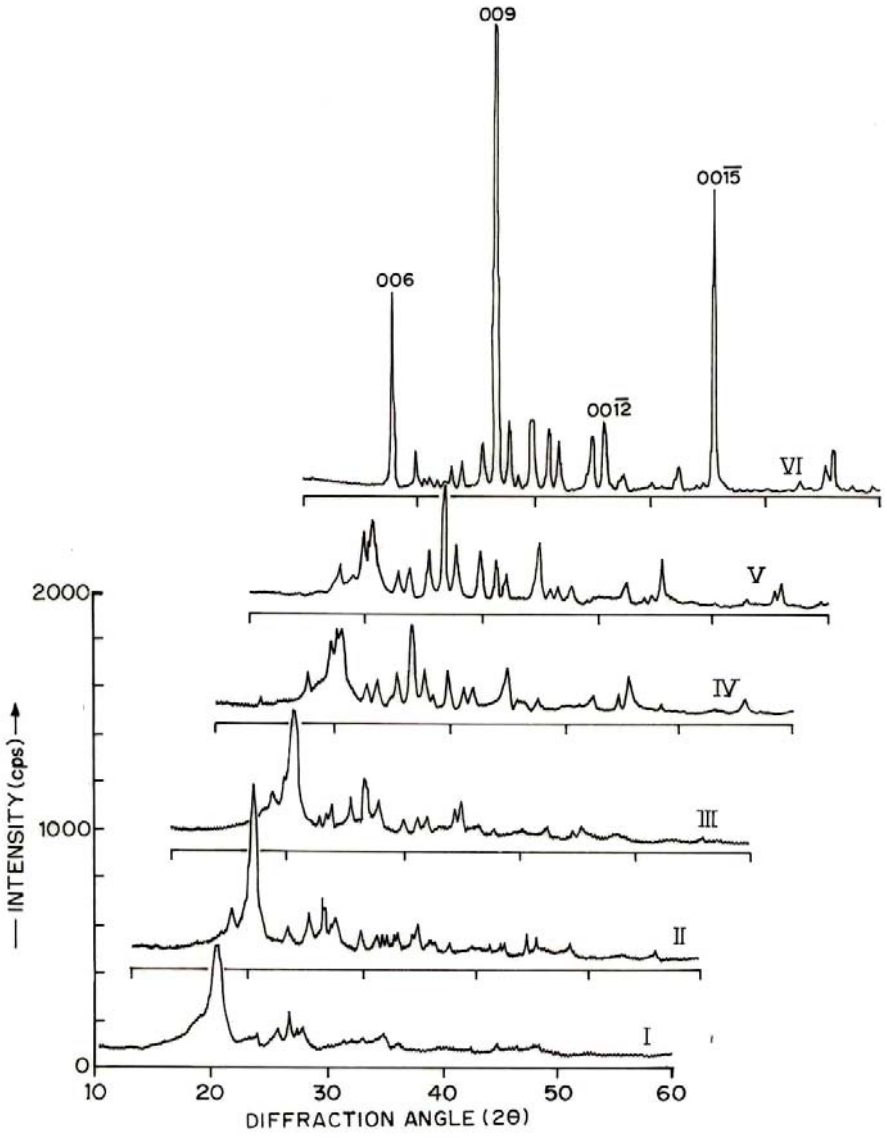

Figure 3.17 WAXD scans for muscovite mica after in situ polymerization. Curves I to V correspond to 4, 8, 11, 17 and 30 wt% of muscovite mica. Curve VI represents commercial muscovite without treatment.

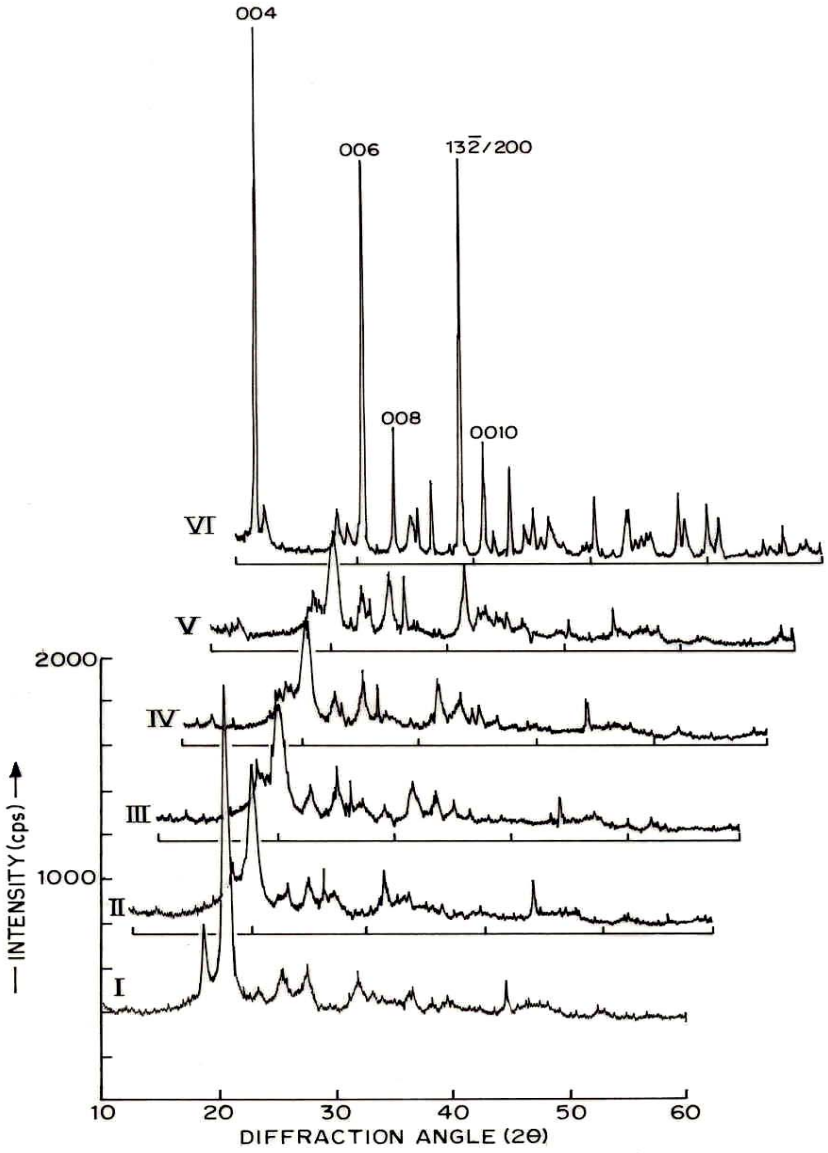

Figure 3.18 WAXD scans for chlorite mica after in situ polymerization. Curves I to V correspond to 4, 8, 11, 17 and 30 wt% of chlorite mica. Curve VI represents commercial chlorite without treatment**.**

The WAXD overlays of phlogopite, muscovite and chlorite for different particle sizes of the initial mica taken for intercalation are indicated in the figures 3.19 to 3.21 respectively. In case of all the micas, we find that the peak intensities subside and the peaks widen as the average particle size of the initial mica taken changes from 120 μ to 41 μ. Here again, we find that there is a drastic decrease in the peak intensities of chlorite even when the average particle size of the mica taken is 120 μ. Once again, this brings out the better intercalating efficacy of chlorite as compared to muscovite and phlogopite which reflects the level of delamination directly. This is further corroborated by the crystallite sizes calculated by Scherrer's formula[21] from the WAXD data, which will be presented later in the chapter.

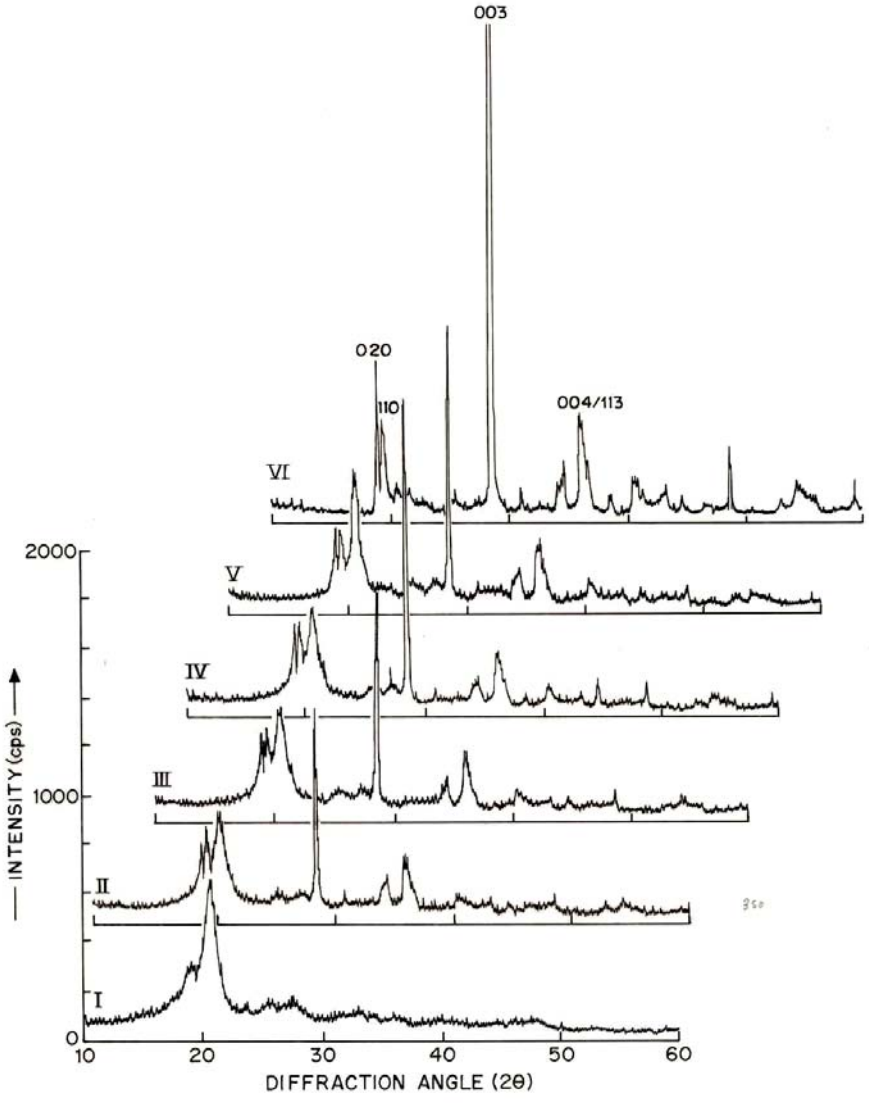

Figure 3.19 Effect of initial mica particle size in delamination of phlogopite during in situ polymerization. Curves II to V correspond to average particle sizes of 41, 48, 72 and 120 μ. Curve I indicates pure PPS and curve VI is for commercial phlogopite without treatment.

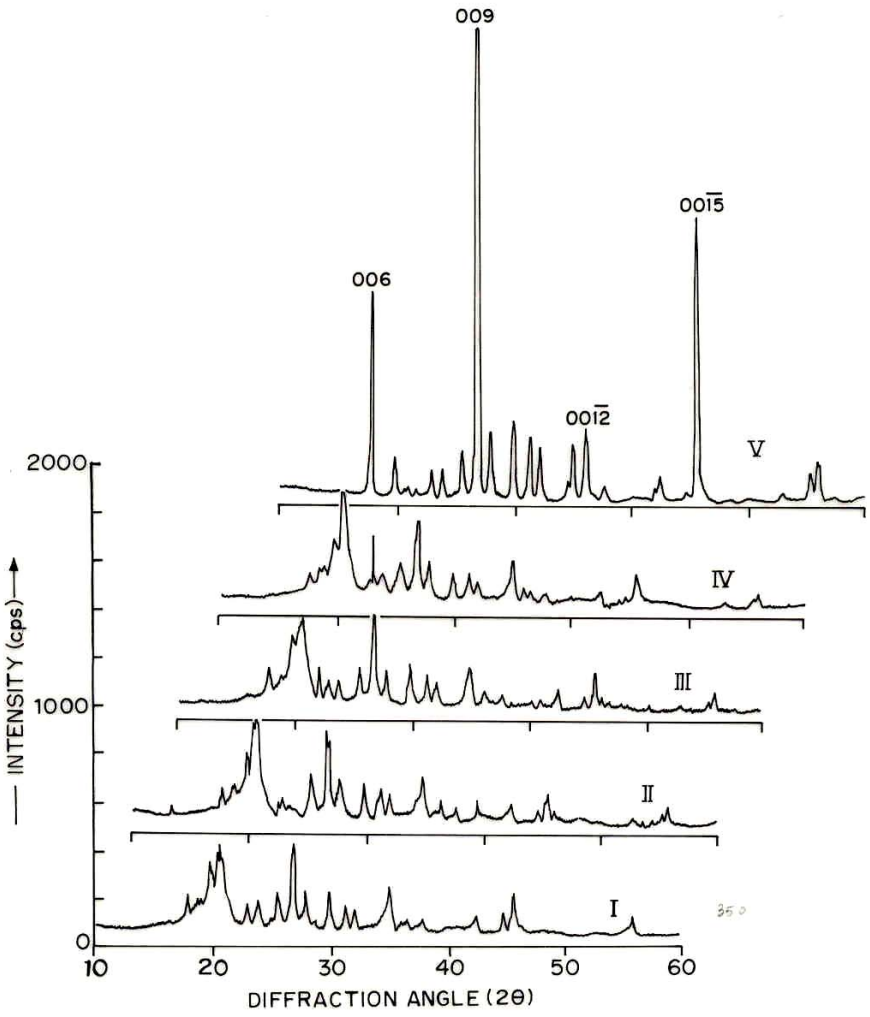

Figure 3.20 Effect of initial mica particle size in delamination of muscovite during in situ polymerization. Curves I to IV correspond to average particle sizes of 41, 48, 72 and 120 μ and curve V is for commercial muscovite without treatment.

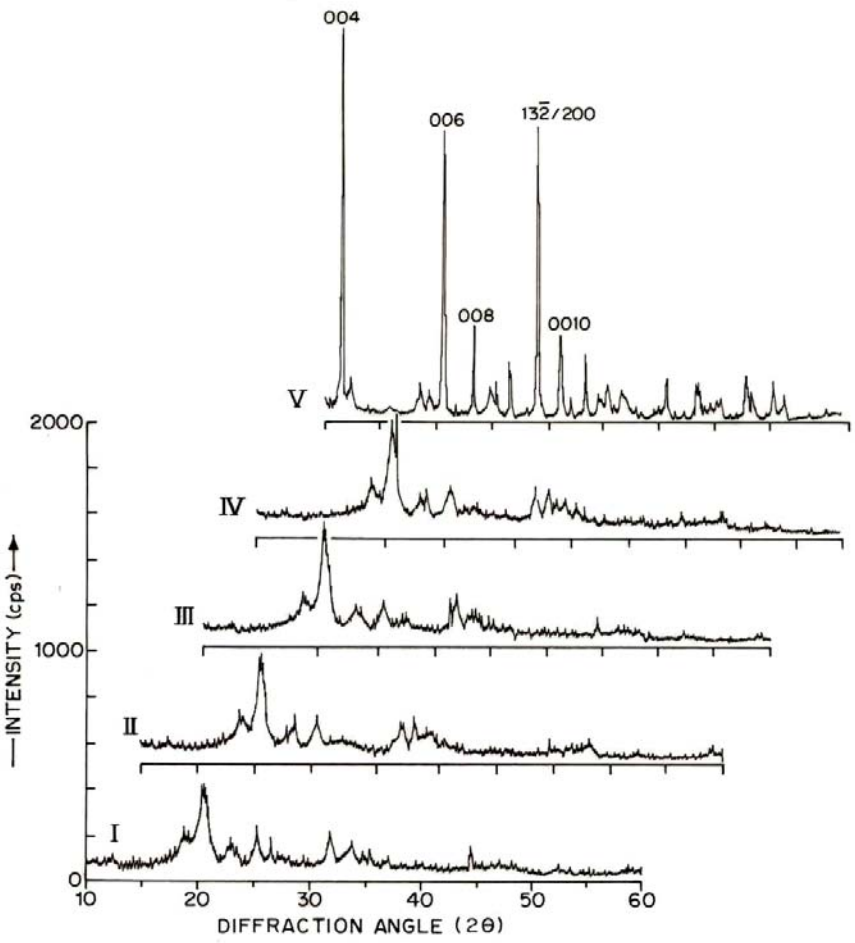

Figure 3.21 Effect of initial mica particle size in delamination of chlorite during in situ polymerization. Curves I to IV correspond to average particle sizes of 41, 48, 72 and 120 μ and curve V is for commercial chlorite without treatment.

The crystallite size of these various types of mica after in situ polymerization was estimated from full width at half the maximum intensity of the various peaks using Scherrer's formula. The crystallite sizes calculated along various planes for phlogopite, muscovite and chlorite for different particle sizes and loading levels are depicted in the tables 3.9 to 3.14 respectively.

Table 3.9 L values of phlogopite mica for various particle sizes

Plane	**Untreated mica (nm)**	**Mica / PPS (nm)**			
		120 μ	**72 μ**	**48 μ**	**41 μ**
020	35.81	23.87	23.87	19.89	17.9
003	17.91	17.91	17.91	15.92	14.33
004	18.57	17.69	17.67	16.51	14.85

Table 3.10 L values of phlogopite mica for different loading levels

Plane	**Untreated mica (nm)**	**Mica / PPS (nm)**			
		30%	**17%**	**8%**	**4%**
020	35.81	28.65	17.90	14.32	17.90
003	17.91	17.91	14.33	14.33	-
004	18.57	14.85	14.85	14.85	14.85

Table 3.11 L values of muscovite mica for various particle sizes

Plane	Untreated mica (nm)	Mica / PPS (nm)			
		120 μ	**72 μ**	**48 μ**	**41 μ**
006	45.91	45.30	38.25	37.86	34.42
009	34.96	23.00	23.30	23.00	23.31
00 $\bar{1}$2	23.84	-	-	-	-
00 $\bar{1}$5	49.18	27.99	28.36	27.99	24.58

Table 3.12 L values of muscovite mica for different loading levels

Plane	Untreated mica (nm)	Mica/PPS (nm)				
		30%	**18%**	**11%**	**8%**	**4%**
006	45.91	45.3	34.42	-	-	-
009	34.96	23.00	23.31	23.29	22.99	-
00 $\bar{1}$5	49.18	27.99	24.58	-	-	-

Table 3.13 L values of chlorite mica for various particle sizes

Plane	Untreated mica (nm)	Mica / PPS (nm)			
		120 μ	**72 μ**	**48 μ**	**41 μ**
200	34.85	19.96	19.41	17.95	17.45

Table 3.14 L values of chlorite mica for different loading levels

Plane	Untreated mica (nm)	Mica / PPS (nm)				
		30%	**18%**	**11%**	**8%**	**4%**
200	34.85	19.41	17.46	17.45	13.97	11.63

From the data on crystallite sizes, the extent of reduction in the crystallite sizes with respect to the monomer concentration as well as the initial particle size of the mica used was evaluated and plotted as shown in the figures 3.22 and 3.23 respectively.

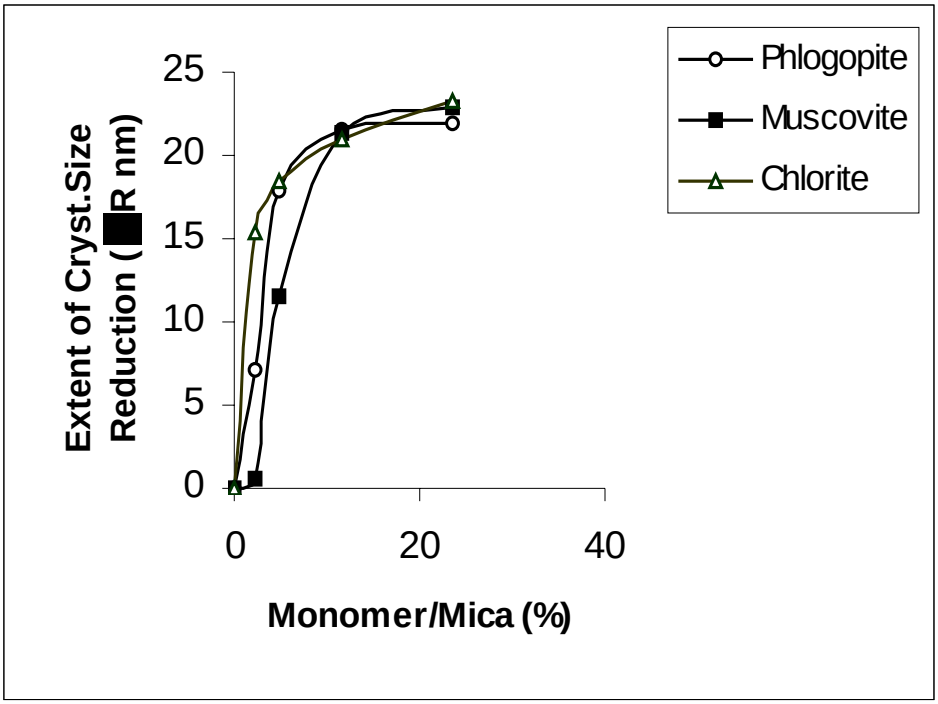

Figure 3.22 Extent of delamination / reduction in particle size in various types of mica by in situ polymerization with different concentrations of monomer used.

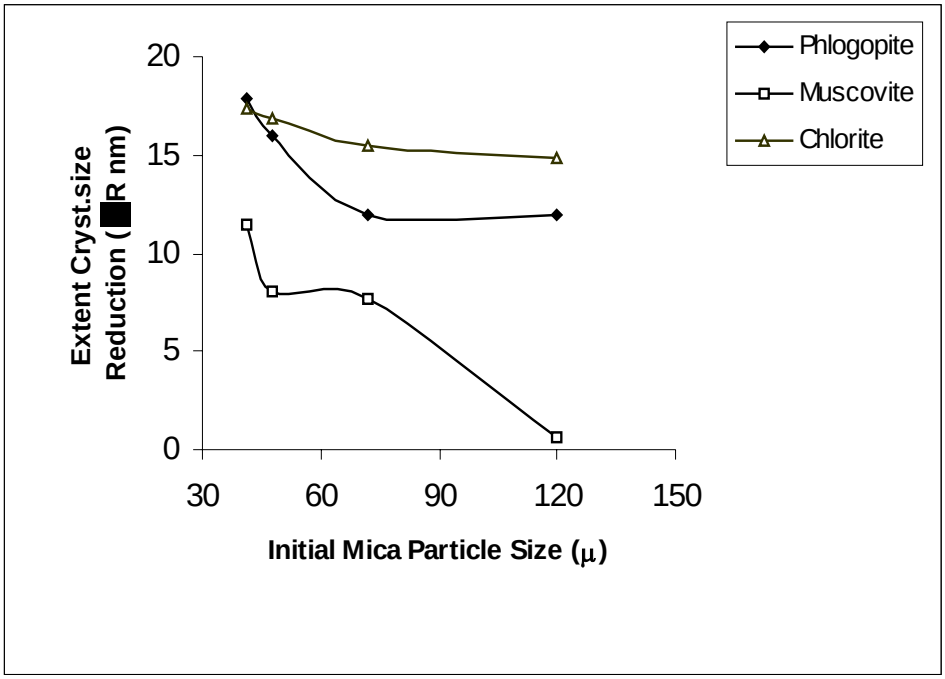

Figure 3.23 The effect of initial particle size of the mica on the extent of particle size reduction by in situ polymerization technique

The crystallite size was found to decrease with decreasing particle size of initial mica and decreased loading levels of mica i.e. higher monomer concentration with respect to mica. Further, the extent of reduction in the crystallite size follows the order chlorite > muscovite > phlogopite which is what was expected from the theoretical calculations and the surface area determinations. Thus, these observations clearly establish the intercalation of 1,4-dibromobenzene in to the mica layers and the formation of nanoparticulate mica in a single step upon in situ polymerization.

3.3.7 TEM Analysis

The nanoparticulate nature of the mica synthesized by in situ intercalative polymerization was proved unambiguously by TEM studies. Since the nano-mica is embedded in a PPS matrix, it was necessary to dissolve the PPS matrix to aid the study. Accordingly, the nano-mica/ PPS samples were dispersed in 2-chloronapthalene at 200 ºC and a drop was cast on to the carbon coated grid to record the TEM. The micrographs of 4 wt. % chlorite mica sample are presented in three different magnifications in the figures 3.24 to 3.26.

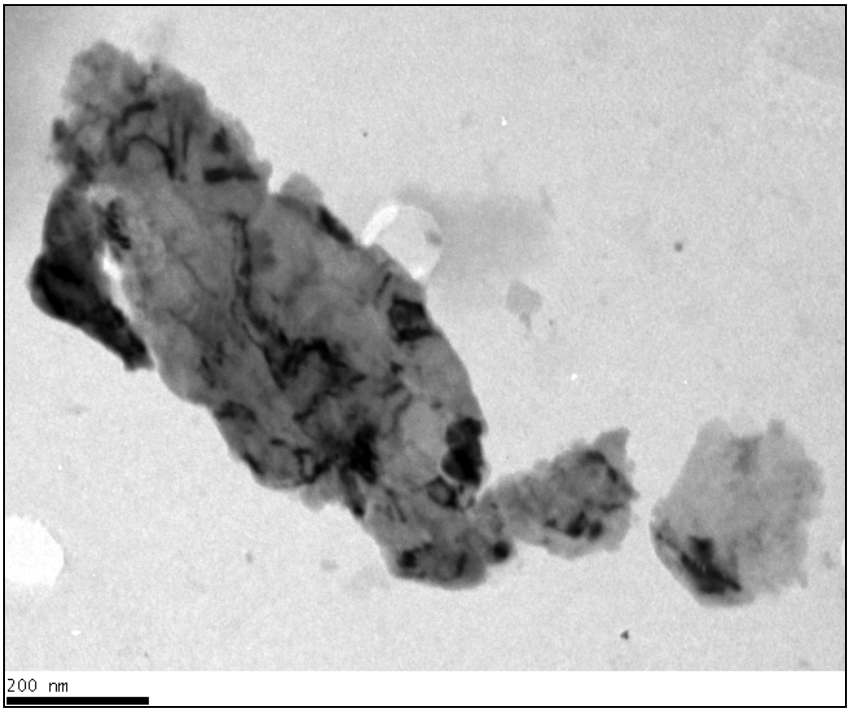

Figure 3.24 TEM of 4 wt. % chlorite mica (scale bar - 200 nm)

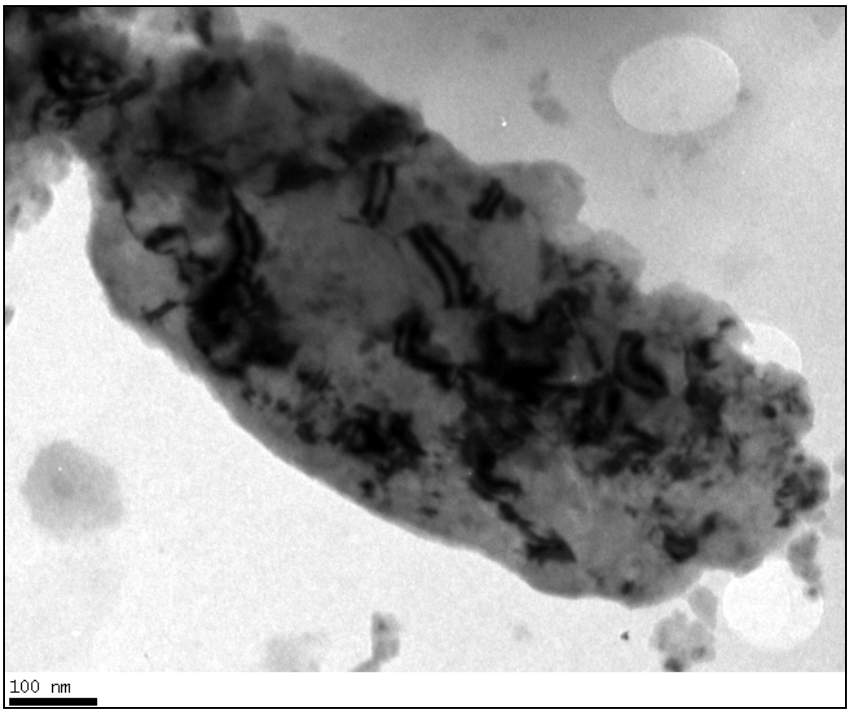

Figure 3.25 TEM of 4 wt. % chlorite mica (scale bar-100 nm)

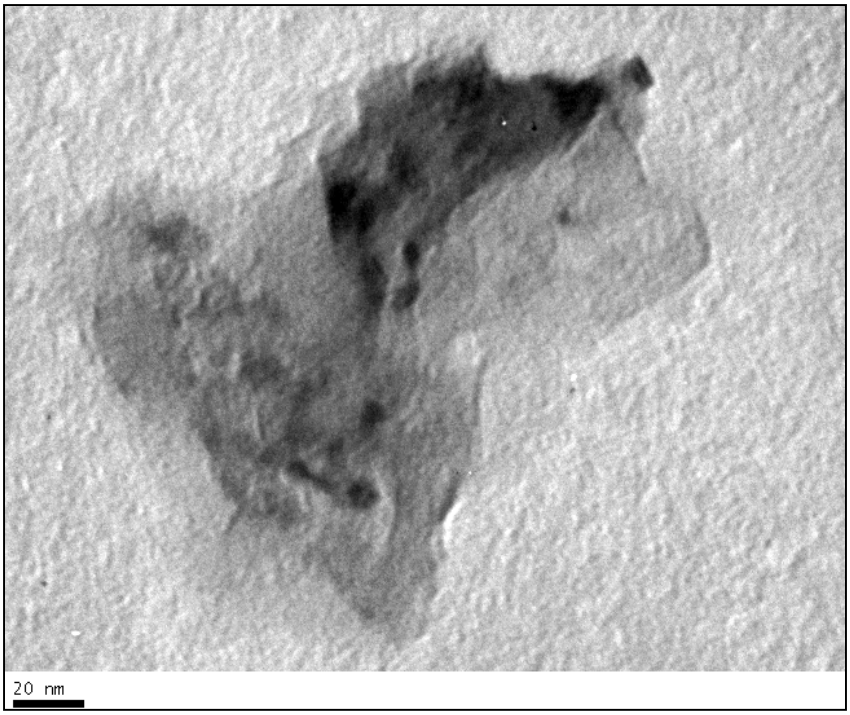

Figure 3.26 TEM of 4 wt. % chlorite mica (scale bar-20 nm)

From the figures, it is evident that the mica gets downsized to the order of around 10 nm upon intercalative in situ polymerization. The dark colored contours seen in the micrographs correspond to the silicate layers. The dispersion of nano-mica in the PPS matrix is evident in the figures 3.24-3.26. The nano-mica is distributed as agglomerated tactoids in the PPS matrix as seen in the figures 3.24 and 3.25.

3.4 Conclusions

A novel synthetic paradigm towards the synthesis of nanoparticles of naturally occurring mica like phlogopite, muscovite and chlorite has been established by intercalative in situ polymerization which has been patented recently.[22] The effect of average particle size and initial loading levels of mica on the extent of delamination have been studied and correlated with the basic framework of unit cell parameters of the various micas used and the available space/ sites for the monomer absorption in the same. The mica crystallite size was found to decrease with decreasing particle size of initial mica and decreased loading levels of mica. Chlorite mica was found to delaminate to a greater extent as compared to muscovite and phlogopite mica, which could be explained on the basis of their respective crystal structures. The nanoparticulate structure of mica has been established by WAXD and TEM studies.

3.5 References

1) www.mineral.galleries.com

2) www.mineralminers.com

3) Sekutowski, D. In *Plastics Additives and Modifiers Handbook*; Edenbaum, J., Ed.; Chapman & Hall: London, 1996.

4) Theng, B. K. G. *The Chemistry of Clay-Organic Reactions*; Wiley: New York, 1974.

5) Brindley, G. W. *Crystal Structures of Clay Minerals and their X-Ray Identification*; Mineralogical Society: London, 1980.

6) Wyckoff, R. W. G. *Crystal Structures*; Interscience: New York, 1968; Vol. 4.

7) Fischer, D.; Caseri, W.R.; Hahner, G. *J. Colloid Inter. Sci.* **1998**, *198*, 337.

8) Yao, H.; Morita, Y.; Kimura, K. *Surface Sci.* **2003**, *546*, 97 .

9) Chen, Y. L.; Chen, S.; Frank, C.; Israelachvili, J. *J. Colloid Interface Sci.* **1992**, *153*, 244.

10) Mackintosh, E. E.; Lewis, D. G.; Greenland, D. J. *Clay and Clay Miner.* **1971**, *19*, 209.

11) Shelden, R. A.; Caseri, W. R.; and Suter, U. W. *J. Colloid Interface Sci.* **1993**, *157*, 318.

12) Duxbury, D. F. *Chem. Rev.* **1995**, *93*, 381.

13) Ogawa, M.; Kuroda, K. *Chem. Rev.* **1995**, *95*, 399.

14) Ogawa, M.; Kawai, R.; Kuroda, K. *J. Phys. Chem.* **1996**, *110*, 16218.

15) Iwasaki, M.; Kita, M.; Ito, K.; Kohno, A.; Fukunishi, K. *Clay and Clay Miner.* **2000**, *3*, 392.

16) Fischer, D.; Caseri, W. R.; Hahner, G. *J. Colloid Interface Sci.* **1998**, *198*, 337**.**

17) Cole, K. C.; Noel, D.; Hechler, J. J. *J. Appl. Polym. Sci.* **1990**, *39*, 1887.

18) Brady, D. J. *J. Appl. Polym. Sci.* **1976**, *20*, 2541.

19) Piaggio, P.; Cuniberti, C.; Dellepiane, G.; Campani, E.; Gorini, G.; Masetti, G.; Novi, M.; Petrillo, G. *Spectrochim. Acta Part A*, **1989**, *45*, 347.

20) Zimmerman, D. A.; Koenig, J. L.; Ishida, H. *Spectrochim. Acta Part A*, **1995**, *51*, 2397.

21) Alexander, L. E. *X-Ray Diffraction Methods in Polymer Science*; John Wiley: New York, 1969.

22) Radhakrishnan. S.; Subramanyam, S. *A Process for the Synthesis of Nanoparticulate Mica*, 160 DEL 2004, US Patent filed.

4(A) Structure Development in Mica / PP Nanocomposites

4.1 Introduction

Isotactic PP (IPP) happens to be the first and most important type of stereoregular polymer.[1] The regular chain structure accounts for its high tendency to crystallize. Its technological and economic significance has elicited a lot of interest amidst the scientific community all over the world.

IPP is polymorphic and exhibits three distinct morphologies with a fourth type also receiving some mention.[2] They are the monoclinic α form, the hexagonal β form, the triclinic γ form and a δ form distinct due to different chain packing geometries of the helices and easily distinguished by their WAXD profiles as shown in the figure 4.1.

The α form is the most conventional and extensively studied polymorph in IPP. Natta and Corradini calculated the unit cell parameters of this form in 1960. It contains four 3-fold helical chains with a = 6.65 Å, b = 20.96 Å, c = 6.5 Å and β = 99.3 °. The equilibrium melting temperature of the α crystals is reported to be in the range of 185 °C to 208 °C, but there is still some speculation in this regard. The β form of IPP crystallizes in a hexagonal unit cell with a = 19.08 Å, c = 6.49 Å, γ = 120 ° and $\alpha = \beta$ = 90 °.[2,4-6] The 300 and 301 reflections in the WAXD of PP are assigned to this crystal form. The melting temperature of the β crystals is found to be between 150-154 °C. The β form in IPP can be obtained through rapid quenching, zone solidification, crystallization in a temperature gradient or by the use of select nucleating agents such as quinacridone dyes or triphenodithiazine. The transition of β to α form can be carried out by drawing at high temperatures or melt crystallization at elevated temperatures close to the melting temperature of the bulk samples.

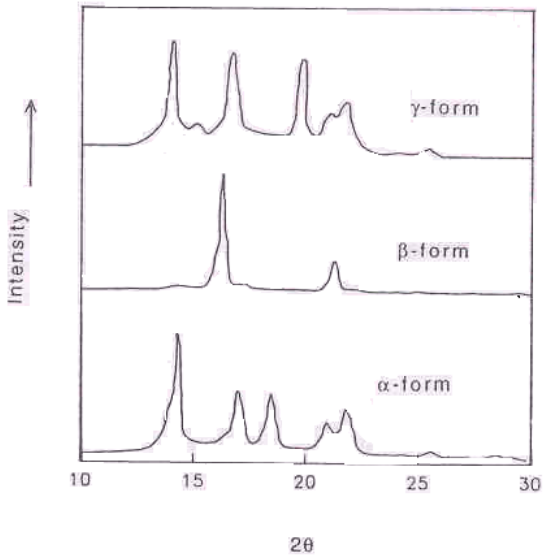

Figure 4.1 Polymorphism in IPP

The γ form[2-4,7-9] of IPP was first noticed in 1960 and can be generated by several methods. It is mainly produced by crystallization at elevated pressures.[8,10] It is also obtained by crystallization of low molecular weight fractions produced by pyrolysis[11] or by crystallization of IPP with small amounts (4-10 %) of ethylene or butene[12]. Another route to this form is by crystallization from the melt of stereo block fractions extracted from a commercial homopolymer using petroleum ether or xylene extraction in the 35-70 °C temperature range.[4] The γ form crystallizes in to an orthorhombic lattice with a = 8.54 Å, b = 9.93 Å, c = 42.41 Å. The melting point of this form is reported to be in the range of 125-150 °C. The γ form transforms to the α form when it is quenched from very high temperatures. The smectic form of IPP has an intermediate crystalline order and this mesomorphic form was first reported by Natta et al. It is prepared by quenching thin sheets of IPP from the melt using ice water. Two reflections at 14.8 ° and 21.2 ° (2θ, Cu Kα) in the WAXD are assigned to this form.

The crystallization characteristics of α IPP under isothermal and non-isothermal conditions have been investigated in great detail in the past. The crystallization studies encompass the wide spectrum of various IPP grades, their particular fractions, low-molecular weight products, polymers of different isotacticities and various propylene comonomers. The morphology and crystallization of IPP has been extensively studied and has been reviewed by Varga[13] and Clark[14] et al. The effect of various additives on the crystallization of IPP has also been documented in the above reference. Novel synthetic protocols towards nanoparticle synthesis have opened up the study of the effect of nanoparticles on the crystallization behavior of PP. Radhakrishnan et al.[15] have studied the structure development and crystallization behavior of PP containing calcium phosphate nanoparticles prepared by matrix mediated growth technique. The nanoparticle filled PP was found to exhibit lower induction times, smaller $t_{1/2}$ values and higher crystallization rates. The ultimate spherulite size was also found to decrease considerably resulting in greater optical clarity. The overall crystallization rate (G) was proportional to the particle size (d) as log G α (1/d). The same group has also studied the effect of calcium carbonate[16] and calcium sulfate[17] on the crystallization of PP and obtained similar results. The effect of different reinforcing fibers in the crystallization of PP has been studied by Kenny et al.[18] using POM and thermal analysis. A dramatic decrease in $t_{1/2}$ and an increase in the overall crystallization rate was observed for all the composites. Transcrystalline zones were identified over the entire crystallization temperature range only for aramid fibers. The crystallization and melting behavior of nano calcium carbonate / PP composites grafted with acrylic acid has been explored by Lin et al.[19] A high content of calcium carbonate was found to increase the crystallization temperature

whereas a low content was not found to exert any nucleating effect. The effect of SWNTs on the crystallization behavior of PP has been investigated by Valentini et al.[20] The SWNTs were found to accelerate the nucleation and growth mechanisms of PP with the effect being more noticeable at a very low filler content of 5 wt.%. The chemical and microstructural changes evidenced by IR and Raman spectroscopy were found to support this observation.

Although there is a wealth of literature on the crystallization characteristics of PP nanoparticle systems as seen above, only a few studies have been reported on the crystallization behavior of clay based PP systems. This is significant in the sense that the number of reports on PP/ clay nanocomposites itself is negligible. The crystallization behavior of PP/ MMT nanocomposites has been investigated by Ma et al.[21] They investigated the isothermal crystallization kinetics by means of DSC and POM. The nanoscale MMT layers dispersed in the PP matrix was found to confine the PP chains and impede crystallization resulting in a decrease in crystallinity. On the other hand, the MMT layers were found to act as heterogeneous nuclei resulting in a dramatic increase of crystallization rate and decrease of the spherulite size with increase in the MMT content.

Thus, the investigation of the effect of nanoparticulate mica synthesized by in situ intercalative polymerization on the crystallization characteristics of PP looks promising. The crystallization behavior of PP/ nanoparticulate mica system and its structure development constitute the scope of work in this section.

4.2 Experimental

(a) Preparation of the Nanocomposite

PP (Indothane, SM85N grade) powder was obtained by precipitating its xylene solution in acetone followed by thorough washing with acetone and drying. The PP/ commercial mica composites and PP/ mica nanocomposites were prepared by taking the desired quantity of mica/ nanomica in PP powder and dry mixing it in an agate mortar. A range of compositions were made by varying the mica/ nanomica content from 2, 5, 10 and 15 wt.% with respect to PP. To study the effect of various particle sizes on the crystallization behavior, the nanomicas of different particle sizes (14, 19 and 23 nm in the case of phlogopite; 24, 27 and 38 nm in the case of muscovite) were taken and the composites made. A small quantity of each of the above compositions was isothermally crystallized on the hot stage of a polarizing microscope and the crystallization behavior investigated as described in section 2.11.3 by mapping the intensity of transmitted light as a function of time under crossed polars.

(b) Melt Crystallization for Structure Development

The powder blended PP/ mica samples (0.3 g) were pelletized using a single end compaction die at a pressure of 3 tonnes for 2 minutes to obtain thin discs (12 mm diameter, 2mm thickness). The pellet was placed in between two glass slides and kept on a hot plate preset at 200 ºC for 10 minutes. The slide was then transferred to another hot plate maintained at 125 ºC and the sample allowed to crystallize isothermally at that temperature for 20 minutes. The sample was then quenched in cold water, dried and analyzed for structure development by WAXD.

To ascertain the effect of processing on structure, some of the injection molded tensile test specimens were also analyzed by WAXD. The DSC of the samples was done to determine various phase transitions, crystallization and melting behavior of PP incorporated with nanomica particles.

4.3 Results and Discussion

The crystallization behavior of PP containing nano-phlogopite, nano-muscovite and nano-chlorite mica was monitored by observing the growth of spherulites from the melt during the crystallization process by POM. POM is the study of microstructure of materials using their interactions with polarized light. Under polarized light, the spherulite appears as a circular area showing a dark distinctive pattern in the shape of a maltese cross. By POM coupled with an image analysis software, the direct relationship between the micro scale change and the overall transformation could be easily related. The image analysis software enabled the recording of the spherulitic images at appropriate intervals as digitized computer files. However, in our case, the intensity of transmitted light was recorded as a function of time. Intensity measurement scores over the measurement of spherulite size in two ways

1) The least spherulite size that can be recorded is 2 μ whereas the intensity can be detected on one pixel size on the screen (< 1 μ).
2) The spherulite size remains the same upon impingement with an adjacent spherulite but its internal structure might change with crystallization, which can be detected very easily by intensity measurements.

The samples were isothermally crystallized at 125 °C. The crystallization curves of all the

samples are presented as a function of intensity of transmitted light (gray scale) versus time. The crystallization curves of PP/ commercial phlogopite, muscovite and chlorite mica composites are presented in the figures 4.2, 4.6 and 4.10 respectively. The crystallization curves of PP / mica (phlogopite and muscovite) nanocomposites made with different mica particle sizes are shown in the figures 4.3 to 4.9, respectively. A representative crystallization curve for PP/ chlorite nanocomposite (mica particle size of 17 nm) is depicted in the figure 4.11. The crystallization profile of PP is also presented in all the curves as a reference. It is well known that at this T_c in pure PP, the spherulites grow to a big size over a period of 7-8 minutes. However, the growth rate is seen to be quite rapid in the case of the nanocomposite samples. The crystallization duration is also short and the ultimate spherulite size is also reduced considerably. The crystallization half time i.e. the time required to attain a spherulite size of half its ultimate value, the growth rate (given by the slope of the crystallization curve) and the induction period of all the samples were tabulated from the crystallization profiles. The variation in background intensity for different samples is due to variation in thickness and transparency. Mica, by itself is a birefringent material and the presence of PPS further adds to the background variations. The crystallization behavior data for all the phlogopite, muscovite and chlorite samples are recorded in the table 4.1, 4.2 and 4.3 respectively. The crystallization behavior of PP/ PPS system was also investigated to determine the extent to which the presence of PPS would influence the crystallization of PP and the effect was found to be negligible. It is seen that the half times of the phlogopite samples are lower than that of muscovite/ chlorite and the growth rates are substantially higher.

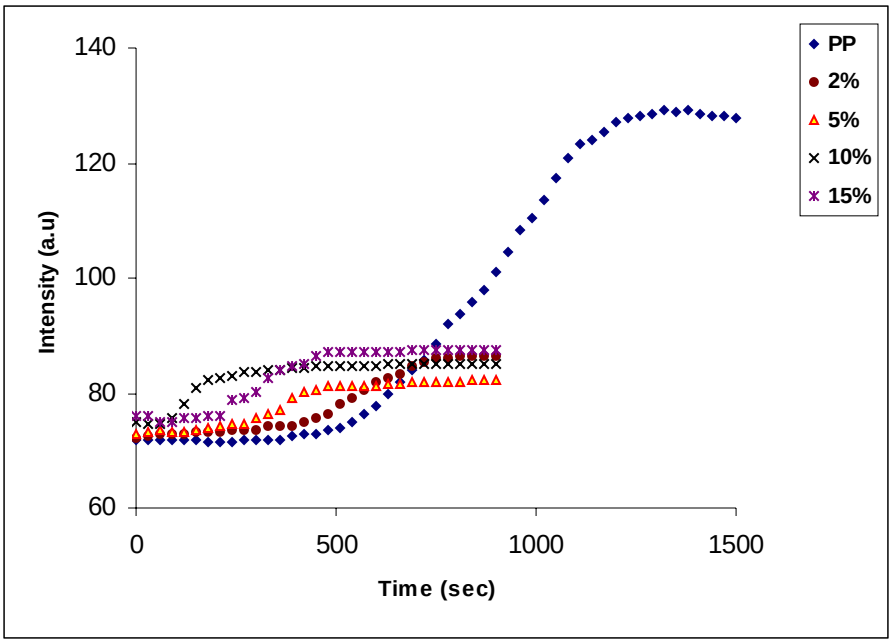

Figure 4.2 Crystallization curve for PP / commercial phlogopite

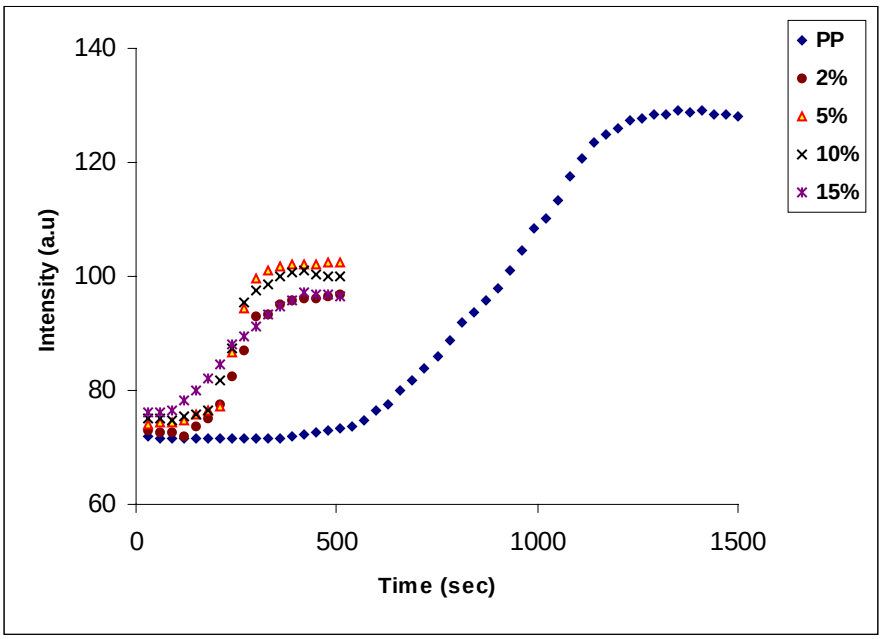

Figure 4.3 Crystallization curve for PP / nanophlogopite (23 nm)

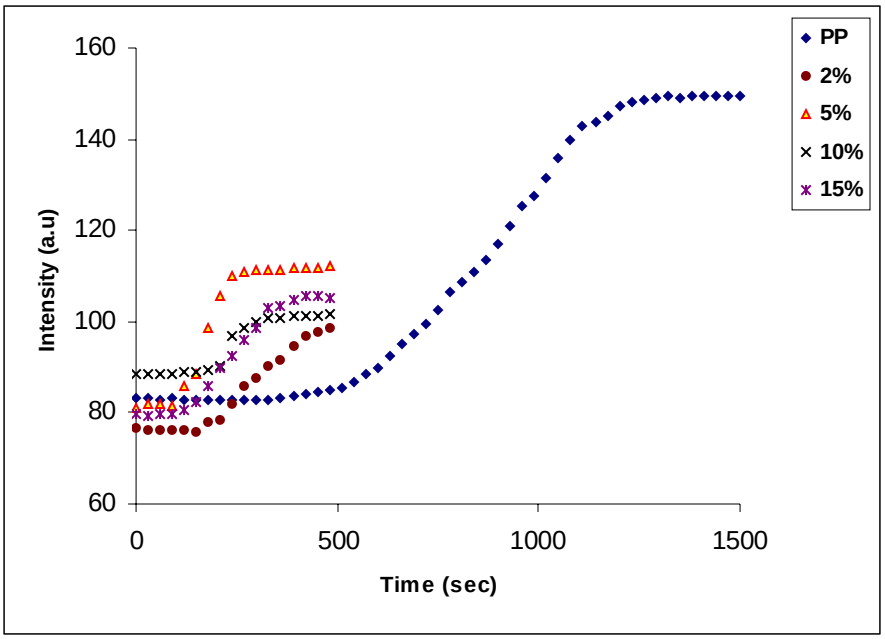

Figure 4.4 Crystallization curve for PP / nanophlogopite (19 nm)

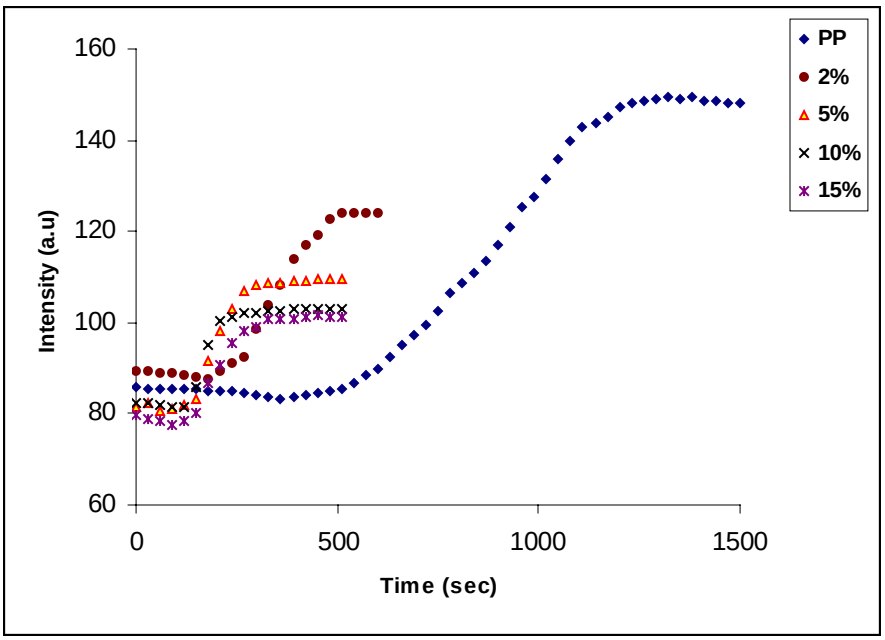

Figure 4.5 Crystallization curve for PP / nanophlogopite (14 nm)

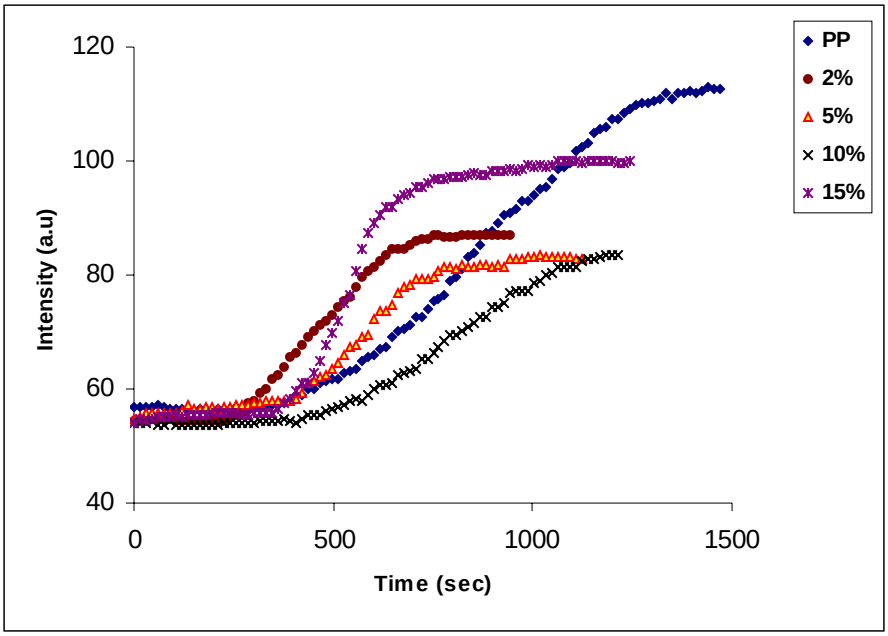

Figure 4.6 Crystallization curve for PP / commercial muscovite

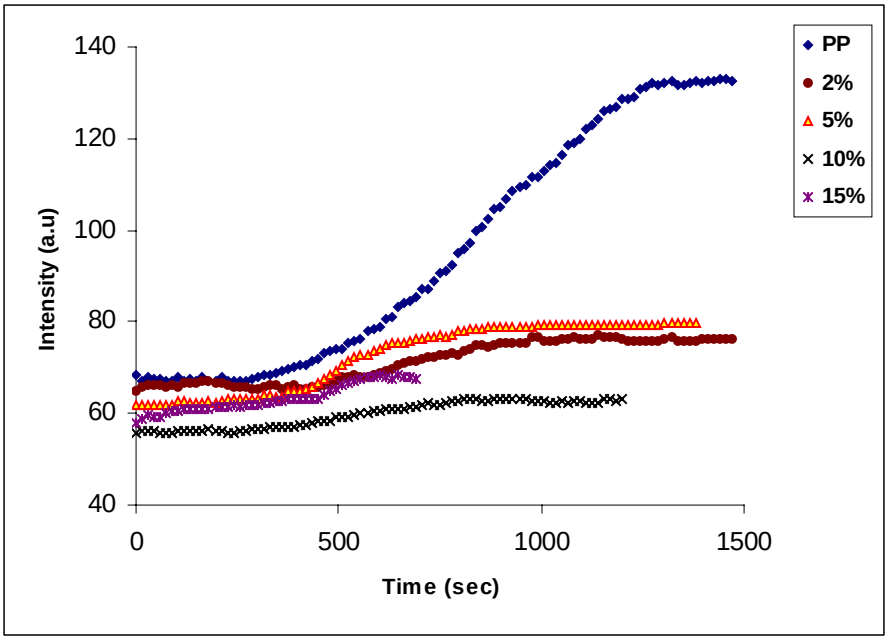

Figure 4.7 Crystallization curve for PP / nanomuscovite (38 nm)

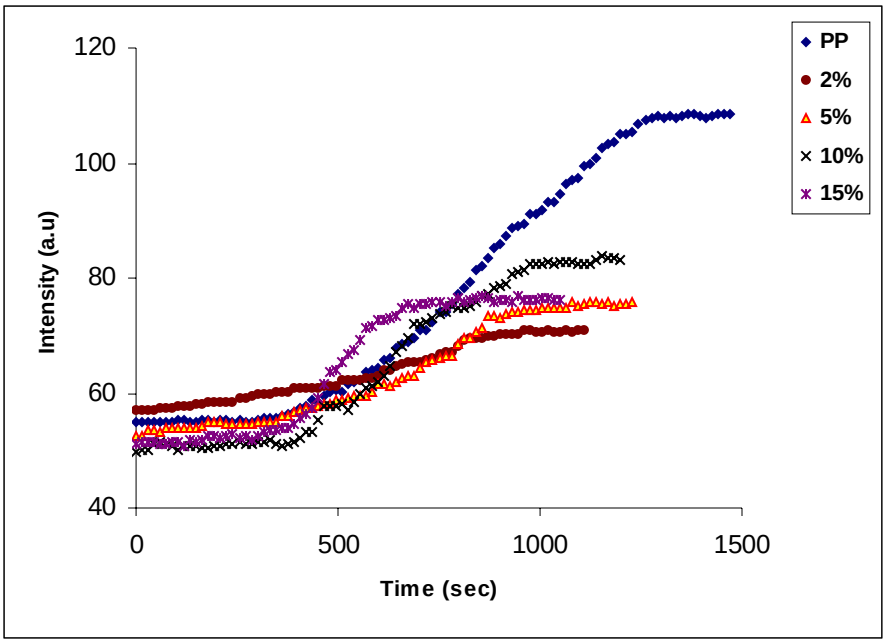

Figure 4.8 Crystallization curve for PP / nanomuscovite (27 nm)

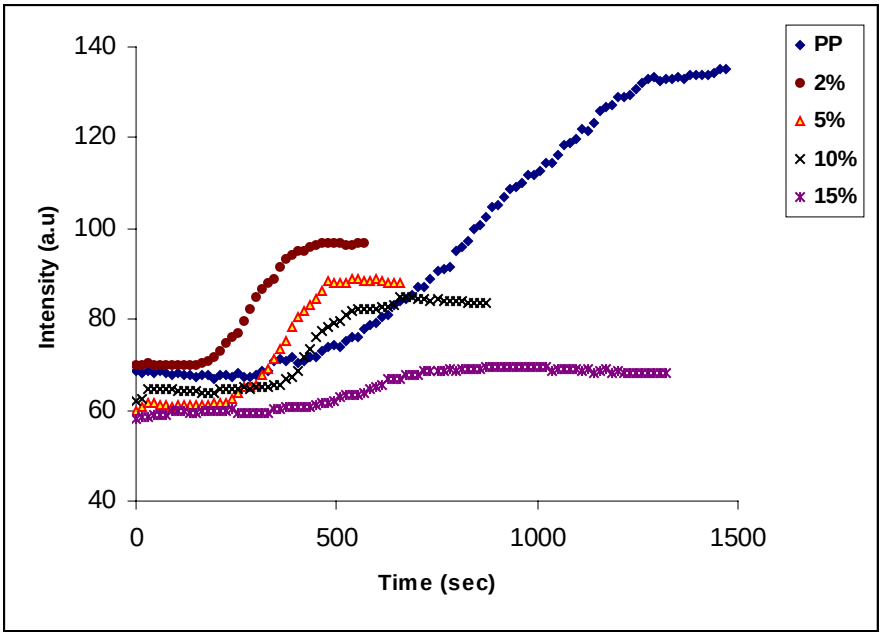

Figure 4.9 Crystallization curve for PP / nanomuscovite (23 nm)

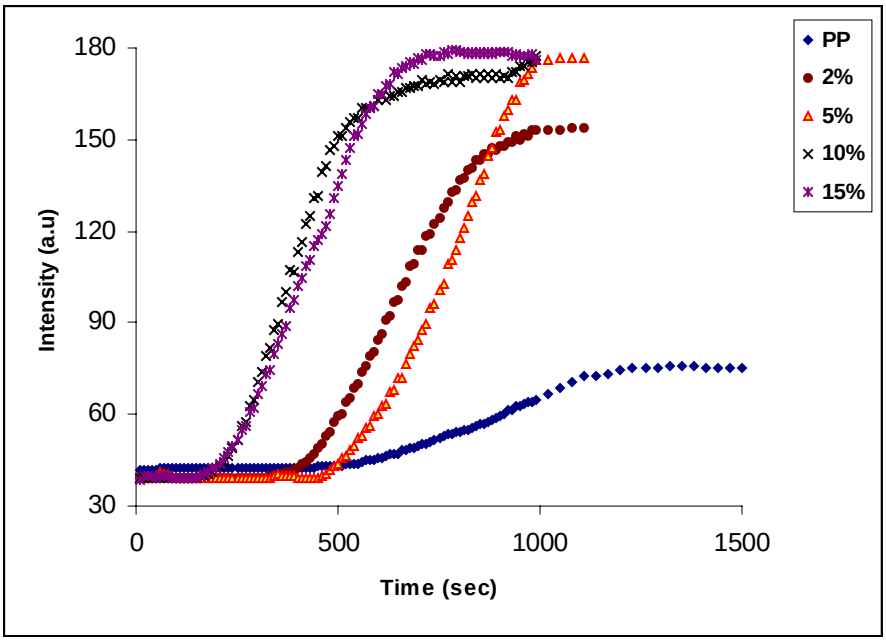

Figure 4.10 Crystallization curve for PP / commercial chlorite

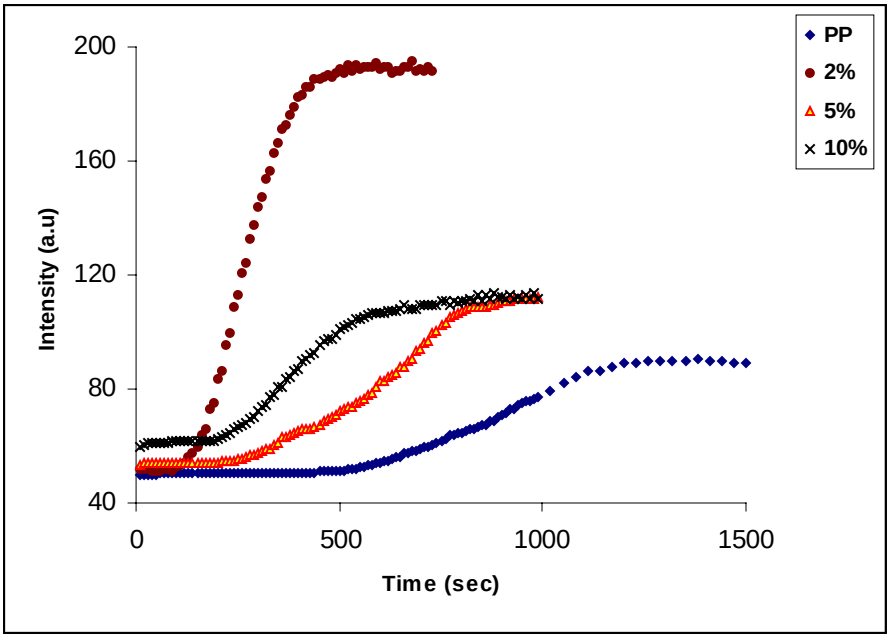

Figure 4.11 Crystallization curve for PP / nanochlorite (17 nm)

These observations could be explained on the basis of the crystallization phenomena in polymers. Primary crystallization in polymers consists of two processes namely nucleation and growth. In the nucleation phase, centres of the new phase are formed and their number increases linearly in time. Nuclei are of three types namely homogeneous, heterogeneous and self-nuclei. During crystal growth, new crystal layers are deposited on the primary nuclei, extending the dimensions of the crystalline phase. Both these processes are temperature dependent and exhibit a maximum at a certain value of temperature (T_c) that exists between T_g and T_m. The T_g and T_m values together decide the ultimate crystallinity value, spherulitic size, etc. High nucleation rates generally lead to high crystallization rates and low $t_{1/2}$ values, resulting in a decrease in the spherulitic dimensions. Hence, a decrease in the spherulite dimension with increase in the filler concentration is expected. However, with further increase in the concentration of the filler, increase in $t_{1/2}$ values with slower growth rates are observed. The reason for this could be speculated to be the agglomeration of filler particles at higher loading levels resulting in an effective decrease in the active surface area for the spherulites to nucleate upon. This trend is observed in all the cases. It is to be noted that the minor variations in the background intensities of various samples are due to variations in sample thickness and transparency. Mica being birefringent by itself, contributes to some variations. Also, there could be variations due to area selection (while analyzing the spot intensity at a particular location in the graphics). However, none of these factors have any significant effect on the crystallization kinetics.

Table 4.1 Crystallization data for PP / nano-phlogopite system

Composition (mica wt. %)	Induction time (sec)	Half time (sec)	Growth rate (μ/sec)
Pure pp	531	859	0.14
Com. phlogopite			
2	385	560	0.23
5	300	361	0.17
10	150	123	0.25
15	158	315	0.13
Nanophlogopite (23 nm)			
2	134	217	0.23
5	154	212	0.30
10	125	208	0.25
15	165	253	0.09
Nanophlogopite (19 nm)			
2	194	305	0.14
5	127	173	0.30
10	183	229	0.40
15	136	249	0.13
Nanophlogopite (14 nm)			
2	183	338	0.14
5	145	191	0.20
10	136	164	0.32
15	131	191	0.13

Table 4.2 Crystallization data for PP / nanomuscovite system

Composition (mica wt. %)	Induction time (sec)	Half time (sec)	Growth rate (μ/sec)
Pure pp	531	859	0.14
Com. muscovite			
2	250	444	0.13
5	380	553	0.10
10	418	764	0.16
15	430	530	0.22
Nanomuscovite (38 nm)			
2	427	658	0.16
5	340	455	0.20
10	300	513	0.16
15	225	415	0.16
Nanomuscovite (27 nm)			
2	358	646	0.15
5	346	423	0.16
10	404	653	0.14
15	364	482	0.14
Nanomuscovite (23 nm)			
2	191	286	0.16
5	266	363	0.16
10	332	435	0.22
15	363	560	0.16

Table 4.3 Crystallization data for PP / nano-chlorite system

Composition (mica wt. %)	Induction time (sec)	Half time (sec)	Growth rate (μ/sec)
Pure pp	531	859	0.14
Com. chlorite			
2	431	642	0.14
5	550	774	0.14
10	226	374	0.16
15	226	426	0.12
Nanochlorite (14 nm)			
2	289	471	0.13
5	387	558	0.11
10	263	437	0.15
15	-	-	-
Nanochlorite (17 nm)			
2	150	260	0.17
5	353	616	0.18
10	237	384	0.10
15	-	-	-
Nanochlorite (19 nm)			
2	221	305	0.17
5	216	295	0.12
10	-	-	-
15	-	-	-

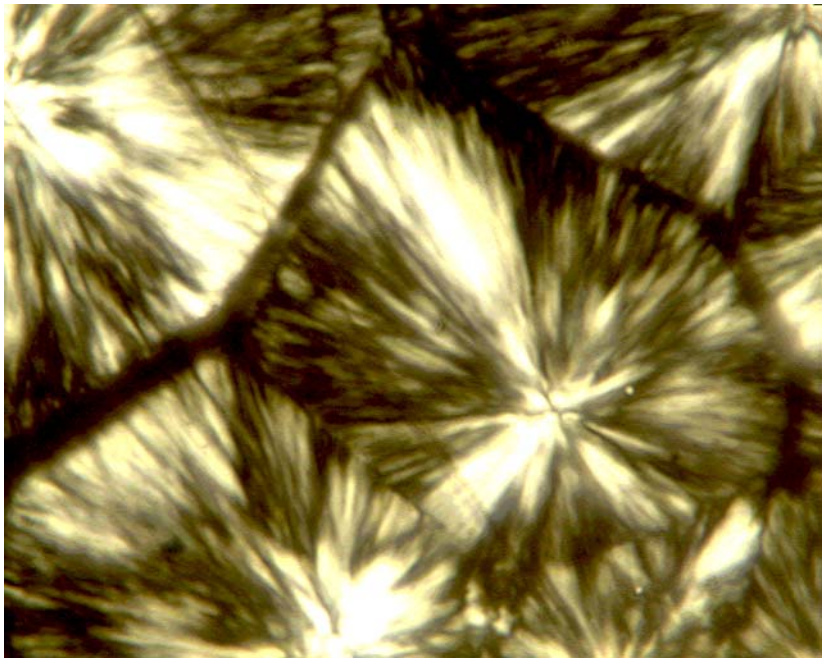

Figure 4.12 Optical micrograph of pure PP (Mag. -1570 X)

Figure 4.12 demonstrates the spherulitic structure of pure PP. Pure PP exhibits a well defined spherulitic structure whereas the structure gets more diffuse in the case of PP/ mica composites and nanocomposites as seen in the figures 4.13a-d. There is also a progressive reduction in the spherulite size as one proceeds from pure PP to the nanocomposite.

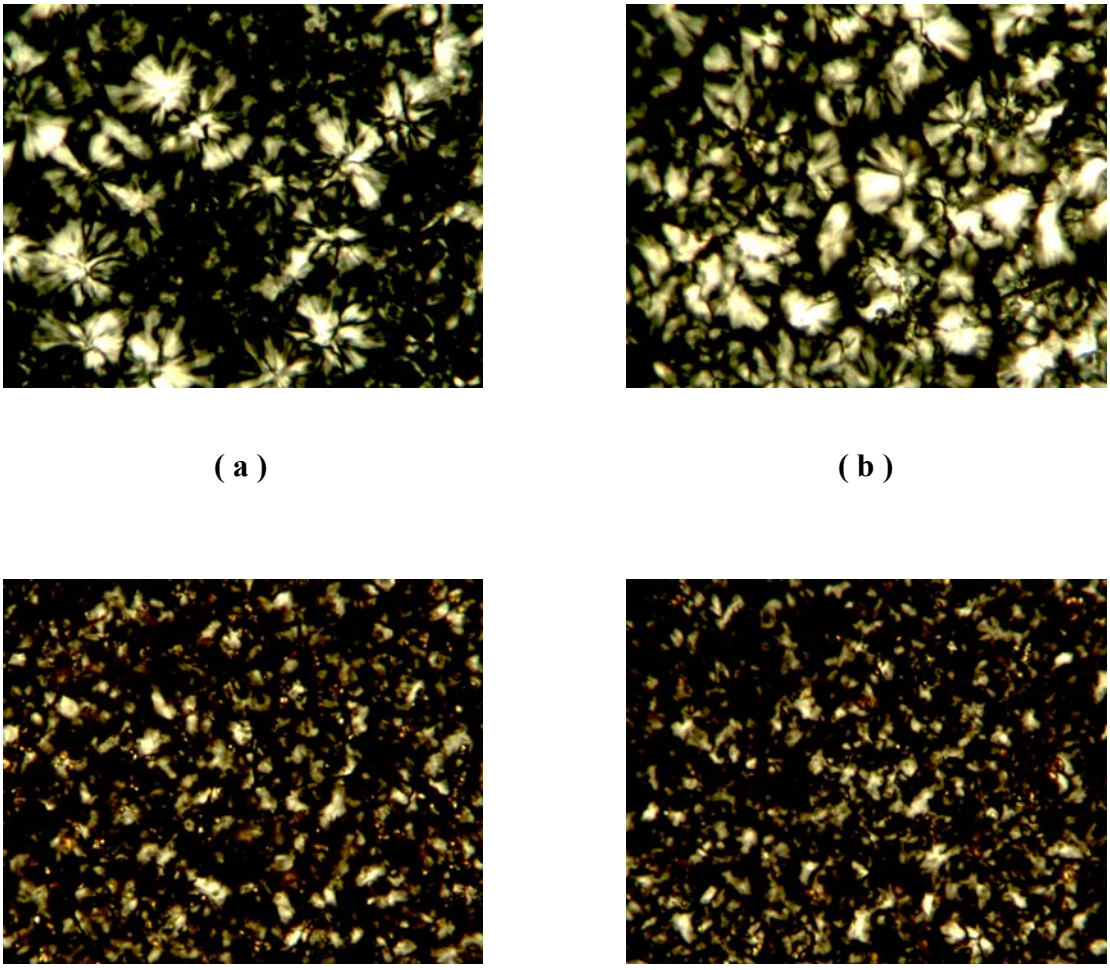

(a) **(b)**

(c) **(d)**

Figure 4.13 Optical micrographs of **(a)** PP/ com. phlogopite **(b)** PP/ com. muscovite **(c)** 2 % PP/ nanophlogopite (mica particle size - 14 nm) **(d)** 2 % PP/ nanomuscovite (mica particle size - 24 nm) (Mag. – 1570 X)

One of the very interesting features of the present work is the exact dependence of the nucleating efficiency on the particle size of the nanomica. This analysis and the subsequent property measurements were performed only for muscovite and phlogopite nanocomposites because of their commercial importance. To evaluate this relationship, the increase in crystallization rate (G) due to nanomica with respect to original i.e. PP without mica $[(G-G_o)/ G_o]$ was plotted as a reciprocal of particle size (after in situ intercalative polymerization) 1/d in semi-log scale as shown in the figures 4.14a and b, respectively. Figure 4.14a connotes to phlogopite mica whereas figure 4.14b corresponds to muscovite mica. From the figures, it follows that the nucleation rate increases as an inverse exponential power of the particle size of mica i.e. $G \alpha \exp (1/d)$. Thus, smaller particle sizes lead to higher nucleating efficiencies. A similar result has been reported from our own group in connection with the crystallization behavior of PP/ nano calcium phosphate system.[15] To bring out the effect of particle size on the crystallization half time of the nanocomposites, the half time was plotted as a reciprocal of the particle size (1/d) as shown in the figures 4.15 a and b, respectively. The crystallization half time decreases as the particle size decreases as evidenced from the plots.

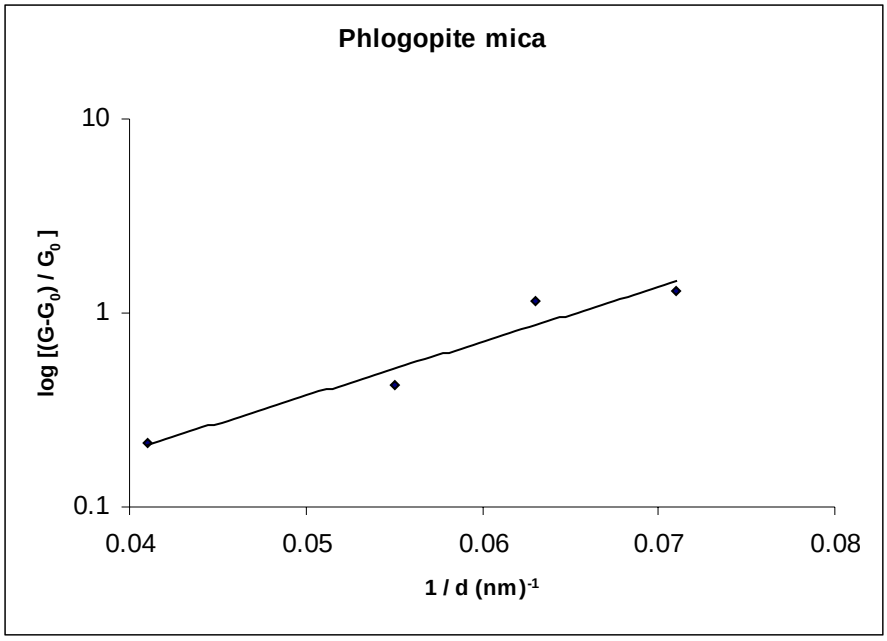

(a)

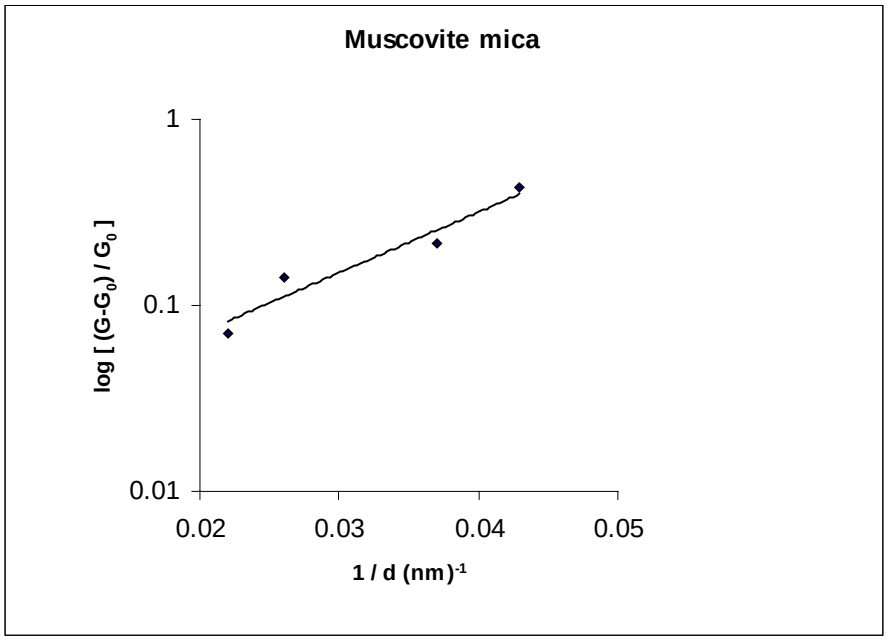

(b)

Figure 4.14 Effect of particle size on the nucleating efficiency of

(a) nanophlogopite (b) nanomuscovite in PP

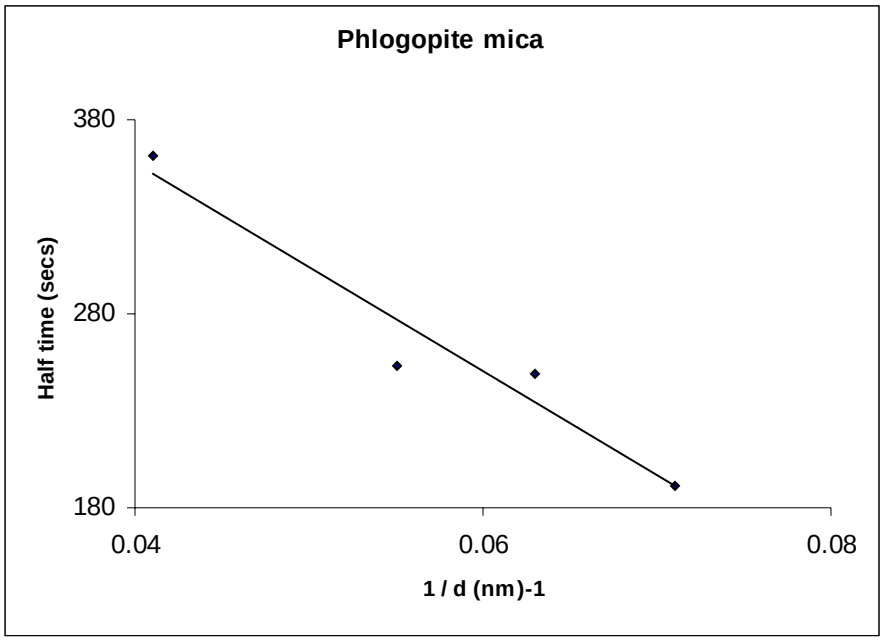

(a)

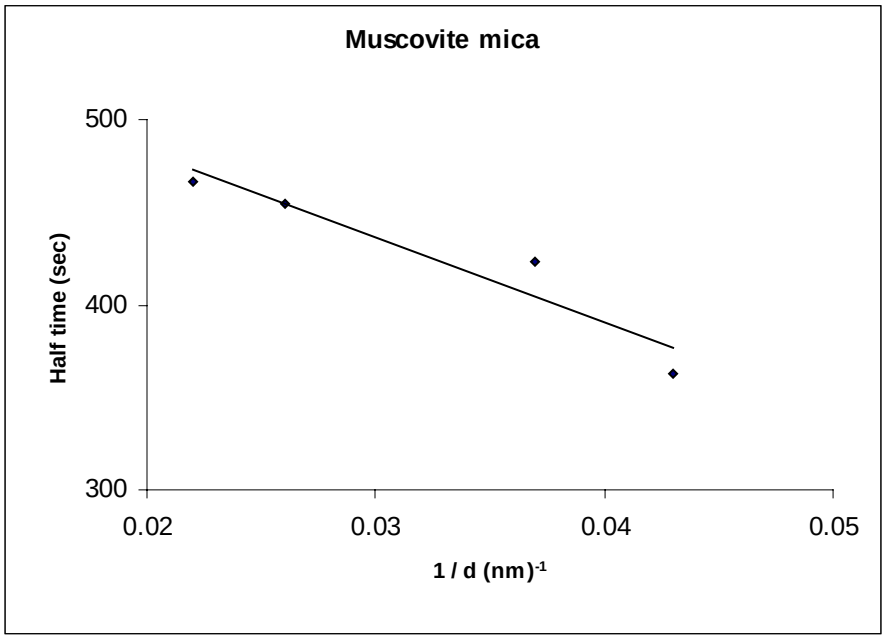

(b)

Figure 4.15 Effect of particle size on the crystallization half times of

(a) nanophlogopite (b) nanomuscovite in PP

The structure development in PP/ mica nanocomposites was investigated by WAXD upon isothermal crystallization of the samples at 125 °C. The WAXD patterns of phlogopite and muscovite mica nanocomposites prepared from micas of different initial particle sizes are represented in the figures 4.16 to 4.21, respectively. IPP shows 5 major Bragg reflections between 10° - 25° (2θ). These reflections are assigned the 110, 040, 130, 111 and 041 planes. It is interesting to note that there is a considerable change in the intensities of the nanocomposite samples as compared to pure PP. An increase in the intensity of the 040 plane (16.72°) with respect to the 110 plane is very obvious from the figures. One other interesting feature to be noted is that the variation in the intensity ratio of these two peaks is greater in the case of phlogopite as compared to muscovite. It is also seen that this ratio increases as one proceeds from a nanocomposite obtained from a mica of larger particle size to a smaller one as evidenced in the figures 4.16 and 4.18. These trends are clearly established in the figure 4.22 wherein the change in I_{040} / I_{110} is plotted as a function of mica particle size for both the phlogopite and muscovite nanocomposites. The I_{040} / I_{110} ratio variation as a function of the mica loading levels is depicted in the table 4.4. It is seen that there is not a tremendous change in the peak intensity ratios as a function of mica loading but is considerable as a function of mica particle size. A gradual increase in the ratio with increased mica loading is noticed in the case of PP/ phlogopite nanocomposites whereas it decreases in the case of PP/ muscovite nanocomposites. The various results on the structure development of PP/ mica nanocomposites can be analyzed in terms of nucleation, growth and the crystallographic interaction between PP and mica. This preference for oriented growth along a particular plane could be explained on the basis of the crystal lattice mismatch theory[22] which states that the substrate influences the

growth of another substance on it if the lattice parameters for the substrate and the growing phase are close to each other. The lattice mismatch (δ) is defined as

$$\delta = \frac{\left| pl_s - ql_g \right|}{\left| l_s \right|} \text{x } 100 \tag{4.1}$$

where l is the lattice parameter along any axis; p and q are integers; s and g denote the substrate and the growing media. If the mismatch parameter δ is less than 10%, then there is a preferential growth or even an epitaxial growth of one phase over the other.

When we compare the lattice parameters of the α phase of PP, (a = 6.65 Å, b = 20.98 Å, c = 6.5 Å and β = 99.3°) with that of phlogopite (a = 5.31 Å, b = 9.21 Å, c = 10.13 Å and β = 100.1°; phlogopite is monoclinic whereas muscovite is hexagonal) the mismatch parameter δ between 3 x (a-axis of PP) and 2 × (c-axis of phlogopite) works out to be around 3 %. In case of muscovite, the δ value between (b-axis of PP) and 4 × (a-axis of muscovite) is about 4.1 %. A better lattice mismatch in the case of phlogopite as compared to muscovite is the reason for its superior nucleating ability. Hence it is likely that the a-axis of PP grows preferentially along the c-axis of phlogopite resulting in increase of the 040 peak intensity. Similarly, we could surmise that the b-axis of PP crystallizes predominantly along the a-axis of muscovite.

It is interesting to mention here that the crystallization behavior of PP/ mica composites has been reported by some authors earlier. They have studied PP incorporated with large mica particles (here similar to commercial grades) and observed extensive transcrystallinity at the PP-mica interface.[23,24] Further, Radhakrishnan et al. have observed in general case of PP containing nucleating additives that the 040 peak intensity

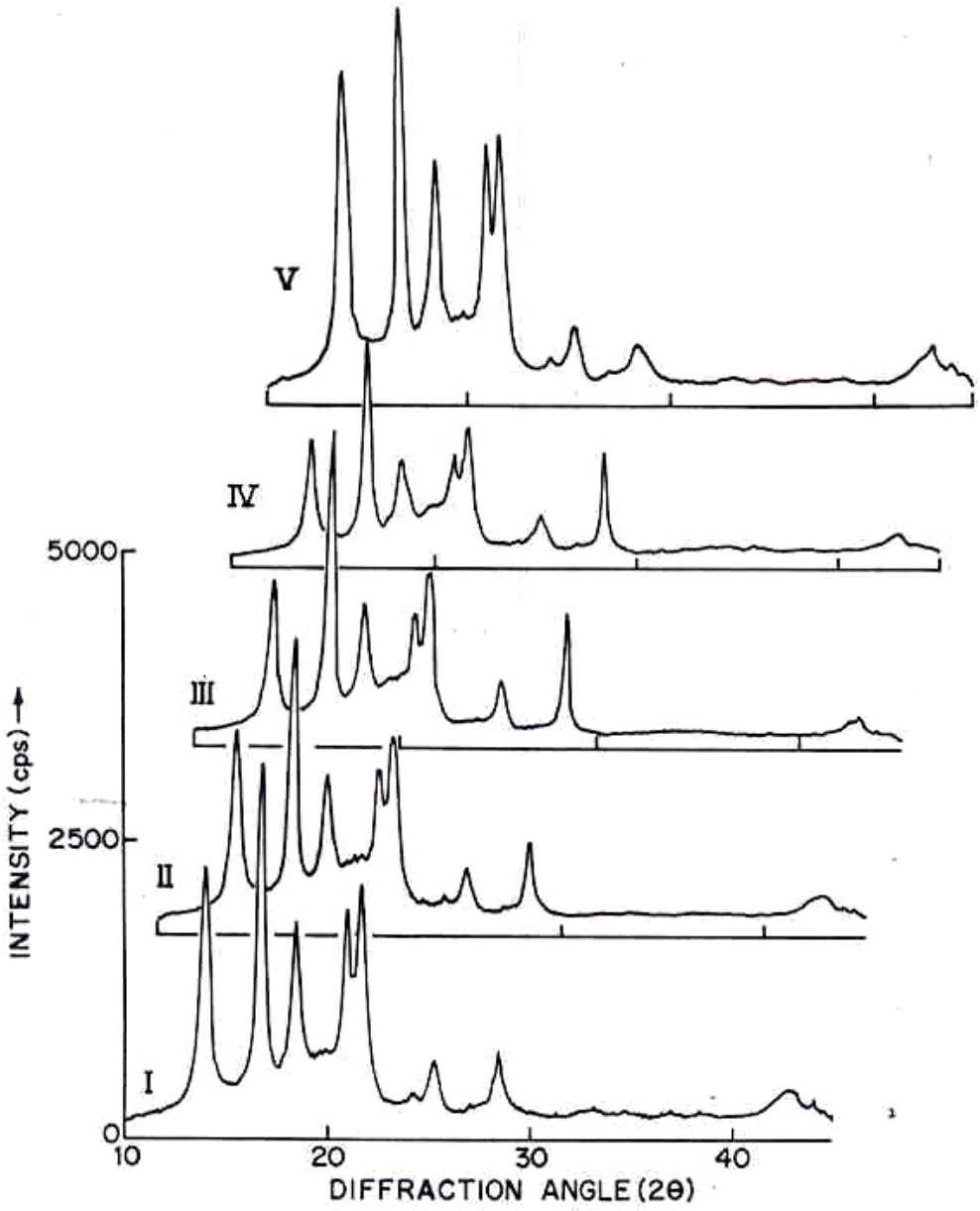

Figure 4.16 WAXD scans of PP/ nanophlogopite (23 nm). Curves I – IV correspond to 2, 5, 10,15 wt. % mica loading and V to pure PP

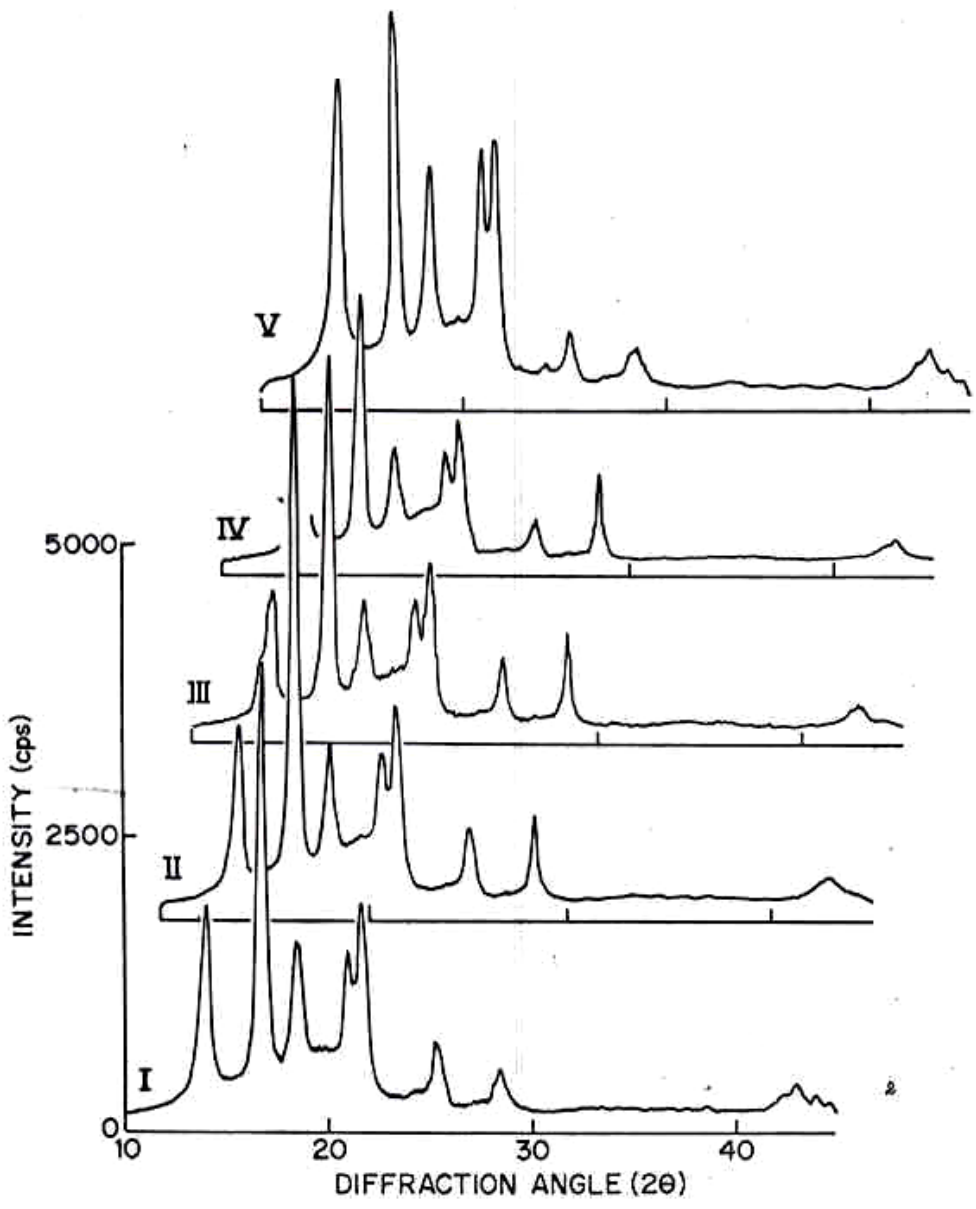

Figure 4.17 WAXD scans of PP/ nanophlogopite (19 nm). Curves I – IV correspond to 2, 5, 10,15 wt. % mica loading and V to pure PP

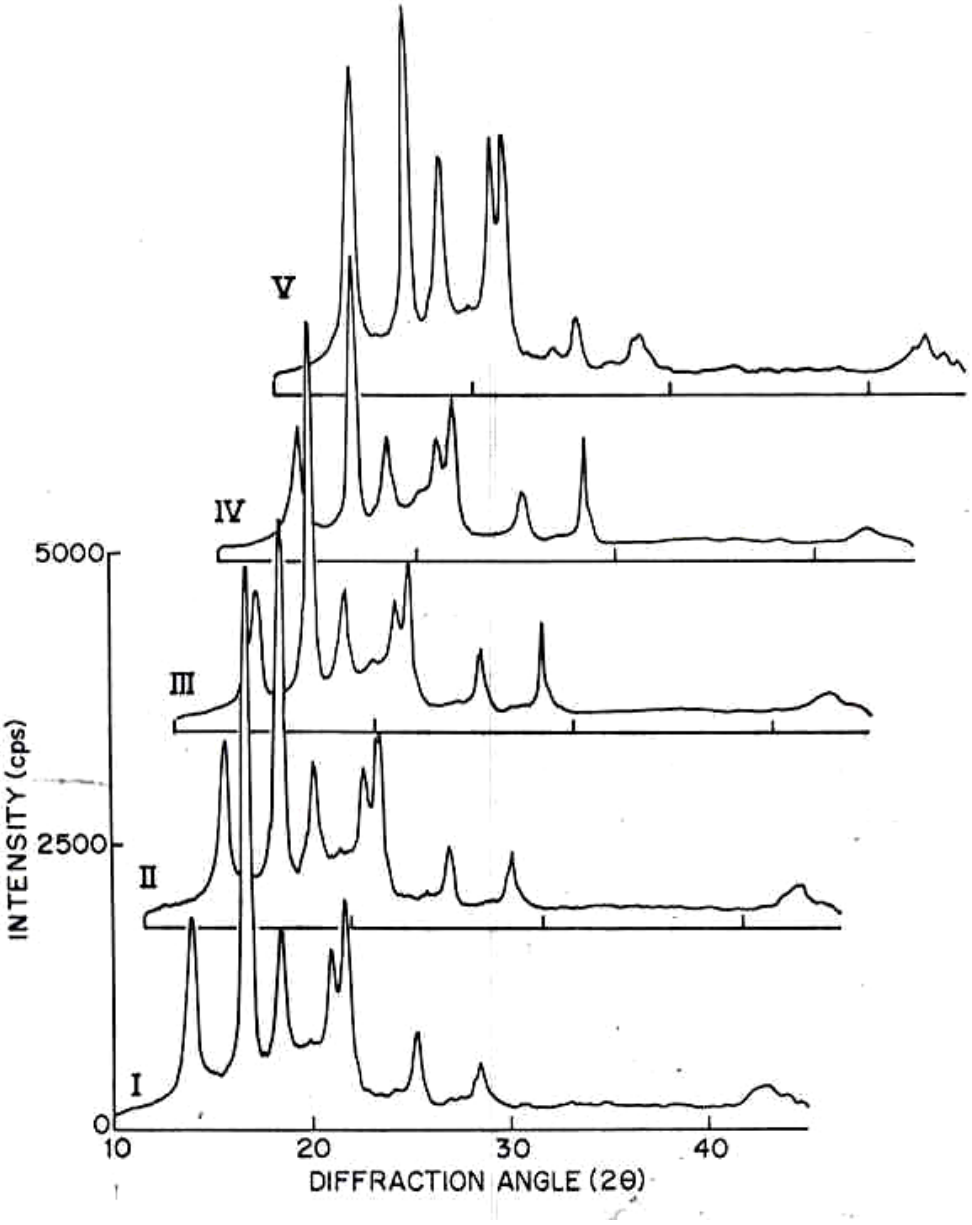

Figure 4.18 WAXD scans of PP/ nanophlogopite (14 nm). Curves I – IV correspond to 2, 5, 10,15 wt. % mica loading and V to pure PP

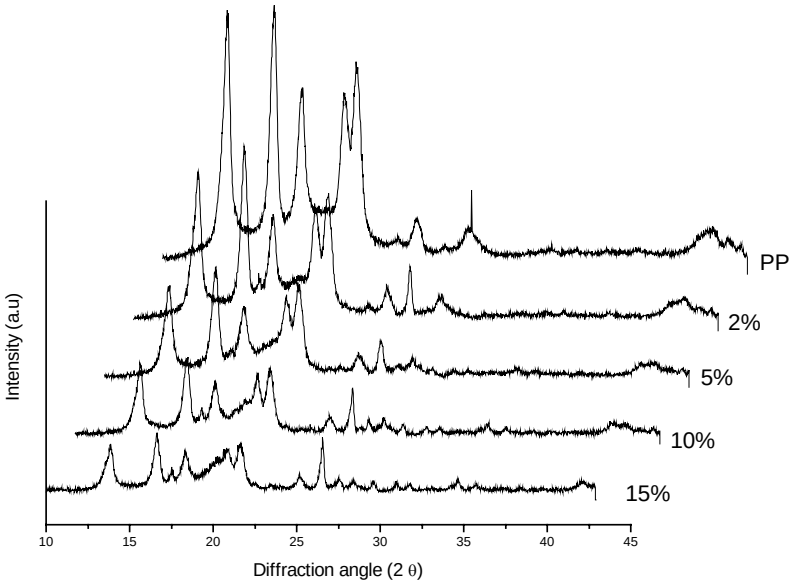

Figure 4.19 WAXD scans of PP/ nanomuscovite (38 nm)

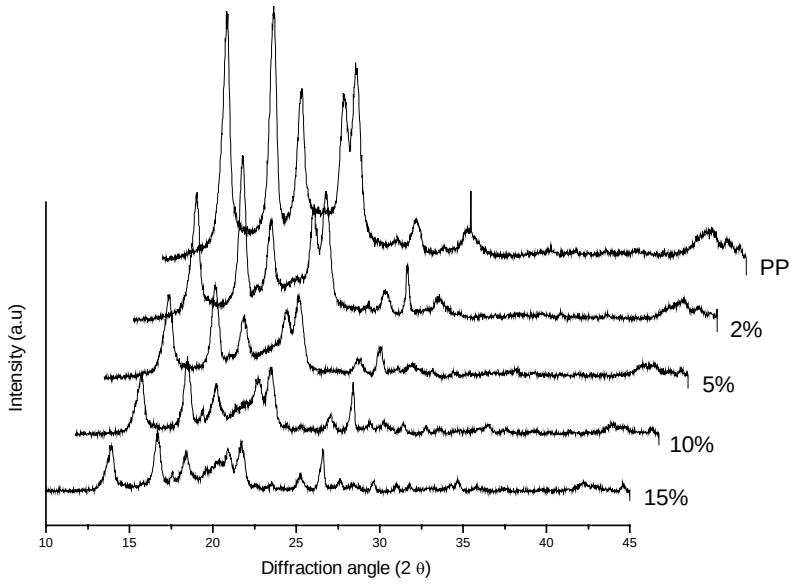

Figure 4.20 WAXD scans of PP/ nanomuscovite (27 nm)

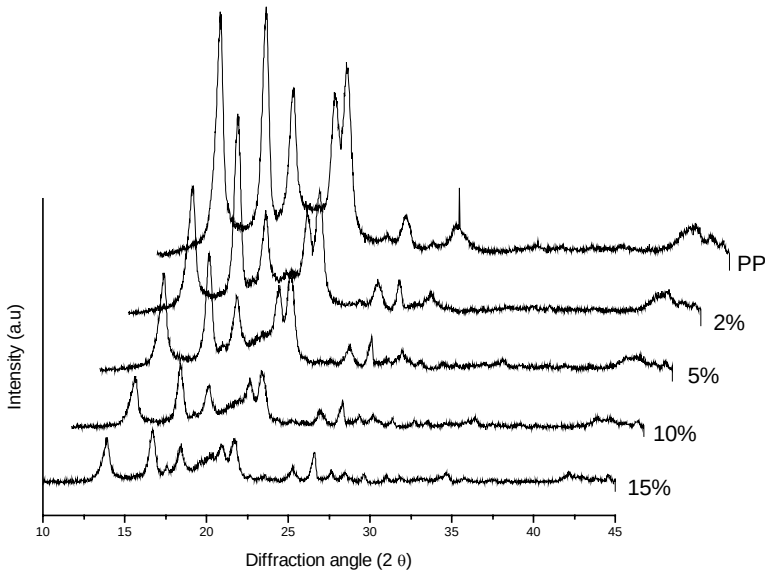

Figure 4.21 WAXD scans of PP/ nanomuscovite (24 nm)

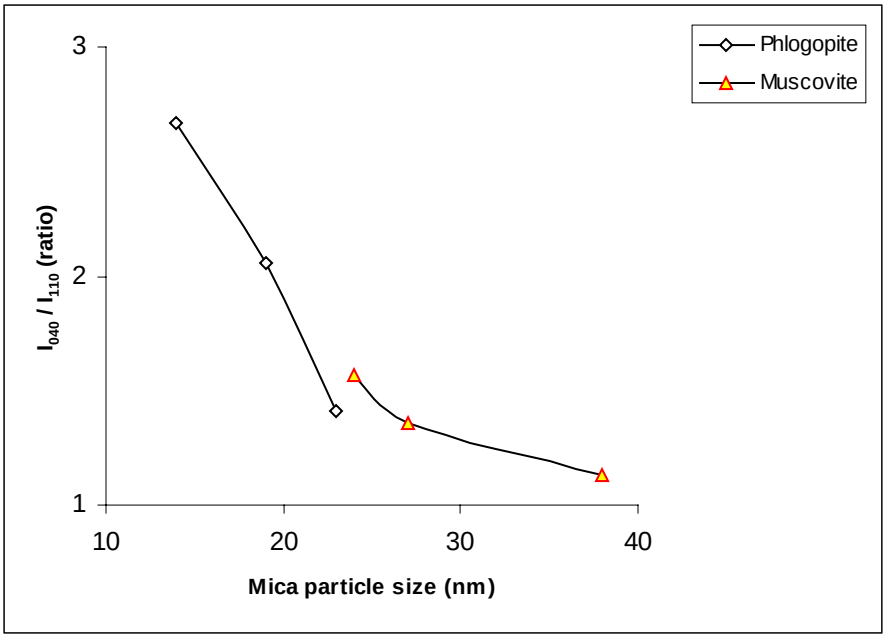

Figure 4.22 I_{040} / I_{110} ratio as a function of particle size for PP/ mica nanocomposites

Table 4.4 I_{040} / I_{110} ratios of melt crystallized PP/ mica nanocomposites

Mica particle size (nm)	**I_{040} / I_{110} ratio**				
	Pure PP	**2%**	**5%**	**10%**	**15%**
Phlogopite mica					
14	1.17	2.67	2.16	2.89	2.22
19	1.17	2.06	2.76	2.6	2.53
23	1.17	1.41	1.42	1.9	1.82
Muscovite mica					
24	1	1.57	1.19	1.21	1.27
27	1	1.36	1.13	1.26	1.31
38	1	1.13	1.16	1.1	1.26

increases when there is transcrystallinity.[15] The present observations here are in agreement with both of the earlier reports.

The nucleating efficacy of nanomica was further confirmed by recording the DSC scans for some of the nanocomposite samples. It is a well known fact that upon nucleation, there is an increase in the crystallization temperature (T_c).[25] This was very much observed in the case of our nanocomposite samples (10 % mica loading) as shown in the figure 4.23. Pure PP exhibits a T_c at 116.6 °C whereas the nanocomposites show a T_c at around 120 °C thereby confirming the nucleating efficiency of mica. Representative DSC thermograms (normalized) of PP/ phlogopite composites and nanocomposites for different loading levels of mica are given in the figures 4.24 and 4.25. The heat of crystallization and melting along with the onset of melting, T_m and T_c values are recorded

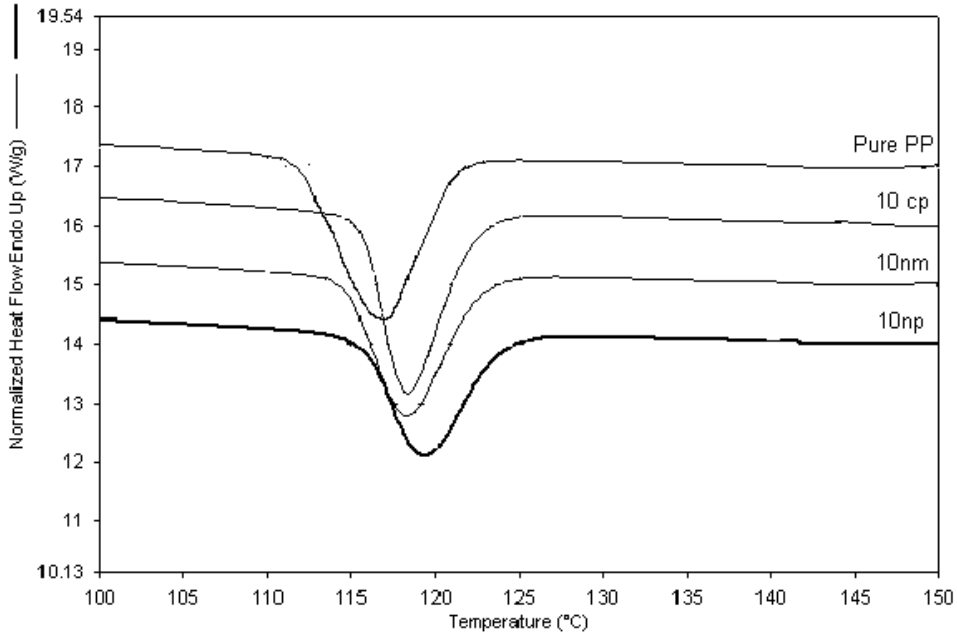

Figure 4.23 Normalized exotherms of pure PP and the nanocomposites

cp – com. phlogopite, nm – nanomuscovite, np - nanophlogopite

in the table 4.5. The values given there are corrected for the mica and PPS content i. e. the original values obtained were divided by the wt.% of mica and PPS present, respectively. Though the commercial PP/ mica composites too exhibit an increase in T_c, the corresponding rise in T_c in case of the nanocomposites is obtained at a much lower loading levels of 3-6 wt.% of nano-mica. It is also seen that the change in T_m is not significant since the nano-mica does not alter the crystallite size of the PP to a great extent. The enthalpy of melting plotted as a function of mica content for both the commercial composites and nanocomposites is shown in the figures 4.26a and b. Since the value of ΔH_m directly reflects the level of crystallinity in the sample, it could be concluded that the PP/ mica nanocomposites show comparable crystallinities as that of the 30 wt.% commercial mica composites but again, at much lower mica loadings of 6-10 wt.%.

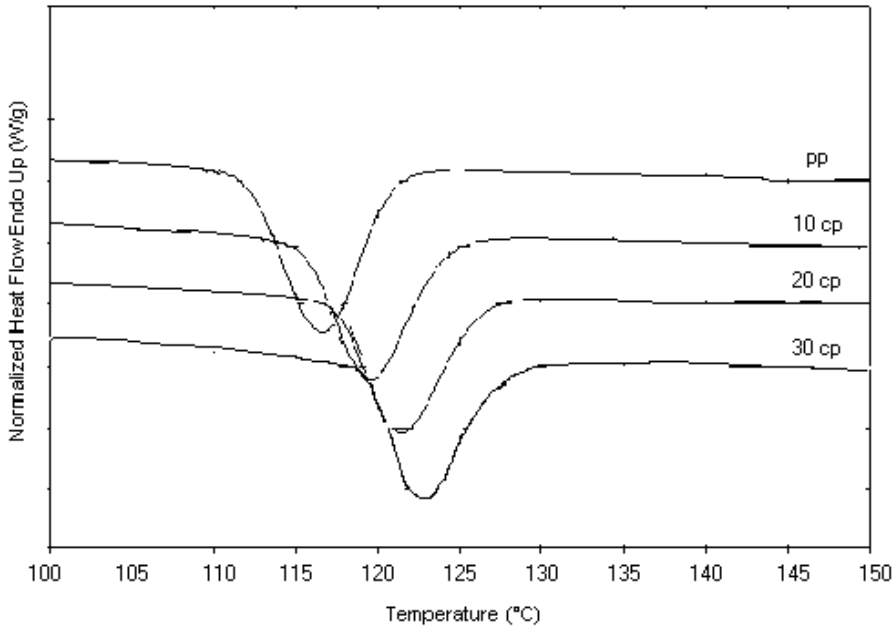

Figure 4.24a Exotherms of PP/ com. phlogopite composites

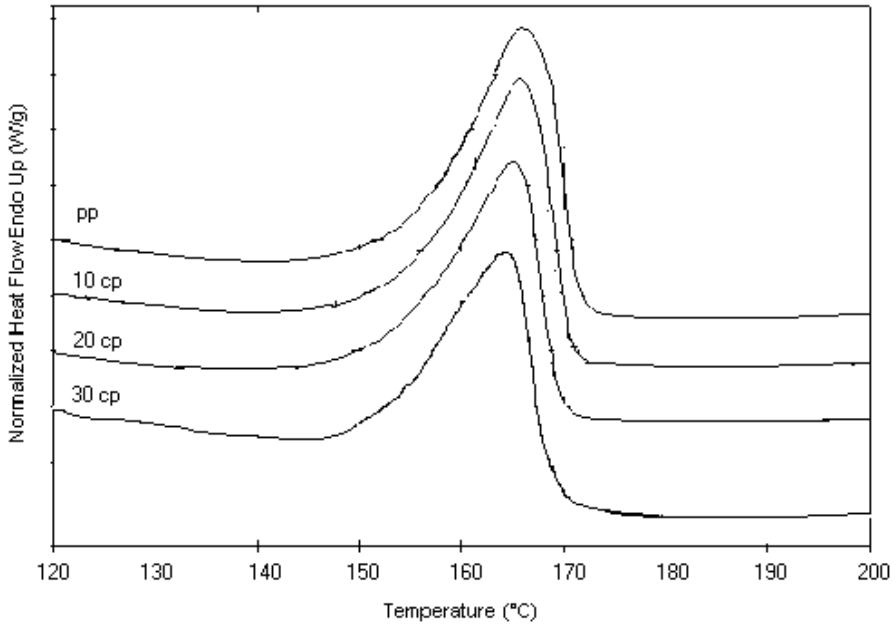

Figure 4.24b Endotherms of PP/ com. phlogopite composites

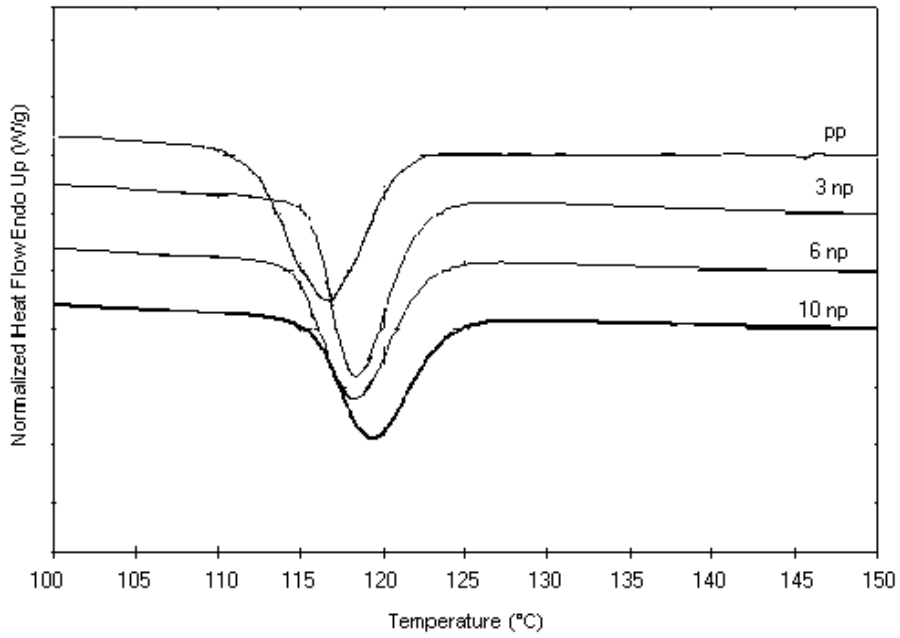

Figure 4.25a Exotherms of PP/ phlogopite nanocomposites

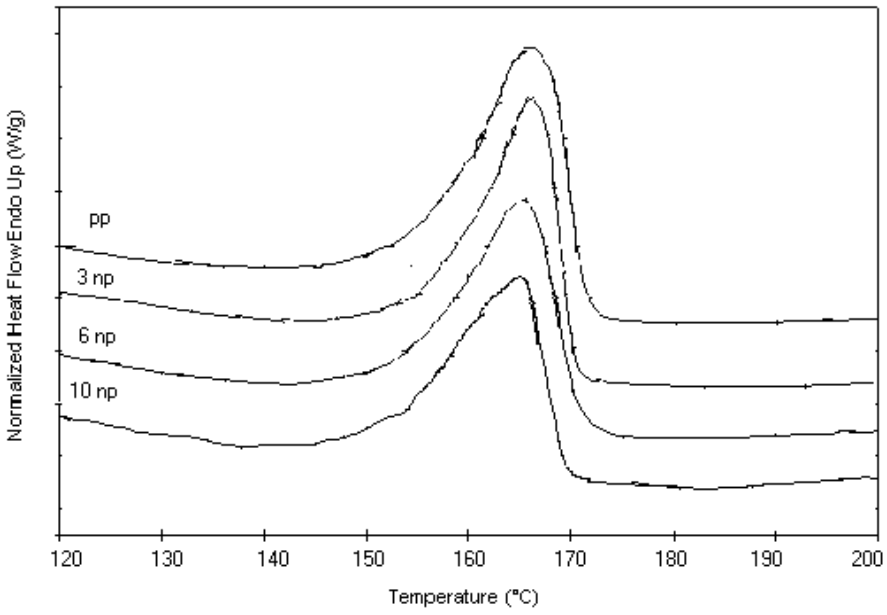

Figure 4.25b Endotherms of PP/ phlogopite nanocomposites

Table 4.5 DSC data for PP/ mica composites and nanocomposites

Composition (wt. %)	**T_c (°C)**	**ΔH_c(*) (J/g)**	**T_m (°C)**	**ΔH_m(*) (J/g)**	**T_m Onset (°C)**
PP	116.6	-98.45	166	68.99	155.3
10 cp	118.3	-97.06	165.6	73.14	153.2
20 cp	121.4	-100.48	163.6	74.72	153.1
30 cp	122.8	-112.48	163.2	87.95	151.3
10 cm	116.7	-101.24	165.3	70	153.8
20 cm	118.8	-105.4	165.1	81.92	152
30 cm	118.7	-115.24	164.3	86.27	151.8
3 np	118.3	-91.3	165.5	70.78	153.3
6 np	118.3	-95.29	165.3	72.11	153.6
10 np	119.2	-96.69	165.2	79.17	156.6
3 nm	118.6	-98.35	165.7	73.87	149.6
6 nm	119.8	-99.36	165.5	71.13	156.1
10 nm	119.4	-99.44	165.2	82.16	156.5

cm – commercial muscovite, cp - commercial phlogopite

nm – nano-muscovite, np – nano-phlogopite

* The enthalpy values have been corrected for the mica and PPS content.

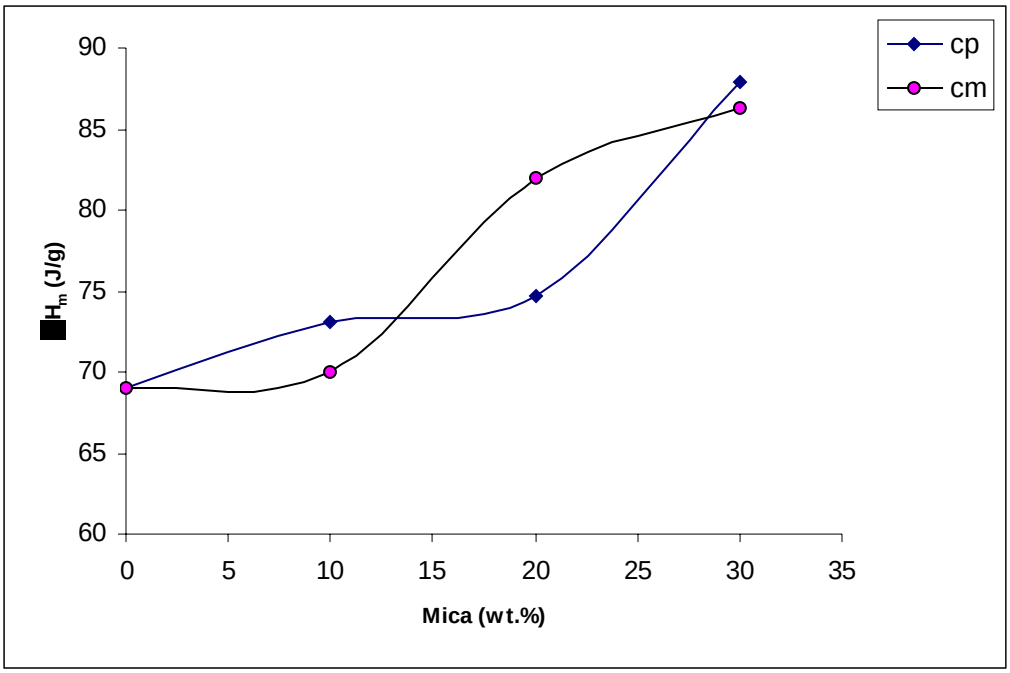

Figure 4.26a ΔH_m variation in PP/ com. mica composites

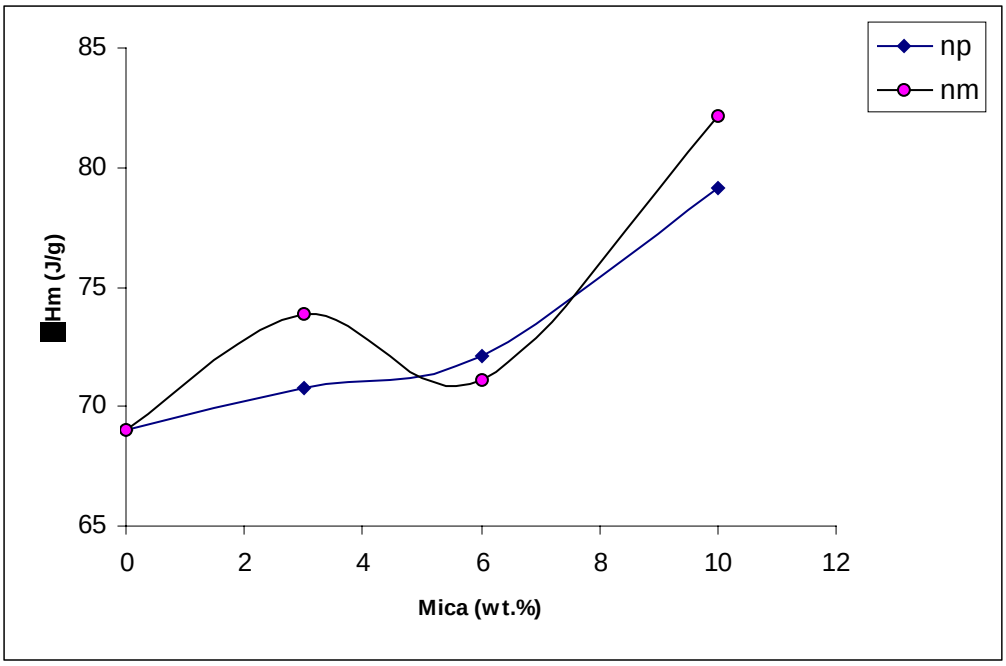

Figure 4.26b ΔH_m variation in PP/ mica nanocomposites

To check out the effect of processing on the structure development of PP/ mica nanocomposites, the WAXD of the injection molded tensile test specimens were done. Figures 4.27 to 4.30 represent the WAXD scans of PP/ mica composites of commercial/ nano phlogopite and muscovite at different mica loading levels, respectively. If one compares the figures 4.29 and 4.30 with 4.18 and 4.21, it is clearly observed that the intensities of reflections at 2 θ = 28.61 (for phlogopite mica corresponding to the 003 plane) and at 26.87 (for muscovite mica corresponding to the 009 plane) increase considerably in the injection molded samples. This is also reflected in the 003 and 009 peak intensities of PP/ commercial mica composites as shown in the figures 4.27 and 4.28. Further, this change becomes more prominent for higher concentration of mica particles. This clearly suggests the orientation of mica particles in the preferred direction i.e. the flow direction of the PP melt during injection molding.

SEM pictures of the injection molded PP/ mica composite and nanocomposite samples were taken after the samples were sectioned in the transverse direction to investigate the microstructure. The micrographs of the composite and nanocomposite samples are presented in figures 4.31a-d, respectively. From the figures, it is clearly evident that the conventional composite consists of large mica flakes with some amount of ordering in the flow direction (in to the plane of the paper) whereas the nanocomposites display a much better homogeneous structure with a good orientation along the flow direction.

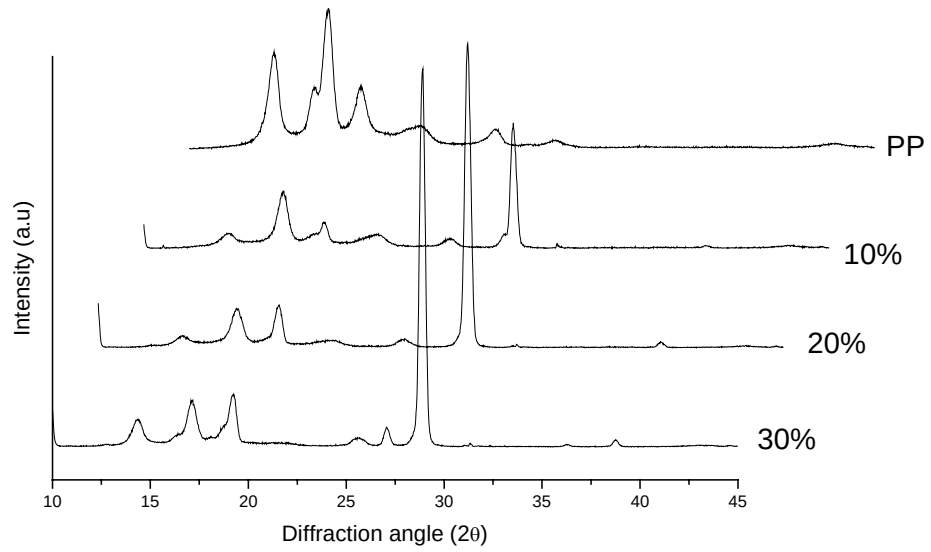

Figure 4.27 WAXD scans of injection molded PP/ com. phlogopite samples

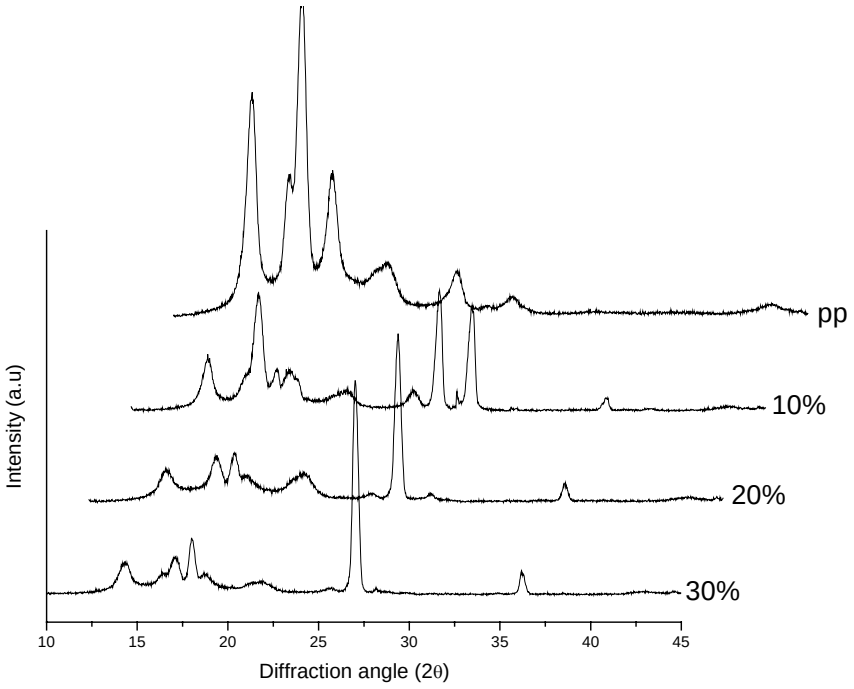

Figure 4.28 WAXD scans of injection molded PP/ com. muscovite samples

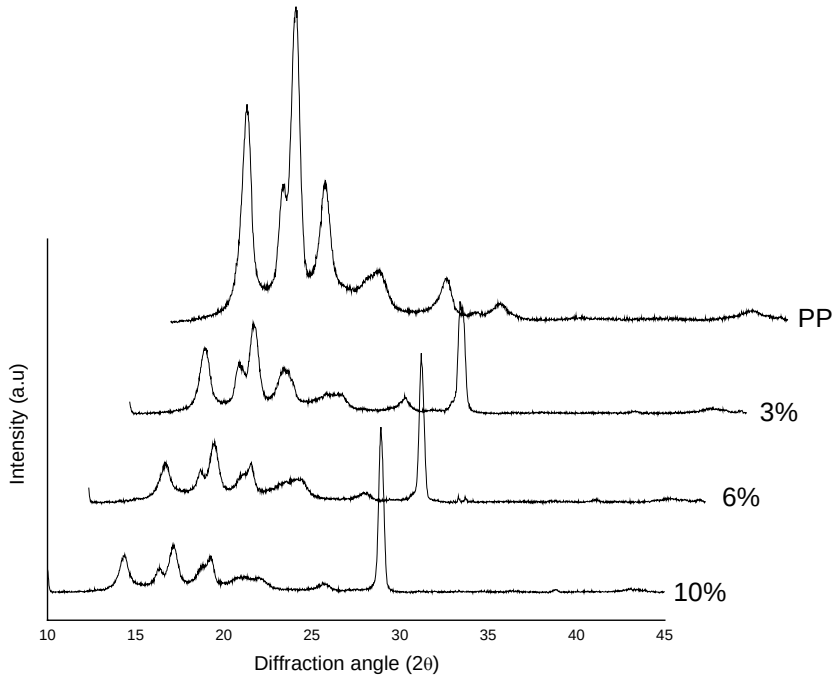

Figure 4.29 WAXD scans of injection molded PP/ nanophlogopite samples (14 nm)

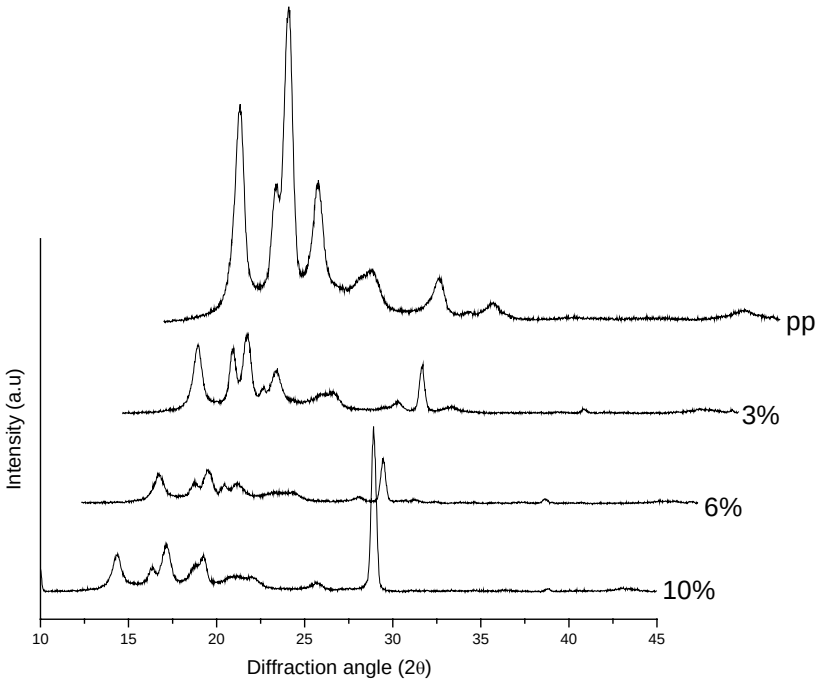

Figure 4.30 WAXD scans of injection molded PP/ nanomuscovite samples (24 nm)

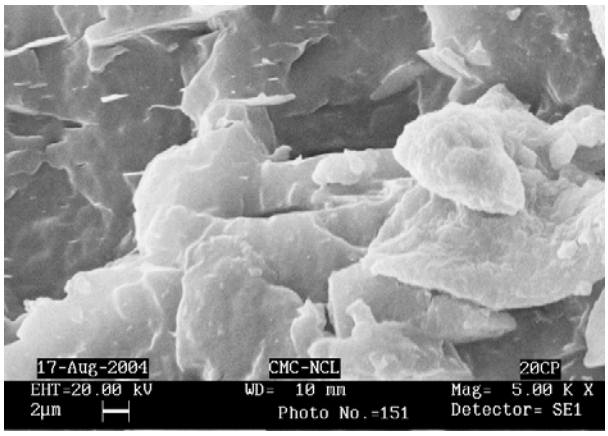

(a)

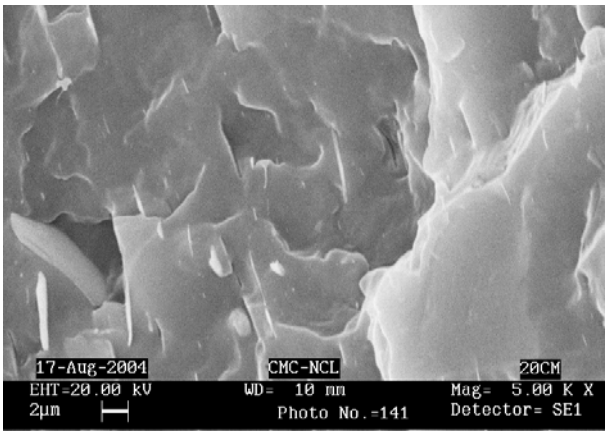

(b)

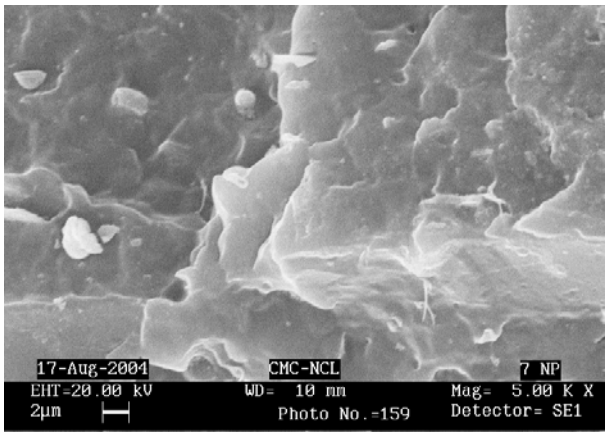

(c)

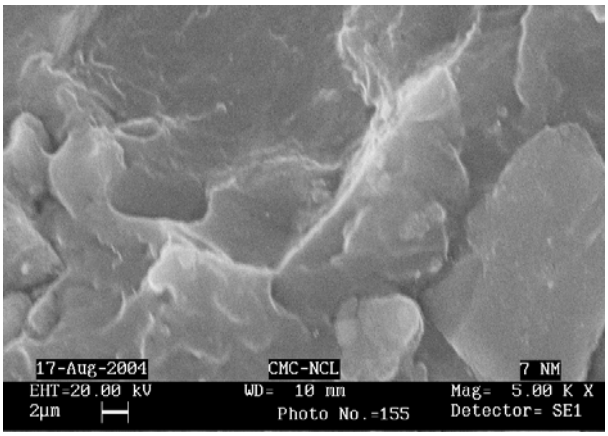

(d)

Figure 4.31 SEM of cross-sectioned samples of PP/ mica composites and nanocomposites

(a) PP/ com. phlogopite (20 wt.%) **(b)** PP/ com. muscovite (20 wt.%)

(c) PP/ nanophlogopite (7 wt.%) **(d)** PP/ nanomuscovite (7 wt.%)

4(B) Properties of Mica/ PP Nanocomposites

4.4 Introduction

PP has been widely used for its good processing properties, high rigidity and excellent mechanical properties. However, to meet various applications, further increase in end use temperature and improved mechanical properties still constitute the main focus of PP modification. PP is also one of the most popular matrices because of its amenability to modifications with various types of additives, which can impart desired properties.[26,27] It can exhibit high impact, high flexural modulus, good heat distortion temperature, etc. which are close to some of the engineering plastics. To improve the competitiveness of PP for engineering plastics applications, it is an important objective in PP compounding to improve crystallinity, interfacial adhesion, reinforcing effect without the loss of other properties such as optical transparency, gloss, flexibility, etc. Nanoparticulate additives are expected to satisfy all these requirements.

In this context, the nanomica synthesized by in situ intercalative polymerization was dispersed in a PP matrix and the properties studied are reported in this section. We surmised that the oligomeric PPS in which the nanomica is embedded might have some compatibilizing role, which was found to be true as will be seen later in the section.

4.5 Experimental

(a) Micro compounding/ Micro injection Molding of PP/ Mica Nanocomposites

The tensile and flexural test specimens for mechanical testing were prepared by micro compounding/ micro injection molding using a DSM MICRO 5 unit with the barrel temperature set at 210 ºC and the speed of the co-rotating screws set at 80 rpm. After

compounding for about 2-4 minutes, the extrudate was fed into the cylinder of the micro injection molding unit whose temperature was preset at 220 ºC. The melt was injected into the mold at room temperature to get the standard test specimen for tensile and flexural tests in the form of a dumbbell and rectangular bar, respectively. A range of compositions of both commercial and nano-phlogopite/ muscovite were prepared. Commercial PP/ mica composites were made with 10, 20 and 30 wt. % of mica whereas PP/ mica nanocomposites were made with 3, 6 and 10 wt. % of nanomica.

(b) Compression Molding of PP/ Mica Nanocomposites

The discs required for dielectric measurements were prepared by compression molding the nanocomposite material using a polymer press. Melt compounded PP/ mica sample (2 g) was introduced in between the platens and molded at 170 ºC for 4 minutes at a pressure of 0.5 tonnes after which it was quenched in cold water. This sample was dried and a small layer of gold was coated on to the discs for dielectric relaxation studies.

The DSC and TGA of these samples were run as described in section 2.11.4 and 2.11.5 respectively. To investigate the orientation of mica in these nanocomposites, SEM of the cross sectioned flexural sample was performed as described in section 2.11.6.The measurement of tensile, flexural and dielectric properties of these PP/ mica nanocomposites were done as given in section 2.11.10 and 2.11.11 and 2.11.9, respectively.

4.6 Results and Discussion

4.6.1 Mechanical Properties

(a) Tensile Properties

The concept of load sharing between the matrix and the reinforcing phase is central to understanding the mechanical behavior of a composite. The stress may vary sharply from point to point, but the proportion of external load borne by each of the individual constituents can be gauged by volume-averaging the load within them.

Mica based PP composites have been studied extensively earlier. Woodhams et al.[28] found that the properties of the molded PP-mica composites exhibit moduli which are much higher than most filled polymers. The tensile strength was found to increase when a silane coupling agent or carboxy modified PP was used. High processing temperature was found to decrease flake damage and improve flow orientation of flakes. Trotignon et al.[29] have investigated the influence of muscovite mica on the tensile and flexural properties and found that an optimum aspect ratio between 100 and 250 μ is ideal for obtaining the best results. Vu-khanh et al.[30] have used the concepts of post yield fracture mechanics to characterize the crack initiation and propagation resistances of PP containing different loadings of mica. A surface treatment technology was developed by Chiang et al.[31] for PP/ mica composites that produce a diffuse interlayer with excellent adhesion between the components. The tensile properties of the PP/ mica composites and nanocomposites studied in this module are presented in the figures 4.32a and b and the other tensile parameters are tabulated in the table 4.5. There is a gradual increase in the tensile modulus of the composites as well as the nanocomposites and a decrease in the % elongation is observed. The nano-mica samples showed considerable tensile elongation at

lower loadings of 3 wt.%, which decreases at higher loadings. It is also seen that the modulus of muscovite mica is greater than that of phlogopite mica, which might have its origin in the extent of silicate layer delamination. It is worth recalling that muscovite mica was downsized to a greater extent than phlogopite mica. One of the outstanding features of the present work is that there is a increase in the tensile modulus of the nanocomposite up to a nanomica loading of 8-10 %, which is much higher than those reported previously. It can also be noted that tensile moduli obtained at 20 wt.% commercial mica loading are obtained at 6-10 wt.% loading of nanomica. An increase in the stress at break and a considerable drop in the break strain and toughness are observed. Effective stress transfer from the polymer matrix to the nanoparticulate mica particles is speculated to be the reason for this behavior. It is also expected that the polymer chains in contact with nanomica might have a distinctly different response from those not in contact because of the mechanical displacement resulting from elongation leading to a modulus rise at lower loadings. At higher loadings, we find that the rate of modulus enhancement drops down which might be due to the presence of agglomerated structures in the polymer matrix.

There exist many failure modes for thermoplastics based on the matrix, filler or the matrix-filler interface.[32] In practice, many important phenomena may take place at the interface, depending on its structure and the stresses generated there. These processes tend to promote plastic deformation of the matrix and can also influence the onset and nature of failure. The interface in the case of the high aspect ratio mica/ PP system might result by mechanical keying ensuring an increased area of contact between the mica and PP. This interface influences the crystallization process of the matrix, which has a direct

bearing on the observed mechanical properties. In the earlier section, it was found that nucleation of spherulitic crystallites occurred preferentially at the mica surface resulting in an enhanced crystallinity in the nanocomposites. Such an increase in crystallinity generally tends to depress the fracture toughness and raise the tensile strength of the matrix. The volume contraction accompanying crystallization sets up residual stresses in the matrix that directly affects the mechanical properties.

The stress-strain curves of the tensile tests for the PP/ mica composites and nanocomposites are depicted in the figures 4.33 and 4.34. Pure PP and composites with low mica loading show yielding behavior with a clearly observable strain whitening. Also, there might be some stress induced crystallization at lower mica loadings, which is apparent in the yielding behavior. However, composites and nanocomposites with a higher mica loading did not show any yielding behavior and brittle fracture was observed soon after reaching the maximum stress. There was also no strain whitening.

The fractured surfaces of the composites and nanocomposites after tensile testing were subsequently examined to ascertain the mode of fracture. Care was taken not to disturb the fractured surfaces while preparing the samples for SEM. The micrographs of a cross-section of injection molded PP and the fractured surface of pure PP after tensile testing is given as a reference in the figure 4.35 a and b, respectively. The fractured surface of pure PP exhibits a fibrillar morphology, which is known to induce plastic deformation in the sample and cause necking and strain whitening. The micrographs of the fractured surfaces of the PP/ mica composites and nanocomposites are shown in the figures 4.36a-d. The nanocomposites exhibit some amount of fibrillar structure whereas the conventional composites display a more diffuse morphology leading to brittle fracture

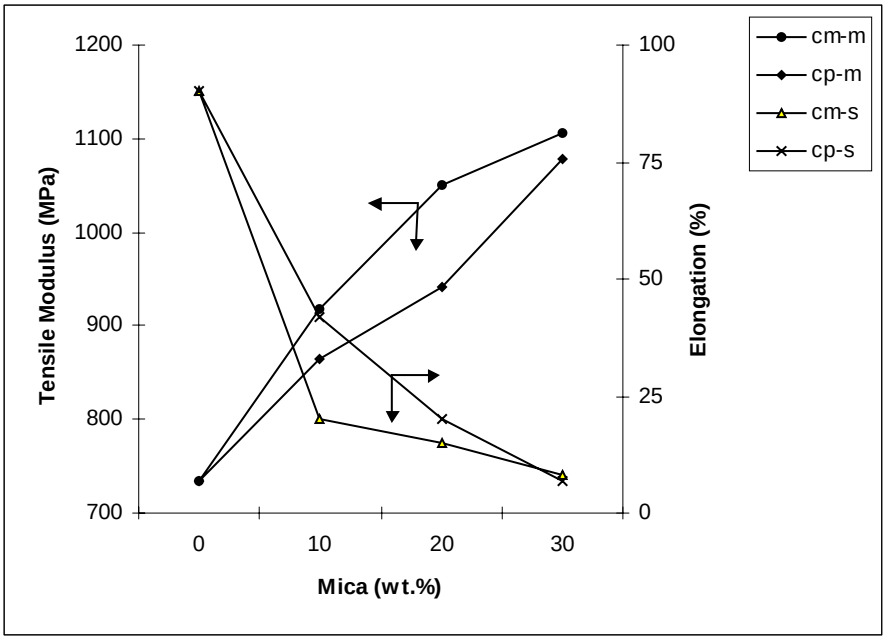

Figure 4.32a Tensile properties of PP/ commercial mica composites

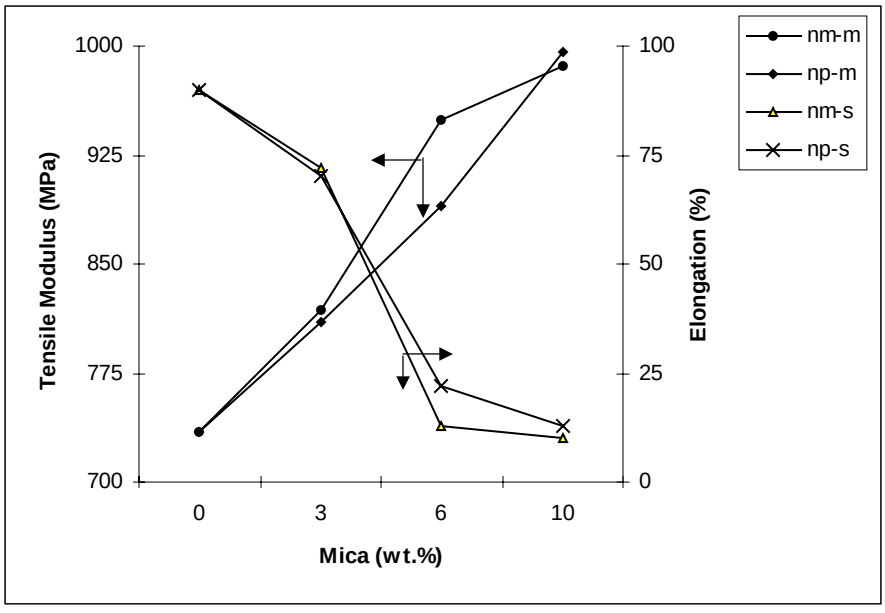

Figure 4.32b Tensile properties of PP/ mica nanocomposites

Table 4.6 Tensile data for PP/ mica composites and nanocomposites

Composition (Mica wt.%)	Max. Stress (MPa)	Max. Strain (mm/mm)	Break Stress (MPa)	Break Strain (mm/mm)	Modulus (MPa)	Toughness (MPa)	Energy at yield (J)
Pure PP	30.54	0.1306	10.63	0.905	735	25.04	0.5889
10 cp	27.76	0.0980	17.46	0.4247	865	7.14	0.4126
20 cp	25.57	0.0777	15.24	0.2014	941	3.77	0.3086
30 cp	24.73	0.0654	12.63	0.0734	1079	1.11	0.2177
10 cm	23.67	0.0837	8.242	0.205	918	3.71	0.3188
20 cm	23.09	0.0666	9.571	0.1541	1051	2.73	0.2196
30 cm	19.59	0.0423	10.50	0.0854	1107	1.29	0.1214
3 np	23.67	0.0971	15.55	0.7071	810	19.81	0.3022
6 np	25.01	0.0806	15.6	0.2240	890	3.92	0.2750
10 np	24.23	0.0531	19.46	0.1291	996	1.97	0.1534
3 nm	26.06	0.0871	7.045	0.7231	819	21.01	0.3133
6 nm	24.86	0.0700	16.73	0.1351	949	2.27	0.2361
10 nm	22.55	0.0486	18.65	0.1025	986	1.92	0.1446

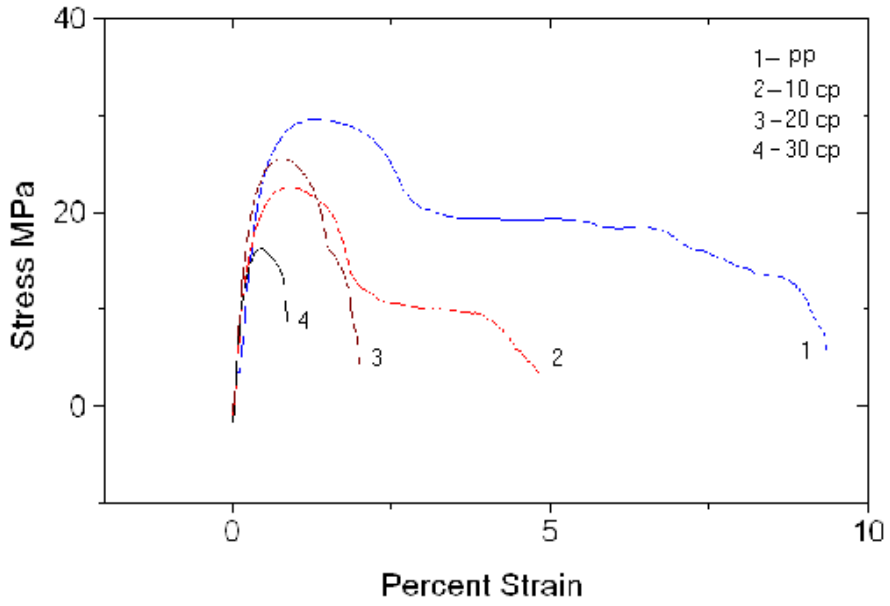

Figure 4.33a Stress Vs Strain curves for PP/ com. phlogopite composites

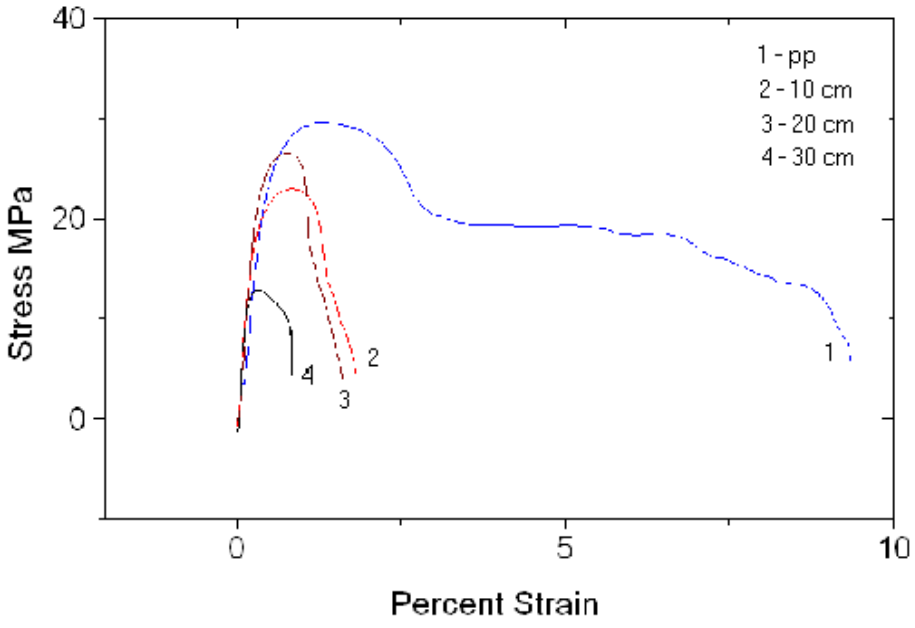

Figure 4.33b Stress Vs Strain curves for PP/ com. muscovite composites

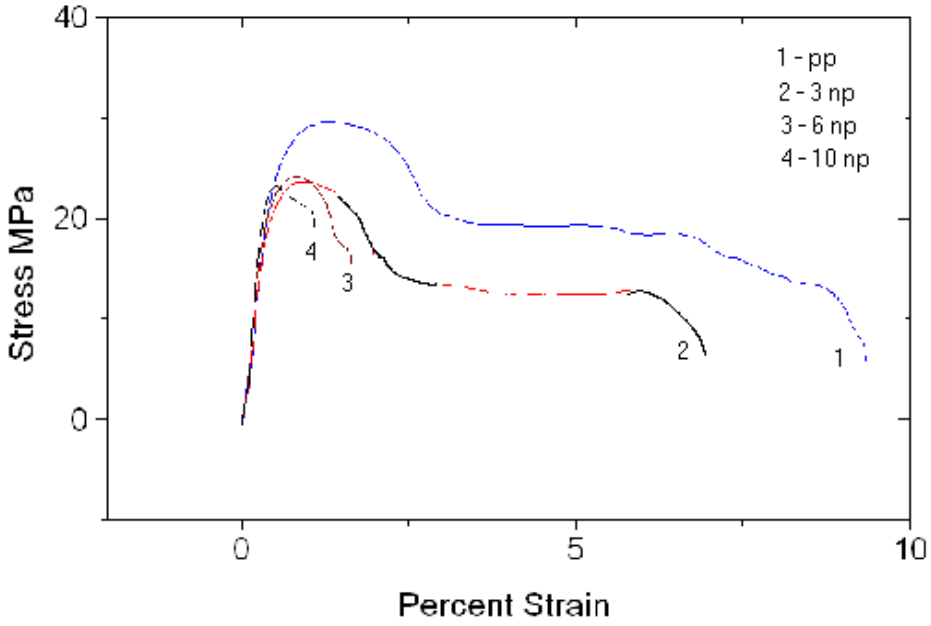

Figure 4.34a Stress Vs Strain curves for PP/ phlogopite nanocomposites

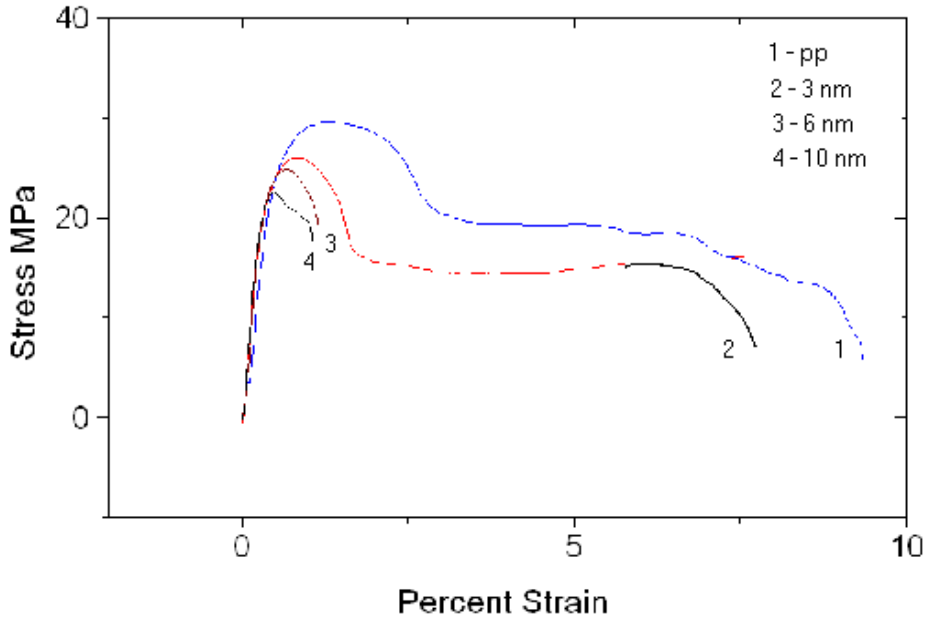

Figure 4.34b Stress Vs Strain curves for PP/ muscovite nanocomposites

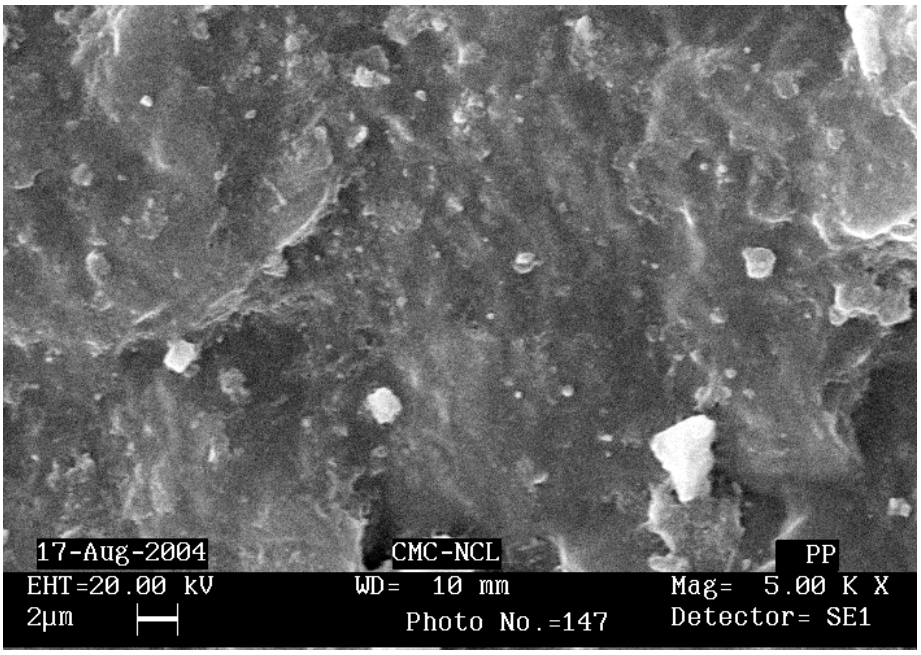

Figure 4.35a SEM of a cross-section of molded PP sample

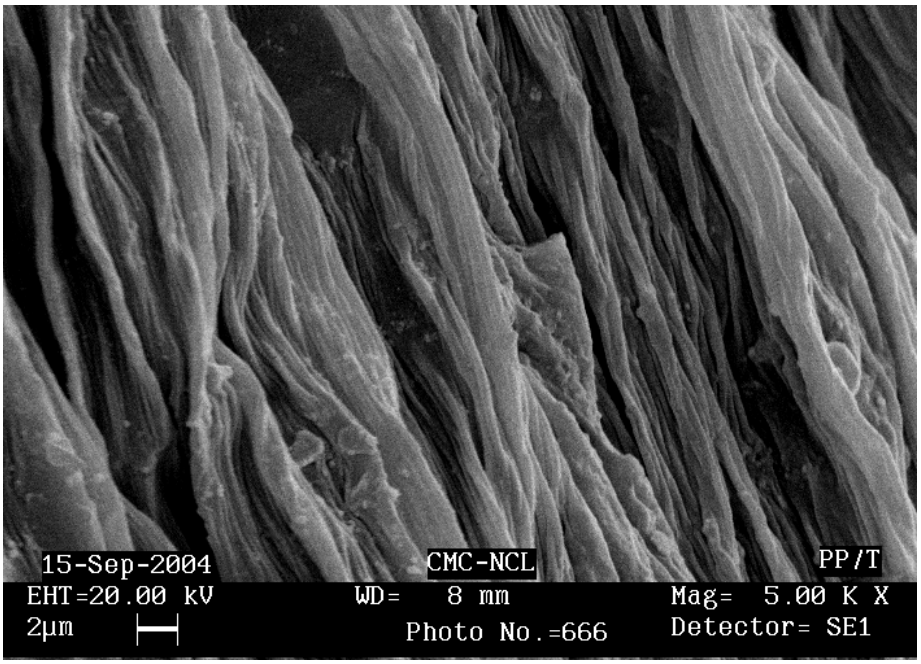

Figure 4.35b SEM of the fractured surface of PP after tensile testing

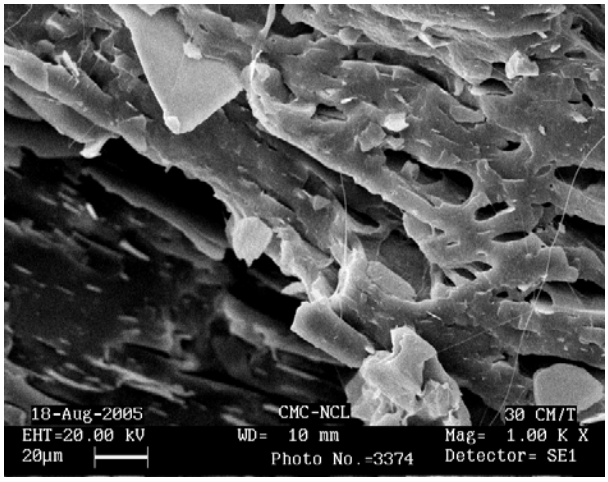

(a)

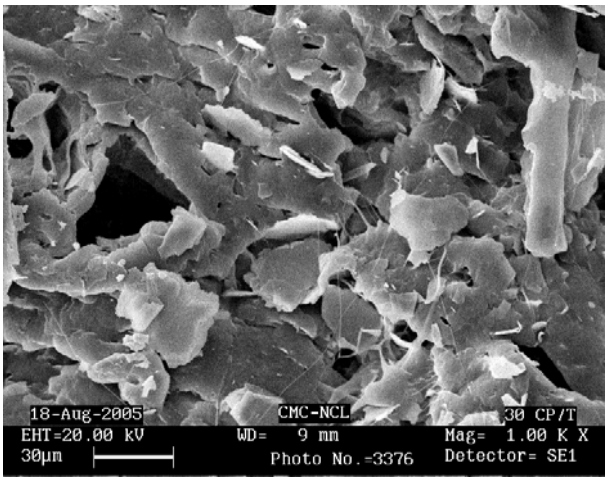

(b)

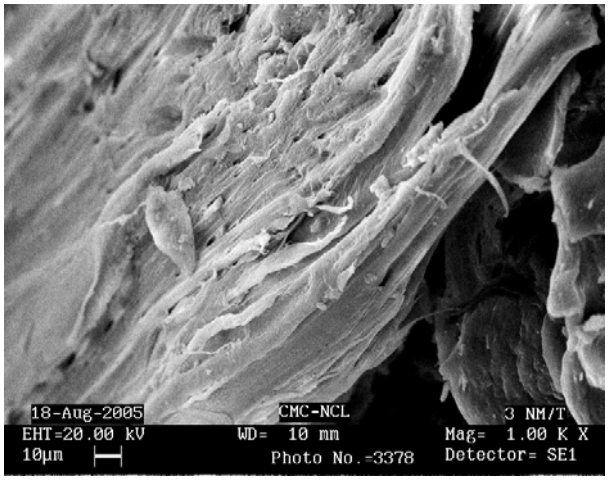

(c)

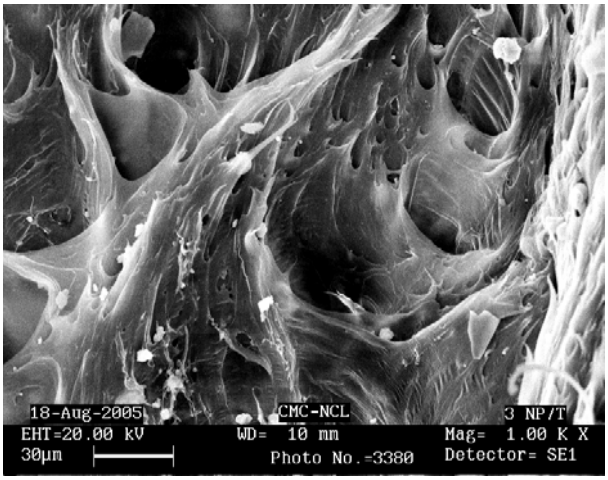

(d)

Figure 4.36 SEM of fractured surfaces of PP/ mica composites and nanocomposites after tensile testing **(a)** PP/ com. phlogopite (30 wt.%) **(b)** PP/ com. muscovite (30 wt.%) **(c)** PP/ nanophlogopite (3 wt.%) **(d)** PP/ nanomuscovite (3 wt.%)

(b) Flexural Properties

Failure in the flexural mode is dependent on the way that the loading is applied and, in particular, on the degree of lateral constraint. Mica, being a high aspect ratio filler tends to buckle under axial compression, which might be the most probable mode of failure. The flexural properties of PP/ mica composites and nanocomposites are depicted in the figures 4.37a and b and the data obtained from the tests are given in the table 4.7. Here again, it is found that muscovite mica exhibits better flexural properties as compared to phlogopite mica. There is a sharp increase in the flexural modulus and strength at lower loading levels that tees off at higher loadings. In this case too, it is found that the nanocomposite delivers flexural properties equivalent to 20-30 wt.% commercial mica at much lower loading levels of 6%.

The stress-strain curves of these flexural tests are shown in the figures 4.38 and 4.39 for both the composites and nanocomposites. The presence of a large number of reinforcing nanomica platelets and the possible orientation of the silicate platelets along the flow direction during injection molding is surmised to be the reason for the observed effects. With higher mica content, the brittleness of the nanocomposite is enhanced.

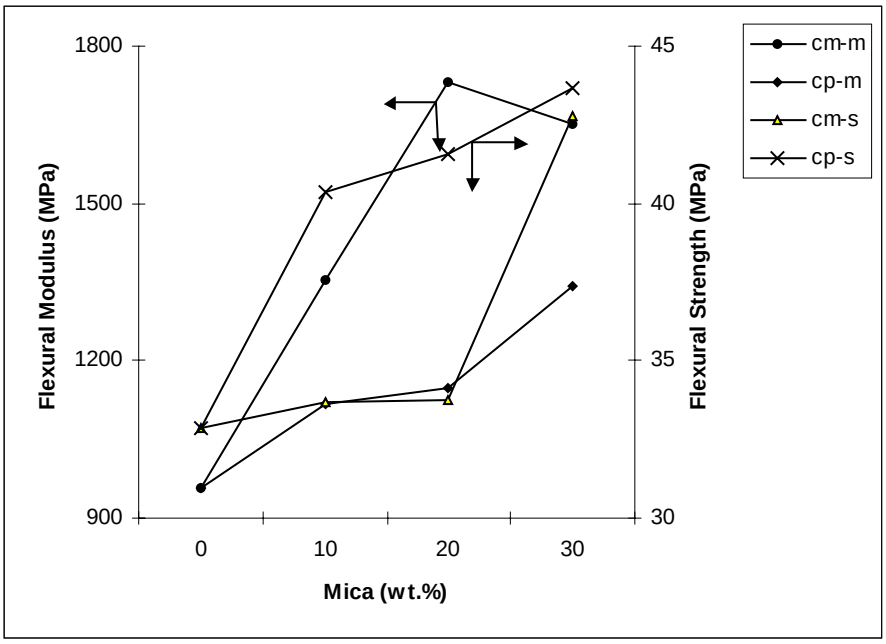

Figure 4.37a Flexural properties of PP/ commercial mica composites

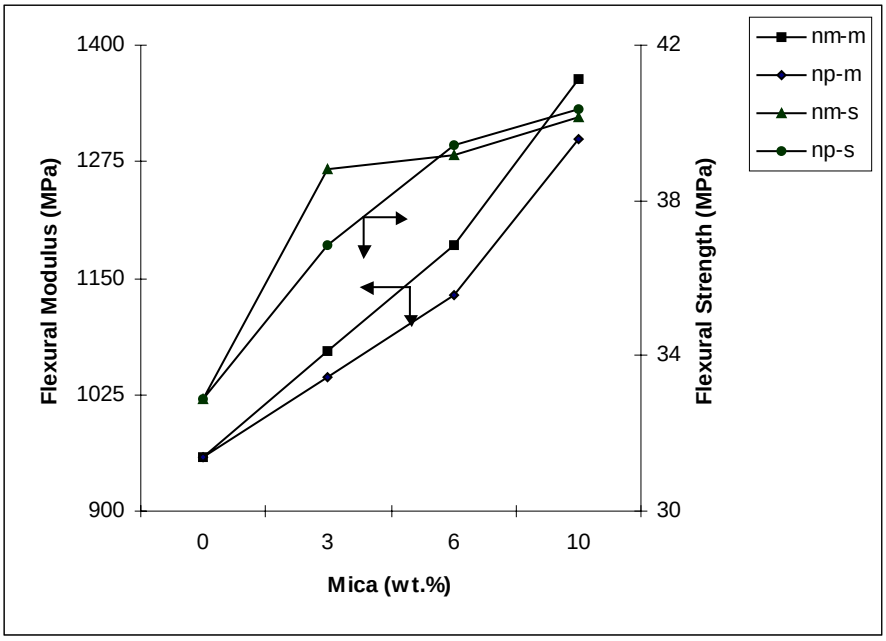

Figure 4.37b Flexural properties of PP/ mica nanocomposites

Table 4.7 Flexural data for PP/ mica composites and nanocomposites

Composition (Mica wt.%)	Yield Displacement (inches)	Yield Strain (%)	Yield Load (KN)	Yield Stress (MPa)	Modulus (MPa)
Pure PP	0.2398	4.65	0.0531	32.86	959
10 cp	0.2492	4.831	0.0657	40.33	1118
20 cp	0.3307	6.412	0.0672	41.57	1146
30 cp	0.2887	5.597	0.0705	43.65	1341
10 cm	0.2984	5.785	0.0544	33.68	1355
20 cm	0.2474	4.795	0.0544	33.72	1732
30 cm	0.2731	5.294	0.0692	42.78	1650
3 np	0.2999	5.814	0.0627	38.83	1043
6 np	0.2992	5.8	0.0632	39.17	1132
10 np	0.2762	5.354	0.0649	40.16	1300
3 nm	0.2428	4.706	0.0595	36.84	1071
6 nm	0.3050	5.912	0.0652	39.42	1185
10 nm	0.2435	4.721	0.0638	40.33	1363

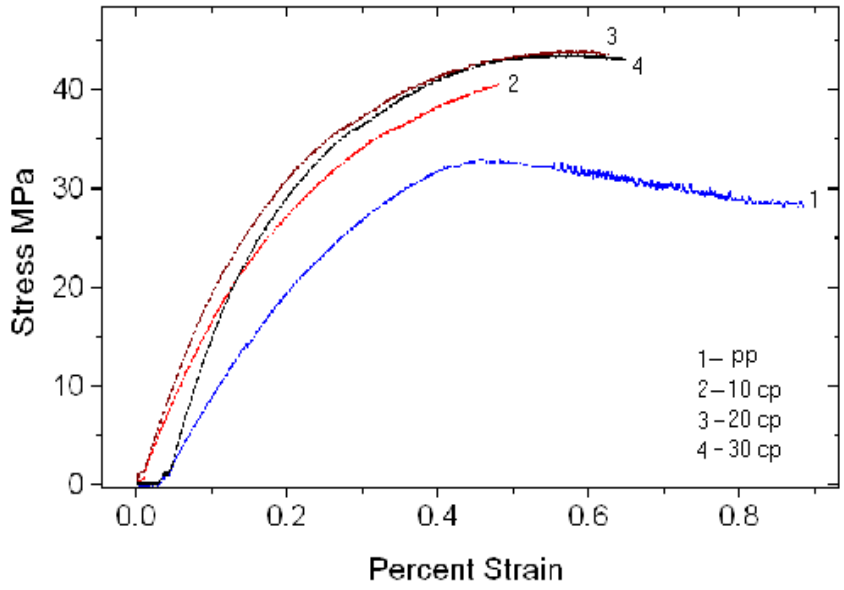

Figure 4.38a Stress Vs % Strain curves for PP/ com. phlogopite composites

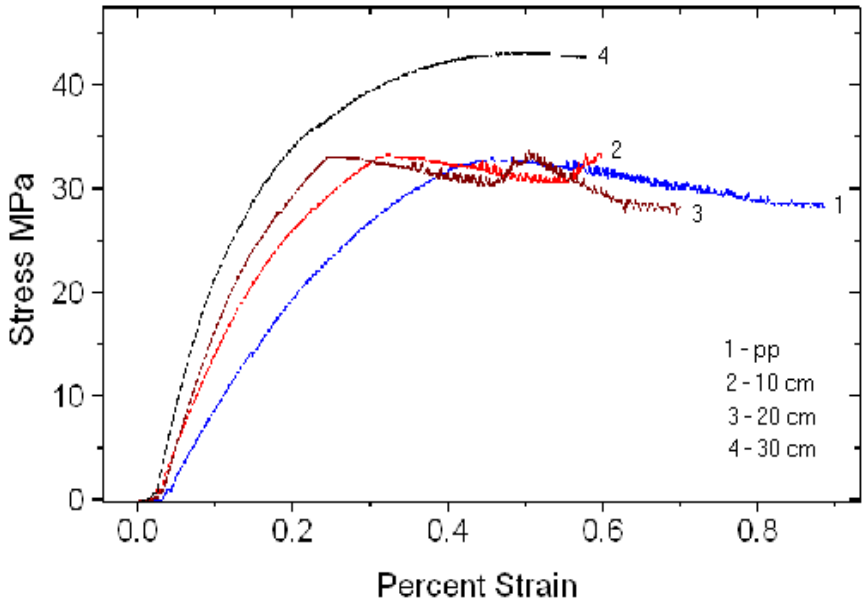

Figure 4.38b Stress Vs % Strain curves for PP/ com. muscovite composites

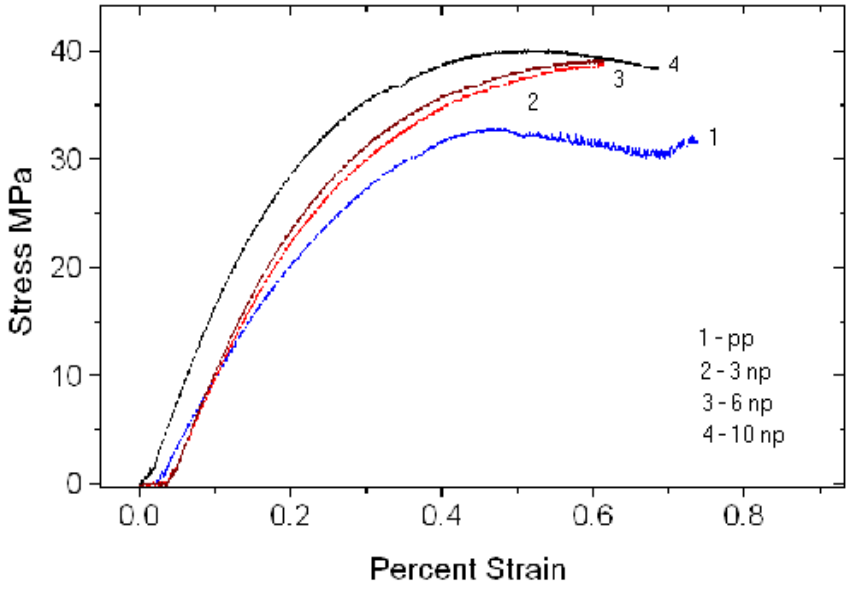

Figure 4.39a Stress Vs % Strain curves for PP/ phlogopite nanocomposites

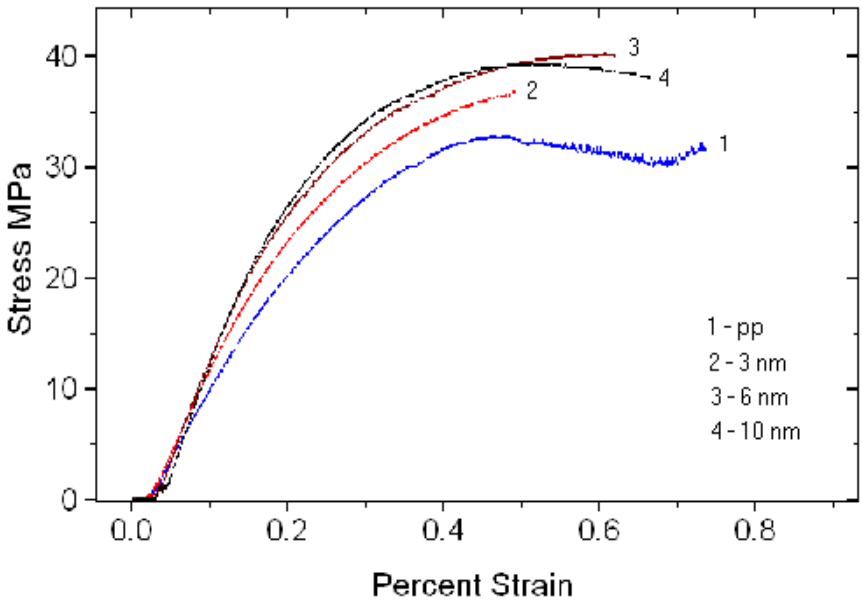

Figure 4.39b Stress Vs % Strain curves for PP/ muscovite nanocomposites

4.6.2 Thermal Properties

(a) Thermo Gravimetric Analysis

The TGA curves for the PP/ mica composites and nanocomposites are represented in the figures 4.40 to 4.43 and the various parameters derived from the thermograms are provided in the table 4.8a. Generally, the incorporation of layered silicates in to the polymer matrix is found to enhance the thermal stability with the silicate acting as a good insulator and mass transport barrier to the volatile products generated during decomposition. The PP/ mica nanocomposites show a dramatic increase of the initial degradation temperature from 353 °C for pure PP to 388 °C for 10% PP/ phlogopite nanocomposite in its characteristic single step degradation process. It is seen that the thermal stability of the nanocomposites is substantially higher than those of the conventional composites. There is also a remarkable increase in the temperature of maximum degradation from 395 °C for pure PP to about 420-430 °C in the case of the composites and nanocomposites.

An interesting observation is worth noting with respect to the % weight loss of the composites and nanocomposites. Pure PP is found to have a weight loss of 98 % at the maximum degradation temperature. PP/ com. phlogopite (10 wt. %) shows a weight loss of 91 % but its expected weight loss is only 88 % when one corrects it for the available mica content i. e. (90 X 98 / 100) since the mica loading in this case is 10 %. When one compares the expected and the actual weight losses (given in table 4.8b) of the composites/ nanocomposites, it is clearly evident that the nanocomposite's thermal stability is far superior to that of the commercial PP/ mica composite.

The overall thermal stability is seen to increase with the increase in the mica loading levels. The stability does not decrease at higher mica loadings thereby confirming the uniform dispersion of the nanomica platelets in the PP matrix. The reason for the improved thermal stability might be speculated to be due to the higher thermal conductivity of mica which results in an efficient heat transfer in the test atmosphere. Since the surface area of the mica platelets is much greater in the case of the nanocomposites at considerably lower loadings, it displays a much lower weight loss as compared to the commercial composites.

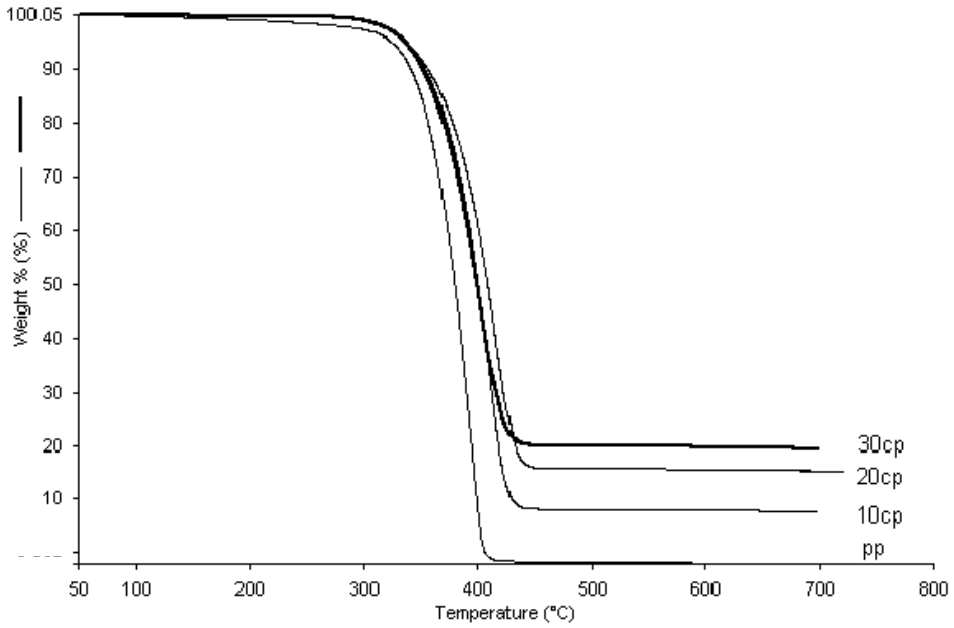

Figure 4.40 TGA curves for PP/ com. phlogopite composites

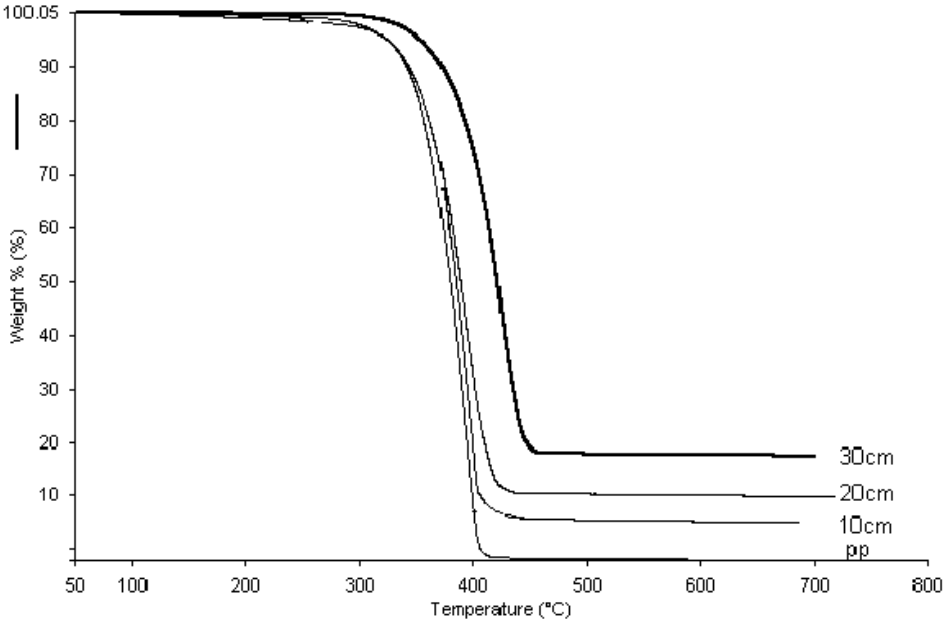

Figure 4.41 TGA curves for PP/ com. muscovite composites

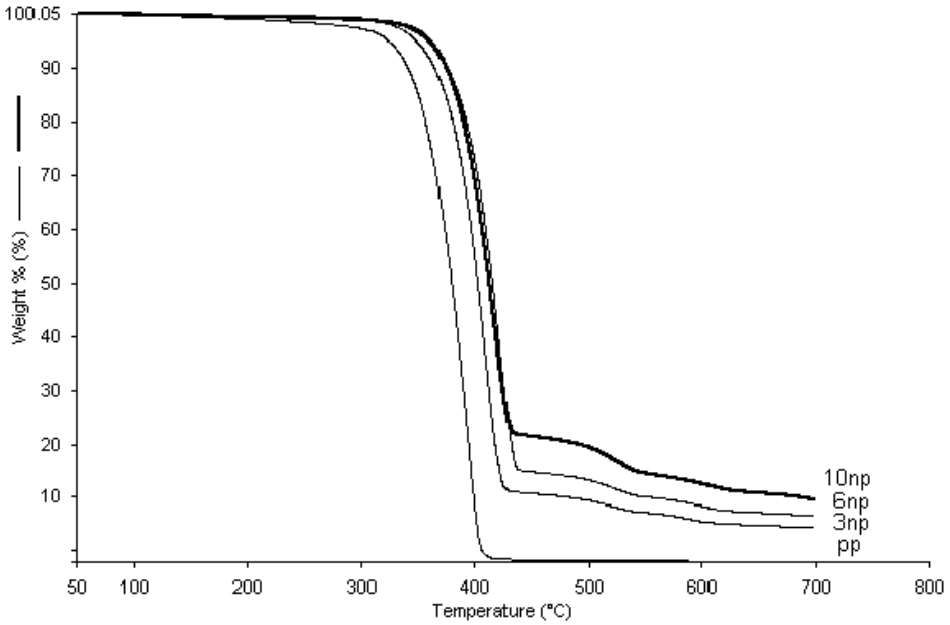

Figure 4.42 TGA curves for PP/ phlogopite nanocomposites

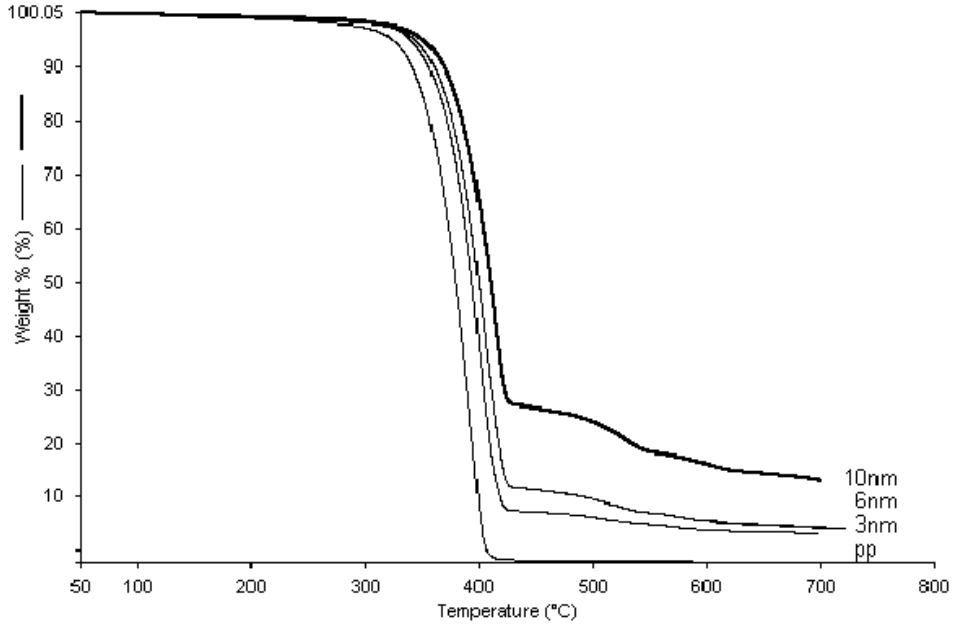

Figure 4.43 TGA curves for PP/ muscovite nanocomposites

Table 4.8a TGA data for PP/ mica composites and nanocomposites

Composition (Wt. %)	**Initial degradation temperatute (Td) (°C)**	**Temperature at maximum degradation Td_m (°C)**	**Wt. loss at Td_m (%)**
PP	353	395	98
10 cp	369	412	91
20 cp	373	413	83
30 cp	378	418	79
10 cm	370	410	90
20 cm	375	425	88
30 cm	389	427	82
3 np	379	410	87
6 np	387	417	82
10 np	388	420	74
3 nm	369	401	89
6 nm	376	404	83
10 nm	378	420	68

Table 4.8b Expected and actual weight loss for PP/ mica composites and nanocomposites

Composition (Wt. %)	**Expected wt. loss at Td_m (%)**	**Actual wt. loss at Td_m (%)**
Pure PP	-	98
10 cp	88	91
20 cp	78	83
30 cp	69	79
10 cm	88	90
20 cm	78	88
30 cm	68	82
3 np	95	87
6 np	92	82
10 np	88	74
3 nm	95	89
6 nm	92	83
10 nm	88	68

4.6.3 Dielectric Relaxation Studies

Dielectric Relaxation Spectroscopy (DRS) probes the interaction of a macroscopic sample with a time-dependent electric field. The resulting polarization, either expressed by the frequency-dependent complex permittivity and conductivity or as an impedance spectrum, characterizes the amplitude and timescale of the charge-density fluctuations within the sample. Such fluctuations generally arise from the reorientation of the permanent dipole moments of individual molecules or from the rotation of dipolar moieties in polymers. There are a few excellent reviews available on this subject.[33,34] Since the relaxation characteristics of semicrystalline polymers are highly sensitive to the crystalline morphology, dielectric relaxation spectroscopy is a potential tool to probe the molecular dynamics in the sample.

Polypropylene has excellent electrical properties like low dielectric loss factor, high volume resistivity, high surface resistivity and is extensively used in high frequency insulating applications.[35,36] The dielectric and dynamic mechanical relaxation of PP as a function of temperature is well documented. [35,37-39] Three relaxation processes have been proposed for PP i.e. a α relaxation localized around 365 K, a β relaxation localized at 280 K and a γ / β' relaxation localized at around 240 K. Though the dielectric properties of PP have been studied in some detail,[40,41] there are no reports available on the dielectric relaxation characteristics of PP/ mica composite/ nanocomposite system to our knowledge. Further, PP has a low dielectric constant, which is sometimes a drawback in applications for capacitors where size reduction is essential. By incorporation of mica which has a much higher dielectric constant than PP, it may be possible to obtain better dielectric properties i.e. high ε^1, low tan δ etc. desired for such applications. Thus, the

effect of nano-mica synthesized by in situ intercalative polymerization on the relaxation dynamics of PP were investigated and compared with that of the commercial PP/ mica composites to ascertain the utility of nanomica in enhancement of dielectric properties.

Dielectric relaxation results in the temperature range 203 K – 353 K for pure PP as well as all the PP/ mica composites and nanocomposites are plotted isochronally (fixed frequency for each curve) as dielectric loss versus temperature in the figures 4.44a to 4.52a. The time-temperature characteristics of all the relaxations observed are plotted in an Arrhenius manner for the respective samples and are presented below the isochronal plots in the figures 4.44b to 4.52b. These data are based on the maximum in the isochronal loss curves for the various samples.

Two distinct relaxations were noticed in these experiments i.e. the β relaxation at 283 K and a β′ relaxation centered at around 243 K for pure PP. The α relaxation reported in literature was not observed in this case. The loss factor in the figure 4.44a shows the usual shape, reaching a maximum whose peak position shifts to higher temperature with increasing frequency. The β relaxation is generally associated with the glass transition of the amorphous fraction of PP whereas the β′ relaxation is associated with the local motions in the amorphous phase of PP.[42] The loss factor is affected by the crystallization process. Pure PP shows a loss maximum around 283 K which shifts to 293 K with 10 wt.% commercial mica loading and 303 K at 30 wt.% mica loading, respectively. With the addition of nano-mica, the loss maximum shifts to 303 K at a very low loading of 3 wt.%. This behavior is along the expected lines. The large offset observed in the loss maximum which is actually the dielectric T_g of the material is due to the reinforcing nature of mica. Incorporation of mica in to the PP matrix results in the formation of a

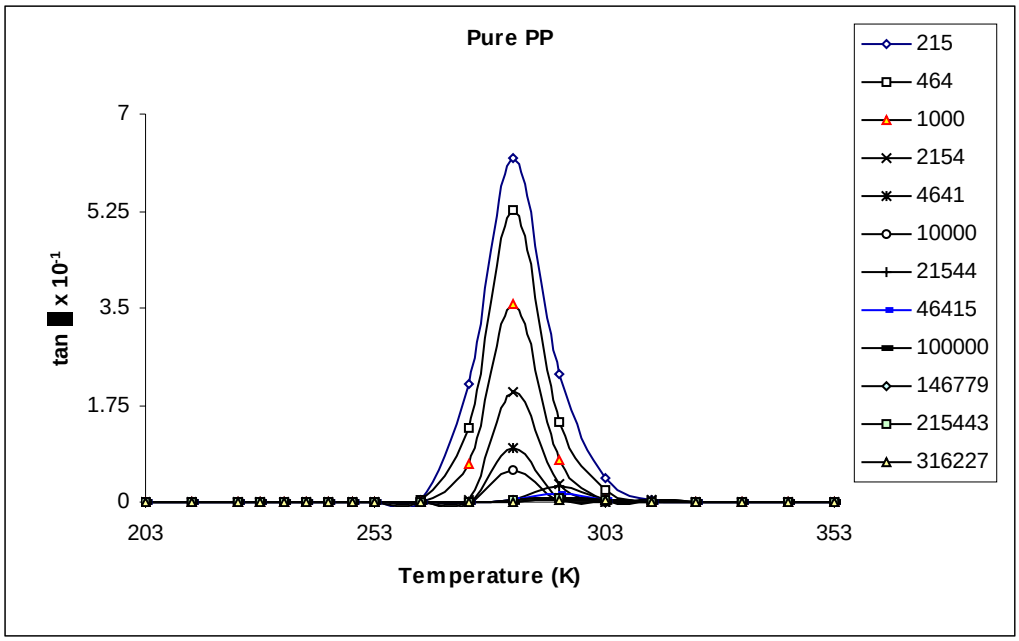

Figure 4.44a Isochron of tan δ Vs T for pure PP at various frequencies (in Hz)

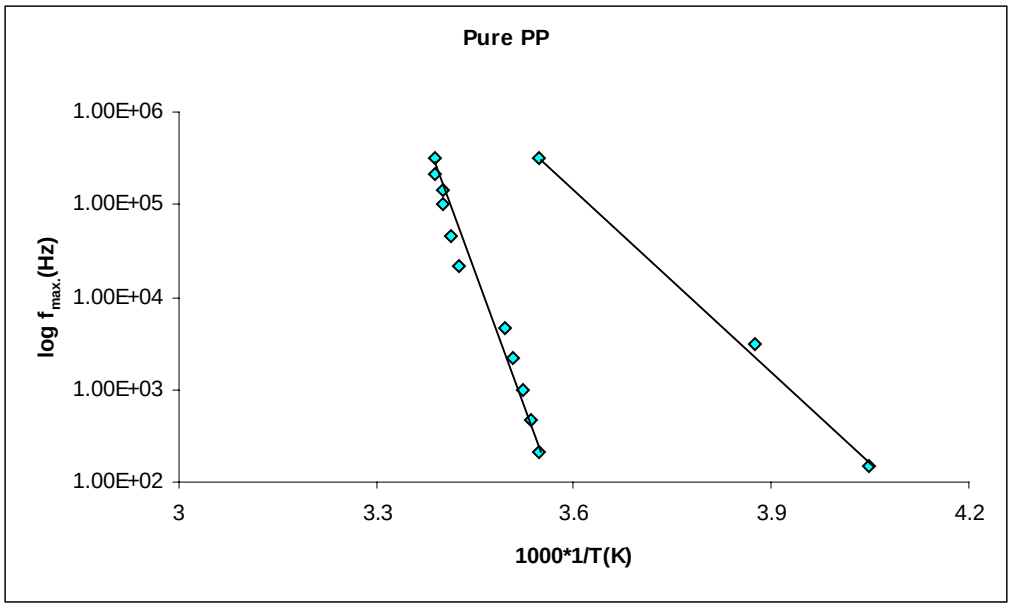

Figure 4.44b Arrhenius plot of frequency Vs reciprocal temperature for pure PP

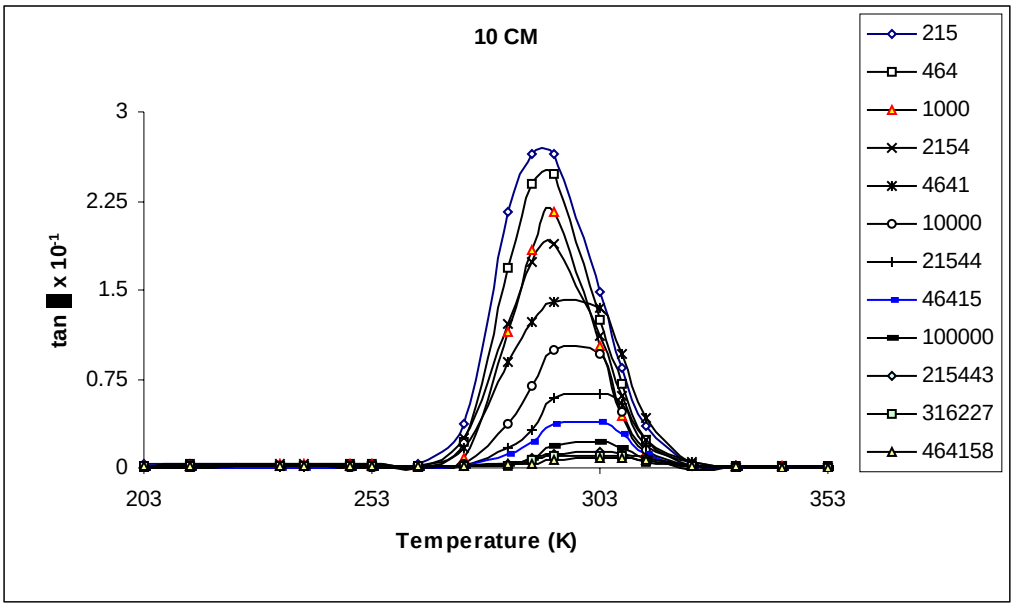

Figure 4.45a Isochron of tan δ Vs T for 10% PP/ com. muscovite (frequency in Hz)

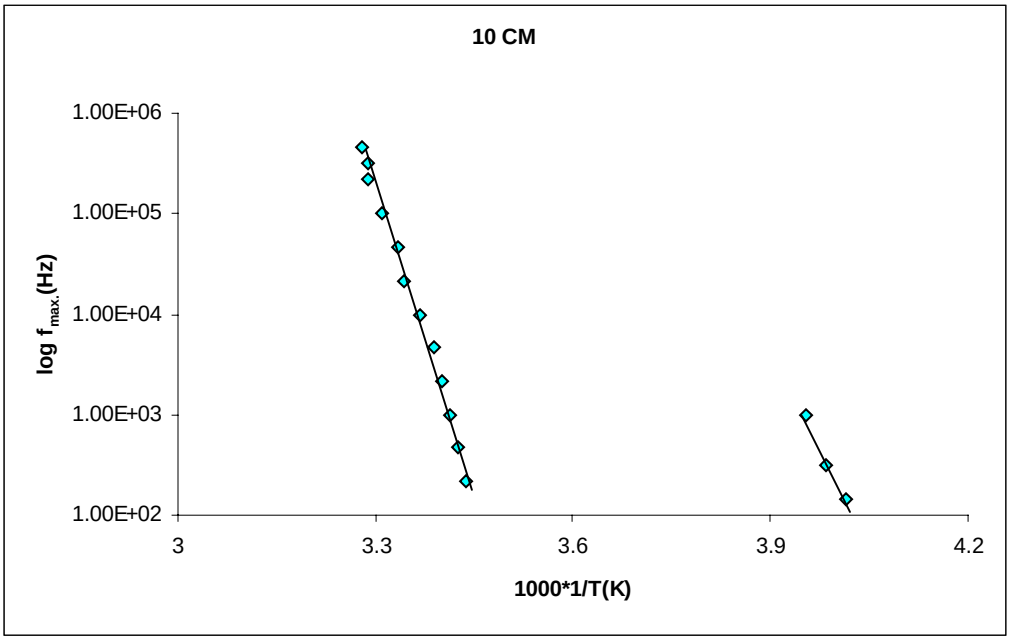

Figure 4.45b Arrhenius plot of frequency Vs reciprocal temperature for 10% PP/ com. muscovite

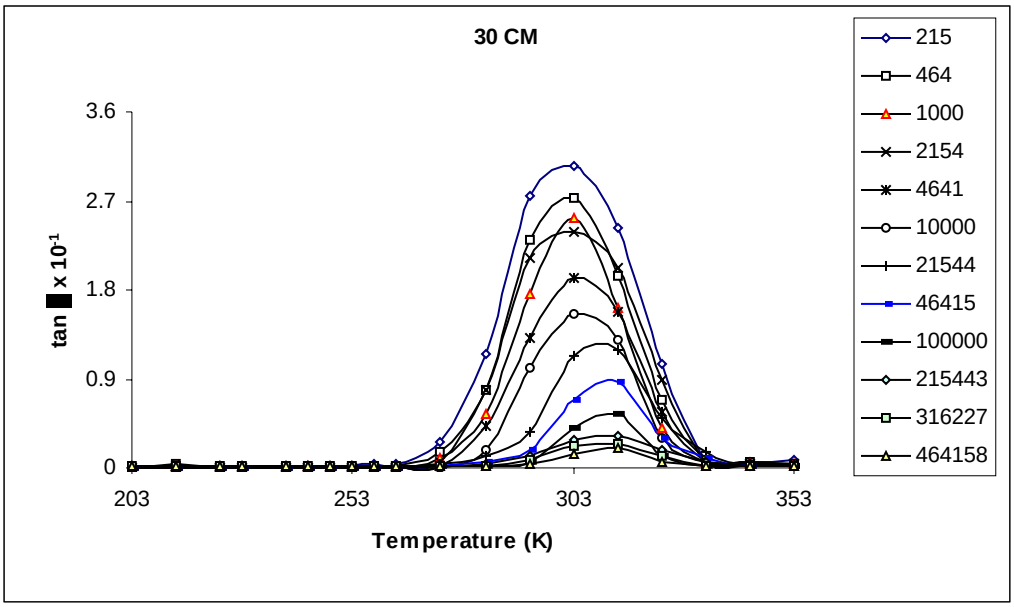

Figure 4.46a Isochron of tan δ Vs T for 30% PP/ com. muscovite (frequency in Hz)

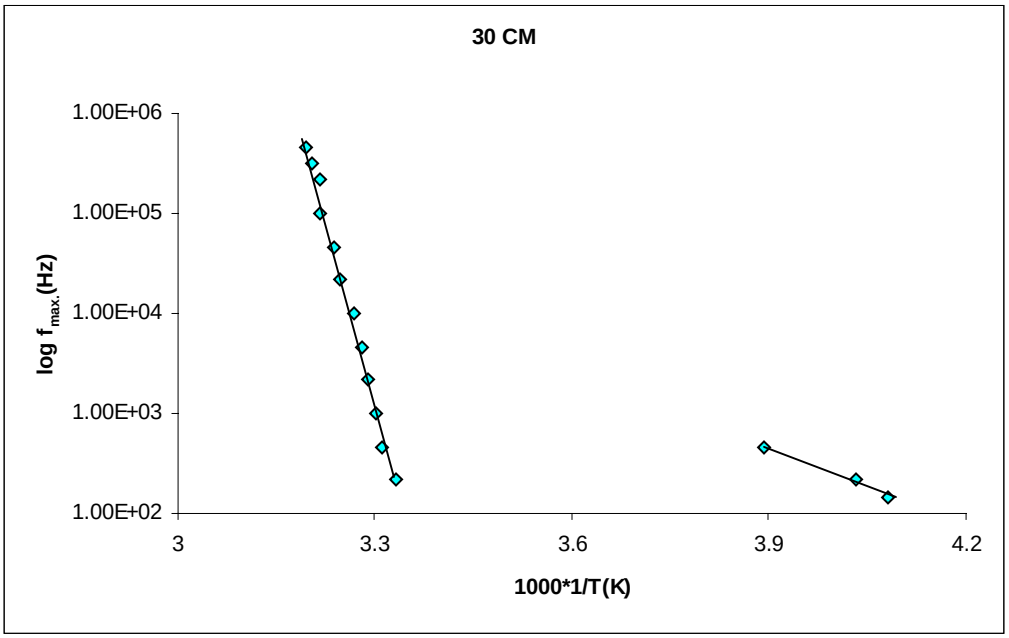

Figure 4.46b Arrhenius plot of frequency Vs reciprocal temperature for 30% PP/ com. muscovite

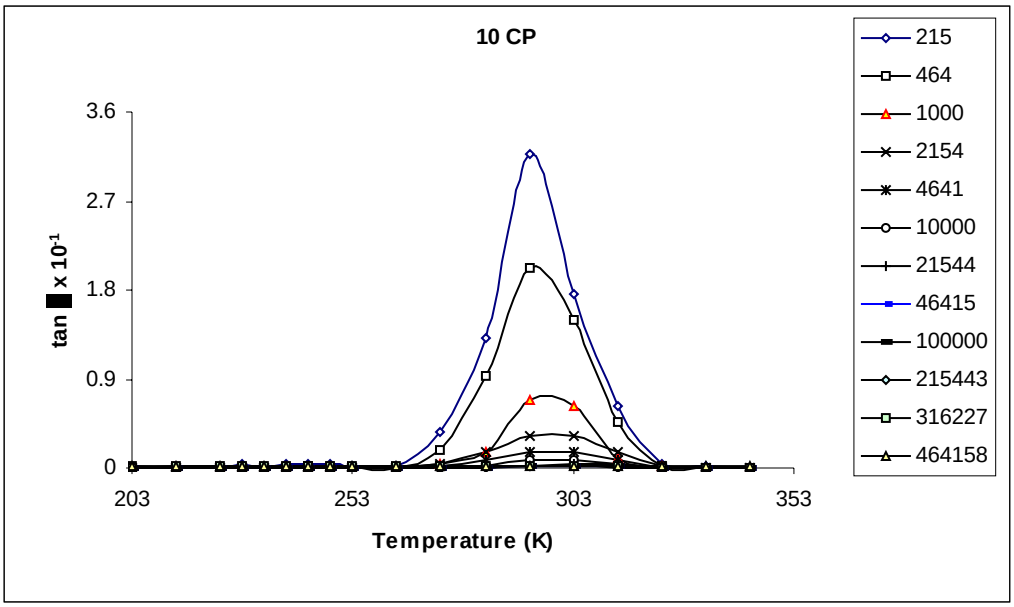

Figure 4.47a Isochron of tan δ Vs T for 10% PP/ com. phlogopite (frequency in Hz)

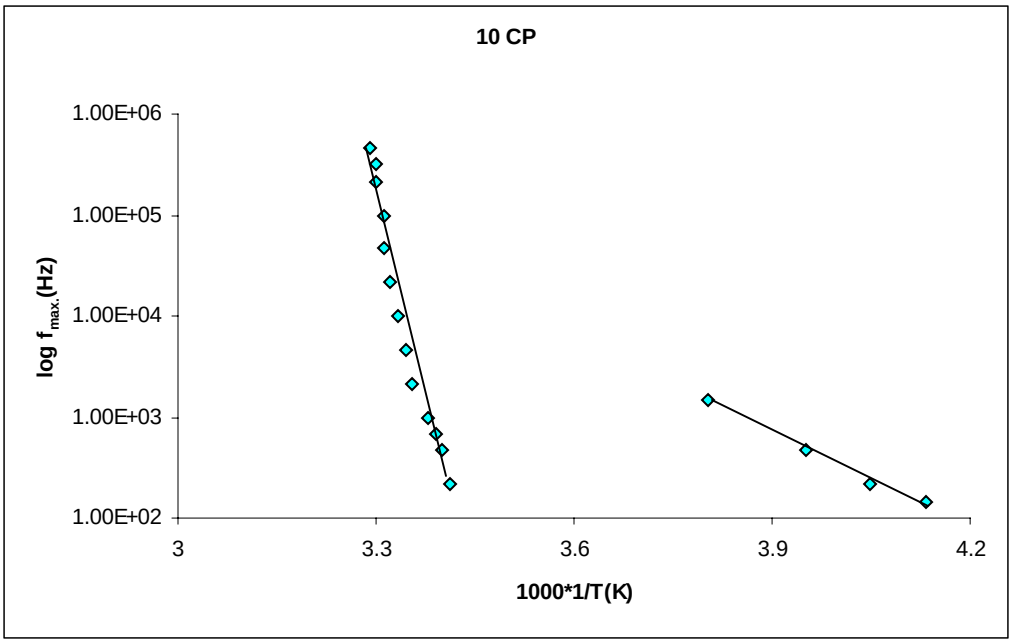

Figure 4.47b Arrhenius plot of frequency Vs reciprocal temperature for 10% PP/ com. phlogopite

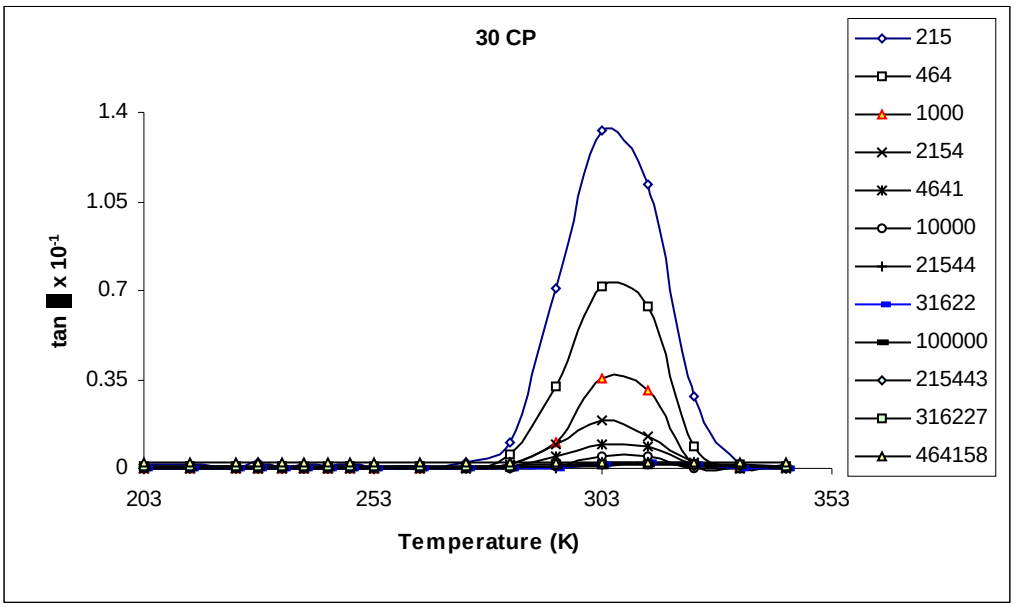

Figure 4.48a Isochron of tan δ Vs T for 30% PP/ com. phlogopite (frequency in Hz)

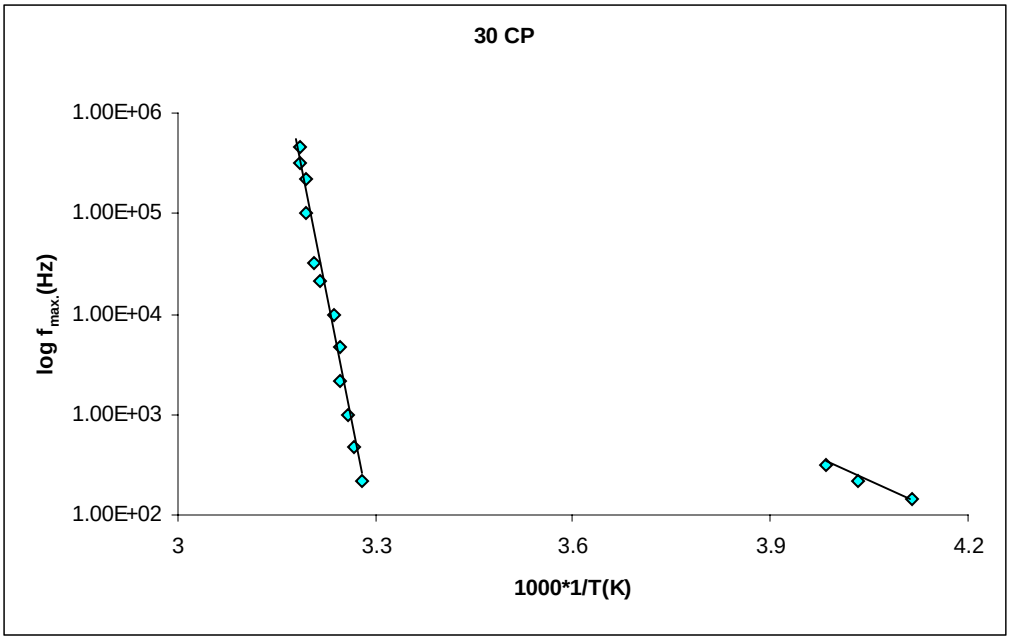

Figure 4.48b Arrhenius plot of frequency Vs reciprocal temperature for 30% PP/ com. phlogopite

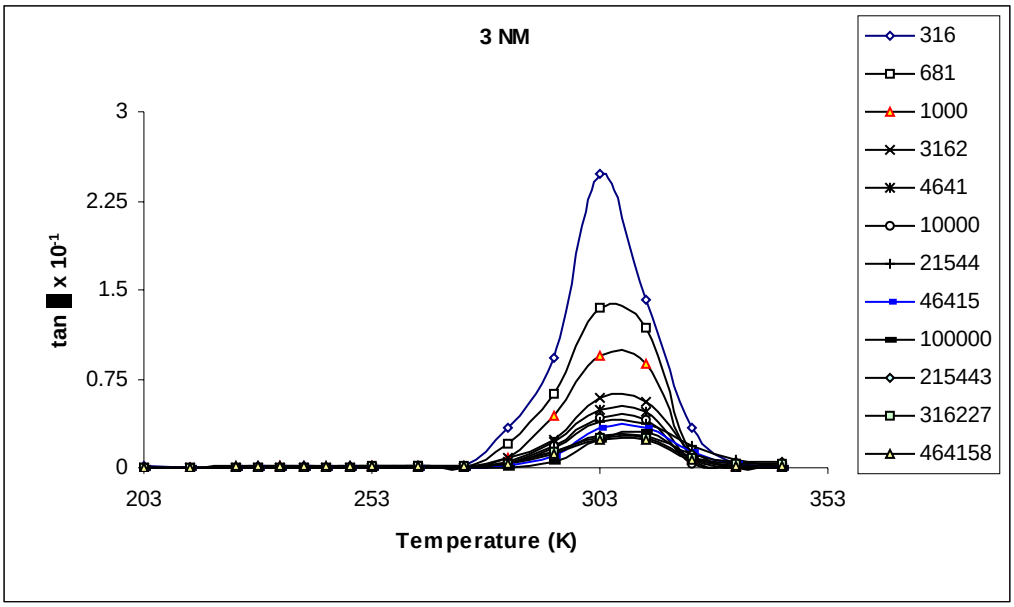

Figure 4.49a Isochron of tan δ Vs T for 3% PP/ nanomuscovite (frequency in Hz)

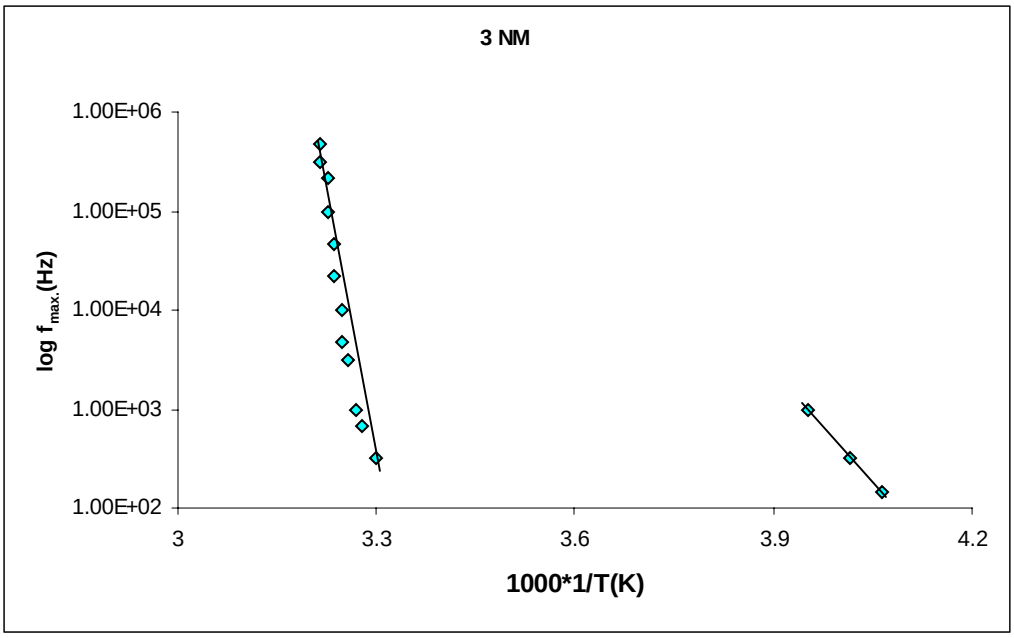

Figure 4.49b Arrhenius plot of frequency Vs reciprocal temperature for 3% PP/ nanomuscovite

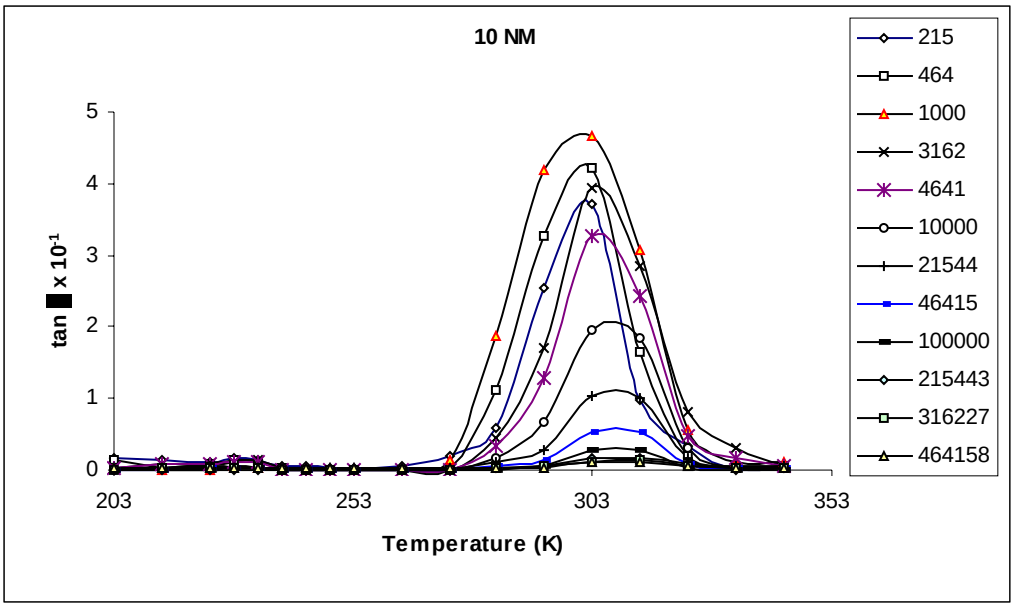

Figure 4.50a Isochron of tan δ Vs T for 10% PP/ nanomuscovite (frequency in Hz)

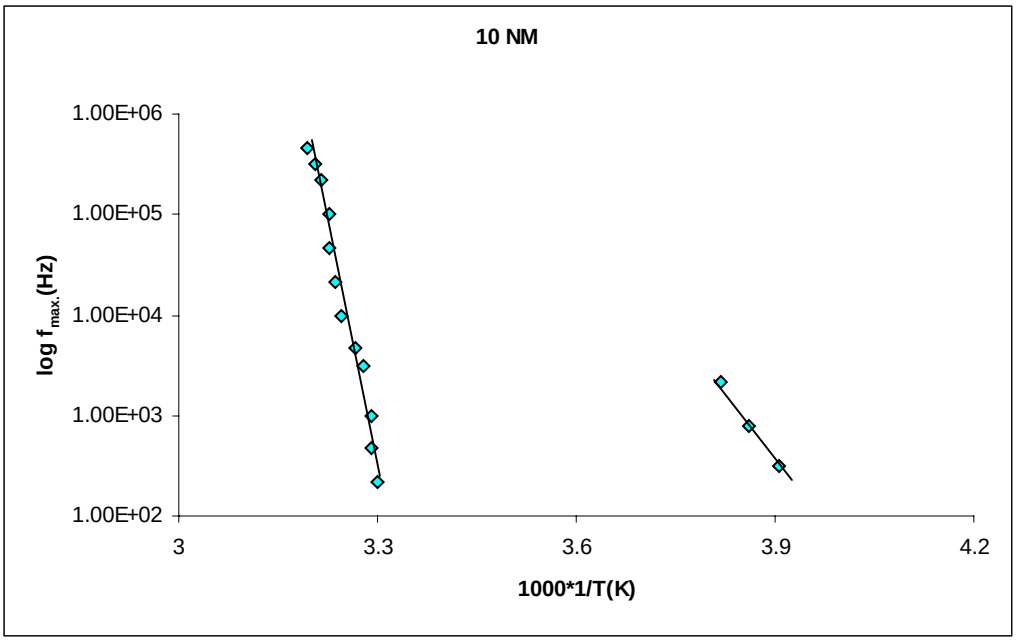

Figure 4.50b Arrhenius plot of frequency Vs reciprocal temperature for 10% PP/ nanomuscovite

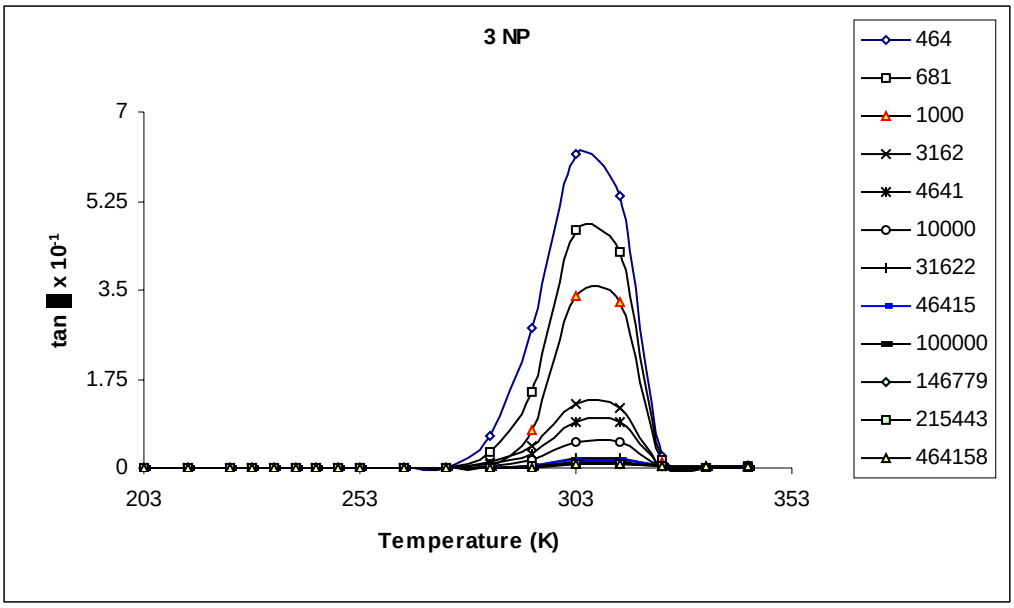

Figure 4.51a Isochron of tan δ Vs T for 3% PP/ nanophlogopite (frequency in Hz)

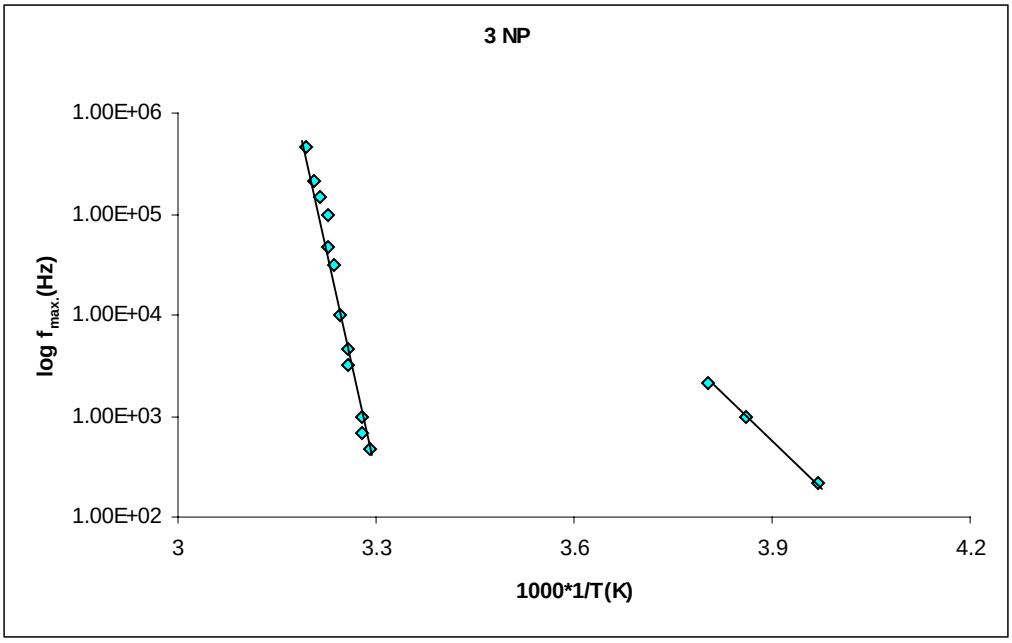

Figure 4.51b Arrhenius plot of frequency Vs reciprocal temperature for 3% PP/ nanophlogopite

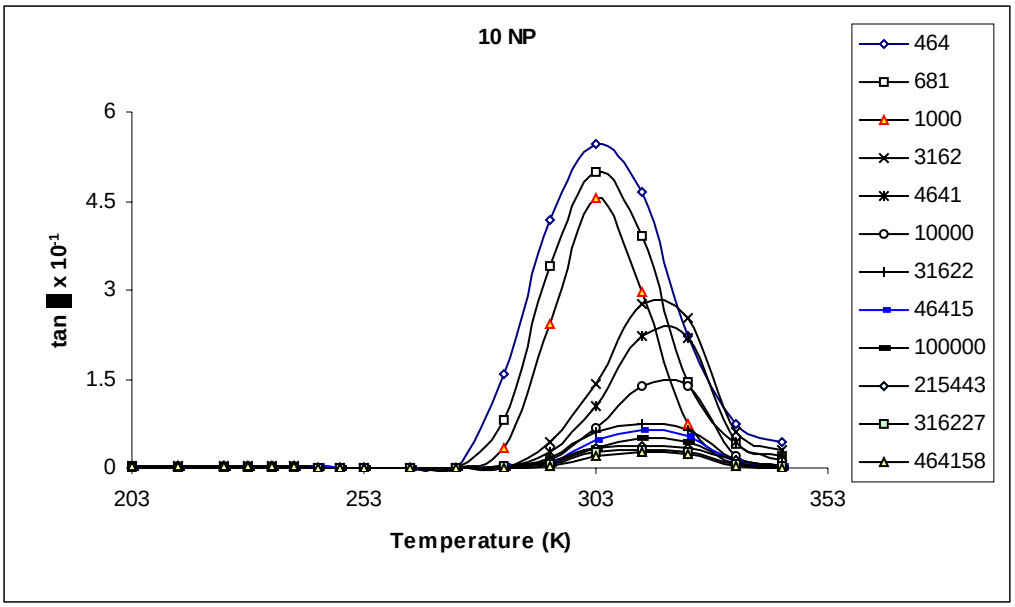

Figure 4.52a Isochron of tan δ Vs T for 10% PP/ nanophlogopite (frequency in Hz)

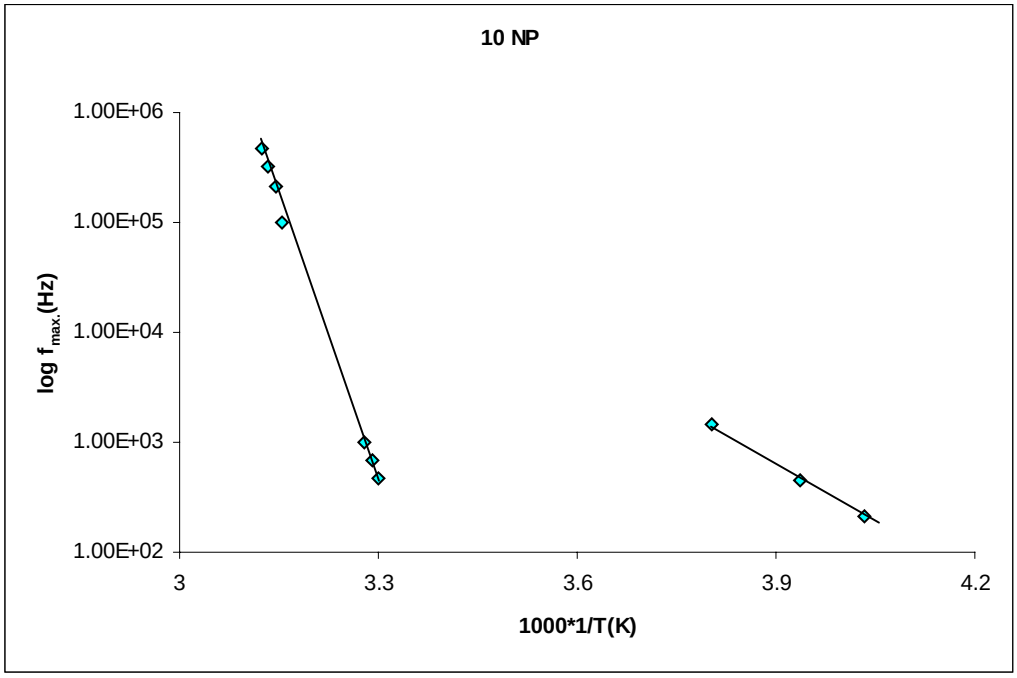

Figure 4.52b Arrhenius plot of frequency Vs reciprocal temperature for 10% PP/ nanophlogopite

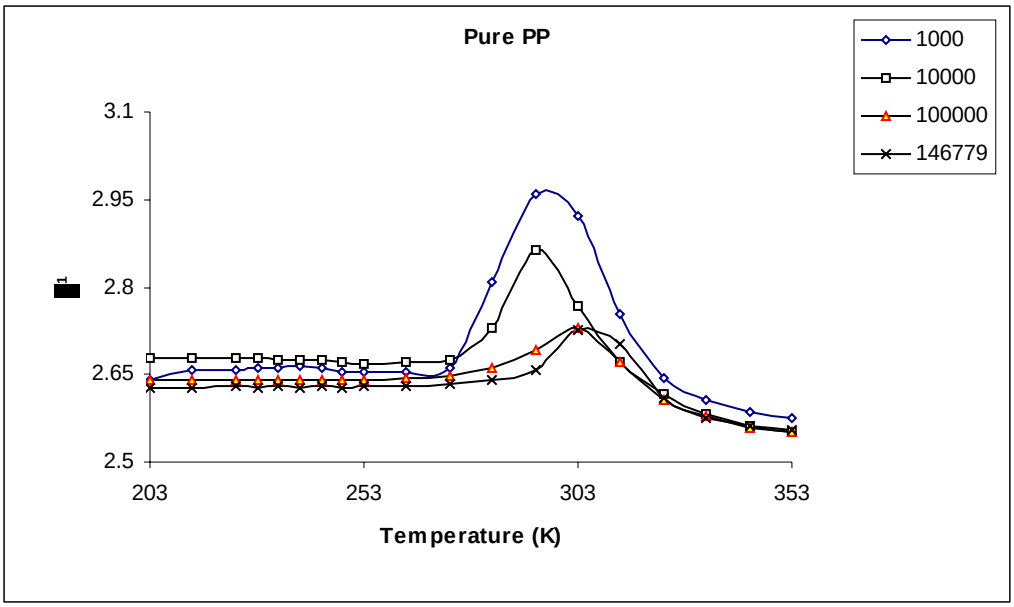

Figure 4.53 Isochron of ε^1 Vs temperature for pure PP (frequency in Hz)

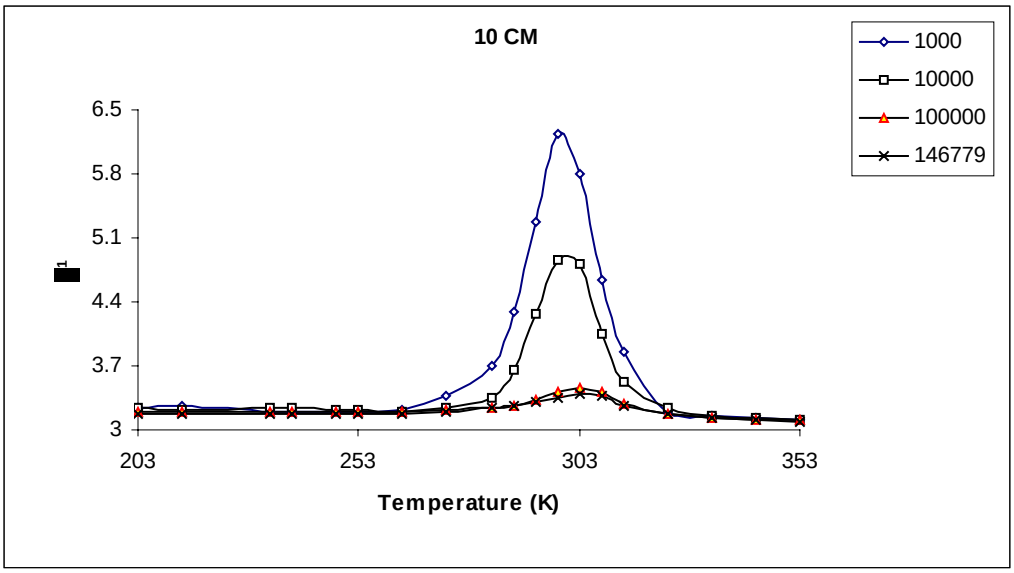

Figure 4.54 Isochron of ε^1 Vs T for 10% PP/ com. muscovite (frequency in Hz)

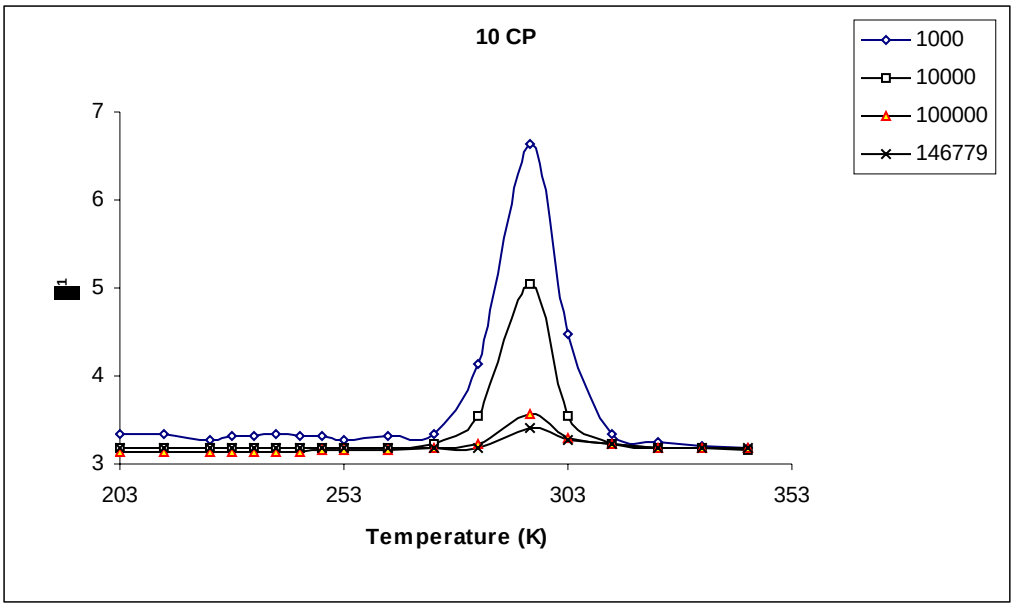

Figure 4.55 Isochron of ε^1 Vs T for 10% PP/ com. phlogopite (frequency in Hz)

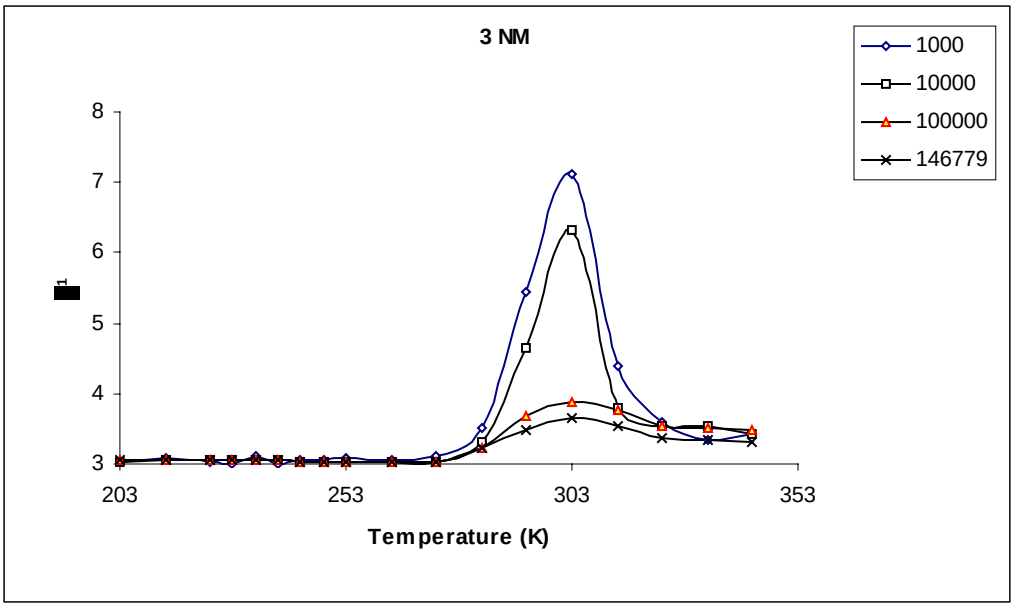

Figure 4.56 Isochron of ε^1 Vs T for 3% PP/ nanomuscovite (frequency in Hz)

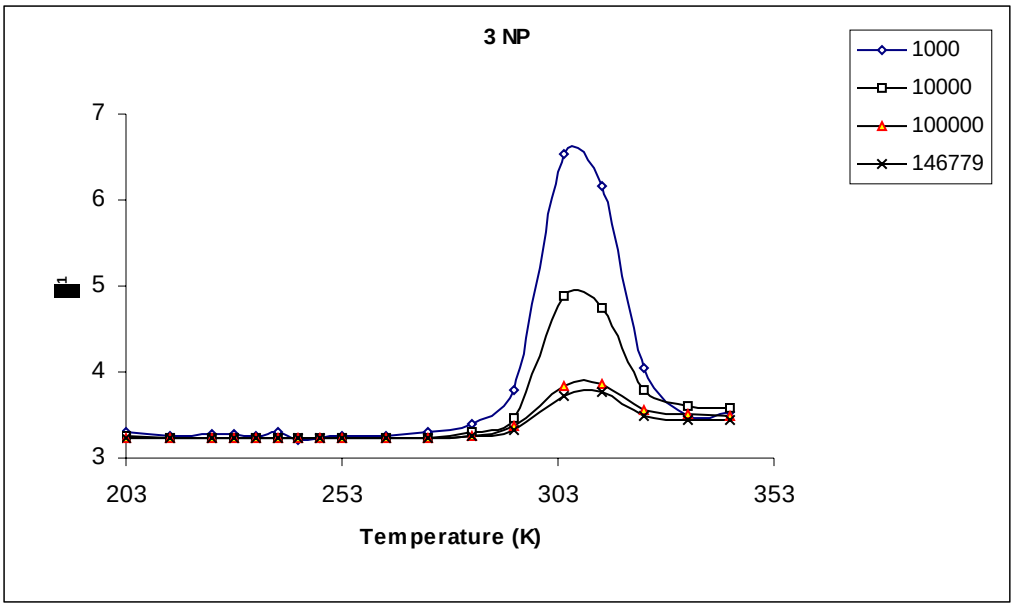

Figure 4.57 Isochron of ε^1 Vs T for 3% PP/ nanophlogopite (frequency in Hz)

rigid network which results in the increase of the dielectric T_g. Representative plots of real dielectric permittivity (ε^1) versus temperature for pure PP and the nanocomposites is given in the figures 4.53 to 4.57. The loss factor and real permittivity of the PP/ mica composites and nanocomposites is represented as a function of mica composition in the figures 4.58a and b. Commercial PP/ muscovite composite exhibits a lower dielectric constant than PP/ phlogopite composite. The dielectric constant of a composite is known to depend on the type of dispersion, orientation and the shape of the filler particles. Muscovite mica is more flaky than phlogopite and a random orientation in the PP matrix might be the reason for the lower dielectric constant of the PP/ muscovite composite inspite of the greater dielectric constant of muscovite as compared to phlogopite. The trend gets reversed in the case of the nanocomposites wherein PP/ muscovite

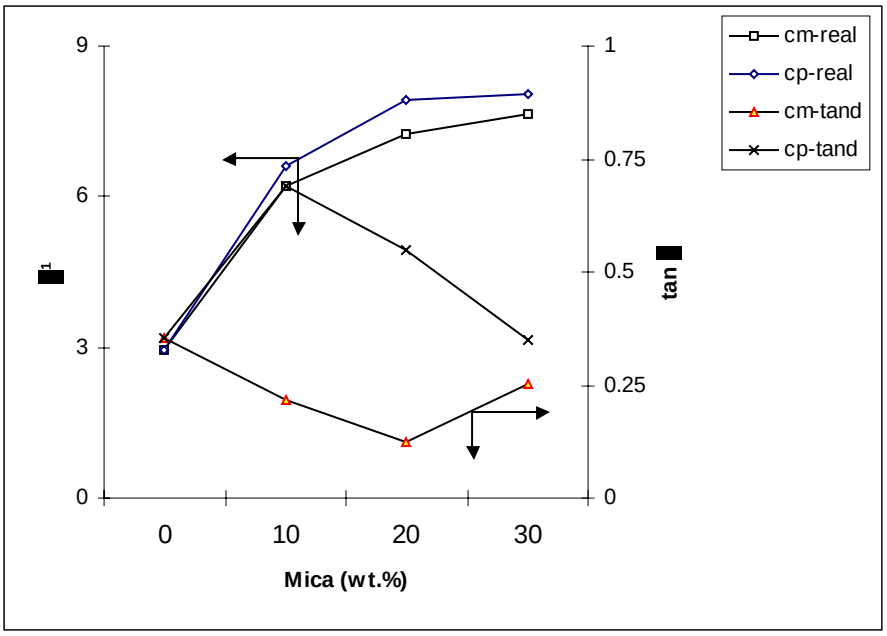

Figure 4.58a ε^1 and tan δ Vs mica loading for PP/ commercial mica composites

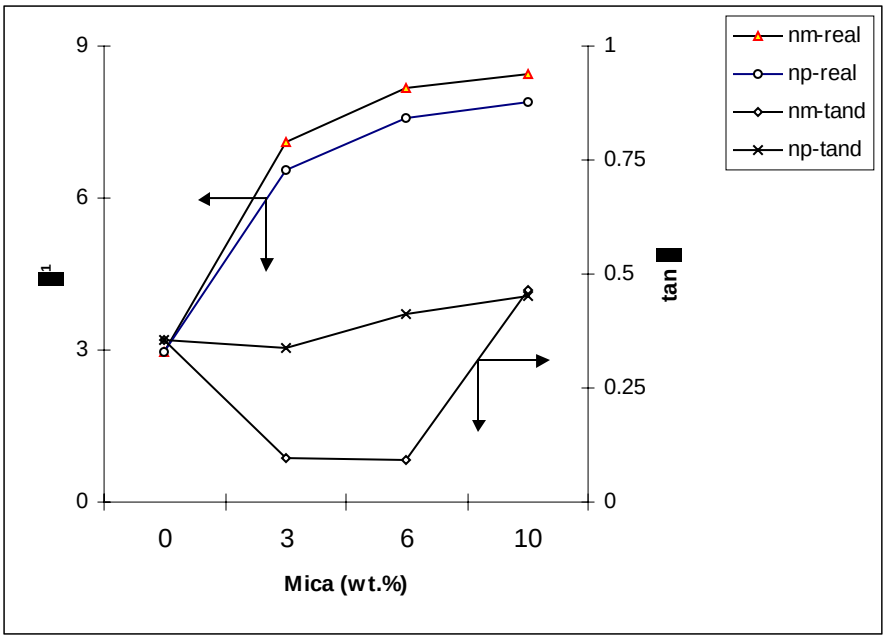

Figure 4.58b ε^1 and tan δ Vs mica loading for PP/ mica nanocomposites

nanocomposites displays a greater dielectric constant than PP/ phlogopite nanocomposites.

The net dielectric constant of a filled polymer composite depends on the dielectric constant values of individual components, volume fraction of the filler and its distribution in the matrix. The trends based on the conventional series-parallel models for muscovite and phlogopite mica are depicted in the figure.4.59. It is quite obvious that the observed

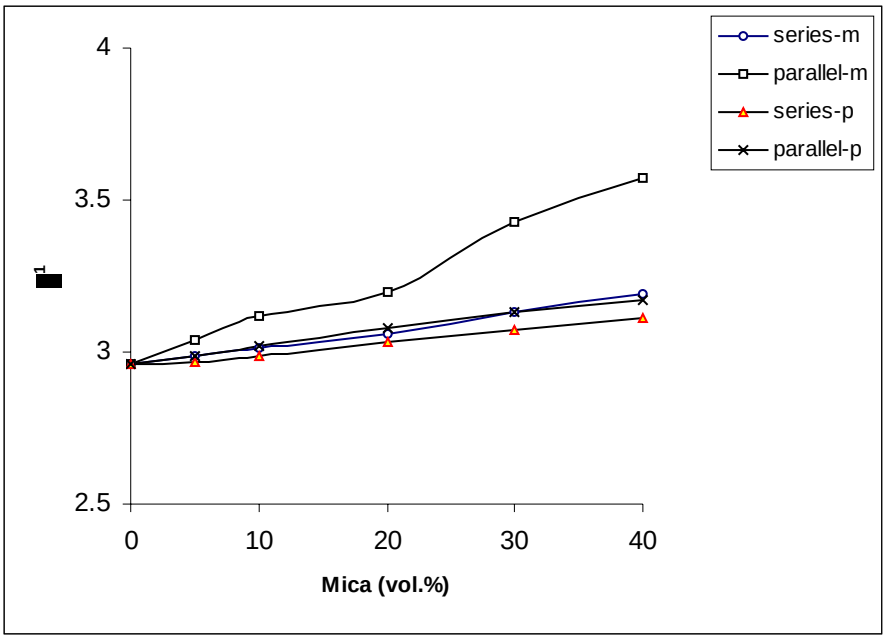

Figure 4.59 Dielectric constants of PP/ mica composites based on series and parallel model (m & p refer to muscovite and phlogopite)

values are far higher than the expected values. In the case of mica, due to the crystal structure and flaky morphology, each particle has a net dipole moment or anisotropy in dielectric constant in the three crystallographic directions. Hence, the orientation of these flakes gives rise to a higher dielectric constant value than in the randomly placed particles. Since the samples were compression molded in the present case, the particles

being flaky, the c-axis of mica would be perpendicular to the film surface, which is the direction of the applied field for DRS measurements. The net dipole moment for each particle will also be the function of number of crystallites available. The delamination in generating muscovite nanoparticles was seen to be more effective than that in phlogopite. Thus, one would expect higher dielectric constant for nanomuscovite as compared to nano-phlogopite. Moreover, nucleation of PP by mica results in a transcrystalline zone in the composites/ nanocomposites, which also contributes to the increase in dielectric constant due to greater orientation. However, this would also depend on the volume fraction of the filler, which governs the number of particles available as determined from their size.

Another striking result from these studies is the dramatic increment in the dielectric constant of the PP/ mica nanocomposites at much lower loading levels of 6 wt.

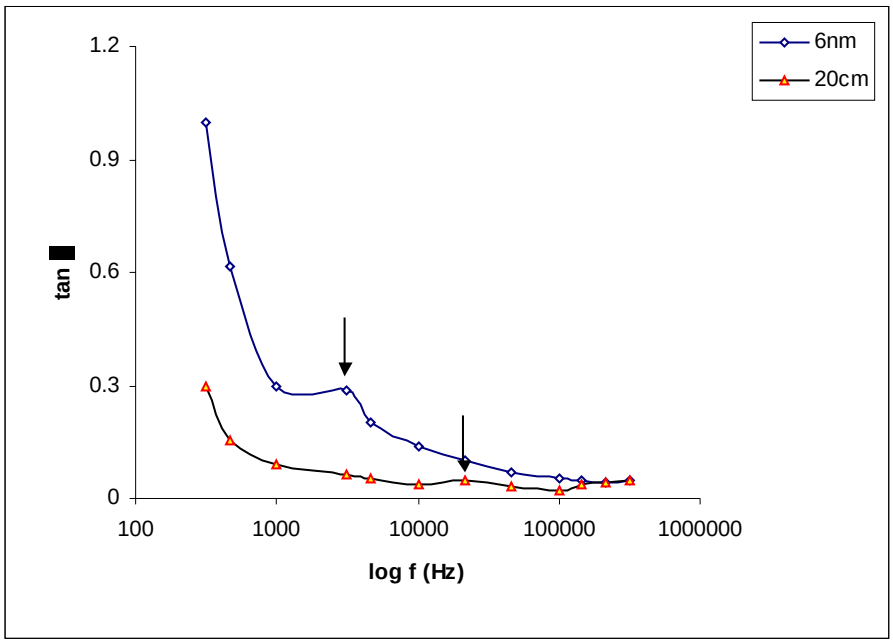

Figure 4.60 MWS effect in PP/ mica nanocomposites

% mica. 6% PP/ nano-mica shows a dielectric constant equivalent to 20% PP/ commercial mica with a significant drop in the loss factor, which could have potential applications as high performance insulators. There is also a substantial evidence of the Maxwell-Wagner-Sillars[43-45] effect in these PP/ mica nanocomposites. The MWS effect is a macroscopic build up of charges at the polymer/ filler interfaces. This occurs, when two materials with large difference in conductivity and/ or dielectric constants are subjected to an electric field. There is an apparent peak in loss factor, which is dependent on the composition, phase morphology, orientation of the phases with respect to the sample and applied field. When the dielectric loss is plotted as a function of the test frequency, MWS effect causes a shift in the dielectric loss towards lower frequencies with a concomitant increase in the tan δ value. This phenomenon is shape dependant[46,47] and is observed when the shape of the inclusion in the polymer matrix changes from a cylinder to a thin flake. Further, the aspect ratio also influences the position of the relaxation peak. This is clearly seen in the figure 4.60, which depicts the isothermal relaxation (298 K) curves for PP containing commercial and nanoparticulate mica.

The data of the loss peak maximum versus reciprocal of temperature for both the observed relaxation processes plotted in an Arrhenius manner were fit to a straight line whose slope gives the activation energies for the respective processes. The data for the β and β′ processes are tabulated in the table 4.9. The activation energy of the β process in PP, which is associated with the relaxation of the crystalline component is found to increase with the addition of mica. Similar activation energies are observed at much lower loading levels of nanomica for the β process. With increase in the mica loading, the activation energy of the β process is found to increase in both the composites and

nanocomposites. In contrast, the activation energy of the β′ process of both the composites and nanocomposites is found to decrease with increased mica loading. The reason might be the decreased amorphous phase in the composite upon mica addition, which gives a clear indication of the nucleating effect of mica in PP.

Table 4.9 Activation energies of different relaxation processes in PP

Composition (Mica wt.%)	**Activation Energy ($KJmol^{-1}$)**	
	β process	**β^1 process**
Pure PP	155.55	64.81
10 cm	205.24	120.37
20 cm	210.60	55.55
30 cm	194.44	32.40
10 cp	252.77	35.03
20 cp	281.70	30.65
30 cp	345.77	21.60
3 nm	275.46	54.58
6 nm	273.66	64.81
10 nm	311.33	78.46
3 np	291.66	60.18
6 np	300.92	50.64
10 np	185.18	37.52

4.7 Conclusions

The crystallization behavior of PP/ mica nanocomposites has been investigated in detail. Incorporation of nanomica in PP was found to decrease the induction time and crystallization half time with a concomitant increase in the growth rate resulting in smaller spherulites as compared to pure PP. It was found that the half times of the nano-phlogopite samples were lower than that of muscovite and the growth rates, substantially higher. Nanomica was found to nucleate PP and the nucleation rate was found to increase as an inverse exponential power of the particle size of mica i.e. finer mica particles were found to have higher nucleating efficiencies. Increase in the intensity of 040 peak with respect to the 110 peak in the WAXD of PP/ mica nanocomposites and a considerable shift in the T_c noticed in the DSC's of the nanocomposites reaffirmed the nucleating prowess of nanomica for the α form of PP. PP/ mica nanocomposites showed comparable crystallinity as that of 30 wt.% PP/ com. mica composites at much lower mica loadings of 3-6 wt.%. These observations were verified theoretically by lattice mismatch calculations with nano-phlogopite proving to be a better nucleator than nano-muscovite and nano-chlorite. The orientation of nano-mica particles along the flow direction and its homogeneous dispersion in the PP matrix upon processing were established by SEM.

A gradual increase in the tensile modulus of the nanocomposites was noticed up to a nanomica loading of 8-10 wt.%, which is much higher than those that have been reported previously. A gradual decrease in the % elongation as a function of mica loading was also noticed with the nanocomposites displaying a greater yield than the composites. The modulus of muscovite was found to be greater than that of phlogopite mica. Pure PP and composites with low nanomica loading were found to show yielding behavior with a

clearly observable strain whitening whereas higher mica loadings were found to show brittle fracture. The flexural modulus and strength were found to rise sharply at low nanomica loadings. Tensile and flexural properties obtainable with 30 wt.% commercial mica were attained with 6 wt.% nanomica loading.

The PP/ mica nanocomposites showed a dramatic increase in the initial degradation temperature from 353 °C for pure PP to 388 °C for 10 wt.% PP/ phlogopite nanocomposite, which establishes its thermal stability. A remarkable increase in the temperature of maximum degradation from 395 °C for pure PP to about 420-430 °C in the case of the composites and nanocomposites was observed. The % degradation of PP at the maximum degradation temperature in case of the nanocomposites was much lower than that of the commercial composites, which could be attributed to the relatively higher thermal conductivity of mica.

Two distinct relaxations were noticed in the dielectric relaxation studies i.e. the β relaxation centered at 283 K and a β′ relaxation at around 243 K for pure PP. The loss maximum was found to shift to higher temperature with increasing frequency for all the PP/ mica composites and nanocomposites. Pure PP showed a loss maximum at around 283 K, which was found to shift to 293 K with 10 wt.% commercial mica loading and 303 K at 30 wt.% mica loading. A dramatic increment in the dielectric constant of the PP/ mica nanocomposites at much lower loading levels (6 wt.%) was noticed which could be attributed to the anisotropy of mica particles, nucleation and creation of an oriented transcrystalline zone. There was also a substantial evidence of the Maxwell-Wagner-Sillars effect operating in these PP/ mica nanocomposites. The activation energy of the β process in PP was found to increase with the increase in mica loading in both the PP/

mica composites and nanocomposites whereas the activation energy of the β′ process was found to decrease with increased mica loading.

4.8 References

1) Barbe, P. C.; Lieberman, R. B. In *Encyclopedia of Polymer Science and Engineering*, 2nd edn., Wiley Interscience: New York, 1988, Vol. 13.
2) Natta, G.; Corradini, P. *Nuovo Cimento Suppl.* **1960**, *15*, 40.
3) Addink, E. J.; Bientema, J. *Polymer* **1961**, *2*, 185.
4) Turner-Jones, A.; Aizlewood, J. M.; Beckett, D. R. *Makromolekulare Chemie* **1964**, *75*, 134.
5) Keith, H. D.; Padden Jr, F. J.; Walker, N. M.; Wyckoff, H. W. *J. Appl. Phys.* **1959**, *30*, 1485.
6) Turner-Jones, A.; Cobbold, A. J. *J. Polym. Sci., Part B: Polym. Lett.* **1968**, *6*, 539.
7) Morrow, D. R.; Newman, B. A. *J. Appl. Phys.* **1968**, *39*, 4944.
8) Kardos, J. L.; Christiansen, A. W.; Baer, E. J. *J. Polym. Sci., Part A2* **1966**, *4*, 777.
9) Sauer, J. A.; Pae, K. D. *J. Appl. Phys.* **1968**, *30*, 4950.
10) Pae, K. D.; Morrow, D. R.; Sauer, J. A. *Nature* **1966**, *211*, 514.
11) Lotz, B.; Graf, S.; Wittmann, J. C. *J. Polym. Sci., Polym. Phys. Ed.* **1967**, *24*, 2017.
12) Turner-Jones, A. *Polymer* **1971**, *12*, 487.
13) Varga, J. In *Polypropylene-Structure, Blends and Composites*; Karger-Kocsis, J., Ed.; Chapman & Hall: London; 1995; Vol. 1.
14) Clark, E. J.; Hoffman, J. D. *Macromolecules* **1984**, *17*, 878.
15) Saujanya, C.; Radhakrishnan, S. *Polymer* **2001**, *42*, 6723.
16) Khare, A.; Mitra, A.; Radhakrishnan, S. *J. Mater. Sci.* **1996**, *31*, 5691.

17) Radhakrishnan, S.; Saujanya, C. *J. Mater. Sci.* **1998**, *33*, 1069.

18) Manchado, M. A. L.; Biagiotti, J.; Torre, L.; Kenny, J. M. *Polym. Eng. Sci.* **2000**, *40*, 2194.

19) Lin, Z.; Huang, Z.; Zhang, Y.; Mai, K.; Zeng, H. *J. Appl. Polym. Sci.* **2004**, *91*, 2443.

20) Valentini, M.; Biagiotti, J.; Kenny, J. M.; Santucci, S. *J. Appl. Polym. Sci.* **2003**, *87*, 708.

21) Ma, J.; Zhang, S.; Qi, Z.; Li, G.; Hu, Y. *J. Appl. Polym. Sci.* **2002**, *83*, 1978.

22) Mauritz, K.; Bauer, E.; Hopinger, A. *J. Macromol. Sci. Macromol. Rev.* **1978**, *8*, 1.

23) Xavier, S. F.; Schultz, J. M.; Fredrich, K. *J. Mater. Sci.* **1990**, *25*, 2411.

24) Xavier, S. F.; Schultz, J. M.; Fredrich, K. *J. Mater. Sci.* **1990**, *25*, 2421.

25) Karger-Kocsis, J. *Polypropylene-Structure, Blends and Composites*; Chapman & Hall: London, 1995; Vol. 1.

26) Karger-Kocsis, J. *Polypropylene-Structure, Blends and Composites*; Chapman & Hall: London, 1995; Vol. 3.

27) Karian, H. G. *Handbook of Polypropylene and Polypropylene Composites*; Marcel Dekker: New York, 1999.

28) Okuno, K.; Woodhams, R. T. *Polym. Eng. Sci.* **1975**, *15*, 308.

29) Trotignon, J. P.; Sanschagrin, B.; Piperaud, B.; Verdu, J. *Polym. Comp.* **1982**, *3*, 230.

30) Vu-Khanh, T.; Sanschagrin, B. *Polym. Comp.* **1985**, *6*, 249.

31) Chiang, W.Y.; Yang, Y. D.; Pukanszky, B. *Polym. Eng. Sci.* **1994**, *34*, 485.

32) Hull, D.; Clyne, T. W. *An Introduction to Composite Materials*, 1st ed., Cambridge University Press: New York, 1981.

33) Boyd, R. H. *Polymer* **1985**, *26*, 323.

34) Bur, A. J. *Polymer* **1985**, *26*, 963.

35) MacCrum, N. G.; Read, B. E.; Williams, G. *Anelastic and Dielectric Effects in Polymeric Solids*; John Wiley: New York, 1967.

36) Brydson, J. A. *Plastic Materials*; Butterworths: London, 1989.

37) Martin, B.; Perena, J. M.; Pastor, J. M.; De Saja, J. A. *J. Mater. Sci. Lett.* **1986**, *5*, 1027.

38) Roy, S. K.; Kyu, T.; St. John Manley, R. *Macromolecules* **1988**, *21*, 499.

39) Read, B. E. *Polymer* **1989**, *30*, 1439.

40) Umemura, T.; Suzuki, T.; Kashiwazaki, T. *IEEE Trans. Elect. Insul.* **1982**, *EI-17*, 300.

41) Banhegyi, G.; Karasz, F. E.; Petrovic, Z. *Polym. Eng. Sci.* **1990**, *30*, 374.

42) Quijada-Garrido, I.; Barrales-Rienda, J. M.; Perena, J. M.; Frutos, G. J. *J. Polym. Sci., Part B: Polym. Phys.* **1997**, *35*, 1473.

43) Maxwell Garnett, J. C. *Philos. Trans. R. Soc. Lond.* **1904**, *203*, 385.

44) Wagner, K. W. *Arch. Elektrotechnol.* **1914**, *2*, 371.

45) Sillars, R. W. *J. Inst. Elect. Eng.* **1937**, *80*, 378.

46) Van Beek, L. K. H. In *Progress in Dielectrics*; Birks, J. B., Ed.; Heywood: London, 1967; Vol. 7.

47) Pochan, J. M.; Pai, D. M. In *Plastics Polymer Science and Technology*; Baijal, M. D., Ed.; Wiley Interscience: New York, 1982.

5(A) Structure Development in Mica / PPS Nanocomposites

5.1 Introduction

Poly(phenylenesulfide) is an important high temperature semicrystalline polymer consisting of *para*-phenylene units alternating with sulfide linkages. Although Grenvesse[1] is credited with its first synthesis in 1898, the interest in PPS increased in 1948 when Macallum[2] described the preparation of PPS by the melt reaction of *p*-dichlorobenzene with sodium carbonate and sulfur. PPS became a commercial reality on subsequent value additions by Lenz[3-5], Edmonds and Hill[6]. The crystal structure of PPS was delineated by Tabor et al.[7] who assigned an orthorhombic unit cell with the dimensions a = 8.67 Å, b = 5.61 Å, and c = 10.26 Å. The cell comprises four monomer units, with two polymer chains passing through it. It has a T_m of about 285 ºC, T_g around 85 ºC and has no known solvents below 200 ºC, α-chloronapthalene being the solvent used to solubilize PPS above 200 ºC.[8]

Some of the exceptional characteristics of PPS are

- Outstanding resistance to high temperatures
- Excellent chemical, oil, fuel and solvent resistance
- Precision moldability and excellent dimensional stability
- Great affinity for a variety of fillers and reinforcing agents
- Good stiffness and rigidity
- Attractive balance of physical, mechanical and electrical properties
- Competitive price

This unusual combination of properties translates in to excellent applications like use in pump impellers, ball valves, wear rings, electrical sockets, battery and telephone

components, chip carriers, optical-fiber cables, electronic component encapsulants, and as a thermoplastic matrix for composite materials. PPS is also known to undergo curing reactions upon heating in presence of air that has tremendous implications in the coating industry.

The semicrystalline nature of PPS makes it suitable for accurate studies of its structural and physical properties. Considering that the final properties of the polymer are simple manifestations of the crystallinity changes in the polymer network, the study of crystallization behavior of polymers under different conditions is of paramount importance. The crystallization behavior and structure development of PPS has been explored in great detail over the past three decades. The crystallinity of PPS and its effects on the ensuing properties were investigated in a pioneering study by Brady[9] wherein he found that the flexural modulus, HDT, density and enthalpy of melting tend to increase with a decrease in the flexural/ tensile strengths upon annealing at 260 ºC for 1.5 hours. The rates of overall bulk crystallization of unfilled and glass-fiber reinforced PPS were investigated by Jog and Nadkarni[10] using DSC. They observed the maximum crystallization rate at 170 ºC and found that at a given temperature, the glass-fiber reinforced PPS crystallized at faster rates than unfilled PPS, which was ascribed to the heterogeneous nucleation in filled PPS. The effect of molecular weight, chain branching and chemical nature of the end group counter atom on the crystallization kinetics of PPS were studied by Lopez and Wilkes[11-13] with DSC and optical microscopy. Increasing molecular weights were found to decrease the crystallization rates and the kinetics was found to follow the Avrami equation[14-16] for bulk crystallization. In a later study, the effect of molecular weight fractionation and end group counter ion on the nucleation

density, crystalline growth ratio and bulk crystallization of PPS by DSC, POM, SALS and WAXD were considered by the same authors who found that higher molecular weights resulted in lower crystallinities.[17] The non-isothermal crystallization behavior of PPS has also been investigated by Lopez and Wilkes[18] which was followed by means of the Ozawa equation[19]. The modification of surface structure and crystallinity in compression molded PPS were reported by Radhakrishnan et al.[20] and explained on the basis of plastic deformation and flow during the high pressure molding process. The same author has also reported on the powder processing of PPS blends[21] and the effect of curing on the internal structure of PPS coatings[22]. The non-isothermal crystallization kinetics of PPS/ Vectra-B950 blends have been investigated by Minkova et al.[23] who found that there was a marked increase in the rate and temperature of crystallization upon the addition of 2-50% of Vectra-B950. The type of nucleation and crystal growth geometry were not found to change appreciably. The crystallization kinetics of PPS/ LCP blends have been studied by Gabellini et al.[24] who had found that PPS forms a transcrystalline columnar layer around the LCP fibrils in an earlier study[25]. The crystallization behavior of PPS in blends with HDPE and PET have been explored by Jog et al.[26] The isothermal crystallization studies had showed that PPS crystallization was accelerated in PPS/ PET blend whereas it was retarded in PPS/ HDPE blends. The non-isothermal crystallization of PPS in presence of molten crystalline PA6 was studied by Mai et al.[27] who found that the crystallization peak gets narrower and the crystallization temperature of PPS increases in presence of PA6. The crystallization and melting behavior of PPS/ PES blends have been studied by Shibata et al.[28] They found that the crystallization of PPS was accelerated in the presence of 10 wt.% PES whereas it got

retarded at higher loadings. The single stage[29] and multiple stage[30] melt crystallization of PPS have been reported by Cheng et al. The effects of a magnetic filler Nd-Fe-B on the crystallization of PPS has been explored by Guschl et al.[31] who found that the crystallization parameters were strongly affected by particle size and presence of coupling agents. PPS crystallization has also been reported by Caminiti et al.[32] and Silvestre et al.[33] The advances in the chemistry of PPS have been reviewed by Lopez et al.[34] and more recently by Cebe,[35] respectively.

Though a wealth of information is available on blends of PPS with other thermoplastics, the effect of mica/ nano-mica per se on PPS crystallization and structure development has not yet been reported. This study assumes a lot of significance considering that enhanced crystallinity at the matrix/ mica (high aspect ratio filler) interface could create reinforcement sites leading to appreciable property enhancements. Thus, the structure development and crystallization characteristics of mica/ PPS nanocomposites constitute the focus of work in this section.

5.2 Experimental

(a) Preparation of the Nanocomposite

The commercial PPS/ mica composites and PPS/ mica nanocomposites were prepared by powder blending the commercial mica/ nano-mica with Ryton V-4 grade PPS in an agate mortar. The compositions of the PPS/ mica composites was varied from 5, 10, 20, 30 up to 40 wt. % of mica whereas that of PPS/ mica nanocomposites was varied from 1, 3, 5, 7, 10, 15 up to 20 wt. % of nano-mica. The particle size of nano-phlogopite taken was 19 nm and that of nano-muscovite was 27 nm. To study the effects

of annealing on PPS/ mica composites and nanocomposites, the powder blended PPS/ mica samples (0.3 g) were pelletized using a single end compaction die at a pressure of 3 tonnes for 2 minutes to obtain thin discs (12 mm diameter, 2mm thickness). These pellets were then annealed at 250 °C for 1.5 hrs and analyzed by WAXD.

(b) Melt Crystallization for Structure Development

The PPS/ mica pellet was placed in between two teflon sheets, heated on a hot plate set at 300 ºC for 5 minutes after which it was transferred on to another hot stage maintained at 250 ºC and crystallized isothermally for 90 minutes. Later, the sample was quenched in cold water, dried and analyzed by WAXD for structure development.

The crystallization characteristics of the PPS/ mica nanocomposites were monitored by DSC of the melt crystallized and annealed samples.

5.3 Results and Discussion

The structure development and crystallization behavior of PPS/ mica nanocomposites was addressed in a different manner as compared to those which are reported in literature. Pellets of PPS/ mica composites and nanocomposites prepared from the powder blends were annealed at a temperature of 250 ºC for 2 hours. The WAXD profiles before and after annealing gives an idea of the extent to which the PPS crystallites get reorganized in the presence of mica and nano-mica particles. The WAXD plots of the melt crystallized samples (T_c-250 ºC) and the DSC's were also obtained to study the structure development upon melt crystallization. One of the very noteworthy observations in the present study was the dramatic change in the intensities of the peaks

corresponding to the 200(2θ = 20.56) and 110(2θ = 18.86) planes of PPS, respectively upon annealing. These are depicted in the figures 5.1a and b for PPS/ mica and PPS/ nano-mica, respectively before and after annealing. The 200/ 110 ratio in general, was found to reduce on increased mica loading and the intensity of the 200 peak found to increase upon annealing. From the results, we can surmise that annealing in presence of both muscovite and phlogopite reorients many crystallites of PPS along the 200 plane. Also, the ratio falls steeply for phlogopite as compared to muscovite and also for commercial mica as compared to nano-mica as seen in the figures. This study assumes a lot of significance in the context of virgin PPS being considered inappropriate for high strength applications because of its low impact strength. But, PPS composites are found to possess substantial strength when mixed with inorganic fillers. The semicrystallinity of PPS is believed to enhance crystallization at the matrix/ filler interface thereby creating reinforcement sites as others have reported for similar composite systems.[36-38] The surface of the filler particle acts as an active site on which the polymer chains can easily adhere, allowing other chains to initiate an ordered crystalline structure around the particle. Due to the relatively high surface area of mica, the crystallization characteristics of PPS are dramatically altered.

The intensity ratios of the 200/ 110 peaks for melt crystallized PPS/ commercial and nano-mica samples are represented in the figures 5.2a and b, respectively. In this case, we find that there is an increase in the intensity ratio at lower mica loadings, which drops down at higher loadings. This is realized at 5 wt.% loading for commercial micas whereas it is seen at 7 wt.% for the nano-micas. Here again, we find that the ratio falls steeply for phlogopite mica as compared to muscovite and for commercial mica as

compared to the nano equivalent. The origin of this behavior is not very clear and it could be speculated to be a function of the mica distribution and orientation in the samples.

Another interesting feature in these studies is the variation in the intensities of the two major mica peaks (003 and 020 peaks of phlogopite; 009 and 006 peaks of muscovite). The I_{003} / I_{020} ratio of phlogopite and I_{009} / I_{006} ratio of muscovite composites and nanocomposites are represented in the figures 5.3a and b. The ratios for the melt crystallized samples are given subsequently in the figures 5.4a and b. It is seen that the intensity ratio decreases for both phlogopite and muscovite mica composites/ nanocomposites upon sintering. This suggests that many crystallites of phlogopite get oriented along the 020 plane and that of muscovite along the 006 plane during sintering. The ratio is found to increase with increased loading levels of mica. Also, commercial and nano-phlogopite show a greater intensity as compared to muscovite. In the case of the melt crystallized samples, muscovite samples show a greater intensity as compared to phlogopite samples.

The reason for the difference in the two cases might have its origin in the temperature cycle of the respective sintering and melt crystallization processes, which is depicted in the figure 5.5. In case of sintering, the sample is brought to the sintering temperature of 250 ºC gradually from room temperature whereas the melt crystallized sample is brought to the T_c from the melt temperature of 300-310 ºC. Also, the melt crystallized sample is quenched suddenly in cold water due to which it has a lower crystallinity as compared to the sintered sample.

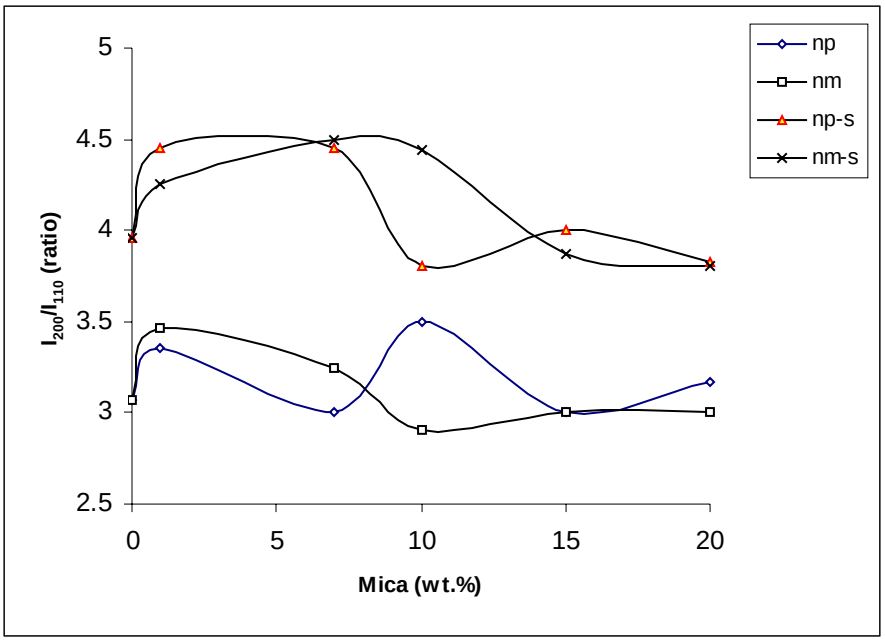

Figure 5.1a I_{200} / I_{110} ratios for PPS/ commercial mica samples before and after sintering

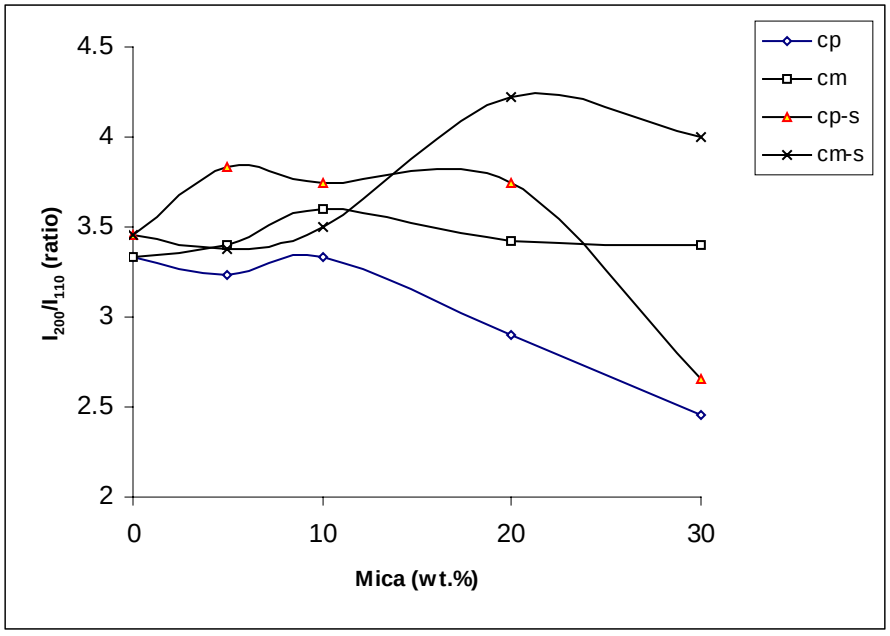

Figure 5.1b I_{200} / I_{110} ratios for PPS/ nanomica samples before and after sintering

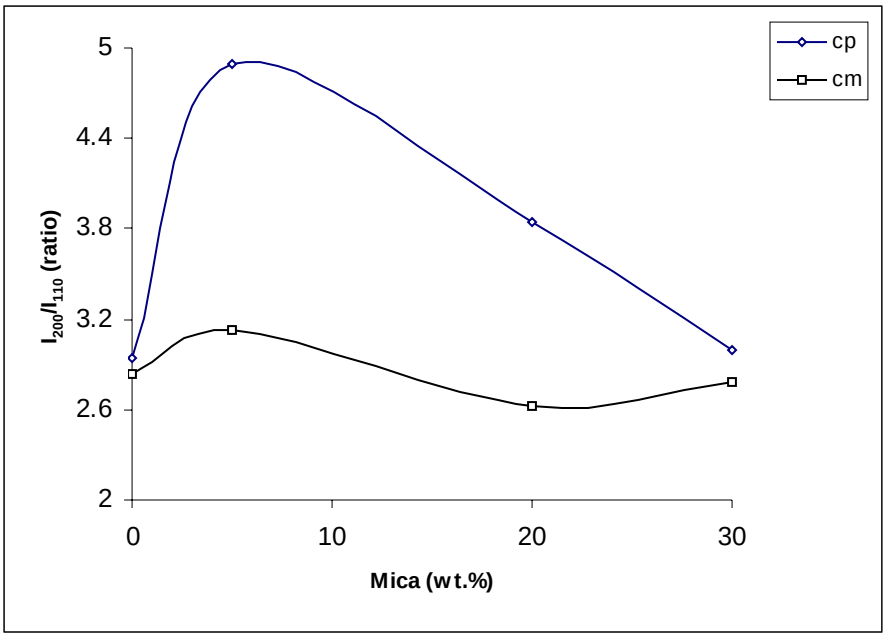

Figure 5.2a I_{200} / I_{110} ratios for PPS/ commercial mica samples upon melt crystallization (T_c-250 ºC)

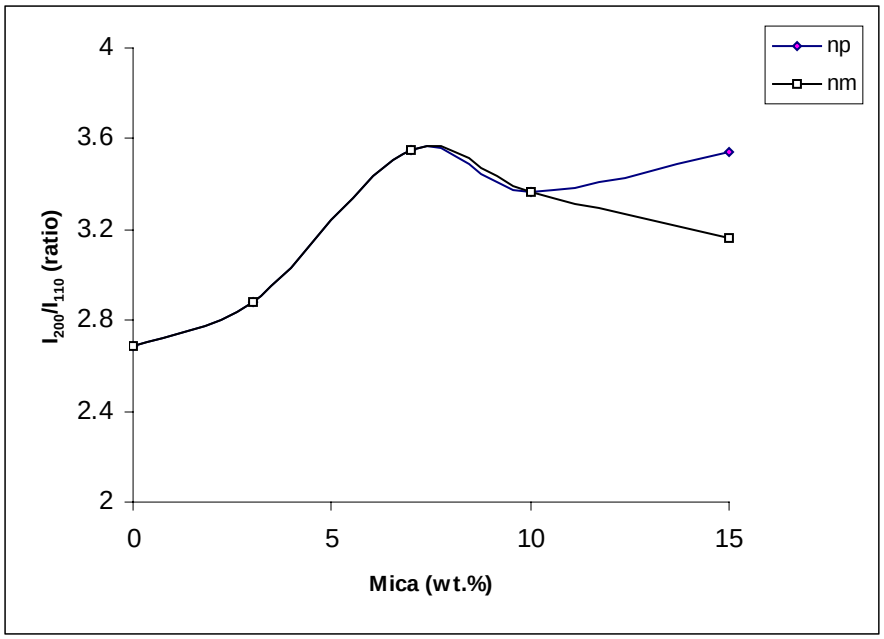

Figure 5.2b I_{200} / I_{110} ratios for PPS/ nanomica samples upon melt crystallization (T_c-250 ºC)

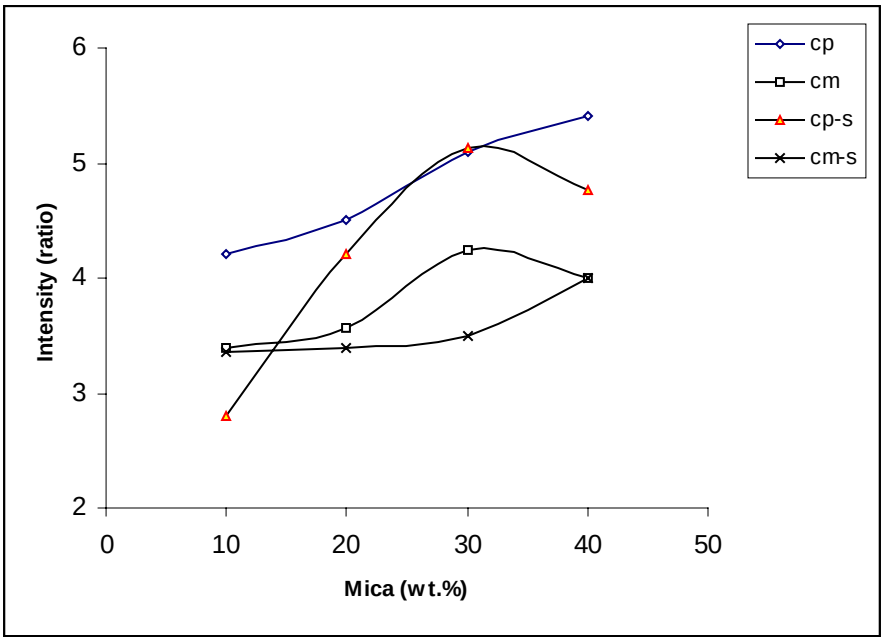

Figure 5.3a Intensity ratios of major mica peaks for PPS/ commercial mica samples before and after sintering

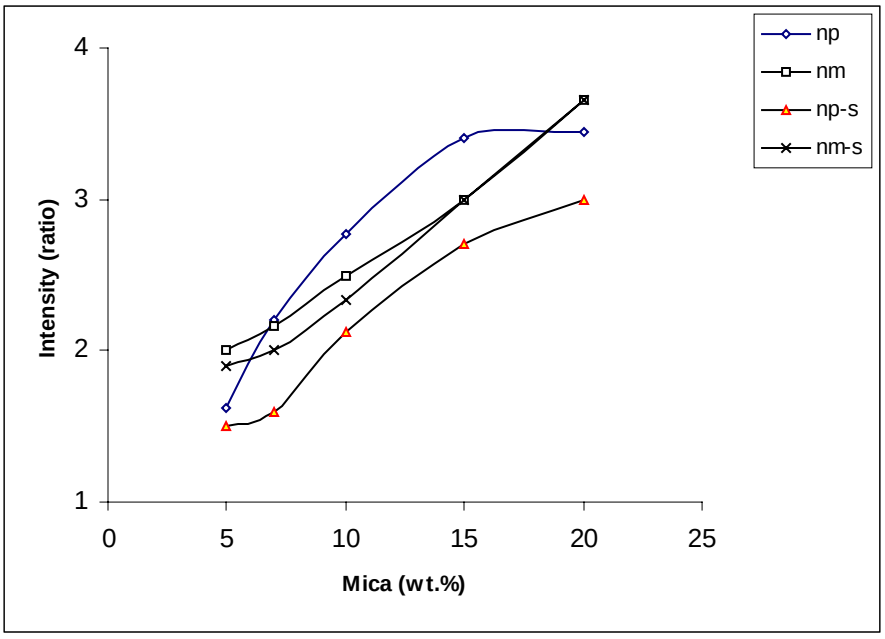

Figure 5.3b Intensity ratios of major mica peaks for PPS/ nanomica samples before and after sintering

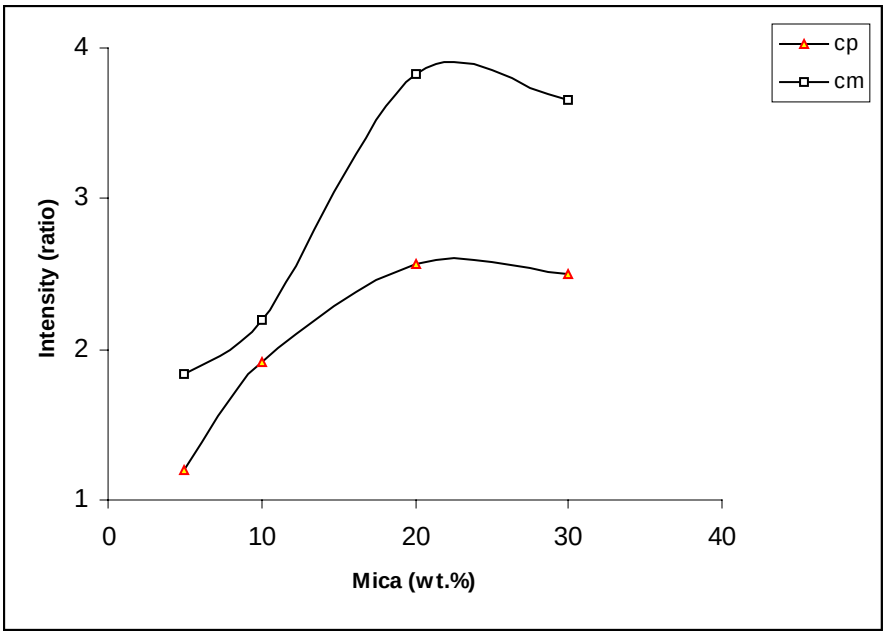

Figure 5.4a Intensity ratios of major mica peaks for PPS/ commercial mica samples upon melt crystallization (T_c-250 ºC)

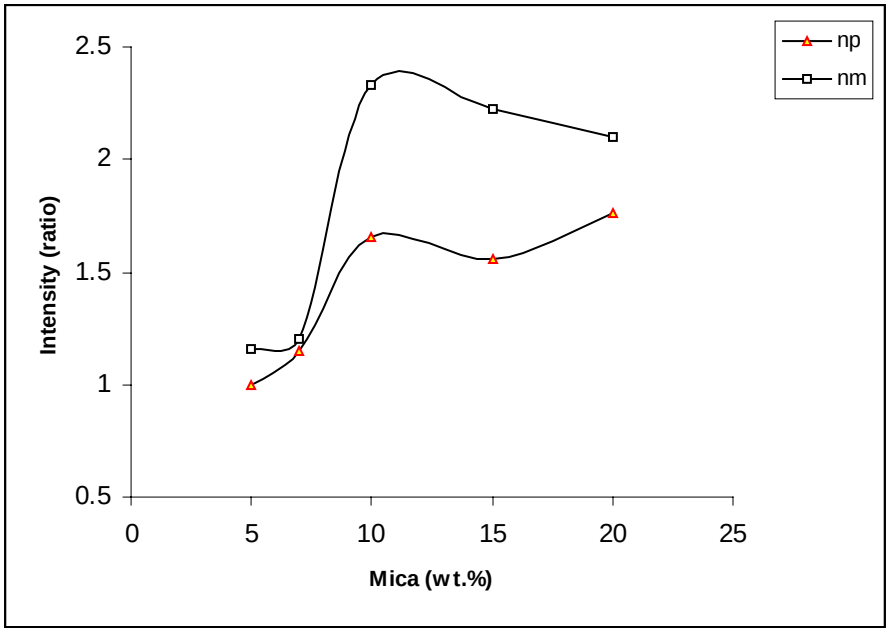

Figure 5.4b Intensity ratios of major mica peaks for PPS/ nanomica samples upon melt crystallization (T_c-250 ºC)

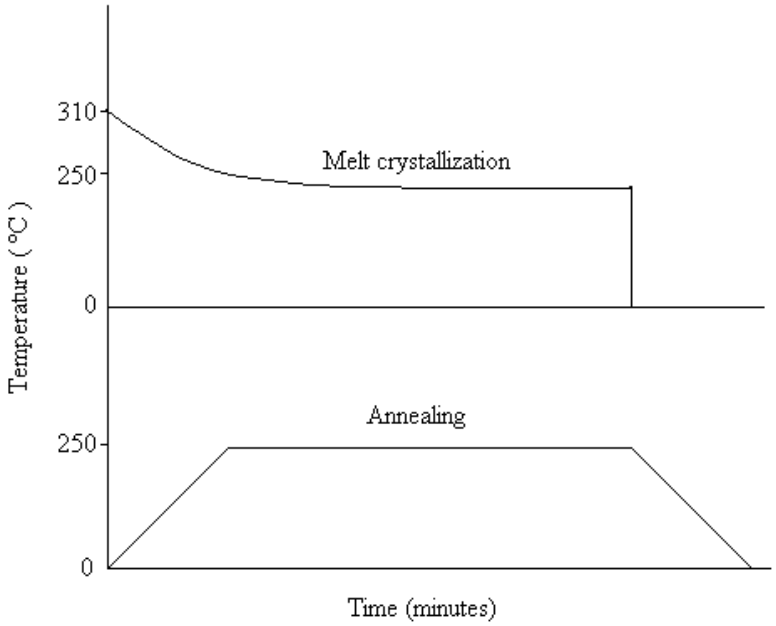

Figure 5.5 Temperature cycle for melt crystallization and annealing process

The WAXD overlays of PPS/ commercial and nano-micas before and after sintering are depicted in the figures 5.6 to 5.9 for various mica/ nano-mica loadings. The WAXD overlays of the melt crystallized PPS/ commercial and nano muscovite, phlogopite micas are displayed in the figures 5.10-5.13. One of the most obvious inferences from these figures is the decrease in the intensity of the peaks corresponding to mica upon sintering. The peaks corresponding to phlogopite mica occur at a 2θ value of 28.61(003 plane) and 18.97 (020 plane) whereas it is seen at 26.87 (009 plane) and 17.84 (006 plane) for muscovite. A slight overlap of the 020 and 006 planes of mica with the 110 peak of PPS is also noticed. With increasing mica content, an increase in the intensity of the 009 peak for muscovite and 003 peak for phlogopite is observed.

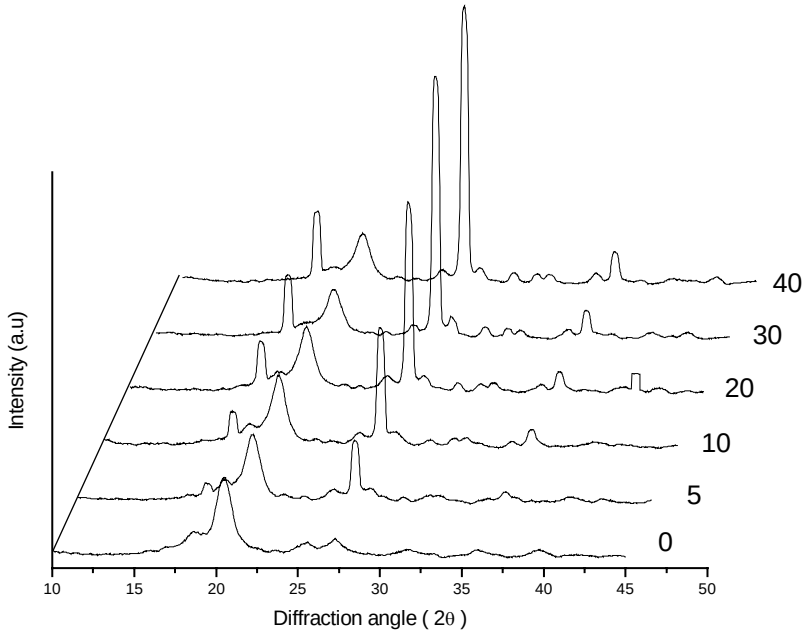

Figure 5.6a WAXD overlays of PPS/ com. muscovite at various mica loadings before sintering

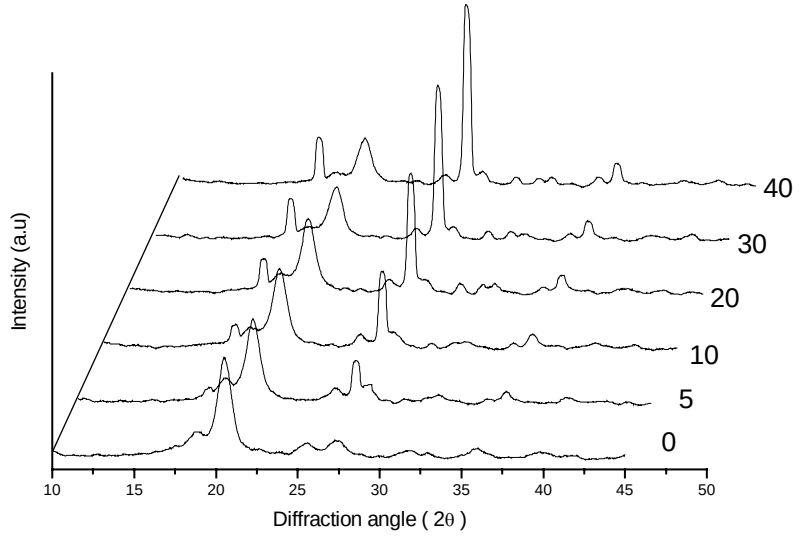

Figure 5.6b WAXD overlays of PPS/ com. muscovite at various mica loadings after sintering

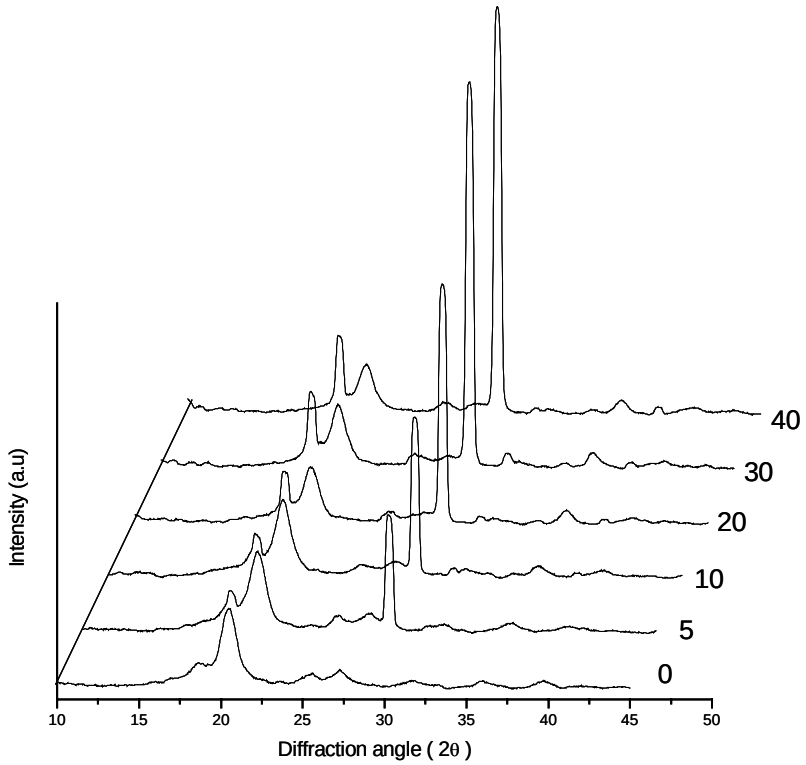
Intensity (a.u)
40
30
20
10
5
0
10
15
20
25
30
35
40
45
50
Diffraction angle (2θ)

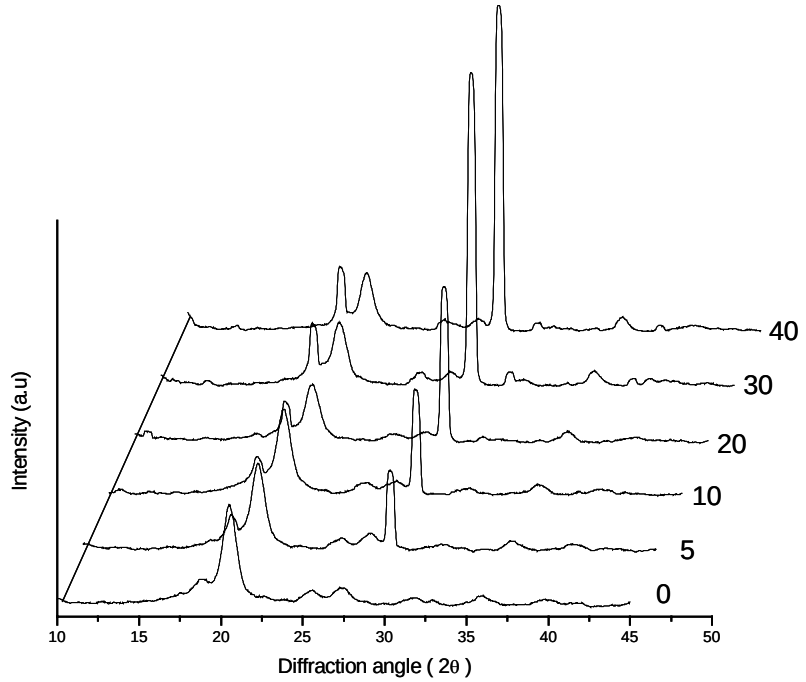
Intensity (a.u)
40
30
20
10
5
0
10
15
20
25
30
35
40
45
50
Diffraction angle (2θ)

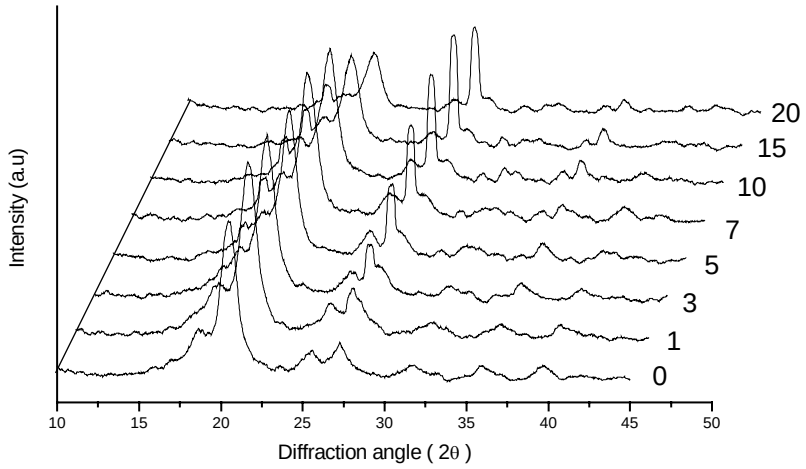

Figure 5.8a WAXD overlays of PPS/ nanomuscovite at various mica loadings before sintering

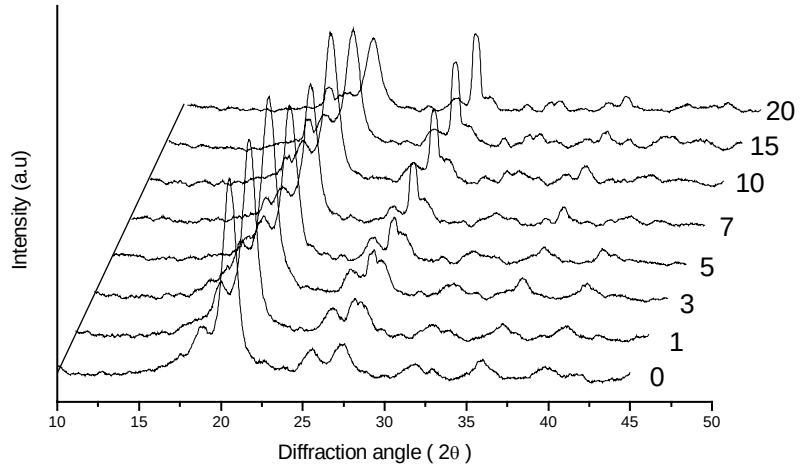

Figure 5.8b WAXD overlays of PPS/ nanomuscovite at various mica loadings after sintering

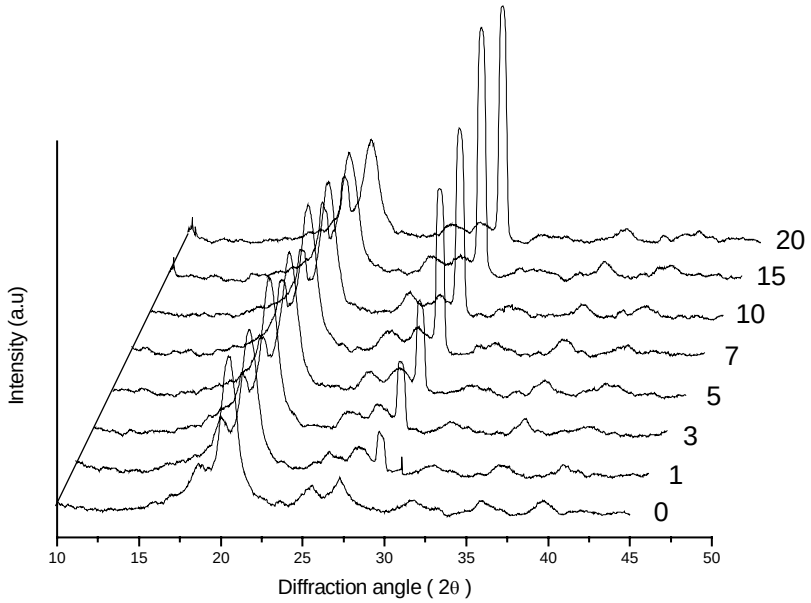

Figure 5.9a WAXD overlays of PPS/ nanophlogopite at various mica loadings before sintering

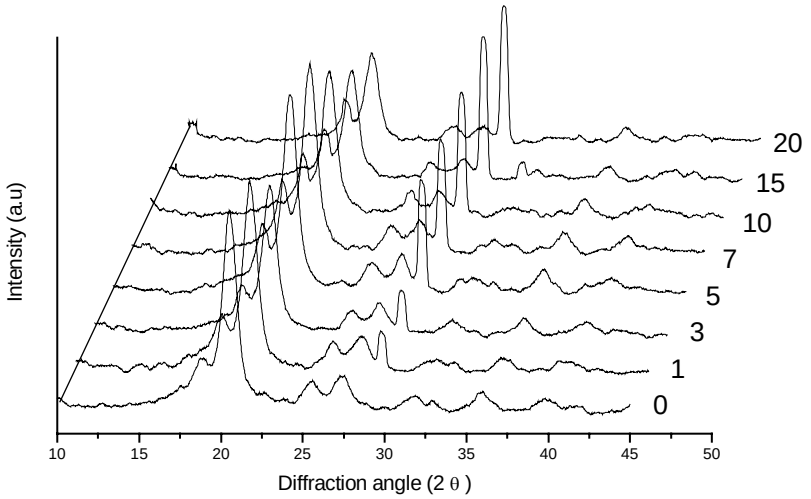

Figure 5.9b WAXD overlays of PPS/ nanophlogopite at various mica loadings after sintering

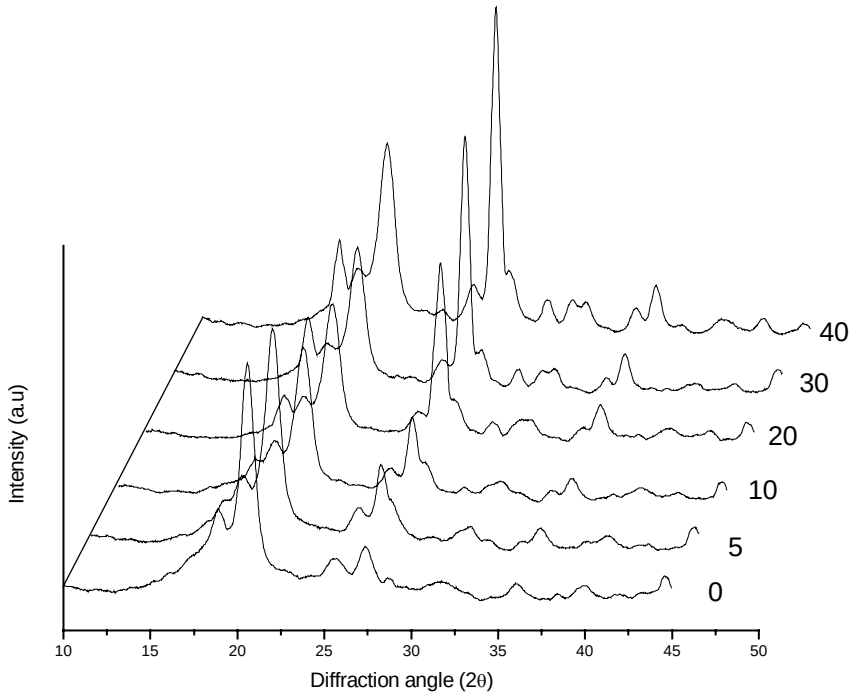

Figure 5.10 WAXD overlays of melt crystallized PPS/ com. muscovite

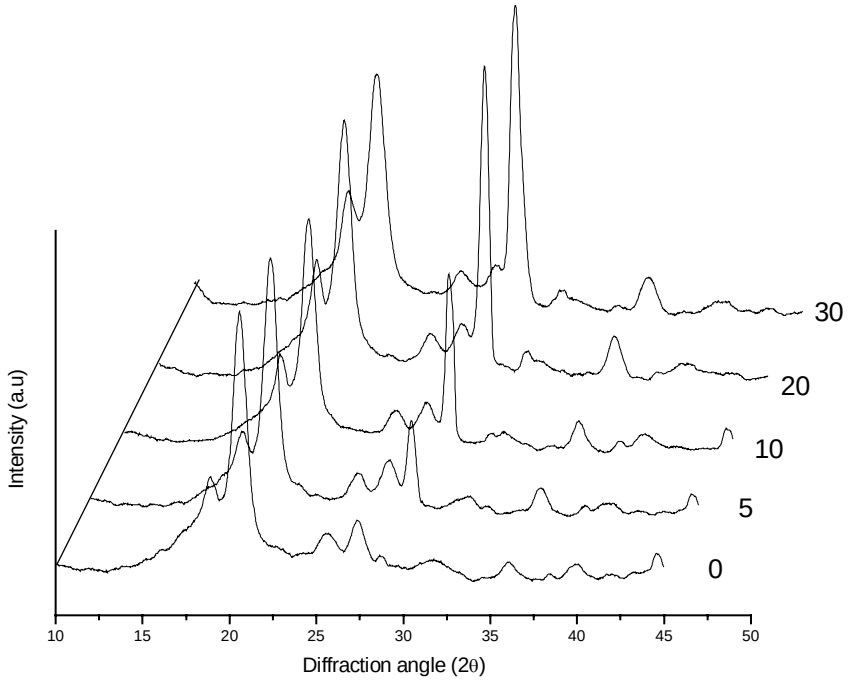

Figure 5.11 WAXD overlays of melt crystallized PPS/ com. phlogopite

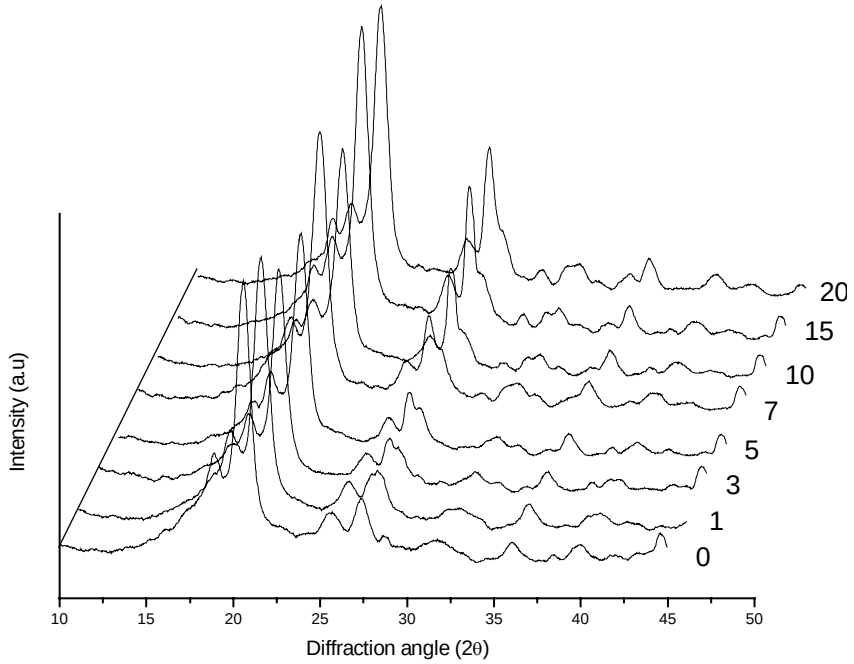

Figure 5.12 WAXD overlays of melt crystallized PPS/ nanomuscovite

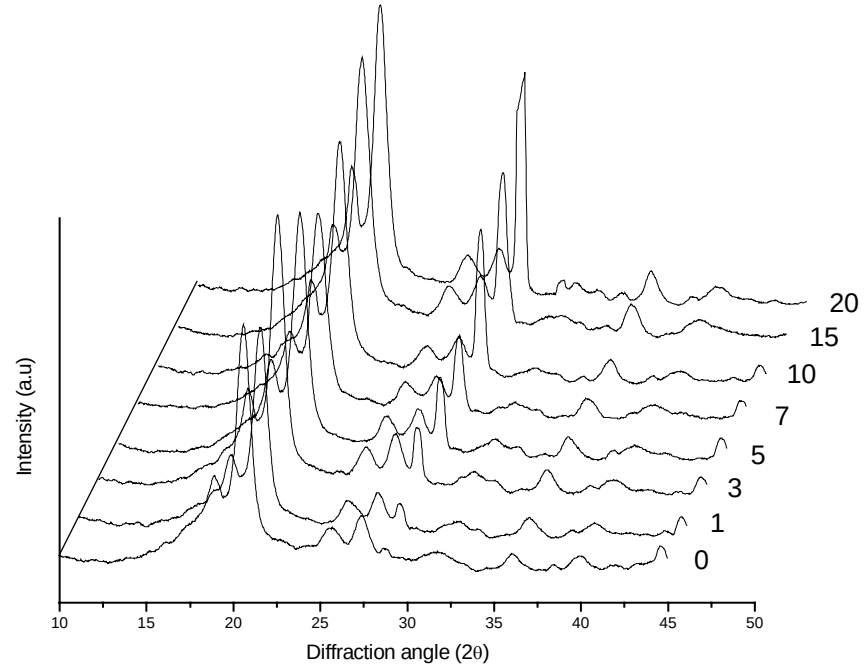

Figure 5.13 WAXD overlays of melt crystallized PPS/ nanophlogopite

This preferred oriented growth of crystallites along the 200 plane of PPS in presence of mica could be analyzed in terms of the crystal mismatch theory as mentioned in section 4.3 of chapter-4. When one looks in to the lattice parameters of PPS, (orthorhombic; a = 8.67 Å, b = 5.61 Å, c = 10.26 Å) muscovite mica, (hexagonal; a = 5.3 Å, c = 30.1 Å) and phlogopite mica, (monoclinic; a = 5.31 Å, b = 9.21 Å, c = 10.13 Å and β = 100.1°) one finds that, δ is about 2.25% between the (c-axis of muscovite) and 3 x (c-axis of PPS) whereas it is 1.2% between the (c-axis of phlogopite) and the (c-axis of PPS). Hence, nucleation and even epitaxial growth may be expected in these samples. Annealing is a phenomenon that is associated with greater polymer chain mobility at higher temperature thus allowing the molecules to arrange themselves so as to produce greater crystallinity.

In order to confirm the occurrence of nucleation in these systems, the sintered and the melt crystallized PPS/ mica composites and nanocomposites were analyzed by DSC. Representative exotherms and endotherms corresponding to sintered PPS/ commercial and nano-mica are depicted in the figures 5.14-5.17. Interestingly, an increase in the T_c of the annealed PPS/ mica composites and nanocomposites was noticed with increased mica loading. The T_c of pure PPS was observed at 244 ºC whereas it was seen at 246 ºC for 40% commercial muscovite and phlogopite. The maximum T_c of muscovite (20 wt.%) and phlogopite (10 wt.%) nanocomposites were noticed at 247 ºC and 249 ºC, respectively. This is a clear evidence of the nucleating role of mica in PPS. The shift in the T_c of the nanocomposites were observed at relatively lower mica loadings and the shift is greater than that of the corresponding commercial mica composites. The size of the particles is an important factor with respect to the surface energy. As particle size changes, the interaction behavior of the components of the composite is altered

dramatically. This might be surmised to be the reason for the nanocomposites showing a better shift in T_c. A slight increase in the T_m of the PPS/ mica composites and nanocomposites was also noticed at lower mica loadings that consequently decrease at higher mica loadings (30-40 wt.% for commercial and 15-20 wt.% for nano-mica). Two dimensional diffusion controlled growth with heterogeneous nucleation seems to be the probable mechanism of crystallization in this system and hence the increase in T_m. The same trends were observed in the case of the melt crystallized samples too, the difference being the magnitude of shift in T_c. The shift in T_c in this case was found to be marginal as compared to the sintered samples. The DSC data of the sintered and melt crystallized PPS/ mica composites and nanocomposites at different loading levels have been summarized in the tables 5.1 and 5.2, respectively. Here again, one finds that phlogopite mica is a better nucleator than muscovite mica in line with the theoretical predictions. Another significant observation is the gradual increase in the onset melting temperature of PPS, which indicates that the stability of the least stable crystallites in the composite is improved by nucleation.

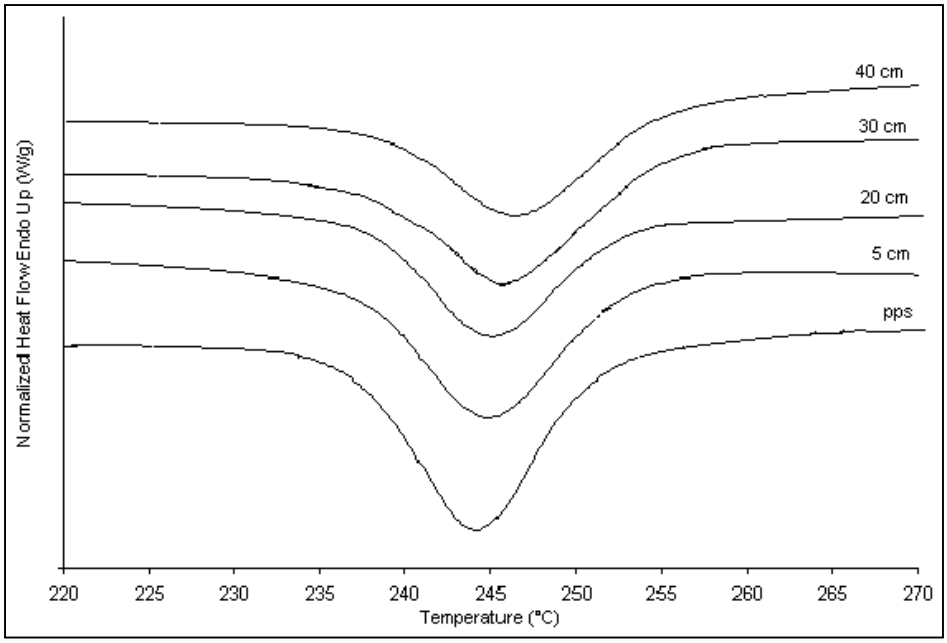

Figure 5.14a Exotherms of sintered PPS/ com. muscovite composites

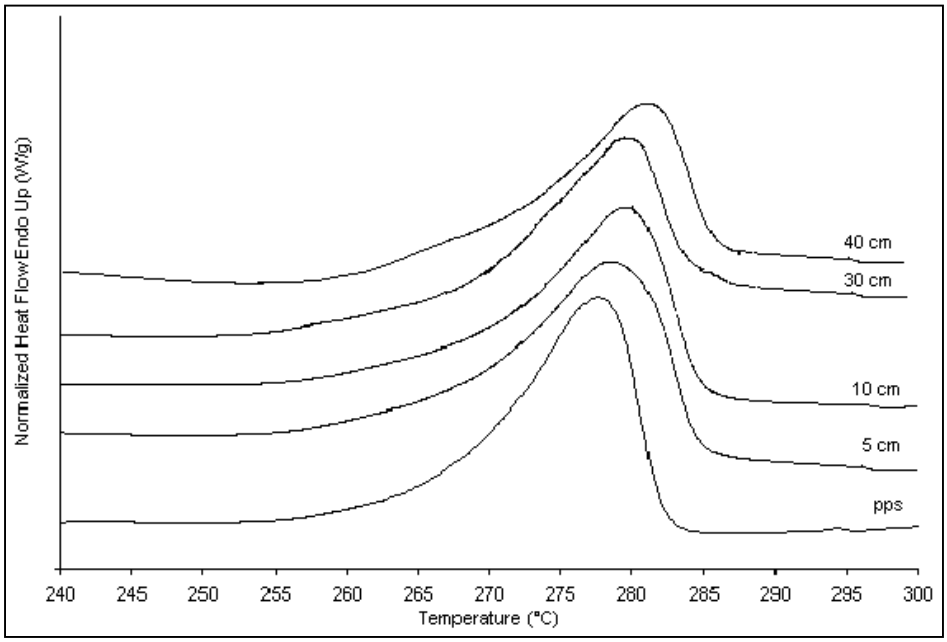

Figure 5.14b Endotherms of sintered PPS/ com. muscovite composites

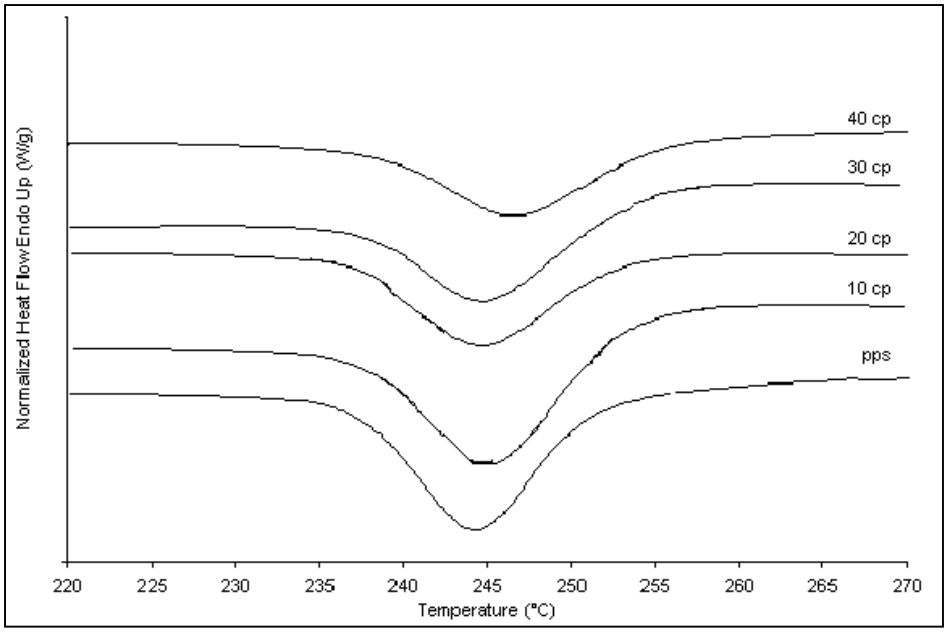

Figure 5.15a Exotherms of sintered PPS/ com. phlogopite composites

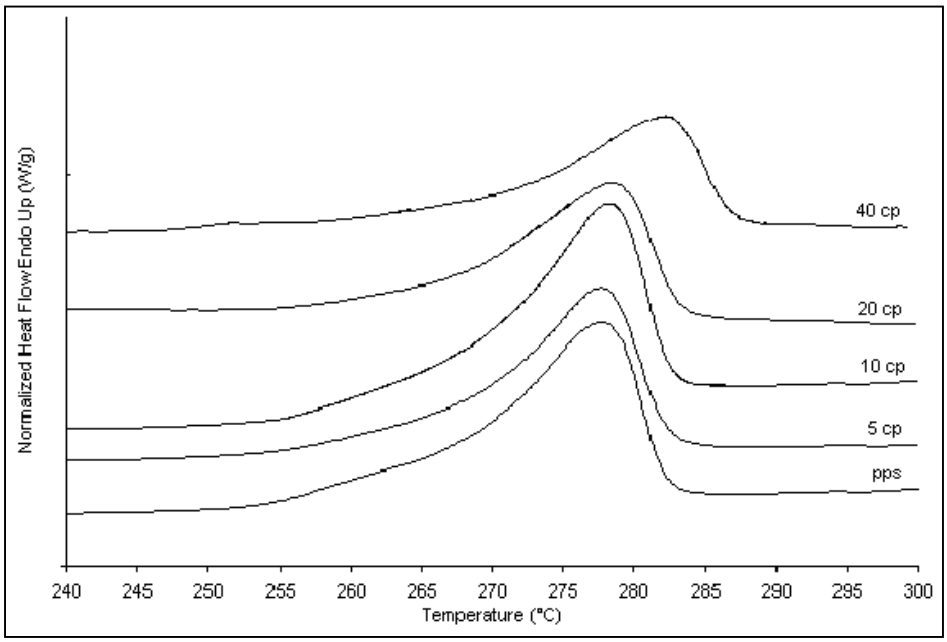

Figure 5.15b Endotherms of sintered PPS/ com. phlogopite composites

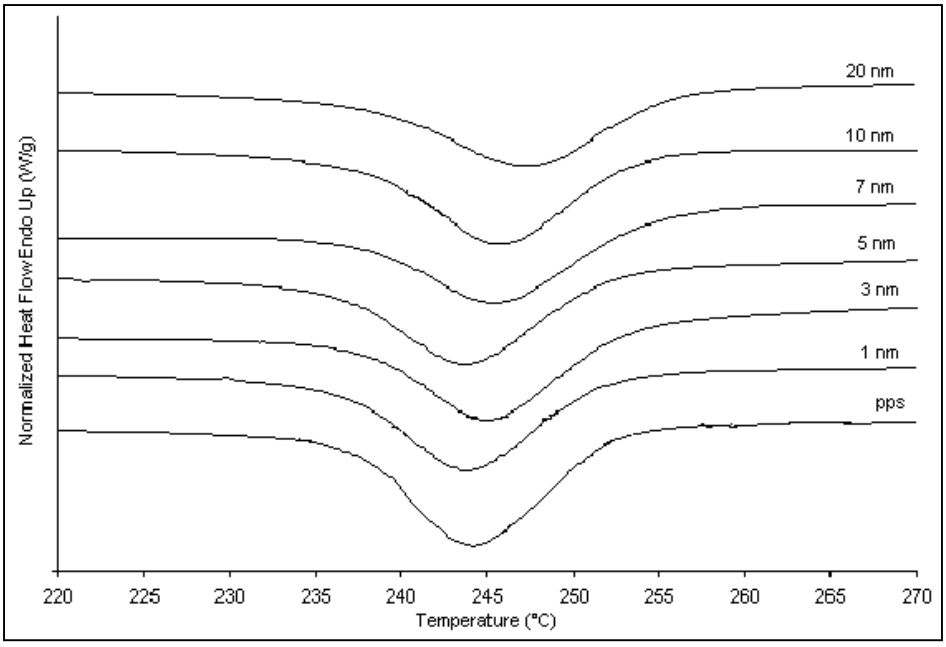

Figure 5.16a Exotherms of sintered PPS/ muscovite nanocomposites

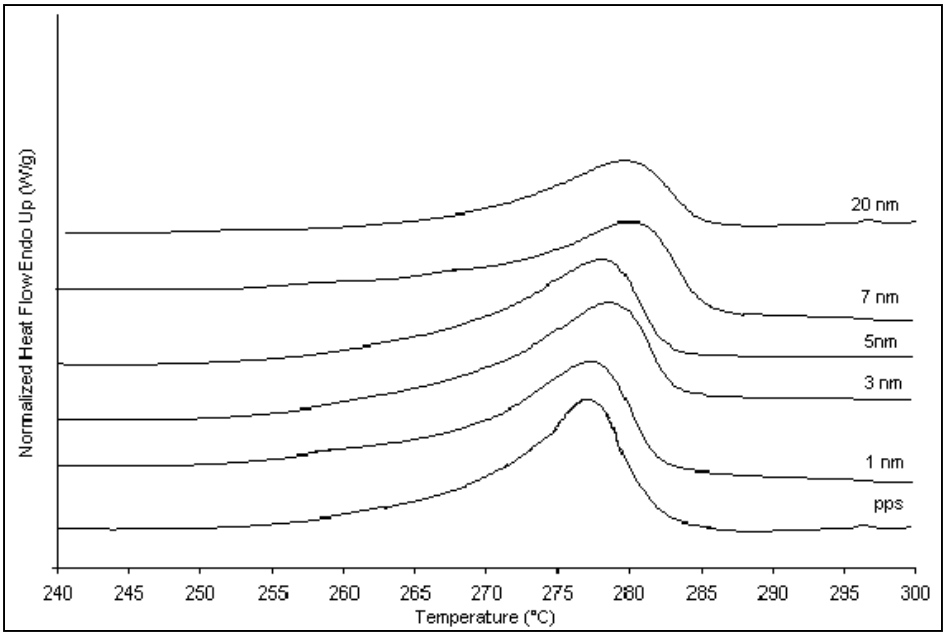

Figure 5.16b Endotherms of sintered PPS/ muscovite nanocomposites

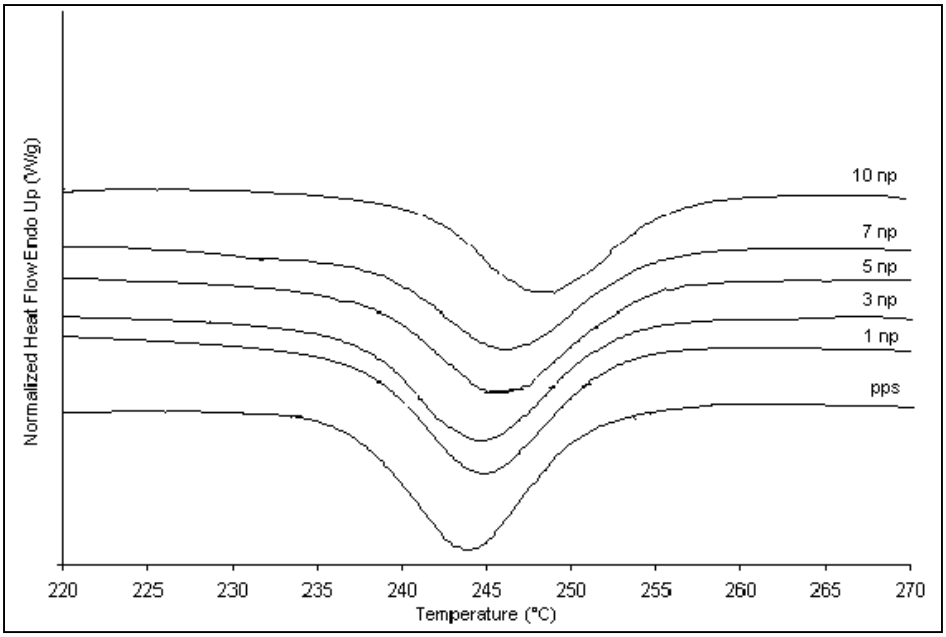

Figure 5.17a Exotherms of sintered PPS/ phlogopite nanocomposites

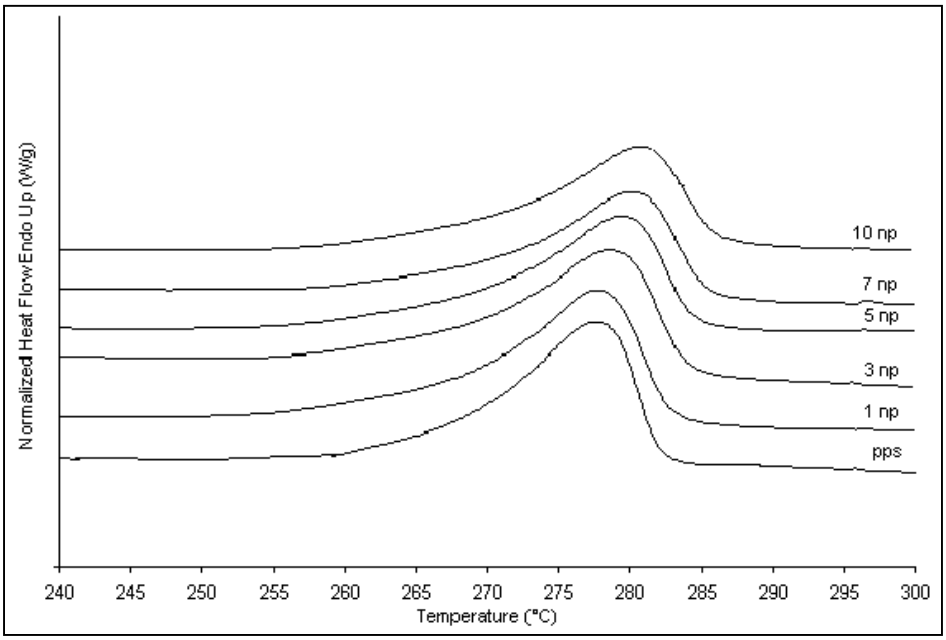

Figure 5.17b Endotherms of sintered PPS/ phlogopite nanocomposites

Table 5.1 DSC data of annealed PPS/ mica samples

Composition (Mica wt.%)	**T_c (°C)**	**ΔH_c(*) (J/g)**	**T_m (°C)**	**ΔH_m(*) (J/g)**	**T_m Onset (°C)**
Pure PPS	244	-38.75	278.3	46.69	265.2
5cm	244.8	-39.2	278.5	58.02	266.5
10cm	246.1	-41.1	279.5	56.13	267.9
20cm	244.9	-40.93	278.4	60.95	267.3
30cm	246.3	-31.64	279.5	59.82	269
40cm	246.4	-48.1	281.1	67.81	269.5
1nm	243.9	-39.23	277.3	53	266.9
3nm	244.9	-37.31	278.5	46.29	267.6
5nm	243.3	-39.08	278	52.87	266
7nm	245.6	-36.84	280.3	44.19	269.4
10nm	245.8	-42.6	276.7	49.81	265.7
15nm	244.3	-50.54	277	45.09	266.4
20nm	247.6	-46.36	279.36	40.71	268.7
5cp	245.6	-38.14	277.6	57.96	266.9
10cp	244.9	-49.33	278.1	64.47	267.3
20cp	241.4	-40.47	278	61.35	268.8
30cp	244.8	-44.35	277.3	60.71	267.1
40cp	246.6	-45.95	282.2	70.5	268.7
1np	244.8	-42.56	277.8	61.01	266.5
3np	244.6	-42.84	278.5	60.1	266.3
5np	245.8	-44.49	279.3	53.7	267.7
7np	246.1	-31.35	280.1	51.35	268.9
10np	249.9	-40.61	280.7	51.4	268.9
15np	245.9	-30.43	278	44.43	268
20np	248.4	-47.58	277	57.15	265

* The enthalpy values have been corrected for the mica content.

Table 5.2 DSC data of melt crystallized PPS/ mica samples

Composition (Mica wt.%)	T_c (°C)	ΔH_c(*) (J/g)	T_m (°C)	ΔH_m(*) (J/g)	T_m Onset (°C)
Pure PPS	244.9	-26.72	276.7	31.21	264.5
5cm	247.1	-37.35	280.8	32.06	273.3
10cm	246.8	-36.18	279.3	31.12	271.2
20cm	247.3	-35.33	280.8	39.39	272.5
30cm	245.6	-39.51	277.5	35.62	268.9
40cm	245.1	-42.81	276.8	40.73	268.4
1nm	245.8	-34.96	279.3	37.45	270.2
3nm	244.9	-38.59	276.3	33.94	267.6
5nm	244.6	-36.5	280.7	36.06	270.7
7nm	242.3	-39.91	278.7	41.22	271.1
10nm	243.6	-36.91	283.2	42.56	271.7
15nm	245.8	-43.55	276.8	34.27	266.8
20nm	244.8	-45.6	274.5	36.53	265.8
5cp	246.5	-30.64	278.1	30.9	269.3
10cp	246.4	-38.74	282.3	38.74	274.9
20cp	245.8	-38.11	278.8	38.11	270.5
30cp	245.1	-29.4	282	29.4	276
40cp	245.8	-46.35	281.2	46.35	272.4
1np	246.1	-37.68	276.7	32.18	270
3np	245.9	-35.03	281.8	39.49	278.6
5np	244.8	-38.36	277.6	33.58	269.2
7np	244.9	-37.9	276.3	30.98	267
10np	245.3	-38.9	279.5	34.72	269.3
15np	245.3	-36.02	277.5	30.52	268.5
20np	245.8	-37.58	285	42.88	272.4

* The enthalpy values have been corrected for the mica content.

The enthalpy of melting has been plotted as a function of mica content for both the PPS/ commercial mica composites and nanocomposites. The plots for the sintered composites and nanocomposites are given in the figures 5.18a-b and those for the melt crystallized ones are shown in the figures 5.19a-b. In the sintered samples, the enthalpies of the PPS/ commercial mica composites demonstrate a constant increase with mica loading whereas the enthalpies of the nanocomposites show a slight increase at very low mica loadings (1 wt.%) but decrease at higher loadings. In the melt crystallized samples, both the commercial and nano-micas show an initial increase in ΔH_m that decreases at higher mica loadings. The maximum ΔH_m is observed at 10 wt.% for the commercial micas whereas it is seen at 3-10 wt.% for the nano-micas. Since the ΔH_m value directly reflects the crystallinity in the sample, it could be concluded that annealing results in a greater level of crystallinity in the samples as against melt crystallization.

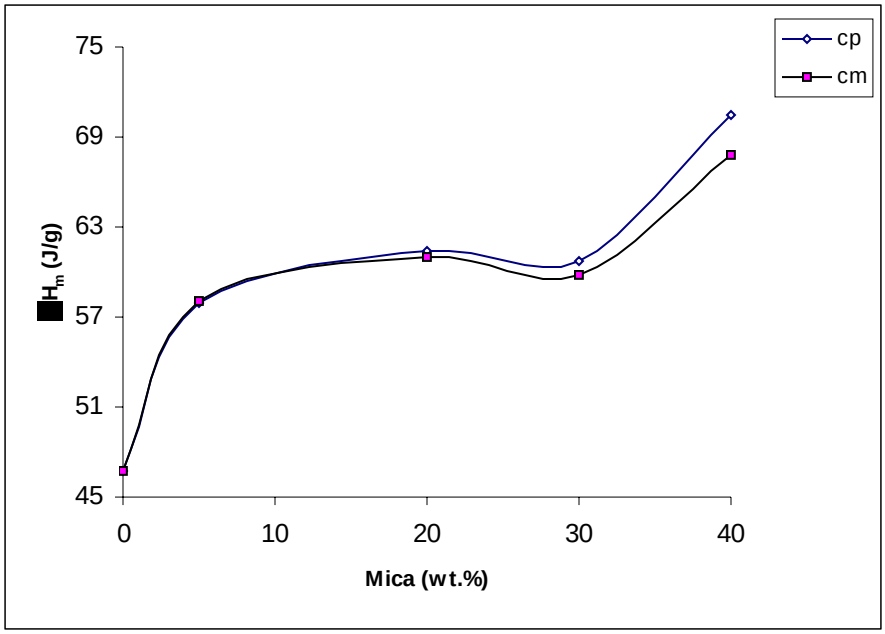

Figure 5.18a ΔH_m as a function of mica loading for sintered PPS/ com. mica composites

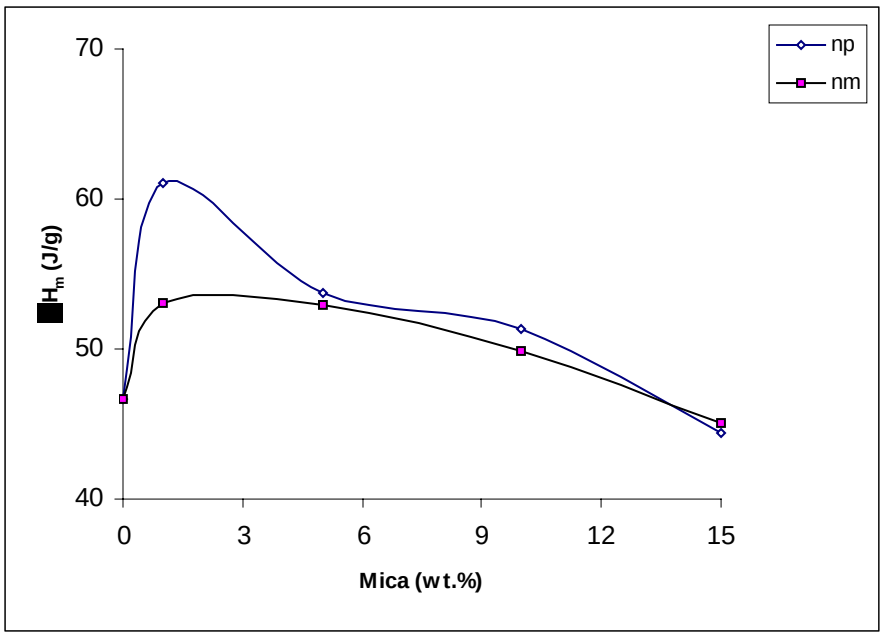

Figure 5.18b ΔH_m as a function of mica loading for sintered PPS/ mica nanocomposites

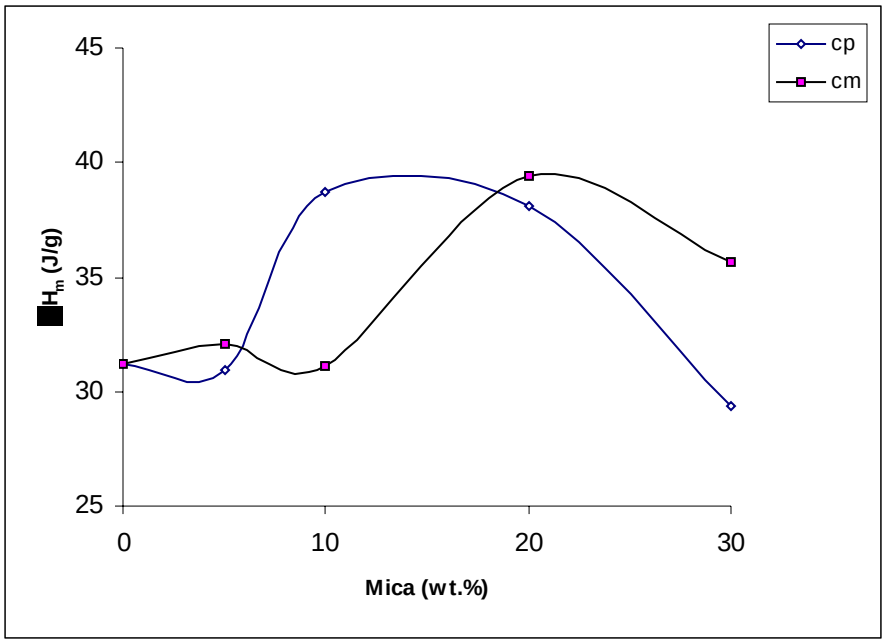

Figure 5.19a ΔH_m Vs mica loading for melt crystallized PPS/ com. mica composites

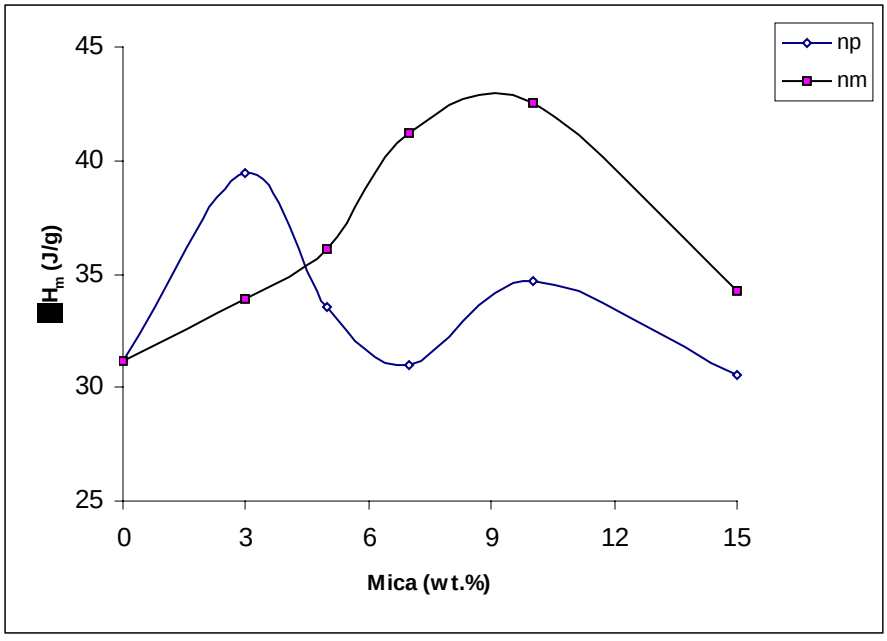

Figure 5.19b ΔH_m Vs mica loading for melt crystallized PPS/ mica nanocomposites

5(B) Properties of Mica / PPS Nanocomposites

5.4 Introduction

PPS has very interesting properties that lead to its use in a wide range of applications. Of these, only the thermal and the dielectric properties were explored by us and hence the ensuing discussions would be restricted to these properties. PPS is known to have excellent thermal stability and retains 40% of its weight even at 1000 °C in nitrogen atmosphere. This extraordinary thermal stability has its origin in the structure of PPS as shown in the figure 5.20 and the subsequent reactions it undergoes on heating.

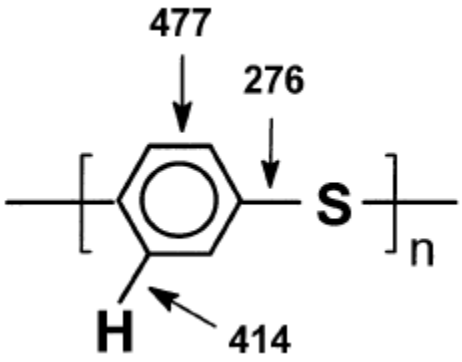

Figure 5.20 The structure of PPS showing the dissociation energy (KJ/mol) of the three different bond types present

The polymer contains only C-C, C-S, and C-H bonds all of which are thermodynamically stable thereby requiring a very large energy input to rupture the molecule. Some of the initial work on the thermal degradation of PPS has been done by Edmonds and Hill.[39] They had studied the degradation of PPS in air and nitrogen and found that the rate of degradation was comparatively lower in nitrogen. The reaction mechanism of the thermal

degradation of PPS has been proposed by Ehlers et al.[40] which has been depicted in figure 5.21.

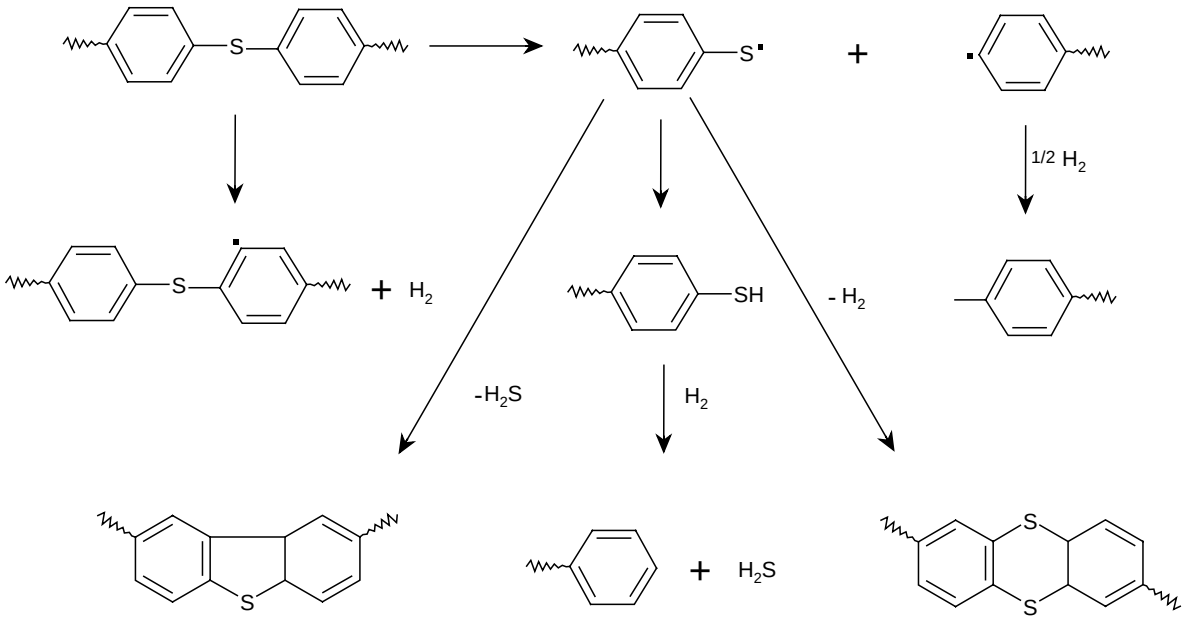

Figure 5.21 Thermal degradation mechanism of PPS

The breakdown mechanism starts by cleavage of C-S bonds and abstraction of hydrogen to form chain fragments with phenyl and phenylmercapto end groups. Further cleavage of the C-SH bonds and abstraction of H leads to elimination of H_2S. The radicals formed by abstraction of H are expected to cause recombination and crosslinking, and low molecular weight dimers and trimers are removed at these high temperatures to form a condensate. The dibenzothiophene structure would form free diphenylsulfide whereas the thianthrene would originate from phenylmercaptan or phenylmercapto end groups. The

crosslinking and cyclization imparts thermal stability to PPS. This property has been utilized in PPS coatings, which have high temperature chemical resistance. Thermal treatment of PPS in air or presence of oxygen has also been used to increase the molecular weight, thermal stability and chemical resistance. In this case oxygen gets incorporated in the crosslinks/ side chain to give "thermoset" type behavior of PPS after high temperature treatment. Most of the studies on the thermal degradation of PPS have been reported at a constant heating rate.[40-44] Recently, Li et al.[45] have investigated the degradation kinetics of PPS by a novel high resolution thermogravimetric technique under four different atmospheres i.e. argon, helium, nitrogen and air. They found that the activation energy of PPS showed a strong dependence on the test atmosphere suggesting different degradation mechanisms in different atmospheres.

There are relatively very few reports on the dielectric relaxation spectroscopy (DRS) of PPS. A seminal work on the dielectric relaxations of PPS containing a fraction of rigid amorphous phase (RAP) spanning a temperature range of 30 ºC-180 ºC was reported by Huo and Cebe[46] in 1992. They found that the RAP in PPS represents chains with a temperature dependent mobility. Kalika et al.[47] have addressed the relaxation characteristics of a series of random PPS copolymers based on sodium hydrosulfide and 1,4- and 1,3-dichlorobenzene monomers by dielectric and dynamic mechanical measurements. They found that the offset in T_g for crystallized samples as compared to the quenched specimens was reduced with increasing meta content. Also, the RAP was found to mobilize fully above T_g for those copolymers containing a high level of *meta*-phenylene units. Recently, El Shafee[48] has reported the effects of solvent treatment on the glass transition characteristics of PPS using DRS. It was found that the solvent induced

crystallinity resulted in a T_g offset well above the glass transition temperature for thermally crystallized PPS materials. The activation energy of the α process was found to be higher for the solvent crystallized PPS.

Thus the study of relaxation characteristics of PPS is of fundamental importance and all the literature cited above deal with only pure PPS. The changes in the molecular dynamics of PPS upon addition of a filler could be easily followed by DRS since the relaxations are extremely sensitive to changes in the crystalline morphology, which in turn is a function of the extraneous inclusion. However, there are no reports on the relaxation characteristics of PPS/ mica composites or nanocomposites. The work described in the following section addresses these aspects along with the thermal stability of PPS incorporated with the nano-mica additive.

5.5 Experimental

(a) Melt Compounding of PPS/ Mica Composites/ Nanocomposites

The desired quantity of nano-mica/ commercial mica was first mixed with Ryton PPS and ground to a fine powder in an agate mortar. This powder was fed into the barrel of a MFI unit at 285 ºC. A small amount of the powder was melt extruded and the strands of the PPS/ mica composites and nanocomposites were obtained. These were cut in to small pieces and subsequently used for molding.

(b) Compression Molding of PPS/ Mica Composites/ Nanocomposites

The melt compounded PPS/ mica samples were compression molded at 270 ºC for 3-4 minutes at a pressure of 0.5 tonnes in between two teflon sheets. It was then quenched in cold water and dried.

The discs obtained upon compression molding were coated on either side as mentioned in section 2.10.2. The TGA of the samples were run as mentioned in section 2.11.5. SEM was done in accordance with the procedure described in section 2.11.6 to prove the homogeneity of the PPS/ mica nanocomposites as opposed to the heterogeneous microstructure in PPS/ mica composites.

5.6 Results and Discussion

5.6.1 Thermal Properties

The DSC results have already been discussed in section 5.3 and only the TGA results are being presented here. The TGA curves for the PPS/ mica composites and nanocomposites are depicted in the figures 5.22-5.25 and the other test parameters obtained are summarized in the tables 5.3a and 5.3b for commercial and nano-mica, respectively. Only a marginal increase in the degradation onset is observed for the nanocomposites whereas the increase is substantial in the case of the PPS/ mica composites. There is also a considerable increase in the maximum degradation temperature of the PPS/ mica composites but it reduces slightly in the case of the nanocomposites.

PPS/ commercial mica composites demonstrate a weight loss of 28-38 % whereas the corresponding PPS/ mica nanocomposites show an apparently higher weight loss of

40-44 %. Figure 5.26 gives the thermogram of a 80:20 blend of commercial Ryton PPS and the lab synthesized PPS. This blend shows a weight loss of 48.66 % at the maximum degradation temperature, which was taken as the reference for tabulating the expected weight loss of the nanocomposites. The expected weight loss of the PPS/ mica composites and nanocomposites were estimated in the same manner as given in section 4.6.2 of chapter-4 and are presented in the table 5.3b. As in the case of PP/ mica nanocomposites, here again we find quite a difference in the values of the actual and the expected weight losses of the PPS/ mica composites and nanocomposites. Thus, we find that the nanocomposite samples demonstrate excellent stability due to which they exhibit a much lower weight loss at the maximum degradation temperature, which might be due to the higher thermal conductivity of mica.

The stability of the PPS/ mica composites is found to increase with increased mica loadings but higher mica loadings in the case of the nanocomposites is found to bring down the maximum degradation temperature. The reason for this is the presence of a large amount of lab synthesized mica in the nanocomposites, which has a lower thermal stability. Increased mica loadings results in an increase in the amount of lab synthesized PPS in the nanocomposite thereby lowering the maximum degradation temperature.

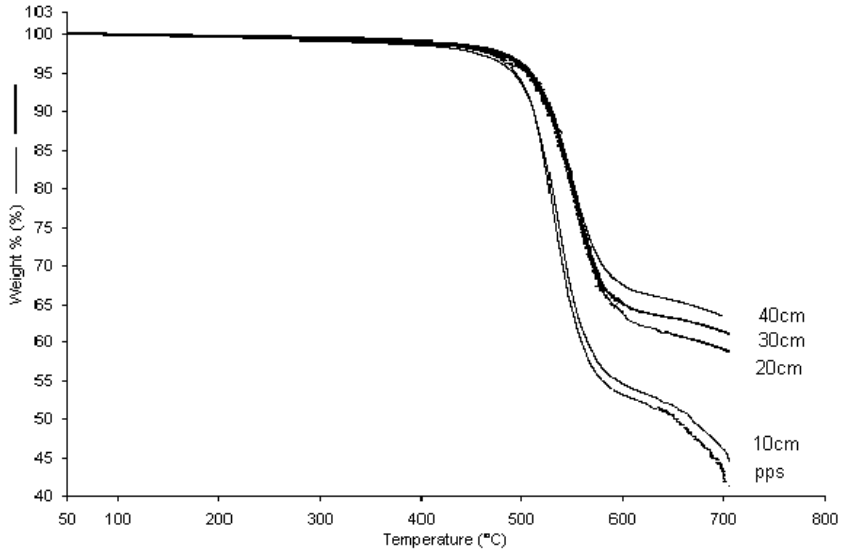

Figure 5.22 TGA of PPS/ com. muscovite composites

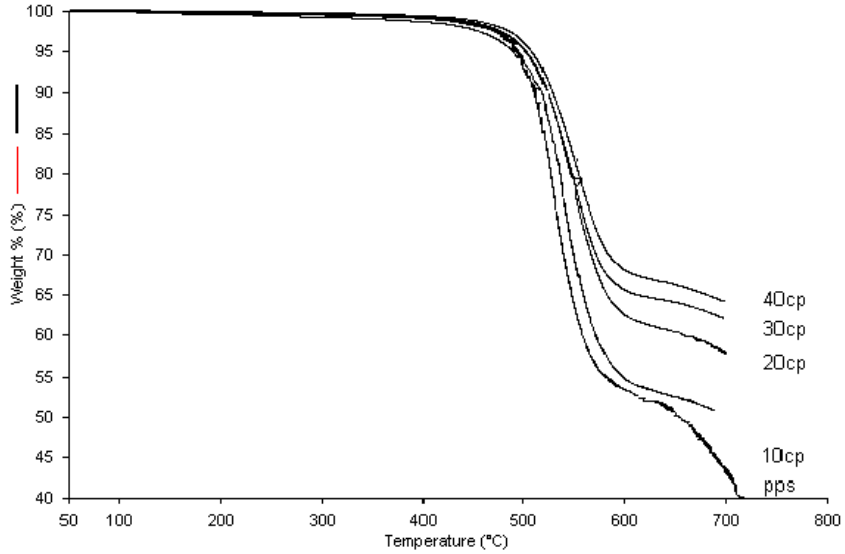

Figure 5.23 TGA of PPS/ com. phlogopite composites

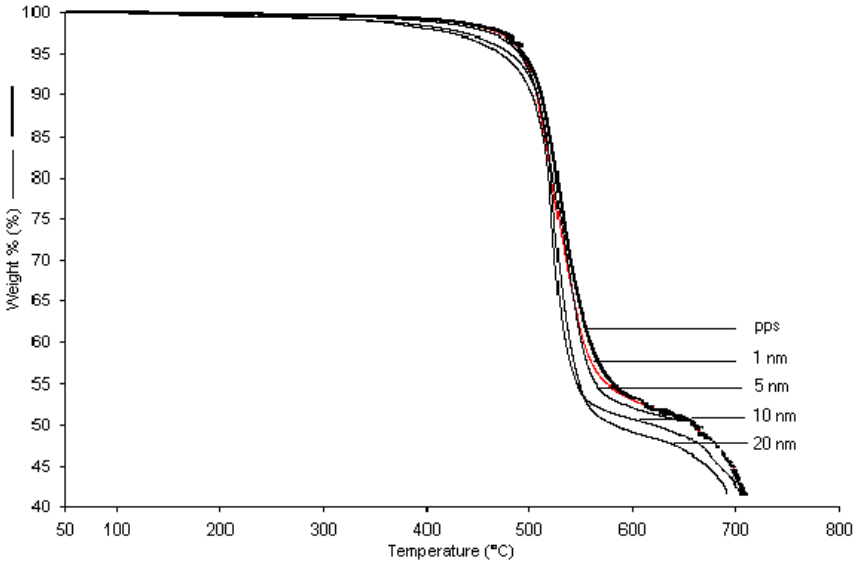

Figure 5.24 TGA of PPS/ muscovite nanocomposites

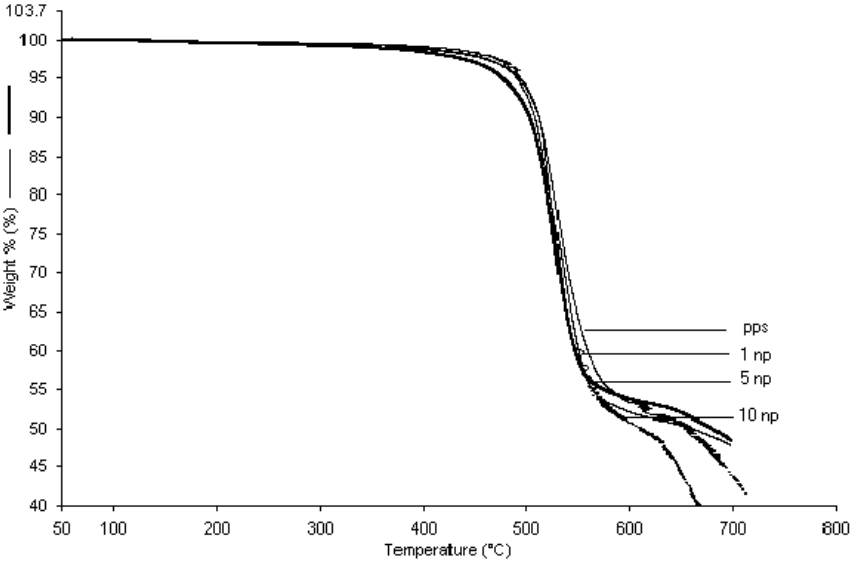

Figure 5.25 TGA of PPS/ phlogopite nanocomposites

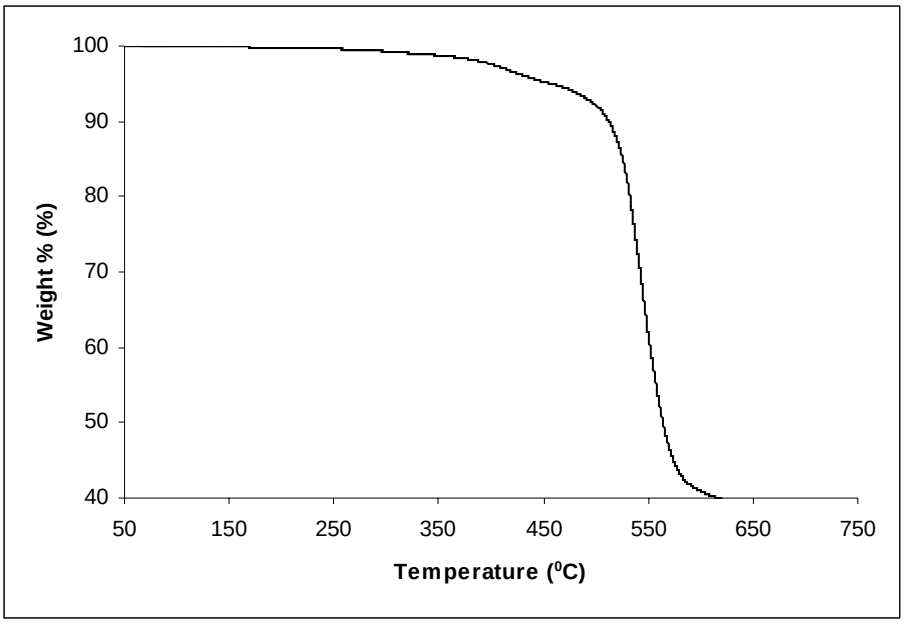

Figure 5.26 TGA of 80/ 20 blend of Ryton PPS/ lab synthesized PPS

Table 5.3 TGA data for PPS/ mica composites and nanocomposites

Composition (Wt. %)	**Initial degradation temperatute (Td) (°C)**	**Temperature at maximum degradation Td_m (°C)**	**Wt. loss at Td_m (%)**
PPS	499	532	38
5 cm	505	537	38
10 cm	506	540	38
20 cm	516	545	32
30 cm	518	549	31
40 cm	518	557	28
5 cp	505	544	38
10 cp	506	546	38
20 cp	506	550	33
30 cp	509	552	31
40 cp	512	554	29
1 nm	499	538	40
3 nm	499	539	42
5 nm	500	536	42
7 nm	502	532	43
10 nm	504	525	41
15 nm	505	521	43
20 nm	506	520	41
1 np	500	521	40
3 np	500	542	43
5 np	501	544	44
7 np	504	539	40
10 np	505	528	40
15 np	506	524	39
20 np	506	522	39

Table 5.4 Expected and actual weight loss for PPS/ mica composites and nanocomposites

Composition (Wt. %)	**Expected wt. loss at Td_m (%)**	**Actual wt. loss at Td_m (%)**
Pure PPS	-	38
80/20 blend	-	48
5 cm	36	38
10 cm	34	38
20 cm	30	32
30 cm	27	31
40 cm	23	28
5 cp	36	38
10 cp	34	38
20 cp	30	33
30 cp	27	31
40 cp	23	29
1 nm	48	40
3 nm	47	42
5 nm	46	42
7 nm	45	43
10 nm	44	41
15 nm	41	43
20 nm	40	41
1 np	48	40
3 np	47	43
5 np	46	44
7 np	45	40
10 np	44	40
15 np	41	39
20 np	40	39

5.6.2 Dielectric Relaxation Studies

Dielectric relaxation results in the temperature range 303 K – 443 K for pure PPS as well as all the PPS/ mica composites and nanocomposites are plotted isochronally as dielectric loss versus temperature in the figures 5.27a to 5.35a. The temperature dependence of peak frequency for all the relaxations observed are plotted in an Arrhenius manner for the respective samples and are presented below the isochronal plots of tan δ with temperature in the figures 5.27b to 5.35b. These data are based on the equation for shift in peak frequency with respect to temperature i.e. $\log f_m = E_a / KT$.

Analysis of the tan δ values reveals a dramatic step wise increase starting at 373 K for pure PPS that progressively shifts to higher temperature as the mica loading increases. This peak is generally associated with the large scale mobilization of the amorphous chains i.e. the glass-rubber α relaxation. The Arrhenius plots suggest the occurrence of also a distinct β process, which might have its origin in the PPS/ mica interface. Representative plots of the isochrons of dielectric constant (ε^1) Vs. temperature for pure PPS, PPS/ mica composites and nanocomposites are provided in the figures 5.36-5.40. It can be seen that the shift in the loss factor to higher temperatures with increasing frequencies can also be observed in the plots of ε^1 Vs temperature. The onset of cold crystallization with increasing temperature in the amorphous sample leads to a sharp decrease in the tan δ of pure PPS at around 403 K, since some portion of the relaxed chains are immobilized by crystallization. Crystallinity leads to a offset in the T_g of the remaining amorphous fraction, and the eventual relaxation of the amorphous material is evident as a recovery in ε^1on the high temperature side of the glass transition loss peak.

The dielectric relaxation of PPS has been studied by Huo and Cebe[46] and they have examined the relaxation curves with respect to crystallinity in the sample. Three regions for the relaxation peak with respect to temperature were noted depending on the crystallinity:

a) for amorphous (quenched) samples, the tan δ peak was observed in the region of 370 – 390 K (1/ T = 2.7-2.55)

b) for partially crystalline PPS, it appeared in the region of 400 - 430 K (1/ T = 2.45-2.35)

c) for highly crystalline samples, it was observed in the range of 415 – 434 K (1/ T = 2.42 – 2.3)

depending on the crystallization temperature. The corresponding activation energies were 457, 397 and 262 KJ/ mol, respectively. The effect of crosslinking on the other hand, gave rise to multiple relaxation peaks above 393 K in the TSDC of PPS which were observed by Yasufuku et al.[49] as well as Quamara et al.[50] Considering these reports, the present results can be interpreted in terms of increase of crystallinity due to incorporation of mica particles in PPS. Lower the particle size, more is the nucleation efficiency and one would expect higher crystallinity. This gets reflected in the appearance of relaxation peaks mainly in the higher temperature region of 400 – 435 K. Higher activation energy value is also observed as expected.

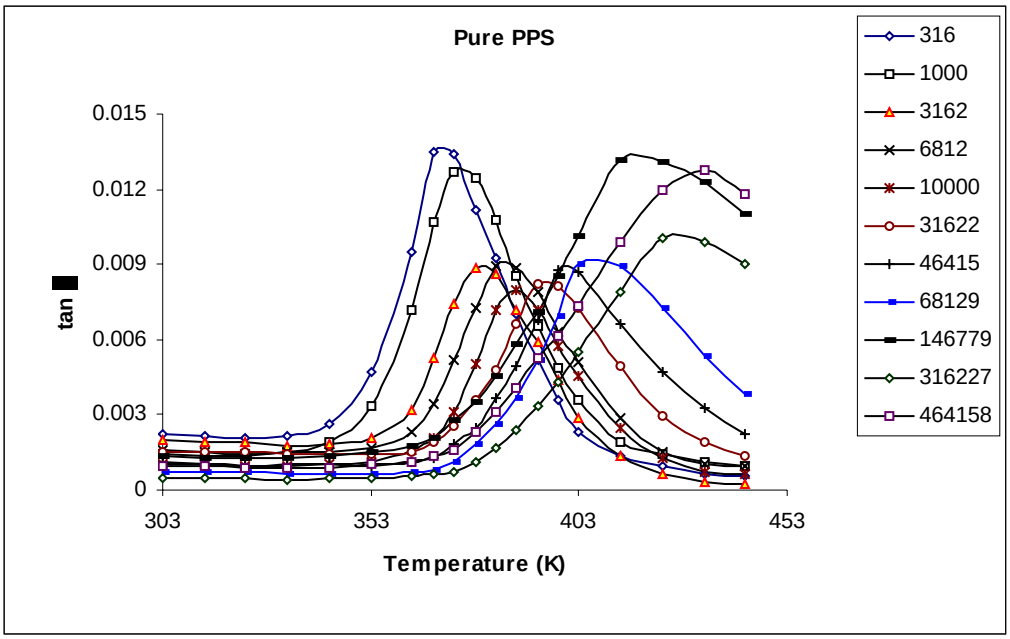

Figure 5.27a Isochron of tan δ Vs T for pure PPS at various frequencies (in Hz)

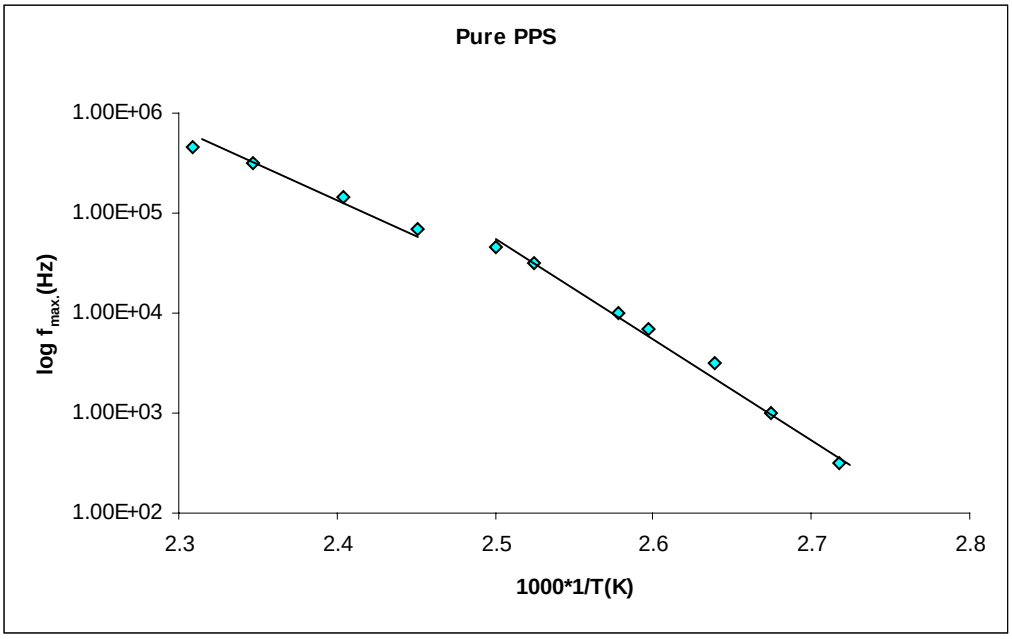

Figure 5.27b Arrhenius plot of frequency Vs reciprocal temperature for pure PPS

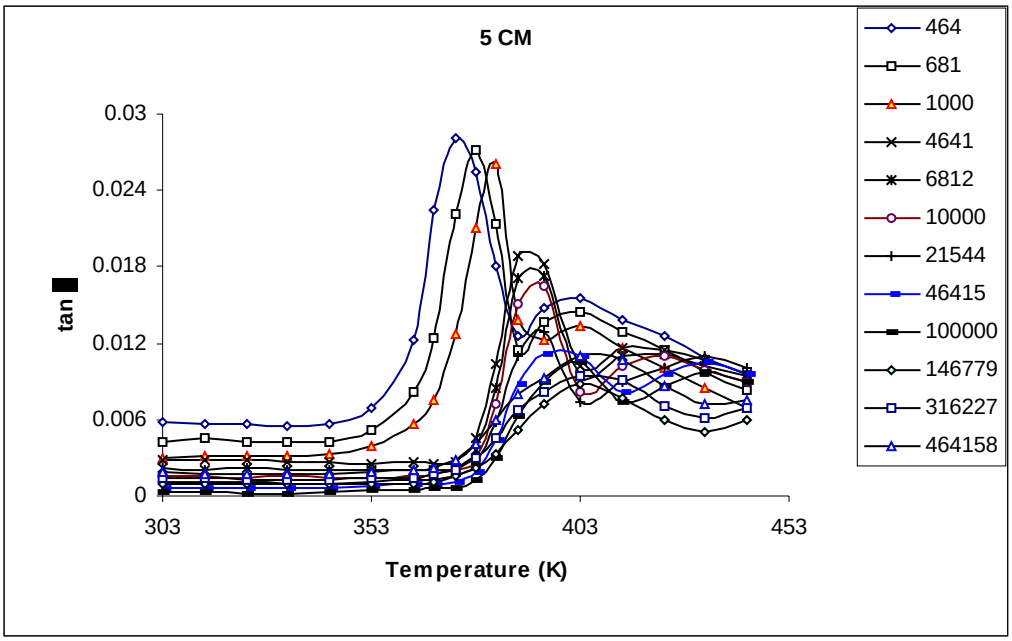

Figure 5.28a Isochron of tan δ Vs T for 5% PPS/ com. muscovite (frequency in Hz)

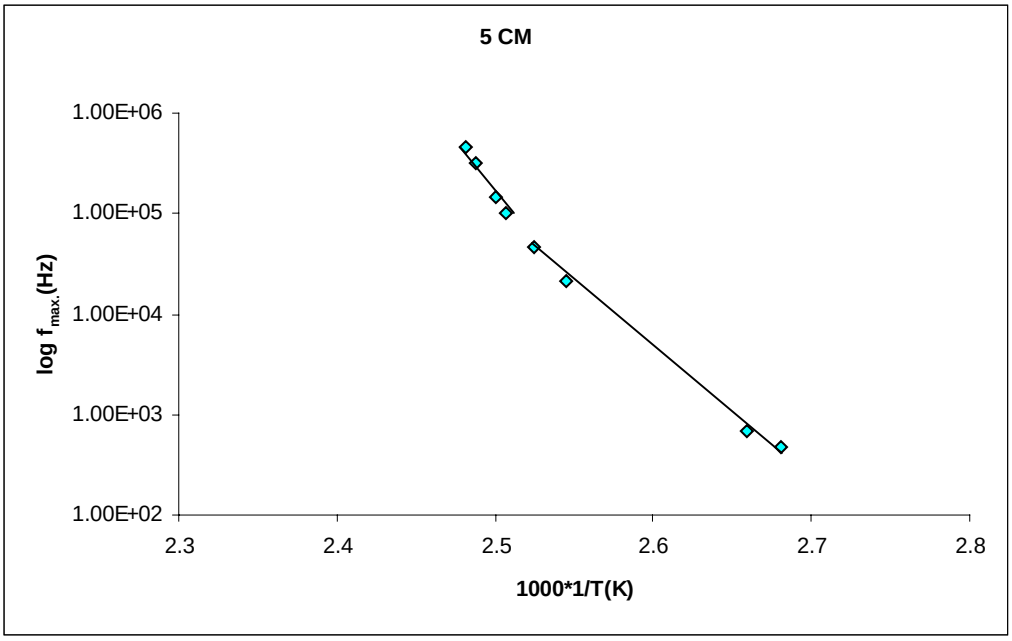

Figure 5.28b Arrhenius plot of frequency Vs reciprocal temperature for 5% PPS/ com. muscovite

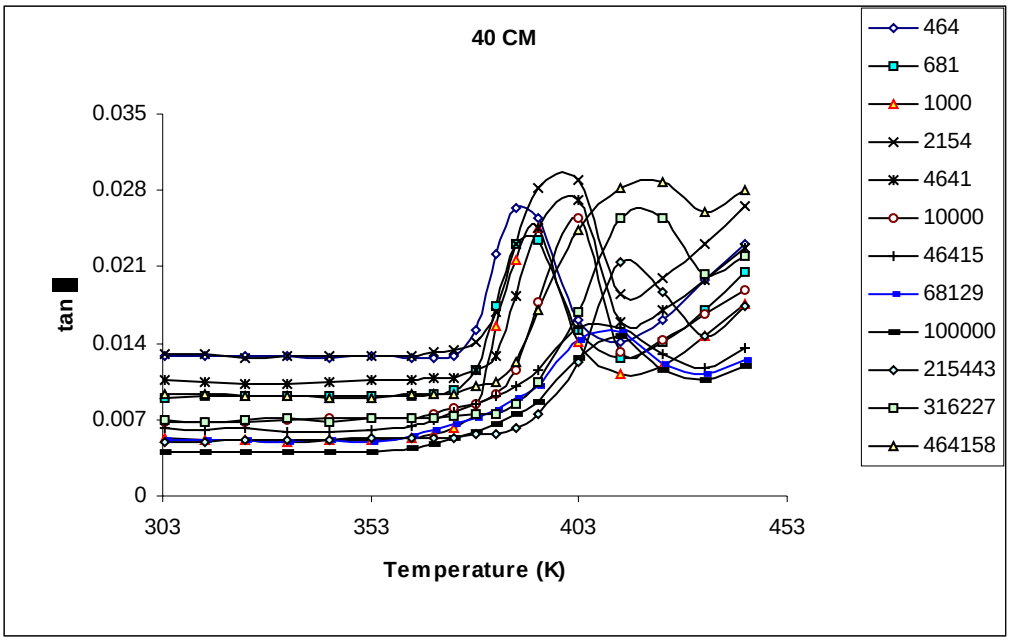

Figure 5.29a Isochron of tan δ Vs T for 40% PPS/ com. muscovite (frequency in Hz)

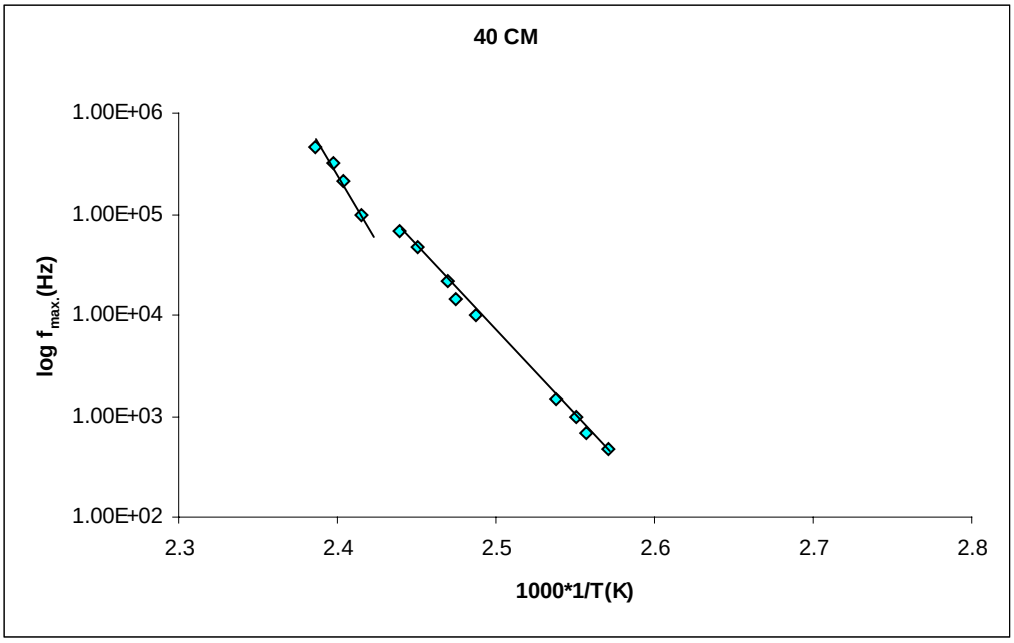

Figure 5.29b Arrhenius plot of frequency Vs reciprocal temperature for 40% PPS/ com. muscovite

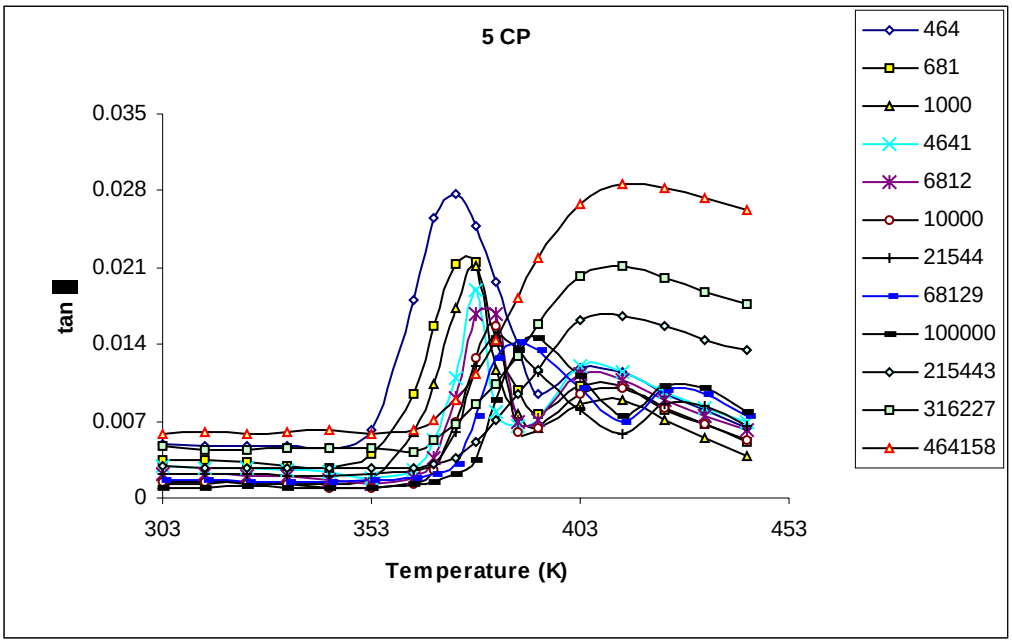

Figure 5.30a Isochron of tan δ Vs T for 5% PPS/ com. phlogopite (frequency in Hz)

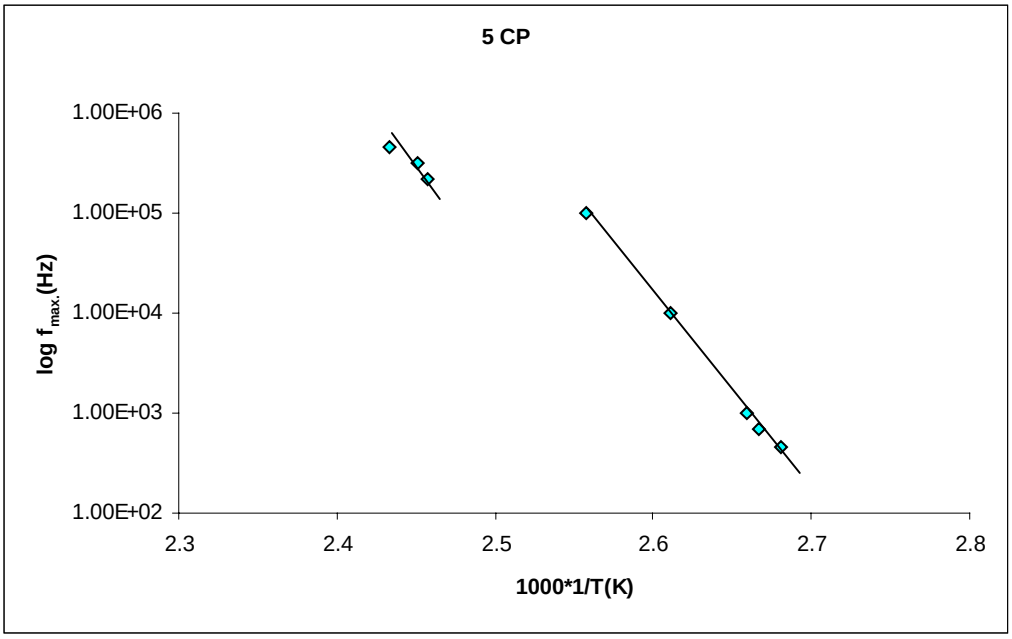

Figure 5.30b Arrhenius plot of frequency Vs reciprocal temperature for 5% PPS/ com. phlogopite

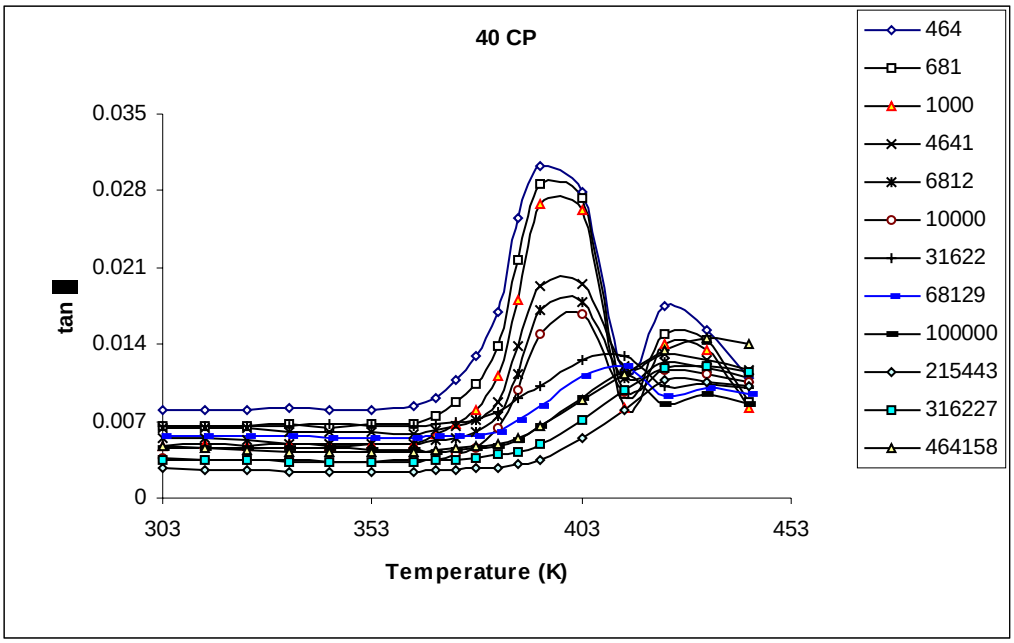

Figure 5.31a Isochron of tan δ Vs T for 40% PPS/ com. phlogopite (frequency in Hz)

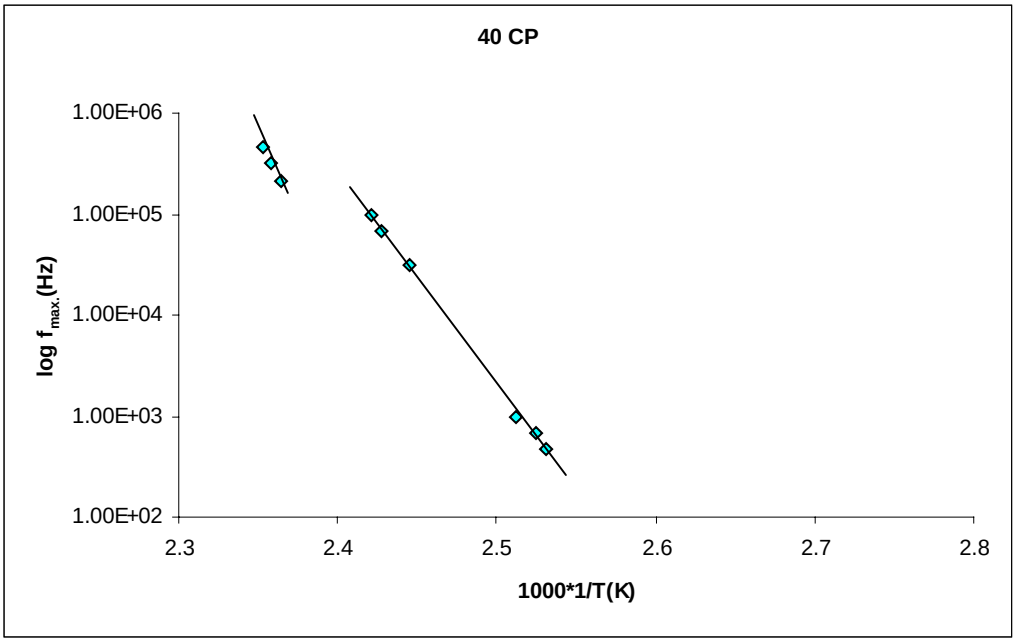

Figure 5.31b Arrhenius plot of frequency Vs reciprocal temperature for 40% PPS/ com. phlogopite

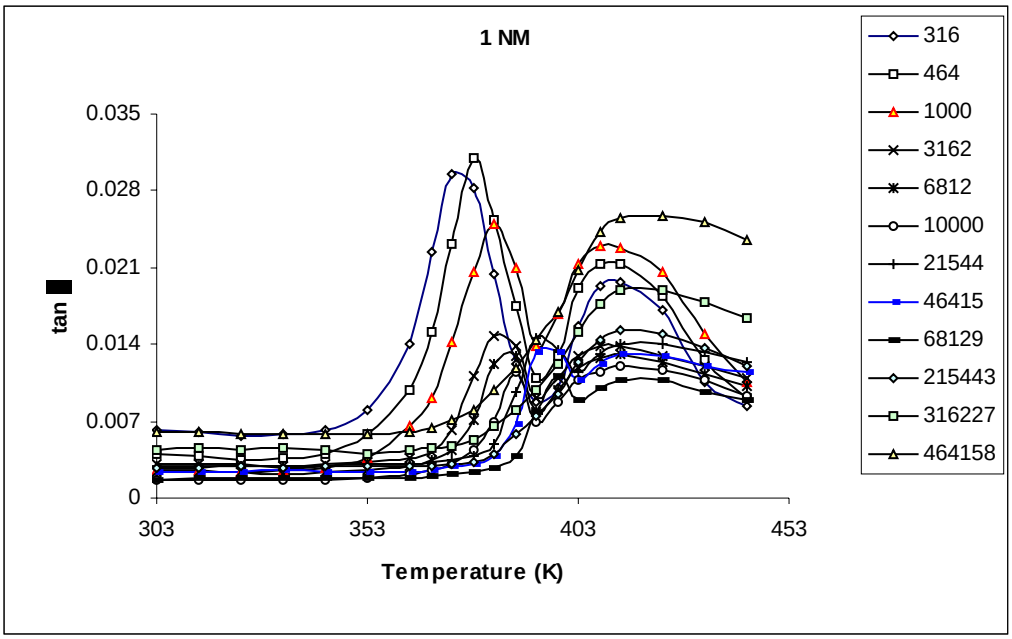

Figure 5.32a Isochron of tan δ Vs T for 1% PPS/ nanomuscovite (frequency in Hz)

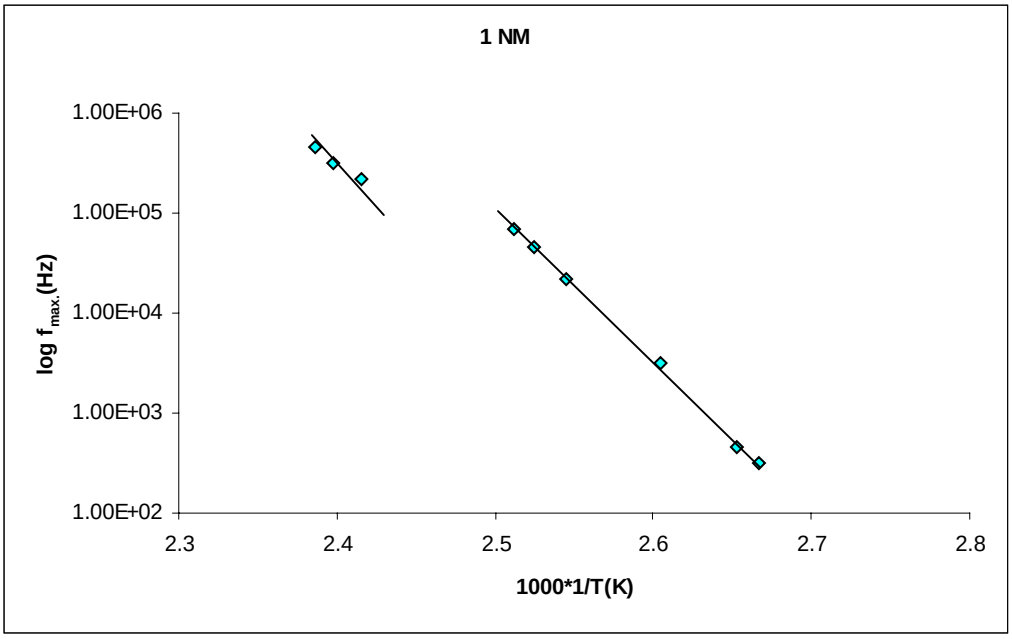

Figure 5.32b Arrhenius plot of frequency Vs reciprocal temperature for 1% PPS/ nanomuscovite

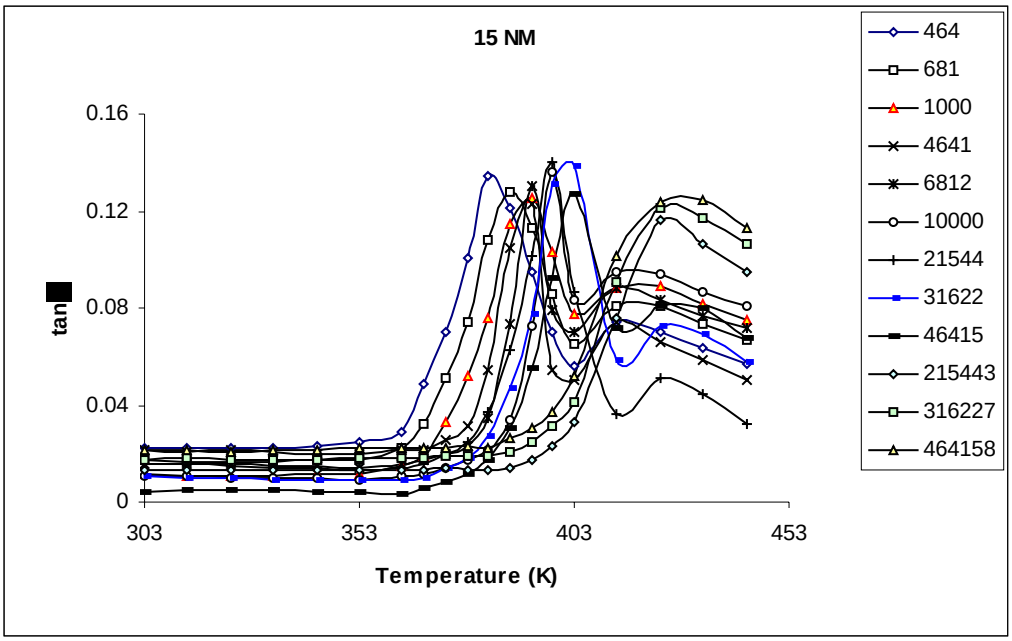

Figure 5.33a Isochron of tan δ Vs T for 15% PPS/ nanomuscovite (frequency in Hz)

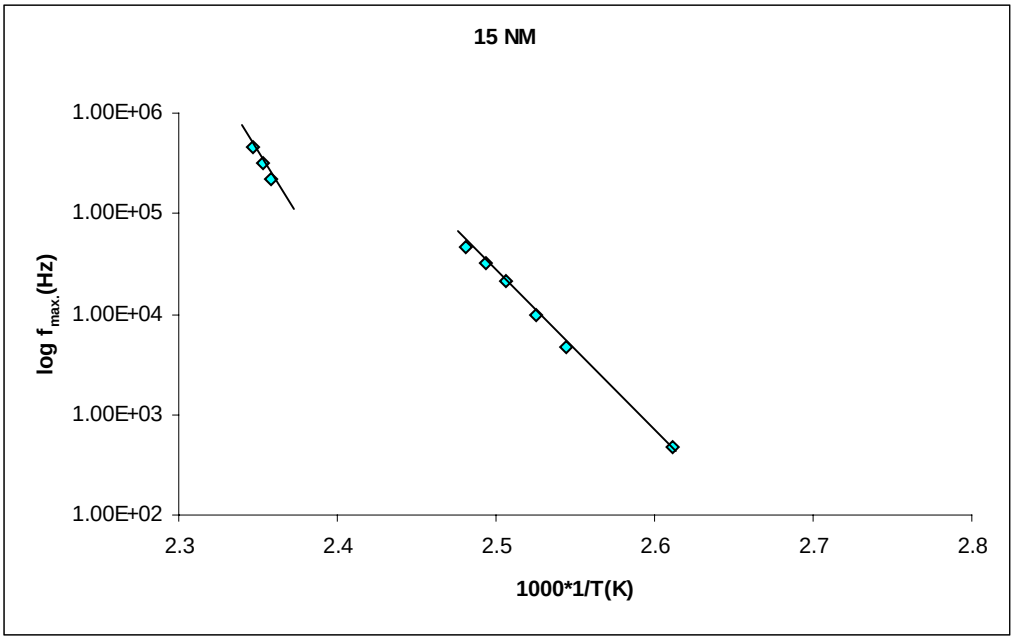

Figure 5.33b Arrhenius plot of frequency Vs reciprocal temperature for 15% PPS/ nanomuscovite

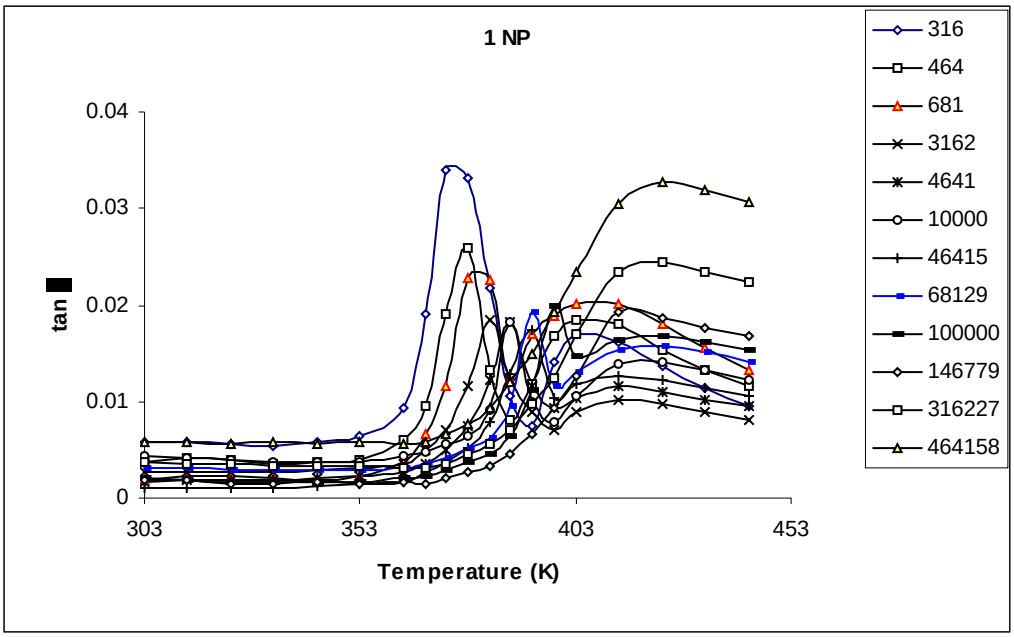

Figure 5.34a Isochron of tan δ Vs T for 1% PPS/ nanophlogopite (frequency in Hz)

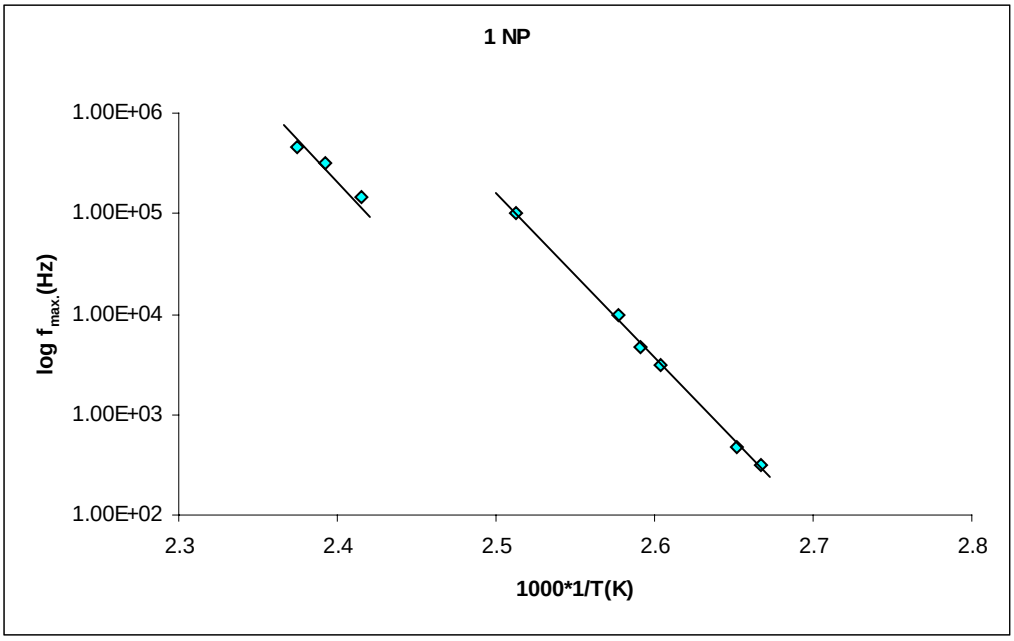

Figure 5.34b Arrhenius plot of frequency Vs reciprocal temperature for 1% PPS/ nanophlogopite

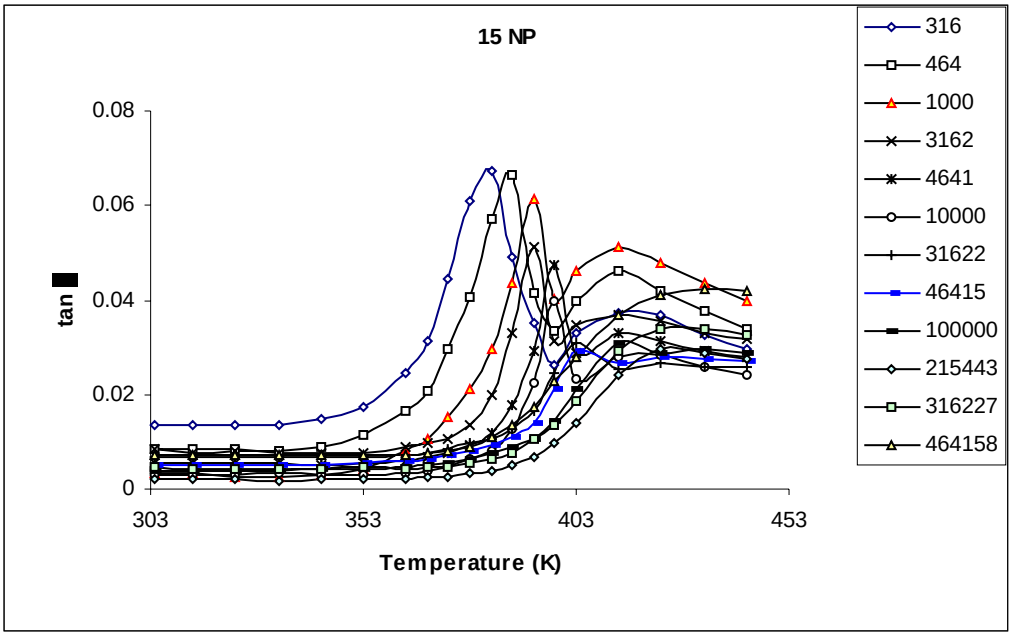

Figure 5.35a Isochron of tan δ Vs T for 15% PPS/ nanophlogopite (frequency in Hz)

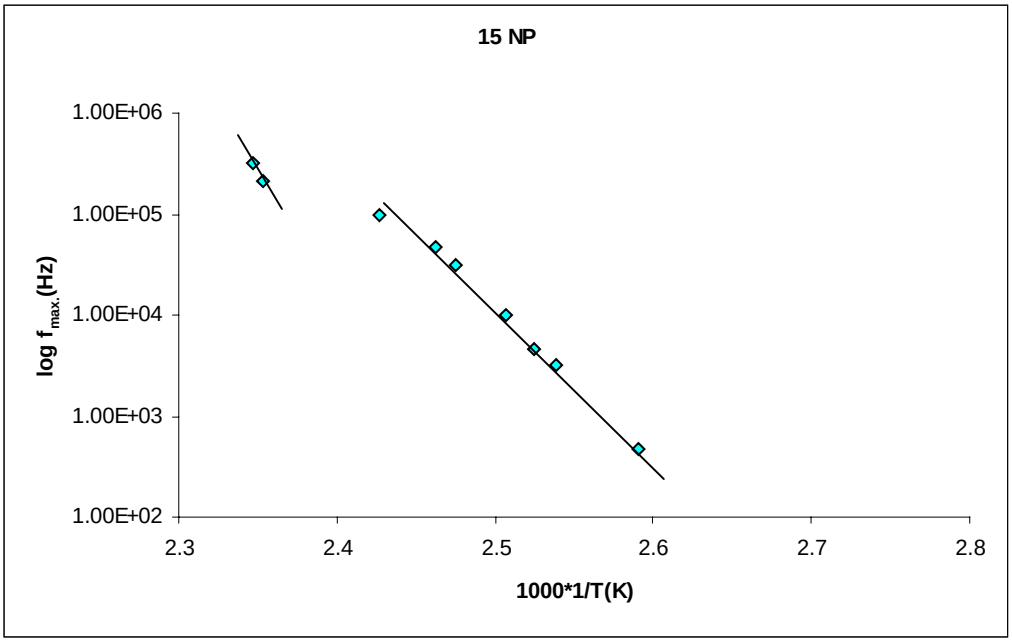

Figure 5.35b Arrhenius plot of frequency Vs reciprocal temperature for 15% PPS/ nanophlogopite

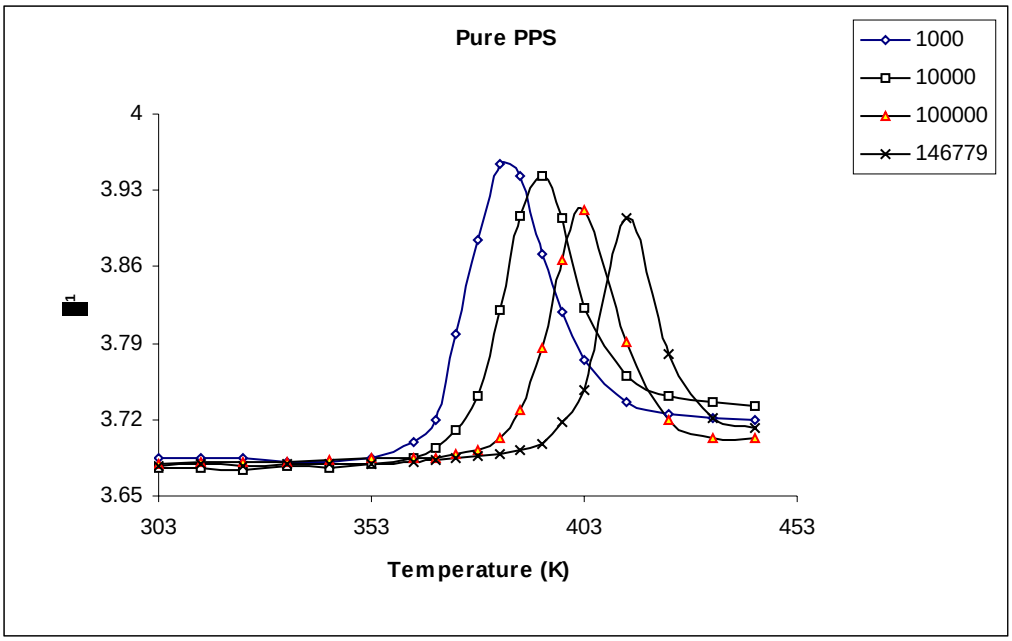

Figure 5.36 Isochron of ε^1 Vs T for pure PPS (frequency in Hz)

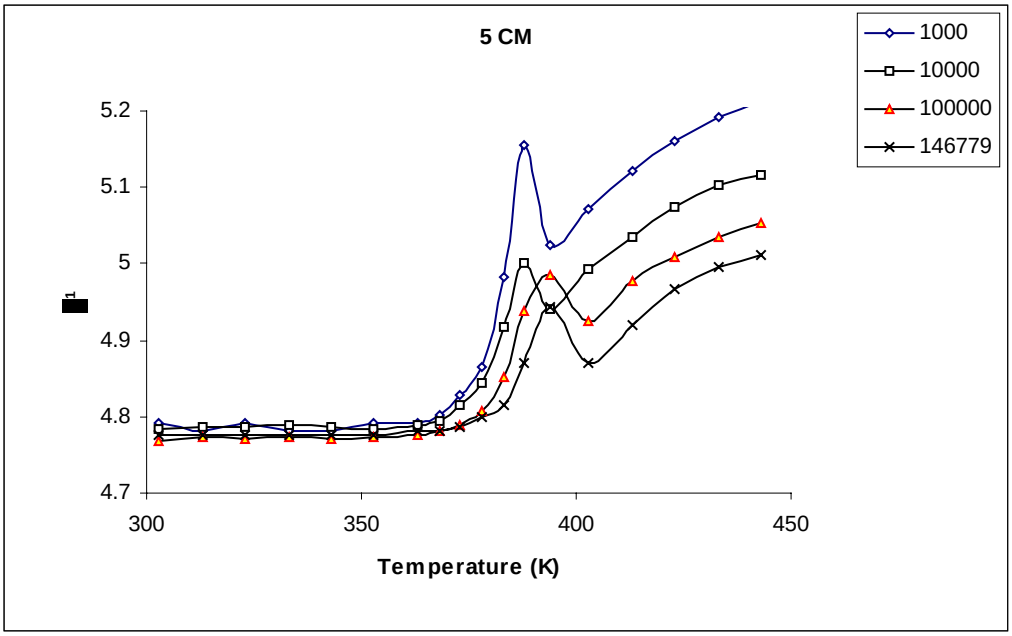

Figure 5.37 Isochron of ε^1 Vs T for 5% PPS/ com. muscovite (frequency in Hz)

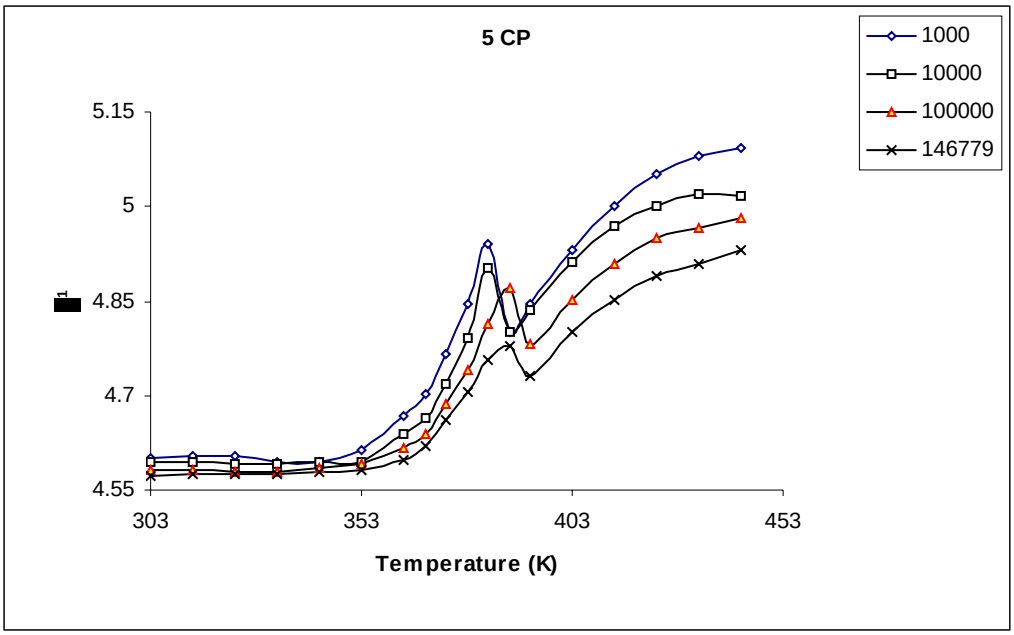

Figure 5.38 Isochron of ε^1 Vs T for 5% PPS/ com. phlogopite (frequency in Hz)

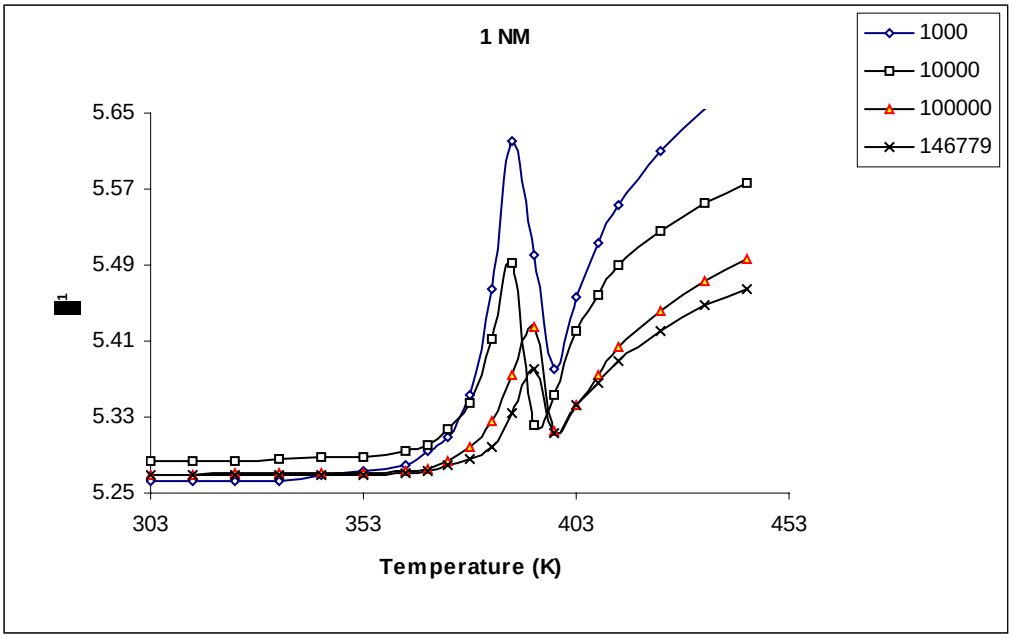

Figure 5.39 Isochron of ε^1 Vs T for 1% PPS/ nanomuscovite (frequency in Hz)

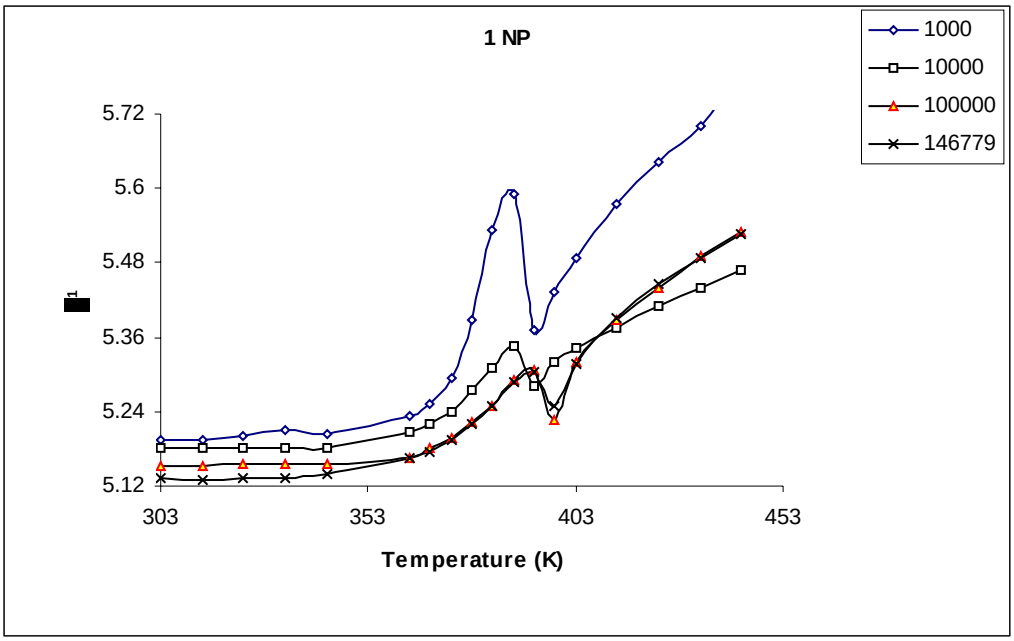

Figure 5.40 Isochron of ε^1 Vs T for 1% PPS/ nanophlogopite (frequency in Hz)

These characteristics are in tandem with those reported previously for pure PPS.[46-48] The same trend is observed in the case of the composites and nanocomposites, the only difference being a further positive offset in T_g due to the presence of mica. Incorporation of mica in to the PPS matrix is expected to increase the rigidity, which could be the reason for the increase in T_g. The loss maximum is observed at 373 K for pure PPS whereas it is seen at 393 K for 40% PPS/ commercial muscovite and phlogopite composites at 1 KHz. It is interesting to note that the loss maximum is observed at 393K in the case of 15% PPS/ mica nanocomposites too. The effect of crystallinity on the strength of dielectric relaxation is observed in the ΔE or peak height of the relaxation in ε^1 in this region (figures 5.36-5.40). These observations are also in agreement with the earlier reports on PPS samples crystallized under various thermal conditions.

The expected dielectric constants for the PPS/ mica composites based on the series-parallel model is given in the figure 5.41. The loss factor and dielectric constant of the PP/ mica composites and nanocomposites is represented as a function of mica composition in the figures 5.43a and b. The dramatic increment in the dielectric constant of the nanocomposites at much lower loadings as compared to the commercial mica composites is noteworthy. As in the case of PP/ mica composites, here again one finds that commercial phlogopite shows a higher dielectric constant than muscovite but nano-muscovite displays a higher dielectric constant than nano-phlogopite.

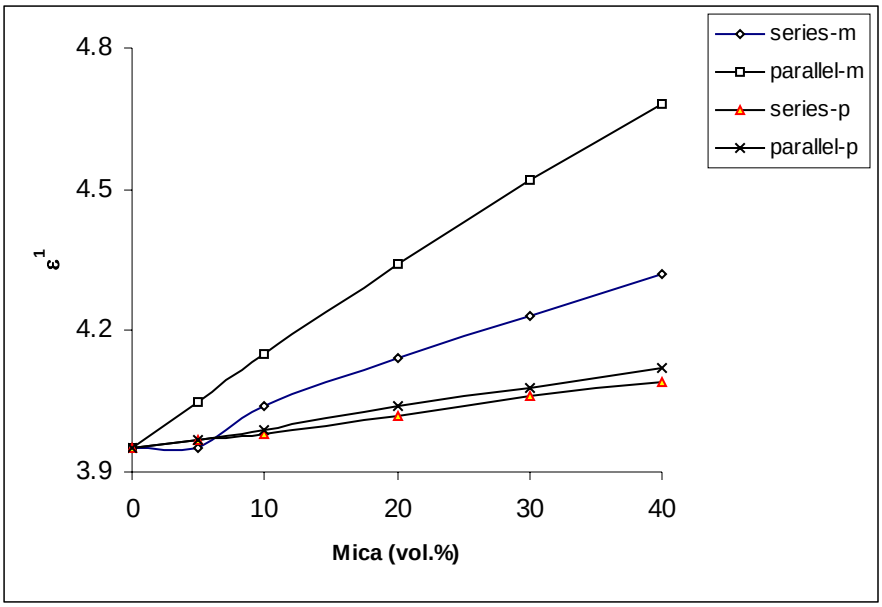

Figure 5.41 Dielectric constants of PPS/ mica composites based on series and parallel model (m & p refer to muscovite and phlogopite)

The marked difference in the dielectric response of mica and nano-mica might have its origin in the manner in which the mica/ nano-mica is dispersed in the PPS matrix. To evaluate this difference, SEM of the cross sections of PPS/ mica composites and nanocomposites were taken to investigate the respective microstructures.

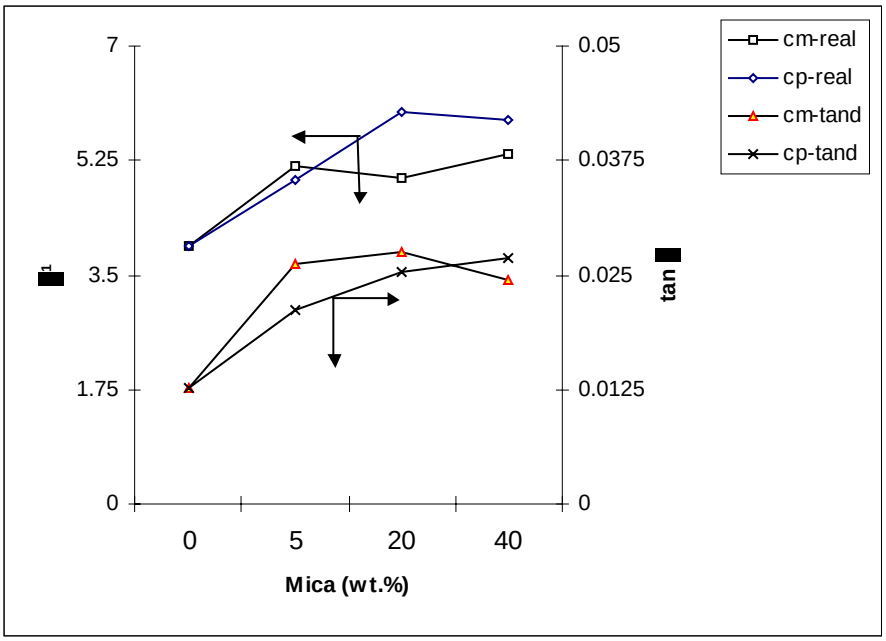

Figure 5.42a ε^1 and tan δ Vs mica loading for PP/ commercial mica composites

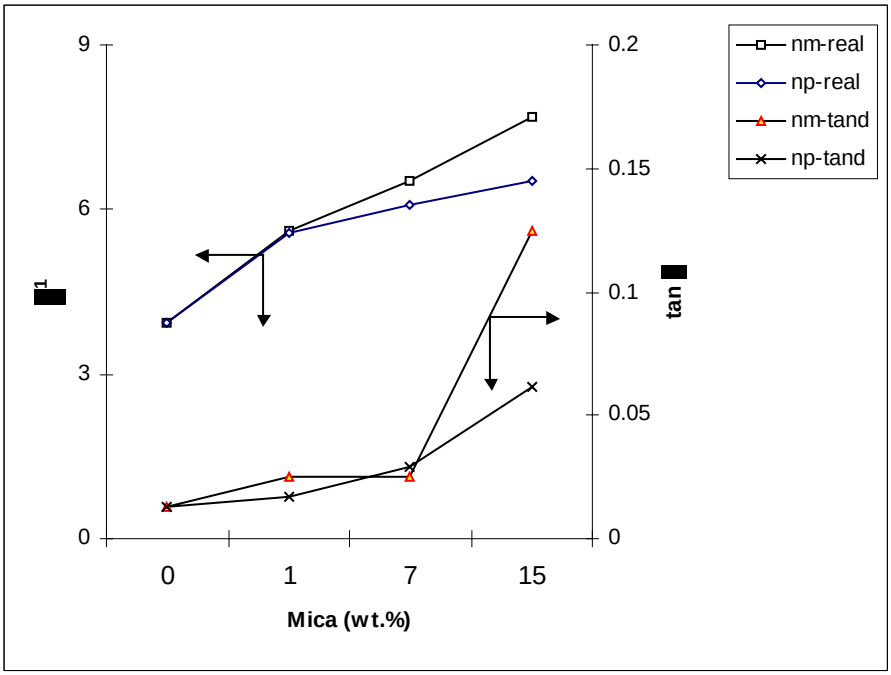

Figure 5.42b ε^1 and tan δ Vs mica loading for PP/ mica nanocomposites

The SEM of pure PPS is represented in the figure 5.43. The SEM's of the PPS/ commercial mica composites and nanocomposites are shown in the figures 5.44a-d, respectively. From the figures, it is very clear that PPS/ mica nanocomposites present a more uniform distribution as compared to the PPS/ commercial mica composites. One finds nano-mica tactoids homogeneously spread in the PPS matrix. Since the morphology at the matrix/ filler interface has a huge bearing on the relaxation dynamics, the microstructure at a single matrix filler interface was evaluated for commercial and nanomuscovite composites. The superior homogeneity and orientation of the nanocomposites is clearly established in this case as seen in the figures 5.45 a-d.

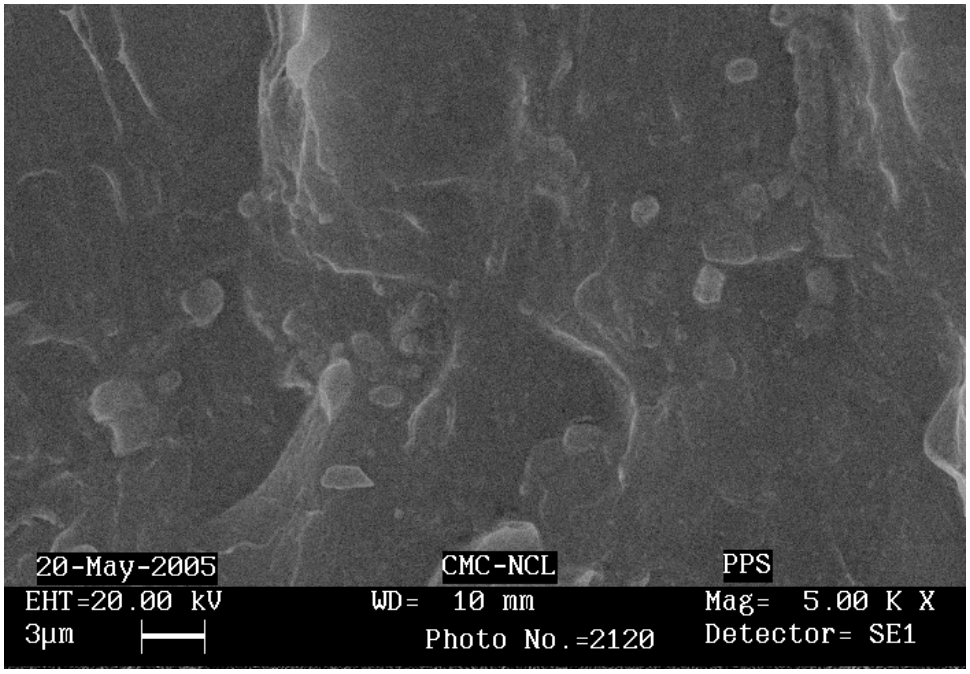

Figure 5.43 SEM of a cross-section of molded PPS sample

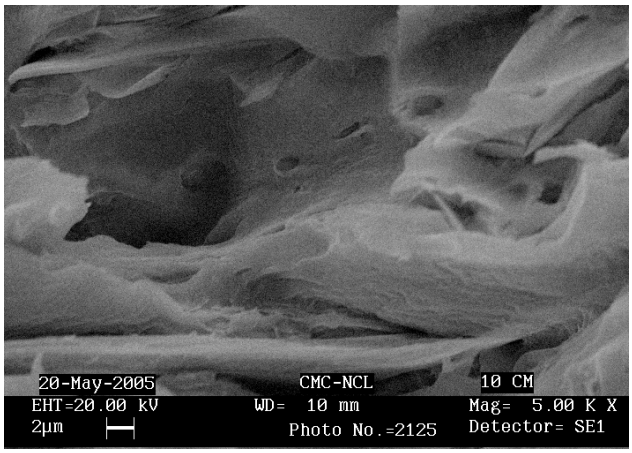

(a)

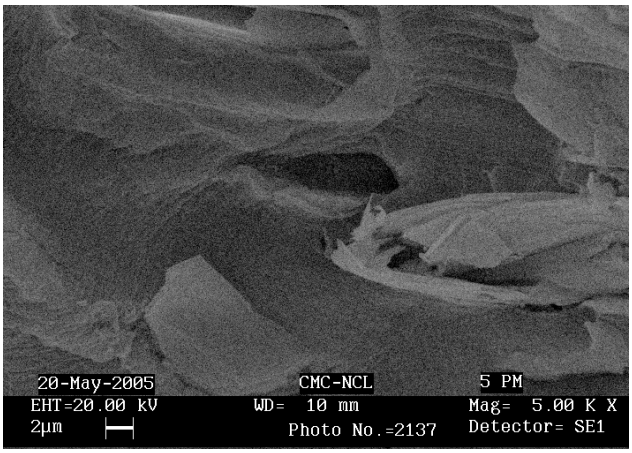

(b)

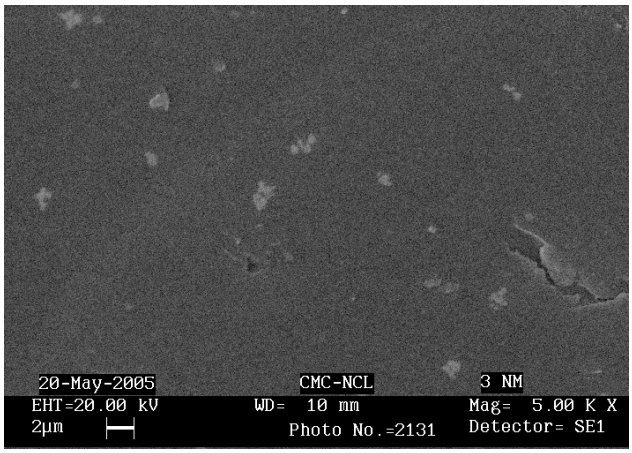

(c)

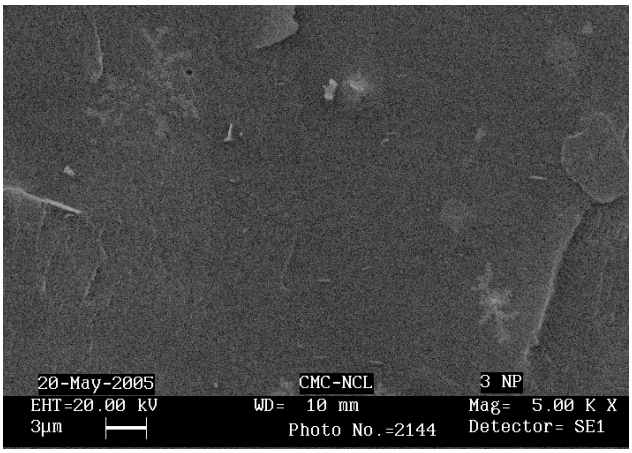

(d)

Figure 5.44 SEM of cross-sectioned samples of PPS/ mica composites and nanocomposites

(a) PPS/ com. muscovite (10 wt.%) **(b)** PPS/ com. phlogopite (5 wt.%)

(c) PPS/ nano-muscovite (3 wt.%) **(d)** PPS/ nano-phlogopite (3 wt.%)

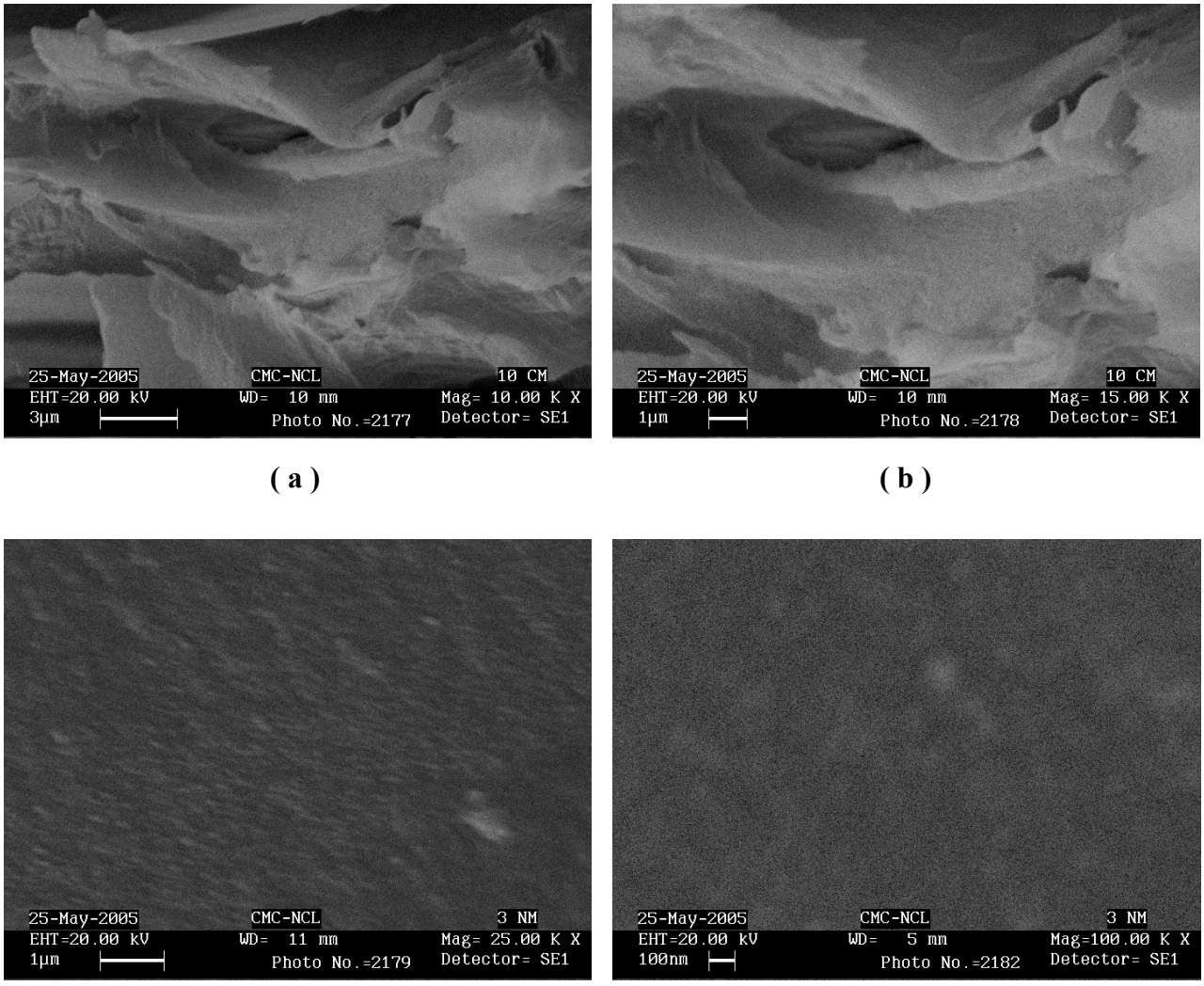

Figure 5.45 SEM of a single PPS/ mica and PPS/ nanomica interface

(a) & **(b)** PPS/ com. muscovite(10 wt.%) at magnifications of 10 K and 15 K

(c) & **(d)** PPS/ nano-muscovite(3 wt.%) at magnifications of 25 K and 100 K

As in the case of PP, the Maxwell-Wagner-Sillars[51-53] effect is also observed in these PPS/ mica nanocomposites. The shift of the loss peak towards lower frequencies with a corresponding increase in the tan δ values[54] is depicted in the figure 5.46.

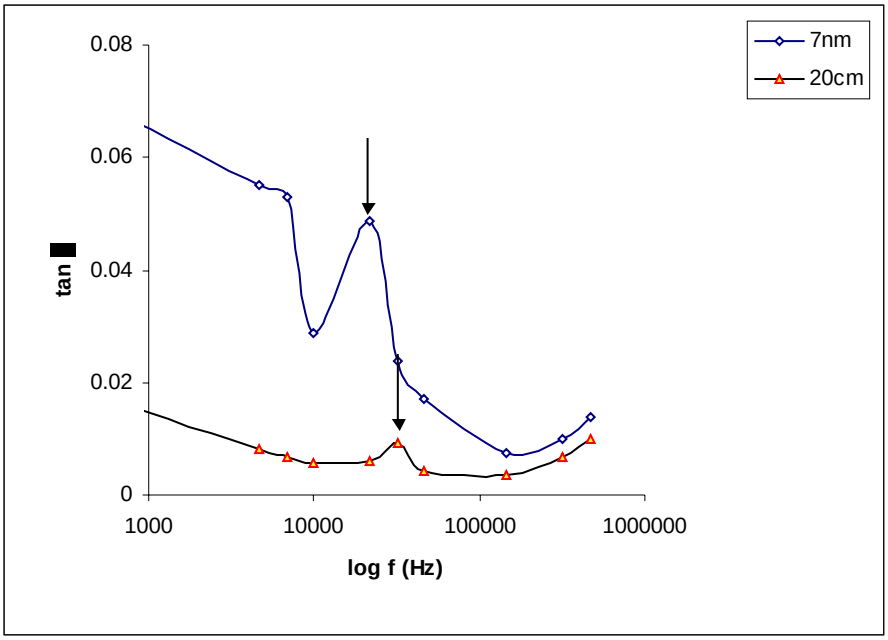

Figure 5.46 MWS effect in PPS/ mica nanocomposites

The activation energy of the α process was obtained from the slope of the Arrhenius plot of log (frequency) versus reciprocal temperature for all the composites and nanocomposites studied. These results are summarized in the table 5.4. The activation energy of the α process was found to increase tremendously with the incorporation of mica in PPS as compared to the original polymer. This can arise from the nucleation of PPS crystallites by mica particles, which lock the polymer chains at the mica interface. It may be pointed out that the effective surface area decreases when the additive concentration increases above certain limit, which leads to lower nucleation efficiency for higher filler concentration.[55] This effect becomes more pronounced for nanoparticulate

mica because of possibility of agglomeration. Nevertheless, the activation energy is higher in all filled PPS as compared to pure PPS.

Table 5.4 Activation energies of different relaxation processes in PPS

Composition (Mica wt.%)	**Activation Energy ($KJmol^{-1}$)**	
	α process	**β process**
Pure PPS	84	109
5 cm	241	159
20 cm	262	146
40 cm	215	175
5 cp	230	189
20 cp	239	183
40 cp	373	257
1 nm	215	196
7 nm	490	183
15 nm	262	190
1 np	207	192
7 np	213	175
15 np	278	164

5.7 Conclusions

The structure development and crystallization behavior of PPS/ mica composites and nanocomposites was analyzed by WAXD and DSC data of the annealed (at 260 ˚C) and melt crystallized (T_c-250 ˚C) samples. The intensity ratio of the 200 plane to that of 110 crystallographic plane of PPS was utilized to quantify the extent of orientation of PPS crystallites in presence of mica and nano-mica. This ratio was found to reduce on increased mica loading and the intensity of the 200 peak found to increase upon annealing. Thus, annealing in presence of both muscovite and phlogopite was found to reorient many crystallites of PPS along the 200 plane. Also, the ratio dropped steeply for phlogopite as compared to muscovite and also for commercial mica as compared to nano-mica. In case of the melt crystallized samples, an increase in the 200/ 110 intensity ratio was realized at lower mica loadings, which was found to drop down at higher loadings. A considerable reduction in the peak intensities (I_{003} / I_{020} for phlogopite and I_{009} / I_{006} for muscovite) of the major mica peaks was also noticed upon sintering. The orientation of PPS crystallites in presence of mica were confirmed theoretically by lattice mismatch calculations.

A positive offset in the T_c of the mica composites and nanocomposites was noticed indicating the role of mica as a nucleant. The offset was found to be greater in the case of nanocomposites as compared to the composites. A slight increase in the T_m of the PPS/ mica composites and nanocomposites was also noticed at lower mica loadings that subsequently decrease at higher mica loadings. The shift in T_c of the melt crystallized samples was found to be marginal as compared to the sintered samples. Phlogopite mica proved to be a better nucleator than muscovite mica in line with the theoretical

predictions. A gradual increase in the onset melting temperature of PPS was noticed which indicates that the stability of the least stable crystallites in the composite is improved by nucleation. The enthalpies of the sintered PPS/ commercial mica composites demonstrated a constant increase with mica loading whereas the enthalpies of the nanocomposites show a slight increase at very low mica loadings (1 wt.%), which decreases at higher loadings. In short, annealing was found to ensure a greater level of crystallinity in the samples as against melt crystallization.

The TGA of the PPS/ mica composites indicated a marginal increase in the degradation onset, a substantial increase in the maximum degradation temperature and a weight loss of 28-38 % whereas the nanocomposites showed a decrease in the maximum degradation temperature. This could be due to the presence of low molecular weight PPS produced by in situ polymerization along with nano-mica, which has a lower stability. The weight loss at the maximum degradation temperature for the PP/ mica nanocomposites was found to be lesser than that of the commercial PP/ mica composites.

The loss peak associated with glass-rubber α relaxation was seen at 373 K for pure PPS and the Arrhenius plots suggested the occurrence of also a distinct β process. The isochrons showed the usual shift in the loss factor and ε^1 to higher temperatures with increasing frequencies. A positive offset in T_g was observed for the PPS/ mica composites and nanocomposites. The significant increment in the dielectric constant of the nanocomposites at comparatively lower mica loadings was noteworthy. These results were interpreted in terms of enhanced crystallinity due to the better nucleating ability of nano-mica as compared to commercial mica. The effect of crystallinity on the strength of the dielectric relaxations was also noticed in the ε^1 isochrons. SEM was used to establish

the homogeneity of the nanocomposite sample, which is also one of the reasons for its altered dielectric behavior. Maxwell-Wagner-Sillars effect was observed in this case too as in the case of PP/ mica nanocomposites. In general, the activation energy of the α process obtained from the relaxation maps was found to increase which could be attributed to the nucleation of PPS crystallites by mica particles that lock the polymer chains at the mica interface. The activation energy of the β process was found to decrease as a function of mica loading.

5.8 References

1) Grenvesse, M. P. *Bull. Soc. Chim.* **1898**, *17*, 599.

2) Macallum, A. D. *J. Org. Chem.* **1948**, *13*, 154.

3) Lenz, R. W.; Carrington, W. K. *J. Polym. Sci.* **1959**, *41*, 333.

4) Lenz, R. W.; Handlovits, C. E. *J. Polym. Sci.* **1960**, *43*, 167.

5) Lenz, R. W.; Handlovits, C. E.; Smith, H. A. *J. Polym. Sci.* **1962**, *58*, 351.

6) Edmonds Jr. J. T.; Hill, H. W. US Patent No: 3,354,129 November 1967.

7) Tabor, B. J.; Magre, E. P.; Boon, J. *Eur. Polym. J.* **1971**, *7*, 1127.

8) Padden, F. J. *Bull. Am. Phys. Soc.* **1982**, *27*, 259.

9) Brady, D. G. *J. Appl. Polym. Sci.* **1976,** *20*, 2541.

10) Jog, J. P.; Nadkarni, V. M. *J. Appl. Polym. Sci.* **1985**, *30*, 997.

11) Lopez, L. C.; Wilkes, G. L. *Polymer* **1988**, *29*, 106.

12) Lopez, L. C.; Wilkes, G. L. *Ibid.* **1989**, *30*, 147.

13) Lopez, L. C.; Wilkes, G. L. Geibel, J. F. *Polymer* **1989**, *30*, 147.

14) Avrami, M. J. *J. Chem. Phys.* **1939**, *7*, 1103.

15) Avrami, M. J. *J. Chem. Phys.* **1940**, *8*, 212.

16) Avrami, M. J. *J. Chem. Phys.* **1941**, *9*, 177.

17) Lopez, L. C.; Wilkes, G. L. *Polymer* **1996**, *37*, 3623.

18) Lopez, L. C.; Wilkes, G. L. *Polymer* **1989**, *30*, 882.

19) Ozawa, T. *Polymer* **1971**, *12*, 150.

20) Radhakrishnan, S.; Nadkarni, V. M. *Polym. Eng. Sci.* **1984**, *24*, 1383.

21) Nadkarni, V. M.; Radhakrishnan, S. *Polym. Eng. Sci.* **1987**, *27*, 547.

22) Joshi, S. G.; Radhakrishnan, S. *Thin Solid Films* **1986**, *142*, 213.

23) Minkova, L. I.; Magagnini, P. L. *Polymer* **1995**, *36*, 2059.

24) Gabellini, G.; Bretas, R. E. S. *J. Appl. Polym. Sci.* **1996**, *61*, 1803.

25) Gabellini, G.; De Moraes, M. B.; Bretas, R. E. S. *J. Appl. Polym. Sci.* **1996**, *60*, 21.

26) Jog, J. P.; Shingankuli, V. L.; Nadkarni, V. M. *Polymer* **1993**, *34*, 1966.

27) Mai, K.; Zhang, S.; Zeng, H. *J. Appl. Polym. Sci.* **1999**, *74*, 3033.

28) Shibata, M.; Yosomiya, R.; Jiang, Z.; Yang, Z.; Wang, G.; Ma, R.; Wu, Z. *J. Appl. Polym. Sci.* **1999**, *74*, 1686.

29) Cheng, J. S.; Cebe, P. *Polymer* **1992**, *33*, 2312.

30) Cheng, J. S.; Cebe, P. *Polymer* **1992**, *33*, 2325.

31) Guschl, P. C.; Kim, H. S.; Otaigbe, J. U. *J. Appl. Polym. Sci.* **2002**, *83*, 1091.

32) Caminiti, R.; D' Illario, L.; Martinelli, A.; Piozzi, A. *Macromol. Chem. Phys.* **2001**, *202*, 2902.

33) Silvestre, C.; Di Pace, E.; Napolitano, R.; Pirrozi, B.; Cesario, G. *J. Polym. Sci., Part B: Polym. Phys.* **2001**, *39*, 415.

34) Lopez, L. C.; Wilkes, G. L. *J. Macromol. Sci., Rev. Macromol. Chem. Phys.* **1989** *C29*, 83.

35) Cebe, P. *Polym. Polym. Comp.* **1995**, *3*, 239.

36) Song, S. S.; White, J. L.; Cakmak, M. *Polym. Eng. Sci.* **1990**, *30*, 944.

37) Caramaro, L.; Chabert, B.; Chauchard, J. *Polym. Eng. Sci.* **1991**, *31*, 1279.

38) Desio, G. P.; Rebenfeld, L. *J. Appl. Polym. Sci.* **1990**, *39*, 825.

39) Hill Jr. H. W.; Edmonds Jr. J. T. *Adv. Chem. Ser.* **1973**, *129*, 80.

40) Ehlers, G. F. L.; Fisch, K. R.; Powell, W. R. *J. Polym. Sci., Part A-1* **1969**, *7*, 2955.

41) Aguilar, M.; Paul, D. R. *J. Polym. Sci. Part B: Polym. Phys.* **1993**, *31*, 1577.

42) Port, A. B.; Still, R. H. *Polym. Degrad. Stab.* **1979**, *1*, 133.

43) Lovell, P. A.; Still, R. H. *Br. Polym. J.* **1990**, *22*, 27.

44) Glatz, F. P.; Mulhaupt, R. *Polym. Bull.* **1993**, *31*, 129.

45) Li, X. G.; Huang, M. R.; Bai, H.; Yang, Y. L. *J. Appl. Polym. Sci.* **2002**, *83*, 2053.

46) Huo, P.; Cebe, P. *J. Polym. Sci., Part B: Polym. Phys.* **1992**, *30*, 239.

47) Kalika, D. S.; Wu, S. S.; Lamonte, R. R.; Makhija, S. *J. Macromol. Sci., Phys.* **1996**, *B35(2)*, 179.

48) El Shafee, E. *Polymer* **2001**, *42*, 8779.

49) Yasufuku, S.; Todoki, M. *IEEE Trans. Electr. Insul.* **1993**, *28*, 330.

50) Quamara, J. K.; Singh, N.; Singh, A. *Macromol. Chem. Phys.* **2001**, *202*, 1955.

51) Maxwell Garnett, J. C. *Philos. Trans. R. Soc. Lond.* **1904**, *203*, 385.

52) Wagner, K. W. *Arch. Elektrotechnol.* **1914**, *2*, 371.

53) Sillars, R. W. *J. Inst. Elect. Eng.* **1937**, *80*, 378.

54) Pochan, J. M.; Pai, D. M. In *Plastics Polymer Science and Technology*; Baijal, M. D., Ed.; Wiley Interscience: New York, 1982.

55) Saujanya, C.; Radhakrishnan, S. *Polymer* **2001**, *42*, 6723.

There has been a tremendous surge of activity in the field of polymer nanocomposites in the recent years. The ability to circumvent classic material performance trade-offs by accessing new properties and exploiting unique synergism between materials have spurred researchers the world over to explore novel synthetic paradigms towards polymeric nanocomposites. With mica fast gaining prominence amongst the various layered silicates, especially in hi-tech applications, investigation of new synthetic strategies for nanoparticulate mica looks promising.

In the present investigations described in this thesis, various types of mica that occur naturally like muscovite, phlogopite and chlorite were downsized to nanoscales by a novel technique of in situ intercalative polymerization by exploiting the ionic interactions between 1,4-dibromobenzene and the gallery ions of mica. The effect of average particle size and initial loading levels of mica on the extent of delamination were studied and correlated with the basic framework of unit cell parameters of the various micas. The crystallite size obtained in the final product after polymerization was found to decrease with decreasing particle size of initial starting mica and loading levels of mica. This clearly brought out the effect of polymerization on the extent of delamination of natural mica. Chlorite mica was delaminated to a greater extent as compared to muscovite and phlogopite mica, which could be explained on the basis of their respective crystal structures; chlorite having largest interlayer spacing among these micas. The nanoparticulate structure of mica was established by WAXD and TEM studies.

The efficacy of the synthesized nanoparticulate mica as a filler was evaluated by investigating its effect on the structure and properties of thermoplastic matrices like PP and PPS in the subsequent modules.

The incorporation of nanoparticulate mica in PP was found to decrease the induction time and crystallization half time with a corresponding increase in the growth rate resulting in smaller spherulites as compared to pure isotactic PP. Nanosize mica was found to nucleate PP and the nucleation rate was found to increase as an inverse exponential power of the particle size of mica i.e. finer mica particles were found to have higher nucleating efficiencies. Oriented growth of PP crystallites along the 040 plane (seen in the WAXD profiles) and a considerable shift in the T_c of the nanocomposites was noticed in the DSC's of the nanocomposites which confirmed that the nanosize mica was a good nucleating agent for the α polymorph of IPP. These observations were confirmed by lattice mismatch calculations, which indicated that nano-phlogopite is a better nucleator than nano-muscovite.

A gradual increment in tensile modulus was evident up to a mica loading of 10 wt.%, which is much higher than those that have been reported previously. The modulus of muscovite nanocomposites was greater than that of phlogopite nanocomposites. Pure PP and composites with low nanoparticulate mica loading showed yielding behavior with a clearly observable strain whitening whereas higher mica loadings showed brittle fracture. The flexural modulus and strength were found to increase sharply even at low concentration of nano-size micas. Tensile and flexural properties obtainable with 30 wt.% commercial mica were attained at 6 wt.% nano-mica loading.

A dramatic increase in the initial degradation temperature from 353 °C for pure PP to 388 °C for 10 wt.% PP/ phlogopite nanocomposite was observed which clearly establishes its thermal stability. A remarkable increase in the temperature of maximum degradation from 395 °C for pure PP to about 420-430 °C in the case of the composites

and nanocomposites was also observed. Also, the extent of degradation of PP at the maximum degradation temperature in case of the nanocomposites was much lower than that of the commercial composites, which could be related to the relatively high thermal conductivity of mica. The orientation of nanomica particles along the flow direction and its homogeneous dispersion in the PP matrix upon processing were established by SEM.

Two distinct relaxations were noticed in the dielectric relaxation studies i.e. the β relaxation centered at 283 K and a β′ relaxation at around 243 K for pure PP. The loss maximum was found to shift to higher temperature with increasing frequency for all the PP/ mica composites and nanocomposites. Pure PP showed a loss maximum at around 283 K, which was found to shift to 293 K with 10 wt.% commercial mica loading and 303 K at 30 wt.% mica loading. A dramatic increment in the dielectric constant of the PP/ mica nanocomposites at much lower loading levels (6 wt.%) was noticed which could be attributed to the anisotropy of mica particles, nucleation and creation of an oriented transcrystalline zone. There was also a substantial evidence of the Maxwell-Wagner-Sillars effect operating in these PP/ mica nanocomposites. The activation energy of the β process in PP was found to increase with the increase in mica loading in both the PP/ mica composites and nanocomposites whereas the activation energy of the β′ process was found to decrease with increased mica loading. This could be explained on the basis of the segmental mobility in the intercrystalline zones as well as the reinforcing effects of mica.

The structure development and crystallization behavior of PPS/ mica composites and nanocomposites were analyzed by WAXD and DSC data of the annealed (at 260 ˚C) and melt crystallized (T_c-250 ˚C) samples. The intensity ratio of the 200 plane to that of

110 crystallographic plane of PPS was utilized to quantify the extent of orientation of PPS crystallites in presence of mica and nano-mica. A tremendous variation in the intensities of the major XRD peaks of mica was also noticed. Annealing in presence of both muscovite and phlogopite was found to reorient many crystallites of PPS along the 200 plane, which were confirmed theoretically by lattice mismatch calculations.

A positive offset in the T_c of the mica composites and nanocomposites was noticed indicating the role of mica as a nucleant. The offset was found to be greater in the case of nanocomposites as compared to the composites. A slight increase in the T_m of the PPS/ mica composites and nanocomposites was also noticed at lower mica loadings that subsequently decrease at higher mica loadings. The shift in T_c of the melt crystallized samples was found to be marginal as compared to the sintered samples, which might have its origin in the difference of the respective temperature cycles. Phlogopite mica proved to be a better nucleator than muscovite mica in line with the theoretical predictions. Annealing was found to ensure a greater level of crystallinity in the samples as against melt crystallization.

The TGA of the PPS/ mica composites indicated a marginal increase in the degradation onset and a substantial increase in the maximum degradation temperature from 532 ˚C for pure PPS to about 545-550 ˚C in the case of the composites and nanocomposites. Another outstanding feature noticed is the much lower weight loss of the nanocomposites as compared to the composites at the maximum degradation temperature.

The loss peak associated with glass to rubber α relaxation was seen at 373 K for pure PPS and the Arrhenius plots suggested the occurrence, also of a distinct β process.

The isochrons showed the usual shift in the loss factor and ε^1 to higher temperatures with increasing frequencies. A positive offset in T_g was observed for the PPS/ mica composites and nanocomposites. The significant increment in the dielectric constant of the nanocomposites at comparatively lower mica loadings was noteworthy. These results were interpreted in terms of enhanced crystallinity due to the better nucleating ability of nanosize mica as compared to commercial mica. The effect of crystallinity on the strength of the dielectric relaxations was also noticed in the ε^1 isochrons. SEM was used to establish the homogeneity of the nanocomposite samples, which results in a high degree of orientation thereby increasing the dielectric constant. Maxwell-Wagner-Sillars effect was observed in this case too as in the case of PP/ mica nanocomposites. In general, the activation energy of the α process obtained from the relaxation maps was found to increase (due to enhanced crystallinity by nucleation and transcrystallinity) and that of the β process was found to decrease as a function of mica loading.

Thus, it could be concluded that naturally occurring mica can be downsized to nanoscales by in situ intercalative polymerization without any prior acid treatment. These various types of nanoparticulate mica synthesized were found to strongly influence the crystallization characteristics and properties of the thermoplastic matrices in which they were incorporated leading to interesting properties that could not be realized by the conventional micron sized mica. This process involves the diffusion of one of the reactants, in this case 1,4-dibromobenzene, in to the interlamellar spacings and subsequent reaction with the same at high temperature causing delamination. It may be pointed out that naturally occurring mica has cleavage planes normal to the *c*-axis and thus it is easier to downsize the particles, even mechanically. However, mechanical

processes have limitations and the maximum downsizing can be only up to a few microns. The present process might be called “polymer assisted cleavage” of mica particles, which leads to even smaller size. This type of technique may be useful in other materials like graphite: expanded graphite could be an example for the same.

It is interesting to mention here that the nano-size obtained for mica in the present studies is in the range of 10-40 nm and not less than 5 nm, which may cause total breakage of the structure. It is essential to retain some crystalline order and flaky morphology so that the particles can give reinforcing effect to the polymer matrix in the final composite. Also, surface treatment with coupling agent/ wetting agent is not essential for the mica obtained by the present process because it is already surrounded by the polymer matrix in which it is made. Thus, the present technique (which has been patented) leads to directly usable product. This new method having many possibilities for synthesizing nanoparticulate additives from naturally occurring minerals opens up a wide area of research, which can be explored by others.

LIST OF ABBREVIATIONS

ABS	acrylonitrile butadiene styrene
AC	alternating current
BA	*n*-butyl acrylate
CCD	closed circuit display
cm	commercial muscovite
com.	commercial
cp	commercial phlogopite
DBB	1,4-dibromobenzene
DC	direct current
DMAA	*N*,*N*-dimethylacrylamide
DMAc	*N*,*N*-dimethylacetamide
DRS	dielectric relaxation spectroscopy
DSC	differential scanning calorimetry
FT	fixed time
FT-IR	Fourier transform infra-red
HDPE	high-density polyethylene
HDT	Heat Deflection Temperature
HEMA	2-hydroxyethyl methacrylate
IPN	interpenetrating polymer network
IPP	isotactic polypropylene

KV	kilovolts
LCP	liquid crystalline polymer
MA	methyl acrylate
Mag.	magnification
MFI	melt flow index
MMA	methyl methacrylate
MMT	montmorillonite
MWS	Maxwell-Wagner-Sillars
N6	nylon-6
nm	nanomuscovite
NMP	*N*-methyl-2-pyrollidone
NNI	National Nanotechnology Initiative
np	nanophlogopite
PA	polyamide
PBO	poly(benzoxazole)
PBS	poly(butylene succinate)
PBT	poly(butylene terephthalate)
PC	polycarbonate
PCL	poly(ε-caprolactone)
PDMS	polydimethylsiloxane
PE	polyethylene
PEA	poly(ethyl acrylate)
PEO	poly(ethylene oxide)

PES	poly(ether sulfone)
PET	poly(ethylene terephthalate)
PEVA	poly(ethylene vinyl alcohol)
PIPN	pseudo-interpenetrating polymer network
PLA	polylactide
PMG	polymer mediated growth
PMMA	poly(methyl methacrylate)
POM	polarized optical microscopy
POSS	polyhedral oligomeric silsesquioxane
PP	polypropylene
PP-MA	maleic anhydride modified PP
PPS	poly(*p*-phenylene sulfide)
PPV	poly(*p*-phenylenevinylene)
PS	polystyrene
PTA	phenyleneterephthalamide
PU	polyurethane
PVP	poly(*N*-vinyl pyrollidone) or poly(2-vinylpyridine) or (4-vinylpyridine)
PVA	polyvinyl alcohol
PVAc	polyvinyl acetate
RAP	rigid amorphous phase
SALS	small angle light scattering
SAN	poly(styrene-*co*-acrylonitrile)
SEM	scanning electron microscopy

SWNT	single walled nanotube
TEM	transmission electron microscopy
TFEA	2,2,2-trifluoroethyl acrylate
TGA	thermo-gravimetric analysis
TMOS	tetramethoxysilane
UV	ultra-violet
WAXD	wide angle X-ray diffraction
Wt.	weight
2MOx	2-methyl-2-oxazoline
2D	two dimensional
3D	three dimensional

LIST OF SYMBOLS

B	constant
C_i	crystallinity index
d	particle size
dF	free energy of formation of nuclei of critical size
E	activation energy for transport across liquid solid interface
E_D	energy of transport in the solid-liquid interface
G	growth rate at temperature T
G_0	constant
ΔG^*	free energy of formation of a stable nucleus
ΔH_c	enthalpy of crystallization
ΔH_m	enthalpy of melting
ΔH^*	Arrhenius activation enthalpy per mole
K	constant
L	crystallite size
l_s	lattice parameter along any axis for the substrate
l_g	lattice parameter along any axis for the growing media
n	Avrami exponent
N	steady state nucleation rate
N_0	constant
p,q	integers
R	universal gas constant

t	time
$\tan \delta$	dielectric loss factor
T	temperature
T_c	crystallization temperature
T_g	glass-transition temperature
T_m	melting temperature
X_t	crystallinity at time 't'
ψ_a	area of the amorphous halo in the WAXD pattern of the sample
ψ_c	area of the amorphous halo in the WAXD pattern of the sample
λ	wavelength
$\Delta\theta$	breadth of the WAXD peak in radians
θ	diffraction angle
ε^*	complex dielectric constant
ε'	dielectric constant (real)
ε''	dielectric constant (imaginary)
μ	micron
α, β, γ	polymorphs of isotactic PP/ dielectric relaxations
δ	lattice mismatch parameter
ω	frequency of the field
τ	relaxation time

List of Publications/ Patents

1. A Process for the Synthesis of Nanoparticulate Mica

   S. Radhakrishnan and **S.Subramanyam**, *160 DEL 2004, US Patent filed.*

2. Synthesis of Nanoparticulate Natural Mica Composites by In situ Polymerization Technique

   S. Radhakrishnan and **S.Subramanyam** (*accepted for publication in International Journal of Nanotechnology)*

3. Crystallization Behavior and Structure Development in PP/ Mica Nanocomposites

   S. Radhakrishnan and **S.Subramanyam** (*Manuscript under preparation*)

4. Mechanical and Electrical Properties of PP/ Mica Nanocomposites

   S. Radhakrishnan and **S.Subramanyam** (*Manuscript under preparation*)

5. Crystallization Behavior and Structure Development in PPS/ Mica Nanocomposites

   S. Radhakrishnan and **S.Subramanyam** (*Manuscript under preparation*)